Mn (III)-containing compounds : synthesis and electrocatalytic properties in the oxygen reduction reaction

Kirill Dosaev

UNIVERSITÉ DE STRASBOURG

UNIVERSITÉ DE STRASBOURG

EDSC
École Doctorale des Sciences Chimiques

ÉCOLE DOCTORALE SCIENCES CHIMIQUES (ED222)

Institut de Chimie et Procédés pour l'Energie, l'Environnement et la Santé (ICPEES-UMR 7515)

THÈSE présentée par :

Kirill DOSAEV

soutenue le : **14 décembre 2022**

pour obtenir le grade de : **Docteur de l'université de Strasbourg**

Discipline/ Spécialité : Chimie / Physique- Chimie

Composés à base de Mn (III): synthèse et propriétés électrocatalytiques dans la réaction de réduction de l'oxygène

Mn(III)-containing compounds: synthesis and electrocatalytic properties in the oxygen reduction reaction

THÈSE dirigée par :

Mme. SAVINOVA Elena	Professeur, Université de Strasbourg

RAPPORTEURS :

Mme. ROTH Christina	Professeur, University of Bayreuth
Mme. MIKHAILOVA Daria	Directeur de recherches, Leibniz Institute for Solid State and Materials Research

AUTRES MEMBRES DU JURY :

Mme. KÉRANGUÉVEN Gwénaëlle	Maître de Conférences, Université de Strasbourg
M. BONNEFONT Antoine	Professeur, Grenoble INP
M. CHATENET Marian	Professeur, Grenoble INP

INVITES :

M. ANTIPOV Evgeny V.	Professeur, Lomonosov Moscow State University (**invité**)
M. ISTOMIN Sergey Ya.	Dr., Lomonosov Moscow State University (**invité**)

Acknowledgements

This PhD story would not have been possible without the participation and help of a lot of people and organizations. I would like to thank all of them.

First of all, I would like to thank **Campus France** for financially supporting my thesis through the Eiffel Scholarship.

Words cannot express how grateful I am to my supervisor **Elena Savinova**. Her help is invaluable. I am very grateful for the regular meetings at which we discussed the results and for invaluable advice in conducting experiments. This dissertation would not be what it is without her help and support.

Supervisors contributed equally to this work from the Moscow State University. Without a discussion with **Evgeny Antipov**, we would not have been able to understand a lot. **Istomin Sergey** has been my supervisor since 2016. During this time, more than one of my works was read, and I am incredibly grateful to him for his patience.

Of course, I cannot but thank **Tsirlina Galina**. Although the discussions with her were difficult for me, I feel that I understood electrochemistry more deeply with each of them.

I would like to thank **Gwénaëlle Kérangueven**, who was always willing to help with experiments and equipment. With her steady hand the lab was always in order. Also, from the first day in France, **Sergey Pronkin** helped me get used to the laboratory. I always knew who I could turn to for help if something was missing.

Special thanks also to **Antoine Bonnefont** from l'Institut de Chimie for always being ready to discuss our results and gave useful advice. Without these discussions, we would not have been able to make sense of all the data available.

I also turn to all the people who help me to characterise the material — **Thierry Dintzer** for SEM/EDX analysis. **Fabrice Vigneron,** who has provided excellent training in BET analysis. **Vasiliki Papaefthymiou** performed a considerable amount of XPS measurements on my samples and only thanks to this we could detect the effects described in this paper. The obtained

XPS data was discussed with **Viktoriia Saveleva**, which made it possible to significantly improve the result of their processing.

I would like to thank **Artem Abakumov** for the opportunity to conduct experiments at Skoltech.

We would not have obtained such informative data without synchrotron measurements at the Bessy-II synchrotron (Germany). Of course, these measurements would not have been possible without the close collaboration with **Juan Velasco Vélez, Jean-Jacques Gallet and Fabrice Bourne.**

During my stay in France, I met many wonderful students. Of course, these are **Benjamin Rotonnelli, Liza Royer, and Viktoria Zemtsova**. It is a pleasure to work in such a friendly and sociable team.

It was also great to work at Moscow State University among my colleagues - **Zoya Bobyleva, Mirza Abdullaev, and Vitaly Shevchenko**. I hope everyone gets a PhD soon.

Ultimately, I would like to thank those without whom our laboratory could not function. **Julien Bertrand**, whose assistance in administrative matters was invaluable. For technical aspects in the lab – **Alain Rach.**

Table of Contents

Acknowledgements 3

List of abbreviations 8

List of Figures ..... **Ошибка! Закладка не определена.**

List of Tables 20

General Introduction 22

1. Literature review 25

1.1 Oxygen reduction reaction 25

1.1.1 Hydrogen peroxide generation 27

1.1.2 Oxygen reduction reaction mechanism on carbon materials 31

1.1.3 Oxygen reduction reaction mechanism on platinum 34

1.2 Oxygen reduction catalysts based on transition metal oxides 37

1.2.1 Spinels 37

1.2.2 Perovskites 39

1.2.3. The role of carbon in oxygen reduction on oxide-carbon compositions 45

1.3 Manganese oxides 47

1.4 Degradation (transformation) processes of oxygen reduction electrocatalysts 57

1.4.1 Degradation processes on platinum surfaces 57

1.4.2 Degradation processes on the surface of 3d metal oxides 59

1.5 Conclusions 62

1.6 References 63

2. Material 73

2.1. Reagents used 73

2.2. Materials synthesis 74

2.3. Characterisation of oxide materials 74

2.4. Analytical methods of analysis 76

2.4.1. Preparation and standardisation of $KMnO_4$ solution 76

2.4.2. Titration of H_2O_2 with standardised $KMnO_4$ solution 77

2.4.3. Oxygen stoichiometry in oxide samples 77

2.5. Electrochemical measurements....78
2.5.1. Electrode and cell preparation....78
2.5.2. Electrochemical measurements....80
2.5.3. Calibration of the mercury oxide electrode in relation to the reversible hydrogen electrode....83
2.5.4. Methods for electrochemical studies of the effect of electrolyte composition....86
2.6. Investigation of the oxide degradation....87
2.6.1. Electrochemical measurements....87
2.6.2. Physicochemical study of oxide degradation....88
2.7 Determination of point of zero charge....90
2.8. References....93
3. AMn_2O_4 spinels (A - Li, Mg, Mn, Cd) as ORR catalysts: The role of Mn coordination and oxidation state in the catalytic activity and their propensity to degradation....94
3.1. Introduction....94
3.2. Materials and methods....96
3.3. Results and discussion....96
3.3.1. Phase composition and microstructure....96
3.3.2. Electrochemical characterization of the spinels....100
3.3.3. Post-mortem XPS study of AMn_2O_4 spinels after various treatments....111
3.4. Conclusions....121
3.5. References....123
4. Investigation of the oxide/electrolyte interface....130
4.1. Introduction....130
4.1.1. Literature review....131
4.1.2. Conclusions and problem statement....141
4.2. Materials and methods....142
4.3. Results and discussion....144
4.3.1. Influence of pH and cations....144
4.3.2. Influence of the scan rate on the interfacial recharging....151
4.3.3. Acid-base titrations....154
4.4. Conclusions....157

4.5. References....158
5. Effect of the Electrolyte Composition on the ORR Kinetics on Mn oxides....163
5.1 Introduction....163
5.1.1 Literature review....164
5.1.2 Conclusions....175
5.2 Experimental....176
5.3 Results and discussion....178
5.3.1 Influence of pH on the ORR and electrochemical hydrogen peroxide reactions....178
5.3.2 Effect of the Na^+ Concentration on the ORR and electrochemical hydrogen peroxide reactions....187
5.3.3 General discussion....193
5.4 Conclusions....200
5.5 References....200
General Conclusions and Outlook....205
Annex....208
Annex to Chapter 3....208
Annex to Chapter 4....210
Annex to Chapter 5....220
Résumé de la thèse en français....228

List of abbreviations

AFC : Alkaline fuel cell

AEMFC : Anion exchange membrane fuel cell

BE : Binding energy

BET : Brunauer, Emmett and Teller method for determining specific surface area by low temperature N_2 adsorption

CN : Coordination number

CV : Cyclic Voltammetry

EASA : Electrochemically active surface area

EDX : Energy-Dispersive X-Ray spectroscopy

FC : Fuel cell

HPOR : Hydrogen peroxide oxidation reaction

HPRR : Hydrogen peroxide reduction reaction

ICDD : International Centre of Diffraction Data

IEP : Isoelectric point

KL : Koutecký–Levich

NEXAFS : Near edge X-ray absorption fine structure

OCP : Open circuit potential

OER : Oxygen Evolution Reaction

ORR : Oxygen Reduction Reaction

PZC : Point of zero charge

RDE : Rotating Disk Electrode

RRDE : Rotating Ring-Disk Electrode

RDS: Rate-Determining Step

RHE: Reversible Hydrogen Electrode

SEM : Scanning Electron Microscopy

SHE: Standard Hydrogen Electrode

VC : Vulcan carbon

XAS: X-ray absorption spectroscopy

XES: X-ray emission spectroscopy

XPS : X-Ray Photoelectron Spectroscopy

XRD : X-Ray Diffraction

XRPD : X-ray powder diffraction

List of Figures

Fig. 1 Oxygen electroreduction scheme proposed by Wroblowa et al. [9].

Fig. 2 Scheme of the anthraquinone method of hydrogen peroxide production.

Fig. 3 Proposed ORR mechanism in an acidic medium based on Pd-Au alloy with low (a) and high (c) Pd content, and volcano-like dependence (b) between the H_2O_2 yield and Pd content in Pd_xAu_{1-x}[19].

Fig. 4 Schematic representation of active centres in carbon materials doped with nitrogen and the corresponding N1s binding energies in the photoelectron spectrum.

Fig. 5 Comparison of various classes of catalysts for the oxygen reduction reaction to H_2O_2 [20] in an alkaline medium.

Fig. 6 Two types of superoxide adsorbed on the surface of a glassy carbon electrode [35].

Fig. 7 Schematic representation of the structure of the electric double layer in an alkaline medium and the ORR process. Subfigures (a) and (b) illustrate the processes of electron transfer to the inner and outer spheres [36].

Fig. 8 The general mechanism of the ORR on platinum proposed by Anastasijevic [43].

Fig. 9 Structures of (a) normal spinel (for example, $MgAl_2O_4$), (b) inverse spinel (for example, $NiFe_2O_4$), and (c) complex spinel (for example, $CuAl_2O_4$) in different representations. Green and purple polyhedrons correspond to octahedral and tetrahedral sites filled with metal cations, respectively. Representative defect locations A, B, and O in spinel AB_2O_4 are shown in panel a. (d) Normal spinel in various projections (111), (311) and (400) [49].

Fig. 10 Crystal structure of cubic perovskite. The A-cation is in the cuboctahedron (CN = 12), and the B-cation is in the octahedron (CN = 6).

Fig. 11 Dependence of the oxygen reduction potential at a 25 μA cm^{-2} current density for perovskites of various 3d metals [51] on the oxygen desorption onset temperature.

Fig. 12 Dependence of the calculated oxygen reduction potential on the Gibbs energy of B-OH intermediate on the catalyst surface [52].

Fig. 13 Dependence of the catalytic activity of perovskites (potential at the current density 25 μA cm^{-2}_{oxide}) on the degree of filling of the e_g orbital of the 3d metal cations [53].

Fig. 14 Interaction of Mn^{3+} e_g-orbital and oxygen π*-orbital [53].

Fig. 15 a) The degree of perovskite structure distortion depending on the chosen substrate. b) Currents in the oxygen reduction reaction (left scale) and oxygen evolution reaction (right scale) at an overpotential of 400 mV [57]. c) ORR current at an overpotential of 400 mV depending on the degree of deformation of the $LaNiO_3$ crystal structure [58].

Fig. 16. Dependence of the ORR current at -20 mV relative to the Hg/HgO electrode on the magnetic moment of the B-cation [57,58].

Fig. 17 Tentative scheme of the oxygen reduction reaction on transition metal oxide proposed in Ref. [55].

Fig. 18 Cyclic voltammogram curves in the supporting electrolyte (a) and RDE curves of the oxygen reduction reaction (b) at a rotation speed of 900 rpm $La_{0.8}Sr_{0.2}MnO_3$ with different carbon loading (from 18 to 820 μg cm^{-2}) and a fixed oxide loading of 91 μg cm^{-2} in 1 M NaOH at a scan rate of 10 mV s^{-1} [61].

Fig. 19 Graphical representation of the processes occurring during the reduction of oxygen on a perovskite/carbon composite. Reproduced from Ref. [62].

Fig. 20 Suggested mechanism of the oxygen reduction on electrodes made of $La_{1-x}Sr_xCoO_{3-\delta}$ /carbon composite. Reproduced from Ref. [66].

Fig. 21 Crystal structure of γ-MnOOH.

Fig. 22 a) Crystal structure of α-Mn_2O_3, b) formation of octahedrons in the α-Mn_2O_3 structure, c) A and A' layers of α-Mn_2O_3 [68].

Fig. 23 Crystal structures of α- MnO_2 (a), β-MnO_2 (b), γ-MnO_2 (c) [69].

Fig. 24 Dependence of ORR kinetic current densities at 0.9 V vs. RHE on the formal potential (E_f) of the interfacial redox Mn(IV)/Mn(III) transition (a), and ORR polarization curves obtained on a rotating disk electrode in oxygen-saturated 1 M NaOH at 900 rpm and potential scan rate 10 mV/s (b) (numbers 1-3 denote Mn_2O_3 samples obtained according to different synthesis methods and hence specific surface area, 4-6 are manganese perovskites of different compositions, 7 and 7' are MnO_2 samples before and after cathodic degradation, respectively, 8 refers to MnOOH, 9 – to Mn_3O_4). Reproduced from Ref. [10].

Fig. 25 The mechanism of the oxygen reduction reaction on manganese oxides proposed in Ref. [10].

Fig. 26 Energy curves for bond cleavage in HO_2^- on Mn_2O_3 (a) and MnOOH (b) clusters [90].

Fig. 27 Study of the cathodic stability of $Sr_{0.5}Gd_{0.5}Mn_{0.75}Co_{0.25}O_{2.98}$ (a-c) and $Sr_{0.5}Gd_{0.5}Mn_{0.25}Co_{0.75}O_{2.87}$ (d-f). CVs with a variable cathodic limit for GC-supported compositions of perovskite oxide and Subunit carbon (loading: 91 μg cm^{-2}_{geo} each) at 10 mV s^{-1} in 1 M NaOH solution saturated with nitrogen (a, d); the corresponding cathodic (⊖) and anodic (⊕) CV charges (b, e); cathodic (⊖) and anodic (⊕) charges extracted from CV obtained in a narrow potential window [0.93; 1.13 V vs. RHE] recorded after applying each cathodic limit (c, f). Reproduced from Ref. [100].

Fig. 28 Dissolution rate of Mn from manganese oxides (α-MnO_2, δ -MnO_2, γ -MnO_2, Mn_2O_3) upon cycling in different potential intervals at 5 mV/s. (a) Data obtained in 0.05 M NaOH solution purged with oxygen (red) and argon (blue). (b) Dissolution of the oxide in 0.05 M NaOH purified from oxygen with argon for various concentrations of H_2O_2 (0, 1, 5, 10 μM) [102].

Fig. 29 Nafion's general formula.

Fig 30 CVs of MnOOH/Sibunit carbon compositions acquired in N_2-purged 0.01 M NaOH + 1.99 M $NaClO_4$ at a scan rate of 10 mV s^{-1} with variable cathodic limit before carbon subtraction (a) and after subtraction of the carbon contribution (c). Oxide loading on the GC surface is 91 μg cm^{-2}, carbon loading is 91 μg cm^{-2}. Current is normalized to the geometric surface of the GC electrode.

Fig. 31 RDE curves of MnOOH/C in 0.1M NaOH + 1.9M $NaClO_4$ for the ORR (blue) and HPOR/HPRR (orange) reactions, shown after background curves have been subtracted.

Fig. 32. Reproducibility of RDE voltammograms acquired for Mn_2O_3 in various electrolytes (as indicated in the panels) at 10 mV s^{-1} and 900 rpm. oxide loading is 91 μg cm^{-2} and carbon loading is 91 μg cm^{-2}. Red, blue and black curves correspond to three independent measurements on newly prepared thin film electrodes.

Fig. 33 Example of a CV of a platinised Pt electrode at a scan rate 10 mV s^{-1} in 0.1 M NaOH purged with N_2 (a) and H_2 (b).

Fig. 34 Nyquist plot of the impedance hodograph (top), described using the presented equivalent circuit and Bode plot - real part of impedance and phase as a function of frequency (bottom). Given for Mn_2O_3/C in 0.1M NaOH.

Fig. 35 The polarisation curves of the electrochemical hydrogen peroxide oxidation/reduction reactions (HPOR/HPRR) acquired for MnOOH deposited on a GC RDE in 0.01N NaOH + 0.84 mM H_2O_2 solution before IR correction (black) and after IR correction (red). Rotation rate 900 rpm. Scan rate is 10 mV/s; Loadings are 91 μg cm^{-2} oxide + 91 μg cm^{-2} carbon.

Fig. 36 CVs of $LaMnO_3$/C и MnOOH/C with variable cathodic limit (left) and anodic limit (right) acquired in different electrolytes (as indicated in the panels). Scan rate is 10 mV/s, oxide loading is 91 μg cm^{-2} and carbon loading is 91 μg cm^{-2}.

Fig. 37 XRPD patterns for MnOOH, Mn_2O_3, $LaMnO_3$ for pristine samples and aged for 1 year in 1 M, 0.1 M and 0.01 M NaOH.

Fig. 38. pH calibration curve. Potential is referred to the Ag/AgCl reference electrode.

Fig. 39 XRPD patterns of Mn_3O_4 (a), $LiMn_2O_4$ (b), $CdMn_2O_4$ (c), $MgMn_2O_4$ (d) along with the position of reflections (orange vertical lines at the bottom) from the ICDD PDF2 database for Mn_3O_4 (#18-803), $LiMn_2O_4$ (#35-782), $CdMn_2O_4$ (#23-826) and $MgMn_2O_4$ (#72-1336).

Fig. 40 SEM images of the spinel materials: Mn_3O_4 (a), $LiMn_2O_4$ (b), $CdMn_2O_4$ (c), $MgMn_2O_4$ (d).

Fig. 41 (a) NEXAFS spectra of Mn_3O_4 (green), $LiMn_2O_4$ (violet), $MgMn_2O_4$ (light brown), $CdMn_2O_4$ (cyan) along with the spectra of the reference samples MnO (black), Mn_2O_3 (red), MnO_2 (blue). (b) Comparison of the Mn oxidation state calculated from stoichiometric composition with the one calculated from NEXAFS data. NEXAFS spectra of (c) Mn_3O_4, (в) $LiMn_2O_4$, (y) $CdMn_2O_4$, (a) $MgMn_2O_4$ and their fitting using a combination of lines for MnO, Mn_2O_3, MnO_2 standard samples.

Fig. 42 CVs with a decreasing cathodic potential limit for GC-supported thin films of oxide/carbon composites in N_2-purged 1 M NaOH at 10 mV s^{-1} registered for Mn_3O_4 (a) $LiMn_2O_4$ (b), $CdMn_2O_4$ (c) and $MgMn_2O_4$ (d). Currents are normalized to the geometric area of the electrode. For each cathodic limit the third CV is shown. Loadings are 91 μg cm^{-2} oxide + 91 μg cm^{-2} carbon.

Fig. 43 Cyclic voltammograms with variable scan rate (from 10 to 1000 mV s^{-1}) for GC-supported thin films of oxide/carbon composites in N_2-purged 1 M NaOH at 10 mV s^{-1} registered for Mn_3O_4 (a) $LiMn_2O_4$ (b), $CdMn_2O_4$ (c) and $MgMn_2O_4$ (d). Currents are normalized to the scan rate and to the geometric area of the electrode. Loadings are 91 μg cm^{-2} oxide + 91 μg cm^{-2} carbon.

Fig. 44 Dependencies of the reciprocal value of the cathodic charge(Q^{-1}) for the spinel samples on the square root of the potential scan rate ($n^{½}$) (a-d) and Q on $n^{-½}$ (e-h). Q is calculated from the CVs in Figure 43.

Fig. 45 (a) CVs in N_2-saturated 1 M NaOH (the tenth cycle is shown for each sample), and (b) RDE voltammograms in O_2-saturated 1 M NaOH at 900 rpm for $MgMn_2O_4$, Mn_3O_4, $LiMn_2O_4$, $CdMn_2O_4$ and α-MnOOH. (c, d) CVs in N_2-saturated (black) and RDE voltammograms in O_2-saturated 1 M NaOH (red) for Mn_3O_4, (c) $LiMn_2O_4$ (d), $MgMn_2O_4$ (e), $CdMn_2O_4$ (f). Blue and green traces correspond to the cathodic and anodic traces, respectively, of RDE voltammograms obtained after subtraction of the background CV in O_2-free supporting electrolyte. (g) The corresponding Tafel plots, and (h) kinetic ORR currents at 0.90 V vs. RHE plotted against the formal potential (E_f) of the Mn(IV/III) red-ox transition, with black symbols - data from this work, blue symbols - data taken from Ref. [12]. Loadings are 91 μg cm^{-2} oxide + 91 μg cm^{-2} carbon. Currents in panels (g, h) are normalized to the BET surface area of the oxides.

Fig. 46 RDE voltammograms in O_2-saturated 1M NaOH at 10 mV s^{-1} for GC supported thin films of Mn_3O_4 (a), $LiMn_2O_4$ (b), $CdMn_2O_4$ (c), $MgMn_2O_4$ (d). Loadings are 91 μg cm^{-2} oxide + 91 μg cm^{-2} carbon. Color codes: 400 (black), 900 (red), 1600 (blue), 2500 (green) rpm. Currents are normalized to the electrode geometric area and corrected to the background currents measured in the N_2 atmosphere. Koutecky–Levich plots for currents at 0.6 V vs RHE (e) extracted from RDE

voltammograms in O_2-saturated 1 M NaOH for Mn_3O_4 (green), $LiMn_2O_4$ (blue), $MgMn_2O_4$ (red), $CdMn_2O_4$ (black). Dashed and dotted lines show the slopes calculated for a $2e^-$, $3e^-$ and $4e^-$ ORR.

Fig. 47 RDE voltammograms in N_2-saturated 1 M NaOH + 0.84 mM H_2O_2 at 10 mV s^{-1} for GC supported thin films of Mn_3O_4, $LiMn_2O_4$, $CdMn_2O_4$, $MgMn_2O_4$ (a-d). Loadings are 91 μg cm^{-2} oxide + 91 μg cm^{-2} carbon. Color codes: 400 (black), 900 (red), 1600 (blue), 2500 (green) rpm. Currents are normalized to the electrode geometric area and corrected to the background currents measured in the H_2O_2-free electrolyte. Koutecký–Levich plots of the (e) anodic (at 1.1 V vs RHE) currents and (f) cathodic (at 0.6 V vs RHE) currents extracted from RDE voltammograms in N_2-purged 1 M NaOH with 0.84 mM H_2O_2 for Mn_3O_4 (green), $LiMn_2O_4$ (blue), $MgMn_2O_4$ (red), $CdMn_2O_4$ (black).

Fig.48. RDE voltammograms acquired in O_2-saturated 1 M NaOH at 900 rpm and 10 mV s^{-1} for Mn_3O_4, $LiMn_2O_4$, and $CdMn_2O_4$ and $MgMn_2O_4$ samples before (black curve) and after (red curve) 6 h soaking in 1M NaOH. Loadings are 91 μg cm^{-2} oxide + 91 μg cm^{-2} carbon. Currents are normalized to the electrode geometric area and corrected to the background currents measured in the N_2 atmosphere.

Fig. 49 CVs of Mn_3O_4 (a), $LiMn_2O_4$ (b), $CdMn_2O_4$ (c) and $MgMn_2O_4$ (d) measured at 10 mV s^{-1} every 2 hours during the day. Electrodes between the measurements were kept in 1M NaOH at OCP (open circuit potential) conditions. Loadings are 91 μg cm^{-2} oxide + 91 μg cm^{-2} carbon. CVs corrected to the background currents measured on Sibunit carbon under the same conditions.

Fig. 50 Mn3p XP spectra for Mn_3O_4 (a), $LiMn_2O_4$ (b), $CdMn_2O_4$ (c) and $MgMn_2O_4$ (d) (pristine samples and after preparation of aqueous suspension using ultrasound, soaking in 1M NaOH for 6 h and after 10 cycles of CV in the potential interval from 0.6 to 1.15 V vs. RHE. Black solid line corresponds to deconvolution of the spectra assuming the presence of Mn(II) (green), Mn(III) (red) and Mn(IV) (blue). Spectra are collected with a laboratory Thermo VG-Microtech spectrometer with Al-cathode (excitation energy 1486.6 eV).

Fig. 51 CVs in N_2-saturated 1 M NaOH in the potential interval from 0.6 to 1.15 V vs. RHE for Mn_3O_4, $LiMn_2O_4$, $CdMn_2O_4$ and $MgMn_2O_4$ samples before (black curve) and after (red curve) ORR experiments. Loadings are 91 μg cm^{-2} oxide and 91 μg cm^{-2} carbon. Currents are normalized to the electrode geometric area. In each case the last CV acquired after ten subsequent cycles is shown.

Fig. 52 XRPD of patterns Mn_3O_4 (a), $LiMn_2O_4$ (b), $CdMn_2O_4$ (c), $MgMn_2O_4$ (d) before (black) and after (red) soaking in 1 M NaOH for 1 year.

Fig. 53 Mn(II), Mn(III) and Mn(IV) speciation in $LaMnO_3$ depending on the electrode potential determined with in situ hard X-ray absorption and emission spectroscopies (XAS and XES). From [7].

Fig. 54 CVs MnO_2/C, Mn_2O_3/C, Mn_3O_4/C, MnOOH/C в N_2-saturated 1 M NaOH measured at 10 mV s^{-1}. From Ref. [10].

Fig. 55. CVs of a thin-film MnO_2 electrode in an aqueous electrolyte of 2 M $LiNO_3$, 2 M $NaNO_3$, and 2 M KNO_3. Scan rate 10 mV s^{-1}. (b) Charge-discharge curves [14].

Fig. 56. Capacity versus pH and pK($-\log C_{KCl}$) for RuO_2 (a) and capacity versus pK for MnO_2 (b)[17].

Fig. 57. Capacity versus pH in Li_2SO_4, Na_2SO_4 and K_2SO_4. The inset shows cyclic voltammograms of MnO_2 in Li_2SO_4 electrolyte with a concentration of 0.1 mol L^{-1} at various pH values. pH was set by adding H_2SO_4 [16].

Fig. 58. CVs of $LaMnO_{3.09}$ (a) and $LaMnO_{2.91}$ (b) at a sweep rate of 40 mV/s at various NaOH concentrations [18].

Fig. 59. Typical plot of charge q at scan rate v as a function of ($n^{-½}$) (a) and 1/q vs. $n^{½}$(b) for (1) $HClO_4$ (2) KOH solution [2].

Fig. 60. Analysis of the j-n dependences for $Sr_{0.5}Gd_{0.5}Mn_{0.75}Co_{0.25}O_{2.98}$ (a-c) and $Sr_{0.5}Gd_{0.5}Mn_{0.25}Co_{0.75}O_{2.87}$ (d-f) according to the Conway's approach: (a, d) slope b of the log j vs. log n dependence and the corresponding Pearson correlation coefficient R^2; (b, e) $jn^{-½}$ vs. $n^{½}$ dependence at 1 V vs. RHE and the corresponding Pearson correlation coefficient R^2; (c, f) pristine CV at 10 mV $s^{-1}$and CVs corresponding to 'fast' (a_1n) and 'slow' ($a_2n^{-½}$) processes. Parameters a_1 and a_2 represent the slope and the intercept of the $jn^{-½}$ vs. $n^{½}$dependence, respectively. Dashed plots indicate parts with a high calculation error formally corresponding to $b > 1$. [21]

Fig. 61 a) Variant of the titration curve for suspension (marked with circles) and blank solution (marked with triangles), b) apparent and true PZC points obtained from a titrimetric experiment using solutions with different ionic strength [23].

Fig. 62 X-ray diffraction patterns of samples a) MnOOH, b) Mn_2O_3, c) $LaMnO_3$, Bar diagrams correspond to the position of reflections from the ICDD PDF2 database #41-1349 and #75-1199 for MnOOH with manganite and groutite structures, respectively (a), #41- 1442 bixbyite - Mn_2O_3 (b), #50-298 $LaMnO_3$ (c).

Fig. 63. CVs in N_2-saturated alkaline solutions for $LaMnO_3$ (a), Mn_2O_3 (b), MnOOH (c) and Sibunit carbon (d) at different OH^- concentrations and constant ionic strength (as indicated in the panels). Evolution of the cathodic and anodic peak positions (*cf.* panels a-c) with the OH^- concentration for $LaMnO_3$ (e), Mn_2O_3 (f), MnOOH (g). Scan rate 10 mV s^{-1}, oxide loading is 91 μg cm^{-2} and carbon loading is 91 μg cm^{-2}.

Fig. 64. CVs in N_2-saturated alkaline solutions at different concentration of Na^+ and constant pH for $LaMnO_3$ (a), Mn_2O_3 (b), MnOOH (c), and Carbon (d). Potentials of the anodic and cathodic peaks plotted against the Na^+ concentration for $LaMnO_3$, Mn_2O_3, MnOOH (e-g).

Fig. 65. Open-circuit potential for $LaMnO_3$, Mn_2O_3 and MnOOH in N_2-purged solutions with varying pH and constant Na^+ concentration (a) and in solutions with varying Na^+ concentration at constant pH (b).

Fig. 66. Cyclic voltammograms with variable scan rate (from 10 to 1000 mV s^{-1}) for GC-supported thin films of oxide/carbon composites in N_2-purged electrolytes of different composition for $LaMnO_3$ (a-d), Mn_2O_3 (e-h), MnOOH (i-m). Currents are normalized to the scan rate and to the geometric area of the electrode. Loadings are 91 μg cm^{-2} oxide and 91 μg cm^{-2} carbon.

Fig. 67. Titration curves for $LaMnO_3$, MnOOH, Mn_2O_3, Sibunit carbon, and oxide-free solution (background - BG) for various background solution (constant pH, different ionic strength).

Fig. 68. Surface charge versus pH determined from titration curves for $LaMnO_3$ (a), Mn_2O_3 (b), MnOOH (c), and Sibunit carbon (d).

Fig. 69 Normalized polarization curves for the HPRR and HPOR on Pt(111) in 1.7 mM H_2O_2 with pH ≤ 5.4 prepared with NaF/$HClO_4$ mixtures on the RHE scale (A) and on the SHE scale. Reproduced from Ref. [2].

Fig. 70 Square scheme for proton-coupled electron transfer. ET - electron transfer, PT - proton transfer, CPET - concerted proton–electron transfer. Reproduced from Ref. [3].

Fig. 71 Conventional adsorbate (a) and lattice oxygen participating (b) oxygen evolution mechanisms on perovskite catalysts. Reproduced from Ref. [9].

Fig. 72 pH dependence of the OER activity on the RHE scale. (a) CV measurements from O_2-saturated 0.03 M KOH (pH 12.5) to 1 M KOH (pH 14) recorded at 10 mV s^{-1}. (b) Specific OER activity (current normalized by oxide BET surface area) at 1.55 V versus RHE after iR correction as a function of pH. The nominal oxide loading is 0.25 mg_{oxide}/cm_{disk}^2. Error bars represent standard deviation of three measurement results. Reproduced from Ref. [8].

Fig. 73 RDE voltammetry curves for O_2 reduction on bare GC electrodes in O_2 saturated solutions of various pH. The potential is given on the SCE scale. Reproduced from Ref. [12].

Fig. 74 Pourbaix diagram for oxygen and hydrogen peroxide equilibria also including the equilibrium for the superoxide/oxygen reaction [14].

Fig. 75 (a) Concentration the protonated (H_2O_2) and deprotonated (HO_2^-) forms of the hydrogen peroxide as a function of solution pH. The total concentration of the hydrogen peroxide is 2 mmol/L. (b) Polarization curves for the oxidation of H_2O_2 or HO_2^- on Au(111) in 0.5 mol/L

$NaClO_4$+2 mmol/L H_2O_2 +x mmol/L NaOH. pH values are indicated in the figure. Electrode rotation speed: 2500 r/min, scan rate: 50 mV/s. Reproduced from Ref. [13].

Fig. 76 Model of non-covalent interactions on the electrode surface proposed in Ref. [25].

Fig. 77 Potential of the OH adsorption/desorption peak calculated by the DFT method at different cationic composition of the electrolyte and different pH plotted against the experimental peak position. Reproduced from Ref. [28].

Fig. 78 a) Cyclic voltammograms of NiOOH at pH 13 in the region of oxygen evolution in different electrolytes. (Solid lines: as received electrolytes; dotted lines: electrolytes purified from iron) b) In situ Raman spectra of NiOOH obtained at 1.7 V at pH 13 in the presence of different electrolyte cations. Reproduced from Ref. [29].

Fig. 79 RDE voltammograms in N_2-purged alkaline solution (at different pH and constant ionic strength) in the presence of 0.84 mM H_2O_2 at 10 mV s^{-1} for GC supported thin films of $LaMnO_3$ (a), Mn_2O_3 (b), MnOOH (c). Catalyst loadings are 91 μg cm^{-2} oxide + 91 μg cm^{-2} carbon. Currents are normalized to the electrode geometric area and corrected to the background currents measured in the N_2 atmosphere.

Fig. 80 RDE voltammograms in N_2-purged solutions of 0.84 mM H_2O_2 in 0.01M NaOH + 1.99 M $NaClO_4$ for GC-supported thin films of $LaMnO_3$ (a) and Mn_2O_3 (b) Panels c) and d) show Koutecký–Levich plots of anodic and cathodic currents for $LaMnO_3$ (c and e respectively) and Mn_2O_3 (d and f respectively). The oxide and carbon loadings are 91 μg cm^{-2} each. Color codes: 400 (blue), 900 (orange), 1600 (green), 2500 (red) rpm. Currents are normalized to the electrode geometric area and corrected to the background currents measured in the N_2 atmosphere.

Fig. 81 RDE voltammograms in N_2-purged solutions of 0.84 mM H_2O_2 for GC-supported thin films of MnOOH at different OH^- concentrations and constant ionic strength: 1M NaOH + 1M $NaClO_4$ (a), 0.1M NaOH + 1.9 M $NaClO_4$ (b), and 0.01M NaOH + 1.99 M $NaClO_4$ (c). Panel d shows Koutecký–Levich plots of anodic (e) and cathodic (d) currents. MnOOH and carbon loadings are 91 μg cm^{-2} each. Color codes: 400 (blue), 900 (orange), 1600 (green), 2500 (red) rpm. Currents are normalized to the electrode geometric area and corrected to the background currents measured in the N_2 atmosphere.

Fig. 82 RDE voltammograms in O_2-saturated alkaline solution (at different pH and constant ionic strength) at 10 mV s^{-1} and 900 rpm for GC supported thin films of $LaMnO_3$ (a), Mn_2O_3 (b), MnOOH (c), and Sibunit carbon (d). Currents are normalized to the electrode geometric area and corrected to the background currents measured in the N_2 atmosphere. Oxide and carbon loadings are 91 μg cm^{-2} each.

Fig. 83 Tafel plots for the ORR on $LaMnO_3$ (a), Mn_2O_3 (b), MnOOH (c), and Sibunit carbon (d) at different NaOH concentration and constant ionic strength. Currents are normalized to the

BET surface area of materials. The currents are given without subtracting the contribution of carbon.

Fig. 84 RDE voltammograms in N_2-purged alkaline solution (at different concentration of Na^+ and constant pH) in the presence of 0.84 mM H_2O_2 at 10 mV s^{-1} and 900 rpm for GC supported thin films of $LaMnO_3$ (a), Mn_2O_3 (b), MnOOH (c). Oxide and carbon loadings are 91 μg cm^{-2} each. Currents are normalized to the electrode geometric area and corrected to the background currents measured in the N_2 atmosphere.

Fig. 85 RDE voltammograms in N_2-purged alkaline solution (at different concentration of Na^+ and constant pH) in the presence of 0.84 mM H_2O_2 at 10 mV s^{-1} for GC supported thin films of MnOOH at different rotational rate (a-d). Catalyst loadings are 91 μg cm^{-2} oxide + 91 μg cm^{-2} carbon. Currents are normalized to the electrode geometric area and corrected to the background currents measured in the N_2 atmosphere. Koutecký–Levich plots of anodic and cathodic currents for $LaMnO_3$ (c and e respectively) and Mn_2O_3 (d and f respectively).

Fig. 86 RDE voltammograms in N_2-purged alkaline solution (0.1M NaOH + 1.9M $NaClO_4$) + 0.84 mM H_2O_2 at 10 mV s^{-1} for GC supported thin films of $LaMnO_3$ (a) and Mn_2O_3 (b) at different rotation rate. Catalyst loadings are 91 μg cm^{-2} oxide + 91 μg cm^{-2} carbon. Currents are normalized to the electrode geometric area and corrected to the background currents measured in the N_2 atmosphere. Koutecký–Levich plots of anodic (e) and cathodic (f) currents.

Fig. 87 RDE voltammograms in O_2-saturated alkaline solution (at different concentration of Na^+ and constant pH) at 10 mV s^{-1} at 900 rpm for GC supported thin films of $LaMnO_3$ (a), Mn_2O_3 (b), MnOOH (c), Carbon (d). Currents are normalized to the electrode geometric area and corrected to the background currents measured in the N_2 atmosphere.

Fig. 88. RDE voltammograms in O_2-saturated alkaline solution (at different concentration of Na^+ and constant pH) at 10 mV s^{-1} and 900 rpm for GC supported thin films of $LaMnO_3$ (a), Mn_2O_3 (b), MnOOH (c), Carbon (d). Currents are corrected to the background currents measured in the N_2 atmosphere and normalized to the diffusion-limited current of carbon.

Fig. 89 Tafel plots for $LaMnO_3$ (a), Mn_2O_3 (b), MnOOH (c), Carbon (d). Currents are normalized to the BET surface area. The currents are given without deducting the contribution of carbon. Currents are corrected to the O_2 concentration assuming 1^{st} order kinetics.

Fig. 90 (a-f) Comparison of the RDE curves for the HPOR/HPRR and ORR in solutions with different pH (a, c, e), and with different concentrations of Na^+ (b, d, f) for $LaMnO_3$ (a, b), Mn_2O_3 (c, d), MnOOH (e, f). Mixed potentials in the presence of H_2O_2 are shown in panels (g) and (h) in solutions with different pH (g), and with different concentrations of Na^+ (h).

Fig. 91. Structures of β-MnO_2 and γ-MnOOH. Pink circles stand for protons.

Fig. S 1 CVs recorded during 1st and 10th cycles of the potential at 0.6-1.15 V of GC-supported thin films of oxide/carbon composites in N_2-purged 1 M NaOH at 10 mV s^{-1} for Mn_3O_4 (a) $LiMn_2O_4$ (b), $CdMn_2O_4$ (c) and $MgMn_2O_4$ (d). Loadings are 91 μg cm^{-2} oxide + 91 μg cm^{-2} carbon. Currents are normalized to the geometric area of the electrode. Note change in the CV shape and peak positions. One cannot exclude that while starting ORR measurements after 2-3 cycles in oxygen-free solution the near-surface layer of spinels is already transformed from its pristine state.

Fig. S 2 Comparison of RDE voltammograms acquired in N_2-saturated 1M NaOH with 0.84 mM H_2O_2 at 10 mV s^{-1} for GC supported thin films of Mn_3O_4, $LiMn_2O_4$, $MgMn_2O_4$, $CdMn_2O_4$ at 900 rpm. Loading are: 91 μg cm^{-2} carbon + 91 μg cm^{-2} oxide. The current is normalized to the geometric surface of the electrode after subtracting the response in the H_2O_2-free solution.

Fig. S 3 Mn 3p XP spectra for Mn_3O_4 (a), $LiMn_2O_4$ (b), $CdMn_2O_4$ (c) and $MgMn_2O_4$ (d) (pristine samples and after preparation of aqueous suspension using ultrasound, soaking in 1 M NaOH for 6 h and after 10 cycles of CV at 0.6-1.15 V potential range. Black solid line corresponds to deconvolution of the spectra assuming the presence of Mn(II) (green), Mn(III) (red) and Mn(IV) (blue). Spectra are collected at ISSIS station of Bessy-II synchrotron and excitation energy 500 eV (λ=1.4 nm).

Fig. S 4 CVs in N_2-saturated alkaline solutions for $LaMnO_3$ (a), Mn_2O_3 (b), MnOOH (c) and Sibunit Carbon (d) at different OH^- concentration and constant ionic strength (as indicated in the panels). Loading are: 91 μg cm^{-2} carbon + 91 μg cm^{-2} oxide. The current is normalized to the geometric surface of the electrode. The scale is relative to SHE.

Fig. S5 CVs with a decreasing cathodic potential limit for GC-supported thin films of oxide/carbon composites in N_2-purged 1 M NaOH at 10 mV s^{-1} registered for Mn_2O_3, $LaMnO_3$, MnOOH and $MgMn_2O_4$ (d). Currents are normalized to the geometric area of the electrode. For each cathodic limit the third CV is shown. Loadings are 91 μg cm^{-2} oxide + 91 μg cm^{-2} carbon.

Fig. S 6 CVs with a decreasing anodic potential limit for GC-supported thin films of oxide/carbon composites in N_2-purged 1 M NaOH at 10 mV s^{-1} registered for Mn_2O_3, $LaMnO_3$, MnOOH and $MgMn_2O_4$ (d). Currents are normalized to the geometric area of the electrode. For each cathodic limit the third CV is shown. Loadings are 91 μg cm^{-2} oxide + 91 μg cm^{-2} carbon.

Fig. S 7 Dependencies of the reciprocal value of the cathodic charge(Q^{-1}) for Mn_2O_3 (a, b), MnOOH (c, d), $LaMnO_3$(e, f) on the square root of the potential scan rate ($n^{½}$) (left) and Q on $n^{-½}$ (right). Q is calculated from the CVs Fig. 66.

Fig. S 8 RDE voltammograms in N_2-purged alkaline solution (at different pH and constant ionic strength) in the presence of 0.84 mM H_2O_2 at 10 mV s^{-1} for GC supported thin films of $LaMnO_3$ (a), Mn_2O_3 (b), MnOOH (c). Catalyst loadings are 91 μg cm^{-2} oxide + 91 μg cm^{-2} carbon.

Currents are normalized to the electrode geometric area and corrected to the background currents measured in the N_2 atmosphere. The scale is relative to SHE.

Fig. S 9 RDE voltammograms in O_2-saturated alkaline solutions for $LaMnO_3$ (a), Mn_2O_3 (b), MnOOH (c) and Sibunit Carbon (d) at different OH^- concentration and constant ionic strength (as indicated in the panels). Loading are: 91 μg cm^{-2} carbon + 91 μg cm^{-2} oxide. The current is normalized to the geometric surface of the electrode. The scale is relative to SHE.

Fig. S10 RDE voltammograms in N_2-purged alkaline solutions with 0.84 mM H_2O_2 for GC-supported thin films of $LaMnO_3$, MnOOH and Mn_2O_3. The oxide and carbon loadings are 91 μg cm^{-2} each. Color codes: 400 (blue), 900 (orange), 1600 (green), 2500 (red) rpm. Currents are normalized to the electrode geometric area and corrected to the background currents measured in the N_2 atmosphere.

Fig. S11 RDE voltammograms in O_2-purged alkaline solutions for GC-supported thin films of $LaMnO_3$, MnOOH and Mn_2O_3. The oxide and carbon loadings are 91 μg cm^{-2} each. Color codes: 400 (blue), 900 (orange), 1600 (green), 2500 (red) rpm. Currents are normalized to the electrode geometric area and corrected to the background currents measured in the N_2 atmosphere.

Fig. S12 Koutecký–Levich plots of cathodic currents for Mn_2O_3, $LaMnO_3$, MnOOH. calculated from Fig. S11.

List of Tables

Table 1 Representative literature data on the activity of manganese oxides in the ORR.

Table 2. Composition of the supporting electrolytes used to study the influence of the electrolyte on the electrochemical behaviour of the catalysts.

Table 3. Composition of the alkaline solutions in which the test substances were dispersed and composition of the titrant solution.

Table 4. Unit cell parameters, BET surface area and electrochemical characteristics of Mn-containing spinels.

Table 5 Specific surface area of the spinels, the charge determined from the CVs of the spinels at a scan rate of 10 mV s^{-1}, the minimum and maximum charge (Q_{min} and Q_{max}) determined from extrapolation of the dependences $Q(n^{-½})$ and $Q^{-1}(n^{½})$. In case of non-linear plots the curves are described by two linear segments (Fig. 44) resulting in two values of Q_{min} and Q_{max}. The calculated charge ($Q_{monolayer}$) corresponds to the average densities of Mn atoms at the surfaces of polycrystalline oxides (see Ref. [12] for details).

Table 6 Peak position and charges for the cathodic and anodic parts of the CVs for oxide/carbon compositions measured at 10 mV s^{-1} before (initial) and after soaking in 1 M NaOH solution for 20 h.

Table 7 The fractions of Mn in different oxidation states, the average oxidation state of Mn calculated from these values, and the A-cation content (x in $A_xB_2O_4$) in the near-surface layer calculated from the laboratory XP spectra.

Table 8 Ratio of cathodic (Q_c) and anodic (Q_a) charges and variation ($\Delta Q_a/Q_a$ and $\Delta Q_c/Q_c$, in %) of anodic and cathodic parts of CVs obtained by integration of CVs and formal potential (E_f) for samples before and after ORR measurements (Fig. 44).

Table 9 Acidity constants (pK_a) and complexation constants (pK_{Cl} and pK_{Ct}) of surface hydroxyl groups for the Mn_2O_3/Ct system (Ct = Li, Na, Cs) [26].

Table 10. PZC and IEP values reported in the literature for Mn_2O_3, MnOOH, $LaMnO_3$.

Table 11. Rate constants for steps k_2, k_3, k_5 of the proposed ORR mechanism (see Fig. 25) estimated by microkinetic modeling (see Ref. [8]) for MnOOH, $LaMnO_3$ and Mn_2O_3.

Table 12. Investigated materials and their BET surface area.

Table 13. Point of zero charge (PZC) determined from titration curves.

Table 14. Concentration of acid sites on the surface of the studied compounds, calculated from titration curves and compared to the Mn surface density estimated from the volume density of Mn cations in the corresponding oxides.

Table 15. The values of the B coefficient at 25 ^{0}C for the most common cations and anions that are part of the background electrolyte in electrocatalysis [24].

Table 16. Ion Specific Constants for Salting-Out Oxygen at 25°C.

Table 17. Concentration of dissolved oxygen in solutions with variable NaOH concentration and constant ionic strength calculated according to Henry's law along with the cathodic limiting ORR current measured for Sibunit carbon at an electrode rotation speed of 900 rpm

Table. 18. Tafel slopes (V/dec) defined for carbon, $LaMnO_3$*, Mn_2O_3*, MnOOH*.

Table 19. Concentration of dissolved oxygen in solutions with a constant content of NaOH and a variable concentration of $NaClO_4$ calculated according to Henry's law. Limiting current for the ORR on Sibunit carbon at an electrode rotation speed of 900 rpm is presented for comparison.

Table 20. Tafel slopes defined for carbon, $LaMnO_3$, Mn_2O_3, MnOOH.

Table 21. Kinetic currents (i_k*) for Mn_2O_3, MnOOH, and $LaMnO_3$ calculated at 0.9 V vs. RHE in solutions with variable OH^- concentration and constant ionic strength.

Table 22. Kinetic currents (i_k*) for Mn_2O_3, MnOOH, and $LaMnO_3$ calculated at 0.9 V vs. RHE in solutions with variable Na^+ concentrations.

General Introduction

Fossil fuels such as gas, oil and coal are being rapidly depleted. In addition, the use of fossil fuels for energy production has a high impact on the environment, so a switch to clean renewable energy sources, such as solar and wind energy, is relevant. However, these energy sources are cyclical and therefore require energy storage, during peak performance, in order to be used efficiently. The use of lithium-ion batteries for this purpose is not practical due to their limited capacity and high cost. Fuel cells (FC) solve several problems in the energy production and storage at the same time. FCs allow converting the chemical energy stored in a fuel into electrical energy with high efficiency and environmental friendliness. The use of a FC in conjunction with an electrolyser makes it possible to create a storage plant in which energy is stored in the form of hydrogen and converted into electricity when needed.

There are several types of FCs and each has its own advantages and disadvantages. The alkaline fuel cell (AFC) was one of the first to be used in practice. In particular, alkaline fuel cells were used in the Apollo and Buran space programs, which speaks for their reliability. Further development of anion-exchange membranes (AEM) made it possible to use them instead of liquid electrolyte in the fuel cell. This gave a new impetus of researchers' interest in studying the processes, taking place in these types of fuel cells.

While the oxygen reduction reaction is faster in alkaline compared to acid medium, its rate at a cathode of an AFC or AEMFC is still slower than the rate of the hydrogen oxidation at the anode. This forces to use catalysts based on noble metals or their alloys (for example, Pt), which, in its turn, considerably increases the cost of AFC and AEMFC and limits their wide application.

The cost and scarcity of platinum are prompting researchers to find new active and stable catalysts for the oxygen reduction reaction in alkaline media for eventual application in AFC and AEMFC. In contrast to acid fuel cells, the use of platinum metals as catalysts is not mandatory for AFC and AEMFC. One of the most promising ways to solve this problem is by switching to 3d metal-based oxide catalysts. Oxides offer great opportunities for researchers, both in terms of the chemical composition and the structural type selection. However, there remain many fundamental questions related to the influence of the composition and structure of 3d metal oxides on their electrocatalytic activity in the ORR, as well as the reaction mechanisms. This can be attributed to the fact that the ORR electrocatalysis is influenced by both 'intrinsic factors', that is chemical composition and structure, and 'extrinsic factors' such as electrolyte composition and the presence of carbon additives (the latter applied to improve electrical conductivity of the electrodes). While numerous studies have been devoted to the influence of the structure and composition of 3d metal oxides on their ORR activity, studies on the influence of the electrolyte composition (pH and cation

concentration) are scarce. In addition, the stability of 3d metal oxides under electrocatalysis conditions has received insufficient attention in the literature.

To answer these questions, the present thesis is divided in five chapters.

Chapter 1 reviews the available literature on the reaction mechanisms of the oxygen reduction reaction on different catalysts (Pt, carbon materials, transition metal oxides) in an alkaline environment and the degradation processes occurring in the catalysts during their functioning.

Chapter 2 describes the synthesis techniques for manganese oxides, which were further studied as electrocatalysts. Protocols of electrochemical measurements and analytical techniques are also presented. Methods used for the data analysis are described as well.

Results of this work and discussion of the results are presented in Chapters 3, 4 and 5.

The goal outlined in **Chapter 3** is to establish the relationship between the composition of Mn oxides and their stability and ORR activity. In order to do so we have chosen manganese oxides with spinel structure of the AMn_2O_4 composition and investigated how the nature of the A element (A - Li, Mg, Mn, Cd) affects speciation of Mn oxidation states, the ensuing stability of the oxide, and its ORR activity.

Chapter 4 and 5 are devoted to studying the effect of electrolyte (pH and the Na^+ cation concentration) on the electrochemical properties of oxides. For this part of the thesis we have chosen to investigate three Mn oxides (Mn_2O_3, $LaMnO_3$ and MnOOH), which have proven to be active and stable ORR catalysts, and for which previous publications have documented grossly different ORR kinetics.

Chapter 4 is devoted to the understanding of the redox and acid-base properties of the oxide/electrolyte interface. It starts with a review of the literature devoted to the approaches to study the acid-base and the interfacial recharging phenomena occurring at the oxide/electrolyte interface. Then, experimental results of the influence of Na^+ concentration and pH on the oxide/electrolyte interface are presented for Mn_2O_3, $LaMnO_3$, MnOOH, and carbon of the Sibunit family. To disentangle the influence of pH and the cation concentration, two series of experiments were realised. In the first one, to unveil the effect of pH, the ionic strength of the solution was kept constant by fixing the concentration of Na^+. In the second set of experiments, to determine the effect of the concentration of Na^+, the concentration of OH^- was fixed. Cyclic voltammetry was used to study the interfacial recharging behavior, while titration was used to study the acid-base properties of the interface.

Chapter 5 is devoted to the investigation of the influence of pH and Na^+ concentration on the kinetics of the oxygen reduction reaction and hydrogen peroxide reduction and oxidation reactions. It starts with the analyses of the data presented in the literature on the effect of electrolyte

composition (pH and cation identity and concentration) on the kinetics of electrocatalytic reactions. Then, the experimental data and their analyses are presented concerned with the influence of the Na^+ concentration and pH on the electrocatalytic properties of Mn_2O_3, $LaMnO_3$, MnOOH, and carbon of the Sibunit family.

Finally, the **General conclusion** and Outlook conclude the work.

At the end of the thesis, additional data can be found in the **Annex** section.

The work was carried out under the joint supervision of Prof. Elena R. Savinova (ICPEES UMR-7515 CNRS-University of Strasbourg) and Dr. Sergei Ya. Istomin and Prof. Evgeny V. Antipov (Lomonosov Moscow State University). Part of the work devoted to the synthesis and characterisation of manganese oxides was mostly performed in Moscow, while electrochemical studies were performed in Strasbourg.

1. Literature review

1.1 Oxygen reduction reaction

Oxygen reduction reaction (ORR) is of the greatest interest in electrocatalysis, due to its great practical importance in many technological processes, including those occurring in electrochemical generators - fuel cells (FCs). Despite a large number of papers published and the long-standing interest of researchers, however, the mechanism of the oxygen reduction on various catalysts is still not fully understood. This is due to the multistep nature of this process and the difficulty of detecting adsorbed reaction intermediates [1].

Oxygen reduction is possible in alkaline, acidic, and near-neutral solutions. In the latter case, the reduction of oxygen takes place in a device that is currently developing rapidly – the microbial fuel cell. Contrary to classical fuel cells, microbial fuel cells use organic molecules that are oxidized by microorganisms as fuel [2,3]. Instead, with classical FCs, either strongly acidic or strongly alkaline electrolytes are typically used. In an acidic environment, the choice of ORR catalysts is limited to noble metals (Pt and its alloys) [4], whereas in an alkaline environment the range of catalysts is wider, including platinum metals, transition metal oxides [5], carbon, gold, and silver [6]. For electrode materials that are stable in both acidic and alkaline environments, (unlike 3d metal oxides, which are often unstable in acidic environments [7]), such as platinum or gold, for example, the reaction rate of the oxygen reduction in an alkaline environment is often higher than in an acidic one.

This review will therefore consider catalysts such as carbon, which is an integral part of the catalytic composition, platinum, which is used in the literature as a reference material, and 3d metal oxides, which are the focus of this paper. The discussion will mainly (with some exceptions) focus on the reduction of oxygen in an alkaline environment.

Two main approaches are used in the literature to compare catalysts - comparison of kinetic currents at a given potential and comparison of overpotentials at a given current. The first approach is preferable since it consists in comparison of kinetic currents being corrected for the mass-transport contribution. Since this approach will be used in this work, the methodology for calculating kinetic currents is described in detail in the experimental section of chapter 2 Nevertheless, a comparison of catalysts according to the overpotential of the oxygen reduction reaction is also often used in the literature. This overpotential is calculated using the formula:

$$\eta = E - E_{eq}\,, \qquad (1)$$

where η is the overpotential, E_{eq} is the equilibrium (Nernst) value of the electrode potential and E is the potential applied to the working electrode [8]. The catalyst with the lowest overpotential

(with potential closest to E_{eq} = 1.229 V relative to the reversible hydrogen electrode (RHE) at 298 K) has the highest activity. The overpotential is estimated at a fixed current density for each catalyst and the current must be small enough to minimize the contribution of the diffusion current.

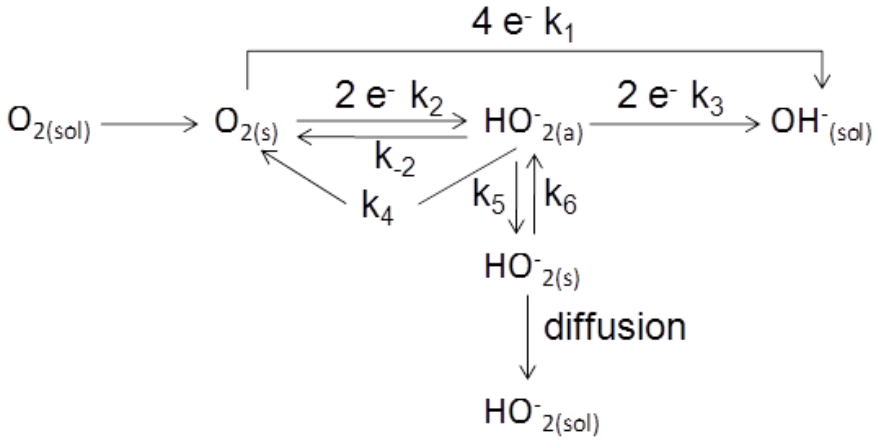

Fig. 1 Oxygen electroreduction scheme proposed by Wroblowa et al. [9].

Wroblowa et al. [9] proposed the oxygen reduction scheme shown in Fig. 1. The steps in this scheme are not elementary. The 4-electron reduction of oxygen to OH^- in this scheme corresponds to step 1 and is characterized by the apparent reaction rate constant k_1. The 4-electron process corresponds to the following reaction:

$$O_2 + 4e^- + 2H_2O \rightarrow 4OH^-,\ E° = 1.23\ V,\ T = 298\ K \qquad (2)$$

This is the preferred process for fuel cell operation because it does not produce a stable intermediate product, hydrogen peroxide, which can be desorbed from the electrode surface.

Oxygen can be reduced to hydrogen peroxide, which corresponds to step 2 with the corresponding apparent rate constant k_2 in Fig.1. In this case, reference is made to a 2-electron mechanism. It is worth noting that, at pH=14, hydrogen peroxide is present predominantly in a deprotonated form:

$$H_2O_2 + OH^- \rightarrow HO_2^- + H_2O\ pK_a = 11.7 \qquad (3)$$

The following reaction corresponds to the 2-electron process:

$$O_2 + 2e^- + H_2O \rightarrow OH^- + HO_2^-,\ E° = 0.77\ V \text{ at pH=14, } T = 298\ K \qquad (4)$$

The peroxide anion can then disproportionate into oxygen and the hydroxide anion:

$$HO_2^- \rightarrow OH^- + \tfrac{1}{2}\ O_2 \qquad (5)$$

The peroxide anion can be further reduced to the hydroxide anion. This process corresponds to reaction 3 with apparent rate constant k_3 in Fig.1:

$$HO_2^- + 2e^- + H_2O \rightarrow 3OH^-,\ E° = 1.71\ V \text{ at pH=14, } T = 298\ K \qquad (6)$$

The pathway whereby oxygen is reduced to the peroxide anion (consuming $2e^-$) and then further reduced to the hydroxide anion (consuming another $2e^-$) is called the (2+2) electron,

pseudo-4-electron, or a series pathway. The ORR on 3d metal oxide catalysts often follows this pathway [10,11]. In Fig. 1, this pathway corresponds to reactions with apparent rate constants k_2 and k_3. It should be emphasized that the steps described above are intended to schematically represent the main processes occurring on the catalyst surface and to indicate the products formed during this process. The reduction reaction mechanism itself is more complicated and consists of several single-electron elementary steps.

1.1.1 Hydrogen peroxide generation

1.1.1.1 Chemical production of H_2O_2

The formation of hydrogen peroxide as a product of the oxygen reduction reaction has often been the focus of research, because of its high corrosive activity and thus highly undesirable presence in the electrolyte. Its accumulation in the system may even prevent the FC from operating. The formation of hydrogen peroxide might also decrease the effective number of transferred electrons (n_{eff}), which leads to a decrease in the efficiency of the whole electrochemical unit. Therefore, when investigating new catalysts, it is desirable for the effective number of electrons transferred to be close to four. This however is not the case when hydrogen peroxide is the target product. Indeed, catalysts for the electrochemical generation of hydrogen peroxide are currently being actively investigated [4].

H_2O_2 is currently produced by the anthraquinone method [12], which consists in hydrogenation of substituted anthraquinones (2-alkyl anthraquinones are used) in an organic solvent over a Pd catalyst [13]. In solution, the resulting dihydroanthraquinone is then oxidized by O_2 to form H_2O_2 and the anthraquinone is regenerated (Fig. 2). H_2O_2 is extracted into the aqueous phase, while anthraquinone remains in the organic phase. This method can produce large quantities of H_2O_2, but before dilution with water, the hydrogen peroxide concentration can reach 95%, which is extremely dangerous. In addition, the resulting product is always contaminated with impurities of organic compounds, and the reduction and oxidation steps of anthraquinone are not carried out with a 100% yield, which requires purification of the obtained hydrogen peroxide from the resulting by-products. This method is not cost-effective in low-tonnage production.

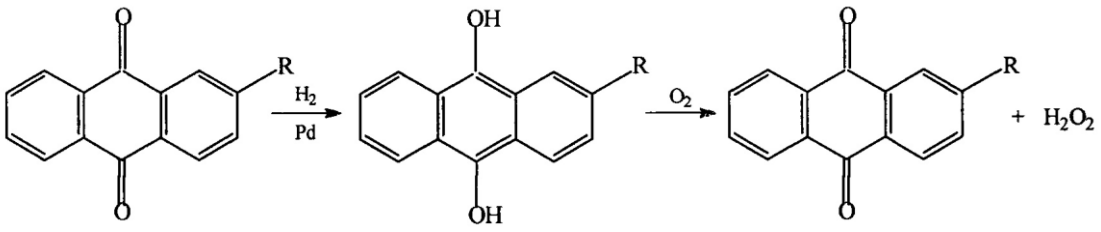

Fig. 2 Scheme of the anthraquinone method of hydrogen peroxide production.

1.1.1.2 Electrochemical production of H_2O_2

Electrochemical synthesis of H_2O_2 is cost-effective and applicable on both large and small scales [14]. The hydrogen peroxide produced is not contaminated with organic compounds, which greatly extends its range of applications and reduces the costs involved in its purification.

H_2O_2 was first produced electrochemically by the reduction of oxygen on a Hg/Au electrode [15] in an alkaline medium. These are however electrodes based on highly porous activated carbon which found commercial applications. Later, with the development of this field of electrocatalysis, new catalysts based on metal alloys, various carbon modifications, and metal oxides were proposed.

As shown in [16], electrodes based on Hg, Au, Ag, Cu, Pt, and Pd are capable of generating hydrogen peroxide, although, with the exception of Hg, this occurs in a limited potential range since increase of the overpotential results in H_2O_2 reduction to water. Metal alloys are of great interest in this context, and several computational studies have been performed to predict chemical composition of the alloy with the highest activity, taking into account the oxygen adsorption energy on the catalyst surface [17,18]. For example, the reaction rate of oxygen reduction on Au in an acid medium is too low for this metal to be considered a catalyst for hydrogen peroxide production. It has been shown, however, that the addition of Pd up to 8 mol % makes it possible to obtain an electrode material with high catalytic activity in the process of H_2O_2 generation [19]. A volcano-like dependence of the hydrogen peroxide yield on the palladium content in the alloy has been observed. This effect is due to ORR to H_2O_2 proceeding directly on the Pd atoms (Fig. 3a). At low Pd content in the alloy, its surface neighbours are only Au atoms. With increasing Pd content (up to ~8 mol %), the number of catalytic centres in the alloy increases and the H_2O_2 yield increases (Fig. 3b). Further increasing the palladium content, however, increases the probability of Pd-Pd pairs. In this case, the ORR proceeds directly through the 4-electron mechanism, with the formation of water molecules (Fig. 3c). In subsequent work, even higher hydrogen peroxide selectivity was achieved on platinum amalgams. By isolating platinum atoms from each other with mercury atoms, it was possible to obtain a catalyst superior in efficiency to the Pd-Au alloy [20].

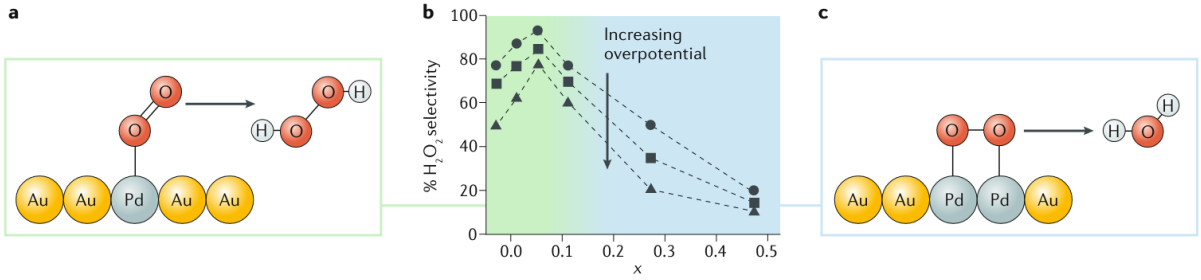

Fig. 3 Proposed ORR mechanism in an acidic medium based on Pd-Au alloy with low (a) and high (c) Pd content, and volcano-like dependence (b) between the H_2O_2 yield and Pd content in Pd_xAu_{1-x}[19].

Although various metals and alloys have demonstrated high efficiency in the ORR electrocatalysis to produce either H_2O_2 or water, most of them include expensive platinum group metals or gold. In this regard, researchers are interested in studying ORR to hydrogen peroxide on various inexpensive materials, such as carbon. For carbon materials, it is quite easy to obtain a high specific surface area, and consequently, a large number of catalytic centres, on which ORR can proceed. With an increase in specific surface area, there is usually an increase in material defectiveness, which should lead to an increase in catalytic activity, as described in [21]. Defects on the carbon surface tend to act as active centres. Coordinatively saturated carbon atoms, on the other hand, are less reactive. In contrast, a deterioration of electrocatalytic properties has been shown for microporous materials, which is probably due to the hindered diffusion of either oxygen into the pores, or the formed H_2O_2 molecules from the pores of such materials [22]. It was shown that improving the electrocatalytic properties of carbon materials is possible by surface activation during thermal or anodic oxidation, whereby various oxygen-containing groups are formed on the surface. On the other hand, it was found that selectivity for hydrogen peroxide formation can be significantly improved by annealing the carbon material in an inert atmosphere, to increase its hydrophobic properties. This improves the diffusion of oxygen to the electrode surface.

Recently, much work has been devoted to the synthesis and study of heteroatom-doped carbon materials exhibiting high catalytic activity in both 2-electron and 4-electron ORR [23–25]. Non-metals such as N S, B, P, etc. have been used as doping atoms [26–28]. N-doped carbon materials are the most widely reported in the literature. Increased scientific interest in these materials is due to the fact that the introduction of nitrogen into the carbon structure leads to an increase in catalytic activity. It was shown, for example, that the oxygen reduction reaction on nitrogen-doped carbon nanofibers did not stop at the hydrogen peroxide formation but proceeded according to the '2 e^- +2 e^-' mechanism. Some publications have stated that oxygen reduction on some nitrogen-doped carbon materials occurs by the 'direct' 4-electron mechanism. In this case,

nitrogen atoms may be present in four different environments, and these might include the following nitrogen types: pyridine, pyrrole, quaternary and N-oxides of the pyridine ring (Fig. 4) [29]. However, the nature of the active sites on N-doped carbon materials is still debated.

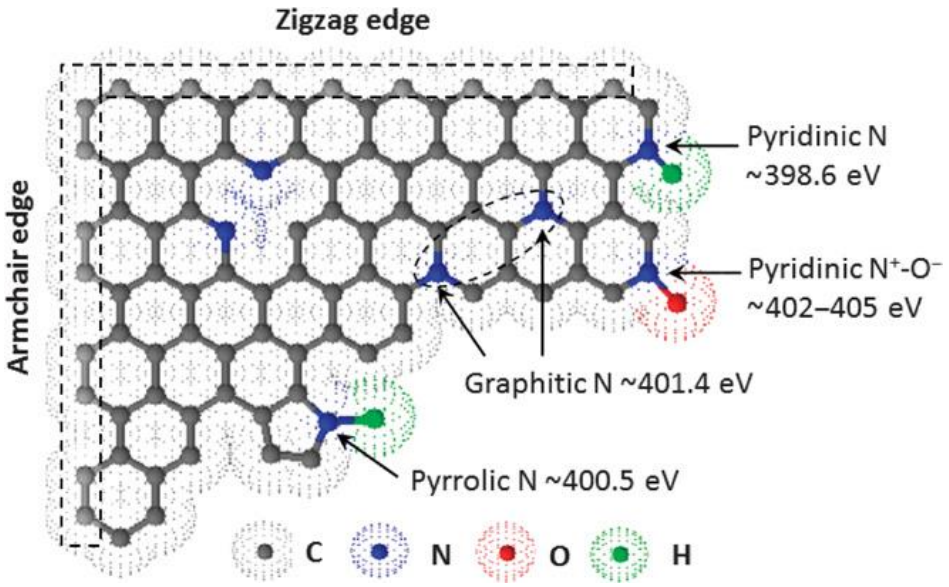

Fig. 4 Schematic representation of active centres in carbon materials doped with nitrogen and the corresponding N1s binding energies in the photoelectron spectrum (reproduced from Ref. [29]).

In [20], a comparison of the various classes of ORR catalysts (Fig. 5) for the electrochemical production of hydrogen peroxide was presented. Amalgam-based Pt-Hg catalysts showed the highest efficiency. The lowest efficiency in terms of H_2O_2 generation was demonstrated by Pt, which is related to the high rate of 4-electron reduction of oxygen on this metal.

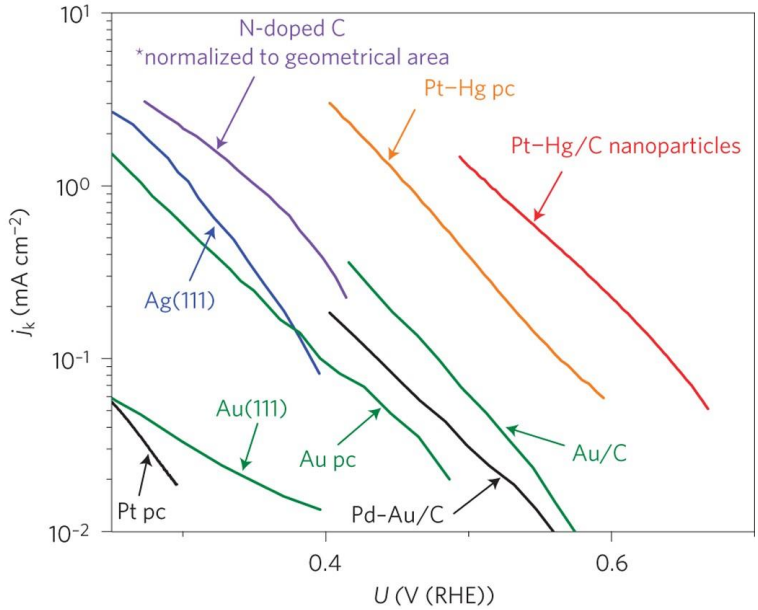

Fig. 5 Comparison of various classes of catalysts for the oxygen reduction reaction to H_2O_2 [20] in an alkaline medium.

1.1.2 Oxygen reduction reaction mechanism on carbon materials

This section provides further details of the electroreduction of oxygen on carbon materials. As mentioned above, carbon materials are widely used in electrocatalytic H_2O_2 production, since they are cheaper than catalysts based on precious metals. Carbon materials are also an integral part of 3d metal oxide composites, acting as a conductive binder (sometimes carrier) and co-catalyst, and having a substantial impact on the ORR kinetics. Thus, to predict electrocatalytic properties and the contribution of carbon to the electrochemical behaviour of composite materials, it is important to understand the mechanism of the ORR on carbon materials. Oxygen reduction itself is a complex multistep process, and various tentative ORR mechanisms have been proposed for different carbon materials (including graphite, graphene, carbon black, carbon nanofibres, mesoporous carbon, activated carbon, etc.). For example, different carbon modifications show different Tafel slopes and different pH dependence [30]. It is not the aim of this chapter to analyse the mechanisms for all carbon materials, but the main 'classical' mechanisms most commonly discussed in the literature will be described.

Morscov and Yeager [31] investigated the kinetics of ORR on annealed pyrolytic graphite and proposed the following reaction mechanism:

$$O_2 + * \rightarrow O_2*^{1} \quad (7)$$

$$O_2^* + H_2O + e^- \rightarrow HO_2^* + OH^- \quad (8)$$

$$2HO_2^* + OH^- \rightarrow O_2 + HO_2^- + H_2O \quad (9)$$

The authors suggested that the reaction proceeds through the adsorption of oxygen onto the graphite surface (7), and the formation of an uncharged intermediate adsorbed on the surface, HO_2 (8). The value of the observed Tafel slope allowed the authors to exclude the superoxide anion formation by adsorption of oxygen on the surface:

$$O_2 + e^- \rightarrow O_2^-* \quad (7')$$

Appel and Appleby studied ORR on activated carbon [32], using the rotating ring disc electrode (RRDE) method. They obtained data showing that the rate of oxygen reduction on charcoal was independent of pH and so proposed two possible pathways for the oxygen reduction.

The first pathway:

The first step is similar (7'), then

$$O_2^-* + H_2O + e^- \rightarrow HO_2^- + OH^- \quad (10)$$

The second pathway:

[1] *- active centre of the electrocatalyst

$$O_2 + H_2O + e^- + * \rightarrow HO_2* + OH^- \quad (11)$$

$$HO_2*+ e^- \rightarrow HO_2^- \quad (12)$$

Thus, if the rate-determining step was (11) or (12), a Tafel slope of 2RT/F would be expected, whereas the experimental Tafel slope was 1.2 RT/F (In a later paper, the authors assumed a slope of 1.5RT/F, based on experiments using an ultra-thin porous electrode).

In contrast to the mechanism proposed by Morscov and Yeager, in the mechanism of Appel and Appleby oxygen adsorption occurs simultaneously with electron transfer from the catalytic centre (11 and 12).

In addition, the mechanism of the ORR on activated carbon in 1 M KOH was investigated with 'labelled' oxygen $^{18}O_2$ [33]. It was shown that all the oxygen atoms of the formed HO_2^- originated from the fed $^{18}O_2$ oxygen, indicating that the O-O bond was not broken during the reaction. In the reverse process - the anodic oxidation of $H^{18}O_2^-$ - the resulting oxygen also contained two labelled oxygen atoms from the hydrogen peroxide.

Studying the kinetics of the ORR on glassy carbon electrodes, the authors of [34,35] concluded that two types of catalytic centres were present on the surface:

$$O_2* + e^- \rightarrow [O_2*]^- \quad (13)$$

$$[O_2*]^- \rightarrow \{O_2*\}^- \quad (14)$$

where $[O_2*]$- and $\{O_2*\}$ are superoxide anions adsorbed on different catalytic centres and step (14) is the migration of the superoxide anion from one catalytic centre to another (Fig. 6).

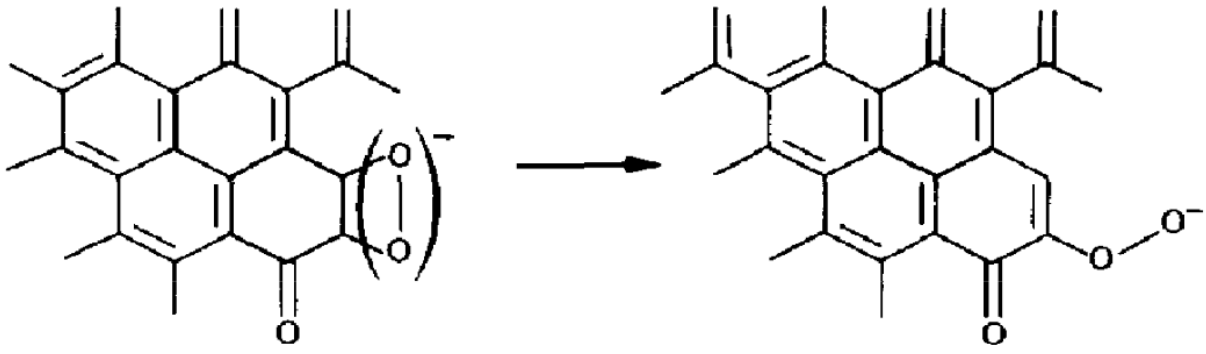

Fig. 6 Two types of superoxide adsorbed on the surface of a glassy carbon electrode (reproduced from [35]).

Taylor and Humffray [34] further speculated that superoxide anion disproportionation occurs:

$$2[O_2*]^- + H_2O \rightarrow O_2 + HO_2^- + OH^- \quad (15)$$

In turn, the following mechanism was deconstructed in paper [35], where the rate-limiting step is the formation of adsorbed HO_2:

$$O_2{}^{*-} + H_2O \rightarrow HO_2{}^* + OH^- \quad (16)$$

$$HO_2{}^* + e^- \rightarrow HO_2{}^{-*} \quad (17)$$

$$HO_2{}^{-*} \rightarrow HO_2{}^- \quad (18)$$

In [30], a fundamentally different mechanism was proposed for carbon black. The authors assumed an outer-sphere mechanism (Fig. 7) for the ORR, making this assumption on the basis of the obtained Tafel slope - 2RT/F:

$$O_2 + e^- \rightarrow O_2{}^- \quad (19)$$

$$O_2{}^- + H_2O \rightarrow HO_2{}^- + OH_{ad} \quad (20)$$

$$OH_{ad} + e^- \rightarrow OH^- \quad (21)$$

It is worth noting that the authors admitted that the first step may also follow the path proposed by Appel and Appleby (11).

The authors suggested that the formation of adsorbed $HO_2{}^*$ (22) is realised on more active materials but pointed out that they have no evidence to confirm or discard this hypothesis.

Despite this, the involvement of the outer-sphere mechanism is quite likely, and it can also occur on other catalysts. The difference between the inner-sphere and outer-sphere mechanisms is that, in the former, the reagent (oxygen, in the current case) adsorbs onto the catalyst surface. It is assumed that, in the outer-sphere mechanism, the second step, the $HO_2{}^-$ generation, is the rate-determining (rds), with OH_{ad} being formed as an intermediate, which was not present in the previously proposed mechanisms. In the last step, hydroxide anion is formed from OH_{ad} in a charge-transfer step, and the surface site is regenerated.

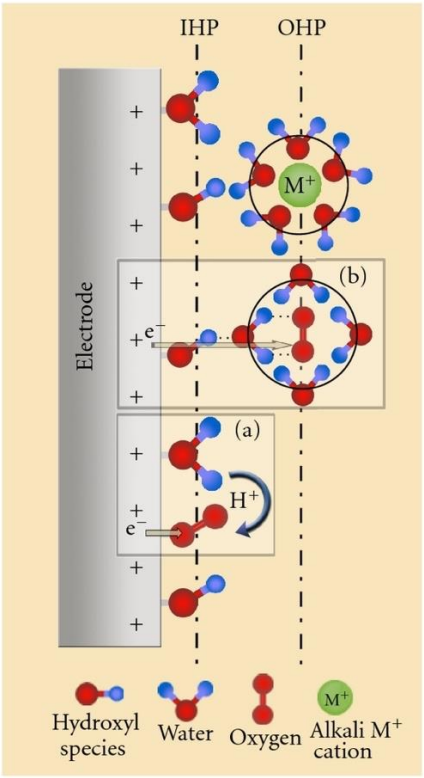

Fig. 7 Schematic representation of the structure of the electric double layer in an alkaline medium and the ORR process. Subfigures (a) and (b) illustrate the processes of electron transfer to the inner and outer spheres [36].

1.1.3 Oxygen reduction reaction mechanism on platinum

Currently, platinum-based catalysts are used for the ORR of acid and alkaline FCs [36]. For a long time, platinum was used as a catalyst for cathodic reaction in FCs, but now many alloys based on it are known to possess higher electrocatalytic activity, and at the same time cost less due to the use of cheaper alloying additives. For example, alloys of platinum with Ni and Co have an activity that is several times higher than that of polycrystalline platinum [37].

Although platinum-based alloys have been studied for many years, platinum itself is a convenient object, both for the study of the ORR mechanism and for its use as a reference material against which the activities of other compounds studied in electrocatalysis are compared. Despite considerable progress being made both using experimental and computational methods, there is no consensus regarding the key elementary steps of the ORR. This is due to the complexity and multistep nature of the oxygen reduction reaction mechanism, which makes it difficult to reliably identify its individual steps by electrochemical and physicochemical methods.

Studies of the mechanism of oxygen reduction reaction on platinum began to appear in the literature more than 50 years ago [38,39]. Work by Dajmanovic [40] and Sepa [39,41,42] on

polycrystalline platinum showed that for two intervals of current densities (low and high), different Tafel slopes (-120 and -60 mV/dec for high and low current densities, respectively) were observed. In addition, pH influence on the ORR was studied. In the low current density interval dE/d(pH)= 3/2 and -1/2 in acid and in base, respectively. In the region of high current densities, dE/d(pH)=1 and 0 in acid and in base, respectively (the scale was relative to SHE). The fractional order of the reaction and its change from the low current to the high current interval was attributed by the authors to changes in the surface coverage with adsorbed oxygen (O/OH). At high current densities (high overpotentials and consequently lower potentials), the oxygen coverage was low and could be described by the Langmuir isotherm. At low current densities (lower overpotentials and correspondingly higher potentials), the coverage of the platinum surface with oxygen was high and could be described by the Temkin isotherm.

Anastasijevic [43], having analysed the mechanisms proposed in the literature (Fig. 8), proposed an extensive scheme that included the different pathways by which the reduction of oxygen in an alkaline medium can occur. k_i represents the rate constant of individual steps; lower indices, SA, A, B and * indicate strongly adsorbed, weakly adsorbed, bulk and near-surface intermediates, reactants and reaction products, respectively.

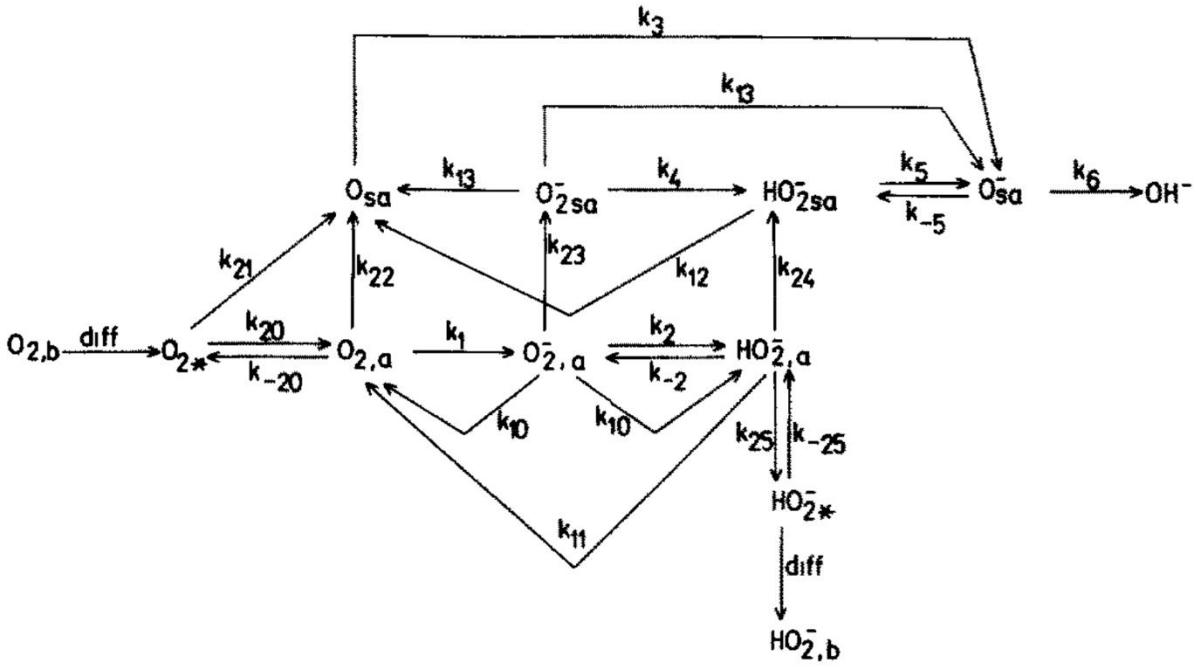

Fig. 8 The general mechanism of the ORR on platinum proposed by Anastasijevic [43].

In recent works the oxygen reduction reaction mechanism on platinum was studied using theoretical simulations and it has been shown, specifically by Nørskov in 2004, that two different pathways may occur simultaneously. This hypothesis was proposed by Nørskov based on the density functional calculations (DFT) of the Gibbs energies of the ORR intermediates [44]. Within

this model, two mechanisms of ORR - associative, involving the HOO* intermediate, and dissociative, involving the dissociation of O_2 molecules on the Pt surface - have been proposed for high and low current densities, respectively.

Acid medium		Alkaline medium	
$O_{2(g)} + * \rightarrow O_2*$	22 (a)	$O_{2(g)} + * \rightarrow O_2*$	22 (b)
$O_2* + H^+ + e^- \rightarrow HOO*.$	23 (a)	$O_2* + H_2O + e^- \rightarrow HOO* + OH^-$	23 (b)
$HOO* + H^+ + e^- \rightarrow O* + H_2O$	24 (a)	$HOO* + e^- \rightarrow O* + OH^-$	24(b)
$O* + H^+ + e^- \rightarrow HO*$	25 (a)	$O* + H_2O + e^- \rightarrow HO* + OH^-$	25(b)
$HO* + H^+ + e^- \rightarrow H_2O + *$	26 (a)	$HO* + e^- \rightarrow OH^- + *$	26(b)

*- active centre of the electrocatalyst

The first step is the adsorption of molecular oxygen on the platinum surface (22 a, b), followed by the reduction of the adsorbed species to the peroxide intermediate HOO (23 a, b). The next step is the reduction of the intermediate involving another electron transfer (24 a, b). An alternative process, involving electron transfer and desorption of the peroxide anion from the platinum surface, is possible:

$$HOO* + e^- \rightarrow HO_2^- + * \quad (27)$$

It has been shown that increasing the concentration of OH^- in the solution leads to a decrease in the HOO* coverage on the platinum surface due to competitive adsorption between the hydroxide and peroxide on the catalytic centres [45].

In the dissociative mechanism, the reduction process starts with the following elementary step (dissociative adsorption of oxygen):

$$O_{2(g)} + * + * \rightarrow O* + O* \quad (28)$$

$$O* + e^- + H^+ \rightarrow OH* \quad (29)$$

$$OH* + H^+ + e^- \rightarrow H_2O + * \quad (30)$$

The molecular oxygen adsorbed on the platinum surface dissociates to form atomic oxygen, which subsequently gains two electrons in two successive steps, to form water. Since there are no intermediates containing the O-O bond on the platinum surface, no hydrogen peroxide is formed.

It is important to note that the mechanisms presented above are inner-sphere, but there is a debate concerning the possibility of the outer-sphere mechanism on platinum in an alkaline medium. The authors of Ref. [46], having shown the increased stability of superoxide radical anion O_2^- in strongly alkaline electrolytes, discussed the possibility of the O_2^- formation through an outer-

sphere mechanism. In [47], the authors discussed a possible mechanism of the oxygen reduction with an outer-sphere electron transfer according to the following mechanism:

$$M\text{-}OH + [O_2(H_2O)_n]_{aq} + e^- \rightarrow M\text{-}OH + (HO_2)_{ad} + OH^- + (H_2O)_{n-1} \quad (31)$$

$$(HO_2)_{ad} + e^- \rightarrow (HO_2^-)_{ad} \quad (32)$$

$$(HO_2^-)_{ad} \rightarrow (HO_2^-)_{aq} \quad (33)$$

Equation (31) involves electron transfer (or tunnelling) from the electrode surface, through the adsorbate layer of OH_{ad} on the platinum surface and at least one solvation shell, to the solvated O_2. The authors assume that this step (31) is not elementary and that it includes the following steps:

$$M\text{-}OH + [O_2 \bullet (H_2O)_n]_{aq} + \bar{e} \rightarrow M\text{-}OH + [O_2^- \bullet (H_2O)_n]_{aq} \quad (34)$$

$$[O_2^- \bullet (H_2O)_n]_{aq} \rightarrow O_2^-{}_{ad} + H_2O_n \quad (35)$$

$$O_2^-{}_{ad} + H_2O \rightarrow (HO_2)_{ad} + OH^- \quad (36)$$

As mentioned above, the efficiency of the oxygen reduction is strongly influenced by the adsorption of hydroxide ions on the platinum surface. This effect explains the strong dependence of the catalytic activity on the crystallographic orientation of platinum. It has been experimentally shown that the activity decreases in the series Pt(111) > Pt(100) > Pt(110) [48], and the half-wave potential shift between the most active and the least active surface is ~110 mV. This is attributed to the fact that two types of adsorbed OH^- the so-called reversibly, and irreversibly, adsorbed forms - are present on Pt(100) and Pt(110) surfaces. Only the reversibly adsorbed form was found on the Pt(111) surface. A very small yield of H_2O_2 was detected on the ring (using a rotating ring disc electrode) in the potential region where the adsorption of OH^- on the Pt(100) and Pt(110) was reversible. However, the peroxide yield increased considerably when the surface was covered by irreversibly adsorbed OH^-.

Thus, although there are different views on the mechanism of the oxygen reduction reaction on platinum, the approaches used to clarify it can be applied to other catalysts, in particular, transition metal oxide catalysts.

1.2 Oxygen reduction catalysts based on transition metal oxides

1.2.1 Spinels

The structural type of spinel is described by the general chemical formula AB_2O_4; A and B cations are distributed in different ratios in the tetrahedral and octahedral positions, respectively. In order to distinguish between cations in octahedral and tetrahedral positions, the following format is introduced: $A_{1-\lambda}B_\lambda(A_\lambda B_{2-\lambda})O_4$. The ions in front of the brackets are in tetrahedral positions, whereas the ions in the brackets are in octahedral positions. $\lambda = 0$ is considered a ‘normal’ spinel (Fig. 9a), $\lambda = 1$ a ‘inverse’ spinel (Fig. 9b) and $0 < \lambda < 1$ reflects complex spinels

(Fig. 9c). In the typical normal spinel oxide $MgAl_2O_4$ (Fig. 9a, d), Mg^{2+} cations occupy the centres of tetrahedral positions and Al^{3+} occupies octahedral positions. Inverse spinels can be described as $B(AB)O_4$. For example, in an inverse spinel $NiFe_2O_4$ (Fig. 9b), half of the Fe_{3+} cations occupy centres of tetrahedral positions, while Ni^{2+} and the remaining half of the Fe^{3+} occupy octahedral positions, which can be expressed as $Fe(NiFe)O_4$. Complex spinels are defined as being intermediate between normal and inverse spinels. One example is the complex spinel $CuAl_2O_4$ (Fig. 9c), in which Cu^{2+} and Al^{3+} cations partially occupy both octahedral and tetrahedral positions ($Cu_{1-\lambda}Al_{\lambda}(Cu_{\lambda}Al_{2-\lambda})O_4$).

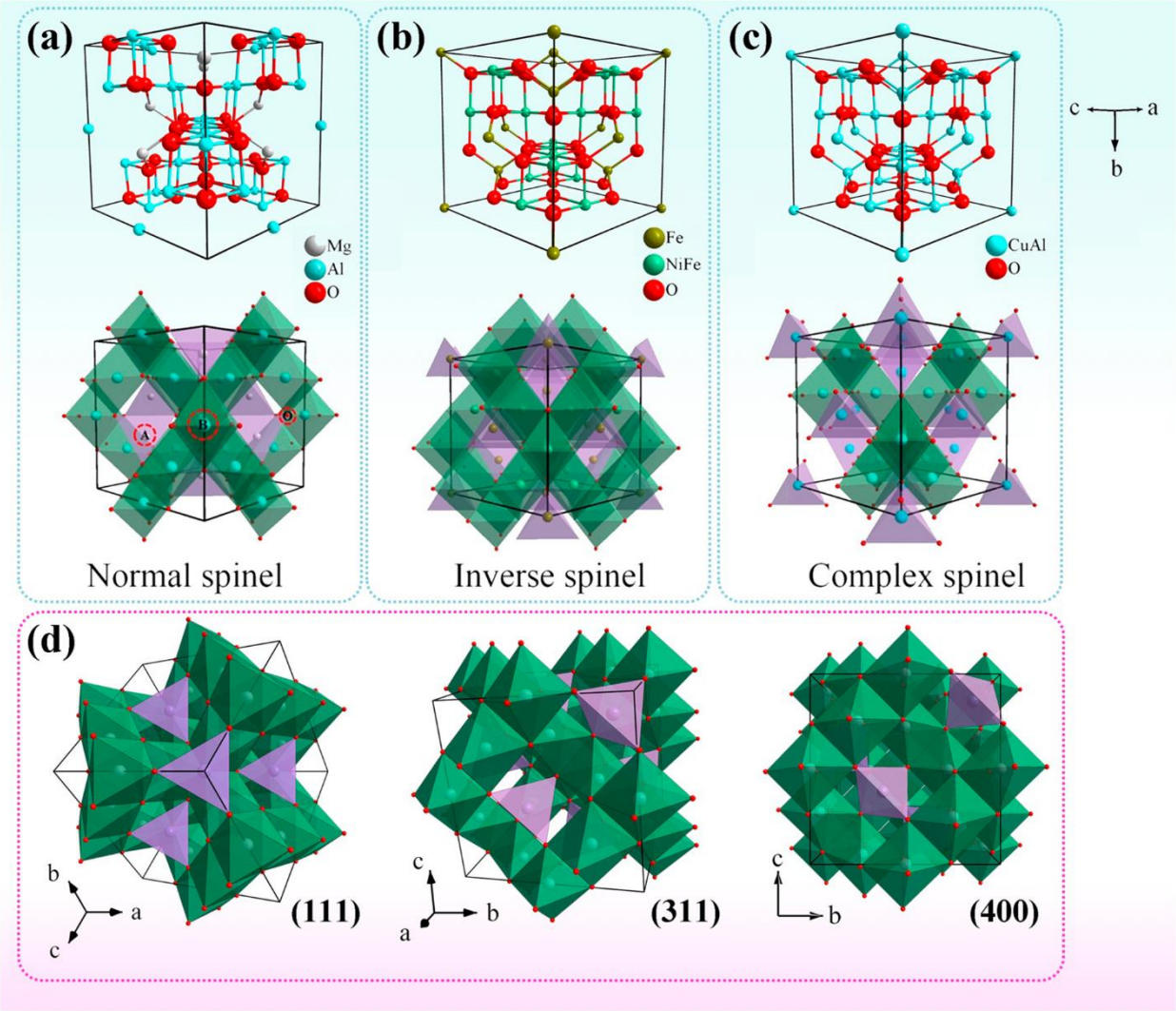

Fig. 9 Structures of (a) normal spinel (for example, $MgAl_2O_4$), (b) inverse spinel (for example, $NiFe_2O_4$), and (c) complex spinel (for example, $CuAl_2O_4$) in different representations. Green and purple polyhedrons correspond to octahedral and tetrahedral sites filled with metal cations, respectively. Representative defect locations A, B, and O in spinel AB_2O_4 are shown in panel a. (d) Normal spinel in various projections (111), (311) and (400) [49].

The reduction of oxygen has been investigated in detail on spinels with different compositions. The electroreduction of oxygen on spinels will be described in more detail in chapter 3, which is devoted to the study of their electrocatalytic activity and stability.

1.2.2 Perovskites

The mineral $CaTiO_3$ was named Perovskite after the Russian mineralogist Perovsky, and as a result, this name was also given to the class of compounds with the same crystal structure, which is ideally described by the formula ABO_3, where the rare-earth or alkaline-earth metal cation A is coordinated by 12 O^{2-} and the transition metal cation forms octahedra with common vertices BO_6 (Fig. 10).

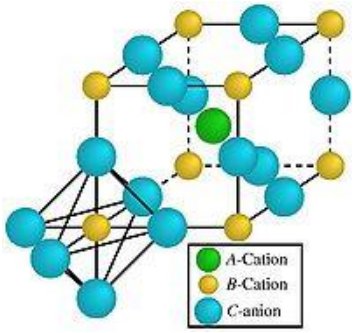

Fig. 10 Crystal structure of cubic perovskite. The A-cation is in the cuboctahedron (CN = 12), and the B-cation is in the octahedron (CN = 6).

Owing to the possibility of varying, in a wide range, the cationic and anionic composition due to isovalent and heterovalent substitution and high thermodynamic stability, wide opportunities for obtaining samples with lattice defects (oxygen non-stoichiometry) make this class of compounds a convenient object for studying the influence of various factors on catalytic activity.

The use of perovskites as catalysts for oxygen reduction was initially demonstrated for $LaCoO_3$ [50]. This study gave impetus to a further search for new catalysts among oxides with a perovskite structure. Thus, a number of perovskites were investigated, for which different 3d metals were used as B cations. As a result of these studies, various volcano-like dependences were constructed. For example, one obvious factor that can influence electrocatalytic activity is the bonding energy of oxygen on the catalyst surface, because, if the bonding energy of the catalytic centre with oxygen is high, the catalyst surface will not regenerate after the reduction cycle, while too low an adsorption energy does not promote the adsorption of oxygen on the surface. Based on

the assumption of proportionality between the adsorption and desorption energies, the authors of [51] suggested which perovskite binds to oxygen most strongly.

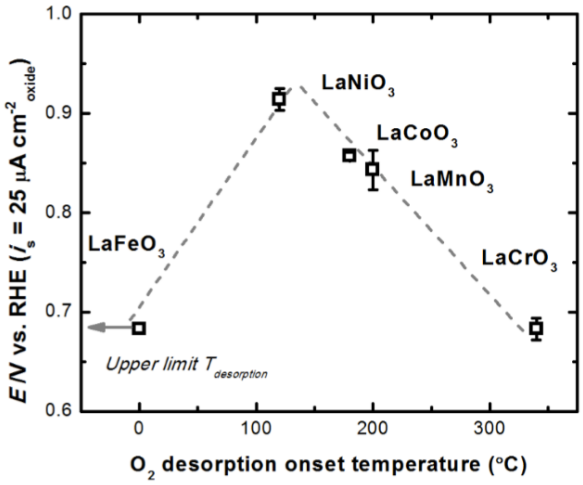

Fig. 11 Dependence of the oxygen reduction potential at a 25 μA cm^{-2} current density for perovskites of various 3d metals [51] on the oxygen desorption onset temperature.

By determining the catalytic activity of ABO_3 perovskites containing different B-cations (Fe, Ni, Co, Mn, Cr) and the same A-cation (La), the dependence (Fig. 11) between the catalytic activity in oxygen reduction reaction and the 'onset' temperature of oxygen desorption was constructed. Perovskites with desorption temperatures between 120°C (Ni) and 200°C (Mn, Co) showed the highest activity.

The use of a catalyst is known to lower the energy barrier of the reaction due to the formation of intermediates. The Gibbs energy of an intermediate adsorption is one of the most obvious descriptors of catalytic activity and its importance was highlighted in [52]. The Gibbs energy of an intermediate is, however, an experimentally undeterminable value, but it can be calculated by various methods. Consequently, it became logical to determine the Gibbs energy of the formation of the B-OH bond. The authors of [52] carried out the calculation using the generalised gradient approximation with Hubbard correction (GGA + Ueff). The calculation was performed for perovskites of composition $LaBO_3$, and for each compound, the reduction process was considered on different AO and BO_2 layers.

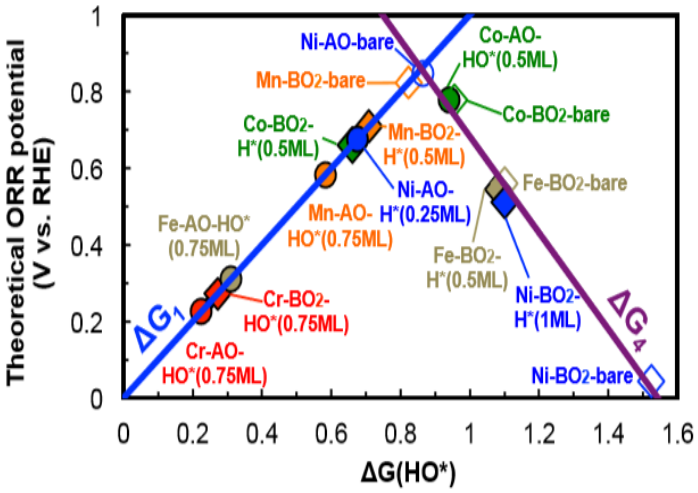

Fig. 12 Dependence of the calculated oxygen reduction potential on the Gibbs energy of B-OH intermediate on the catalyst surface [52].

As a result, the Gibbs energies for the steps were computed:

$B\text{-}O^{2-} + H_2O \rightarrow B\text{-}OH + e^- + OH^-$ (left blue curve ΔG_1) (37)

$B\text{-}OH^- + O_2 + e^- \rightarrow B\text{-}OO^{2-} + OH^-$ (right purple curve ΔG_4) (38)

Figure 12 shows that Co, Ni and Mn perovskites should have the greatest activity, and it is important whether oxygen adsorbs at the AO or BO_2 sites. For $LaMnO_3$ and $LaCoO_3$, the oxygen reduction reaction with the least overpotential occurs on the BO_2 layer. Conversely, for $LaNiO_3$, if the reduction takes place on the BO_2 layer, catalytic activity is lost, but when the reduction takes place on the AO layer it increases considerably.

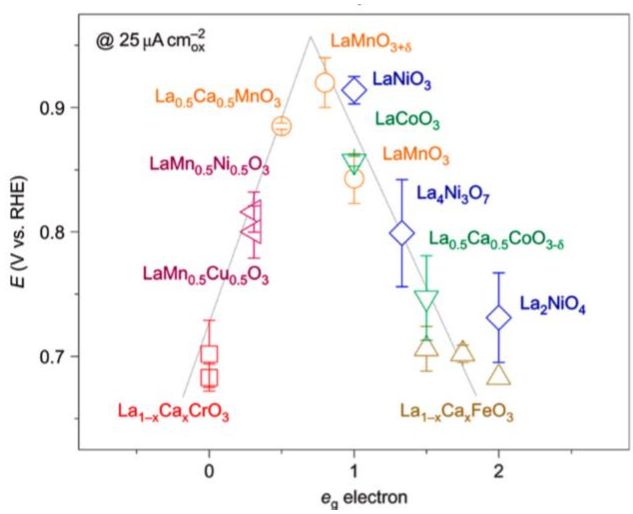

Fig. 13 Dependence of the catalytic activity of perovskites (potential at the current density 25 μA cm^{-2}_{oxide}) on the degree of filling of the e_g orbital of the 3d metal cations [53].

Some authors have discussed the correlation between the electronic structure of metal cations and the electrocatalytic properties of perovskites. The proposed dependence has a volcano-like form, with a maximum at an e_g orbital occupancy of slightly less than 1 (Fig. 13). The maximum corresponds to the lowest overpotential, and the greatest activity corresponds to the perovskite composition $LaMnO_{3+\delta}$. In [54], this effect is attributed to the interaction of e_g orbitals and π*-orbitals of oxygen (Fig. 14).

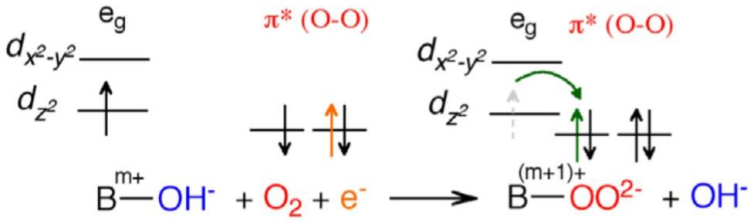

Fig. 14 Interaction of Mn^{3+} e_g-orbital and oxygen π*-orbital [53].

In Ref. [55], the following conclusions about the stability of the peroxo- and hydroxo-complex ($B\text{-}OO^{2-}$ and $B\text{-}OH^-$, respectively) were made:

1) The presence of one electron in the orbital d_{z2} lowers the bonding energy of $B\text{-}OH^-$. This is due to the mutual repulsion of the electron on the B-cation and the negatively charged oxygen of the hydroxyl group. On the other hand, due to the total energy decrease in the system, the peroxy group is stabilised during the electron transfer.

2) If the number of e_g electrons is greater than 1, there is no energy gain through the formation of a peroxocomplex. There is a weakening of the bond between the B-cation and the peroxo group, due to which the rate of the substitution of the hydroxyl group B-OH- for B-OO2- decreases. This case is realized if $LaFeO_3$ is used as a catalyst.

In a number of papers, the presence of strain in the perovskite structure has been proposed as a descriptor of the ORR electrocatalysis. To study the effect of distortions on the catalytic activity, the authors of [56] obtained $LaNiO_3$ films by pulsed laser deposition (PLD). The degree of distortion was varied by selecting the substrate on which the deposition was carried out. As a result, it was found that stretching the $[BO_6]$ octahedron along the z-axis led to an increase in activity. With a strain of less than 2%, activity increased by more than 30%. Conversely, compression led to a decrease in the reaction rate of oxygen reduction, and at a strain of less than 3% activity practically disappeared (Fig. 15).

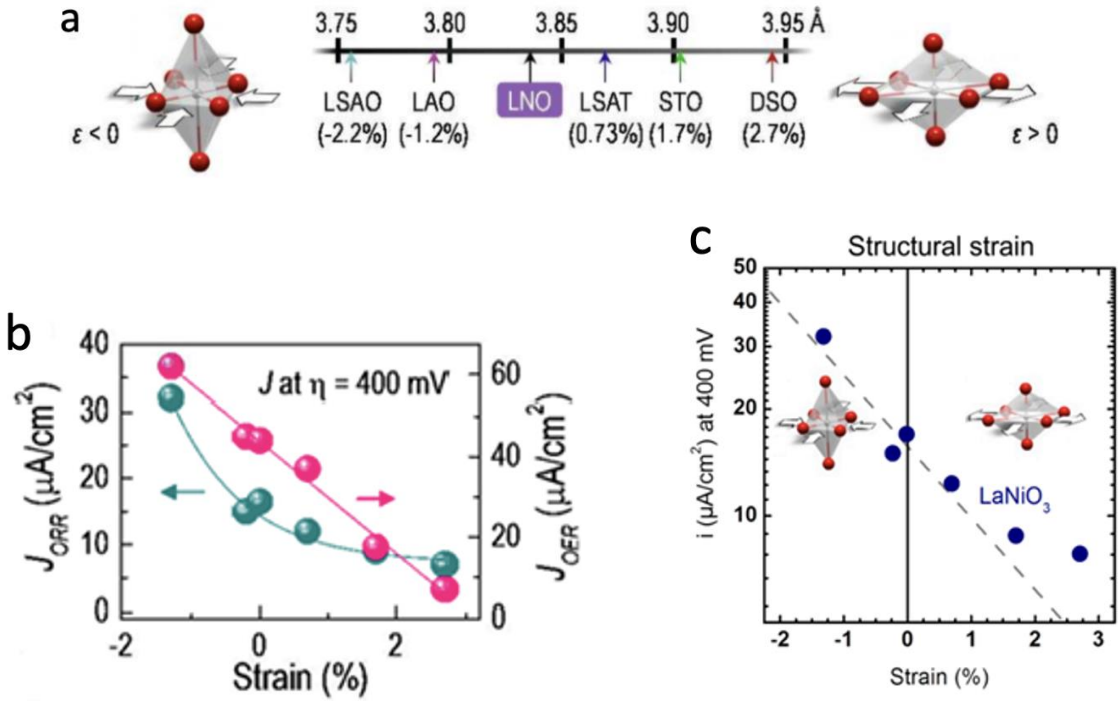

Fig. 15 a) The degree of perovskite structure distortion depending on the chosen substrate. b) Currents in the oxygen reduction reaction (left scale) and oxygen evolution reaction (right scale) at an overpotential of 400 mV [57]. c) ORR current at an overpotential of 400 mV depending on the degree of deformation of the $LaNiO_3$ crystal structure [58].

The relation between the magnitude of the magnetic moment of the B-cation and catalytic activity had already been suggested in earlier work. Such a study was carried out by Larsson and Lennart in 1990 [57]. Fig. 16 shows that, for a series of perovskites of the composition $LaB_{0.5}Mn_{0.5}O_3$ (where B = Cu, Cr, Ni), the lowest magnetic moment corresponded to the highest catalytic activity. Due to a lack of experimental data, however, it is not known whether such a dependence is observed for perovskites of other compositions.

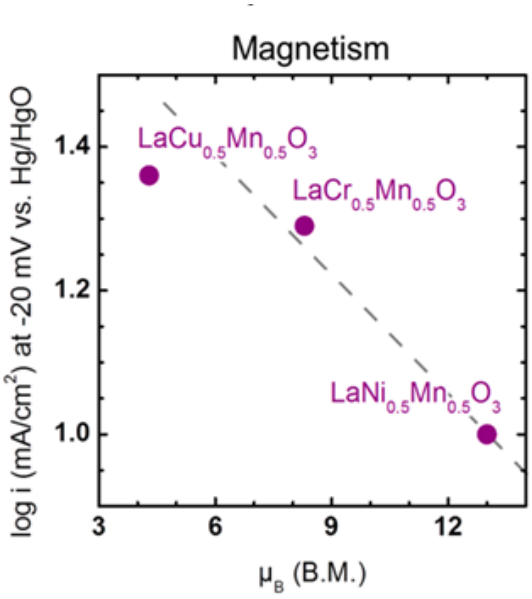

Fig. 16. Dependence of the ORR current at -20 mV relative to the Hg/HgO electrode on the magnetic moment of the B-cation [57,58].

One of the most important steps in the study of a catalyst is to determine the mechanism of the reaction occurring on it. The oxygen reduction reaction has long been studied for oxide-based catalysts, but there are far fewer papers discussing the reaction mechanism than for platinum, which is due to the much more complex processes that occur on the surface of oxide catalysts.

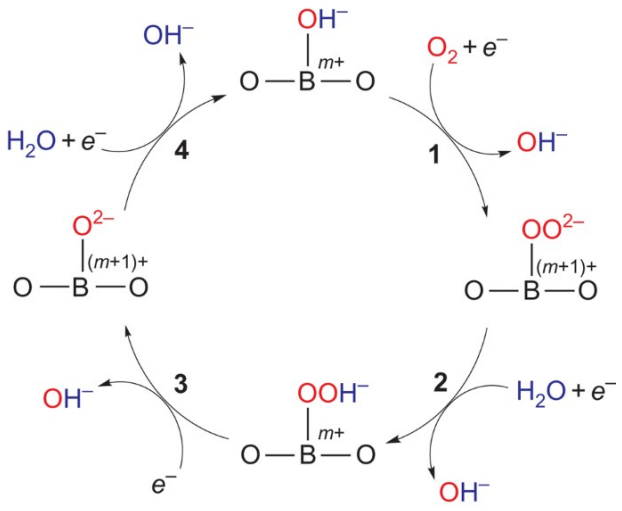

Fig. 17 Tentative scheme of the oxygen reduction reaction on transition metal oxide proposed in Ref. [55].

One of the first mechanisms of the oxygen reduction on perovskites was proposed by Goodenough [55]. In the first step of the proposed mechanism (Fig. 17), the oxygen molecule is adsorbed on the oxide surface and reduced to the peroxide ion OO^{2-}, replacing the OH-group. In this step, the transition metal cation B^{m+} is oxidised to a higher oxidation degree $B^{(m+1)+}$. In the

second step, the peroxo group is protonated to form OOH^- and the transition metal cation is reduced. In the third step, the transition metal cation is oxidised to form an oxide (O_2^- ion in the diagram), with the simultaneous passing of OH^- into the solution. In the fourth and last step, the oxide on the surface is protonated to form the initial hydroxide ion and the transition metal cation is reduced [59]. It is assumed that the step of the oxygen molecule adsorption accompanied by the removal of the OH-group from the oxide surface (step 1) is the rate-limiting one in the oxygen reduction reaction.

1.2.3. The role of carbon in oxygen reduction on oxide-carbon compositions

Many of the 3d metal oxides have low electronic conductivity and, as a consequence, are mixed with carbon for electrochemical applications [60]. It has been shown that the addition of carbon is necessary, even in the case of oxides with high intrinsic electronic conductivity; in this case, the addition of carbon improves the electrical contact between particles (i.e. it reduces contact resistance) and the current collector. In Ref. [61], the effect of carbon additives on oxygen reduction on Co- and Mn-containing perovskites was investigated. The electrode compositions were obtained by physically mixing the oxide and carbon in different proportions. The first observation was that, for both Co- and Mn-bearing perovskites, total pseudocapacity increased with increasing carbon content (see Fig. 18), which was attributed to the increased conductivity of the catalytic layer (due to improved contact between perovskite particles and with the current collector), allowing more centres on the oxide surface to participate in the interfacial recharging processes. It was also found that the difference between the potentials of the anodic and cathodic peaks on the cyclic voltammogram (CV) curves in the background electrolyte decreased, confirming that the addition of carbon reduces the ohmic resistance of the layer. In a study of oxygen reduction on oxide-carbon compositions, it was found that there was a ten-fold increase in the kinetic currents of ORR with a two-fold increase in the pseudocapacity.

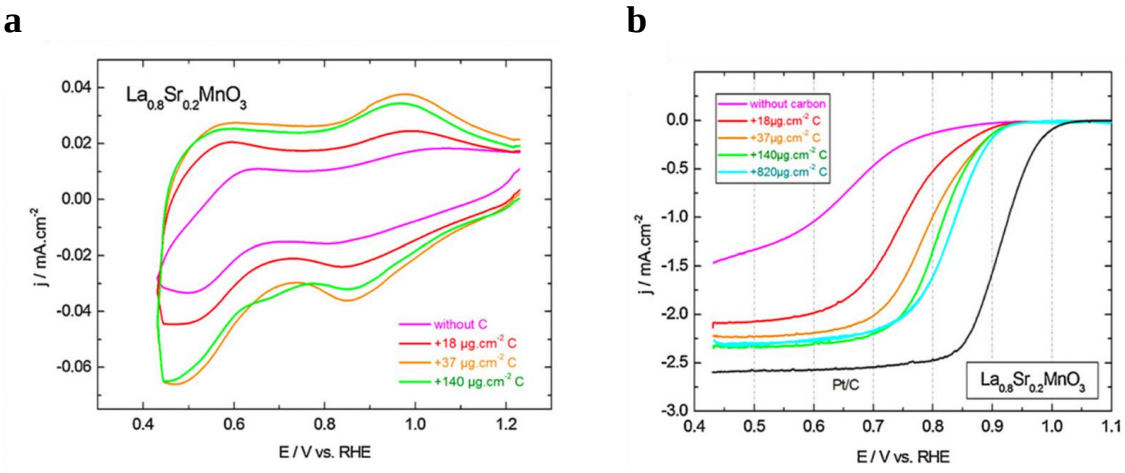

Fig. 18 Cyclic voltammogram curves in the supporting electrolyte (a) and RDE curves of the oxygen reduction reaction (b) at a rotation speed of 900 rpm $La_{0.8}Sr_{0.2}MnO_3$ with different carbon loading (from 18 to 820 µg cm^{-2}) and a fixed oxide loading of 91 µg cm^{-2} in 1 M NaOH at a scan rate of 10 mV s^{-1} [61].

It was concluded that carbon not only serves as a conductive binder, but also as a co-catalyst of ORR (Fig. 19). Indeed, the reduction of oxygen may not only occur on the oxide, but also on carbon, where it is reduced to hydrogen peroxide, with further re-adsorption of hydrogen peroxide onto the catalytic oxide centres and its further reduction.

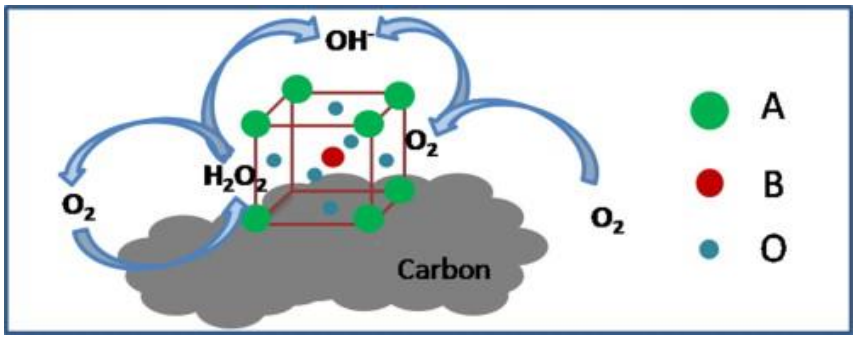

Fig. 19 Graphical representation of the processes occurring during the reduction of oxygen on a perovskite/carbon composite. Reproduced from Ref. [62].

Cobalt-based perovskites were studied in [62]. Based on microkinetic modelling, a mechanism was proposed for the oxygen reduction on perovskite composite with carbon doped with nitrogen as a co-catalyst (Fig. 20).

In [63,64], it was found that the fraction of carbon in the catalytic layer should be optimum. If the carbon content is too low, it is possible that the extent of the utilisation of the oxide surface in electrocatalysis will be below 100%. However, if carbon content is too high, it will compete with the transition metal oxide for the oxygen adsorption, which leads to a decrease of the ORR rate. It was shown that not only the carbon fraction but also its type affects the ORR kinetics [65].

Thus, failure to account for the role of the carbon binder in the ORR can lead to erroneous conclusions, notably to erroneous correlations of activity with the composition and structure of the oxide.

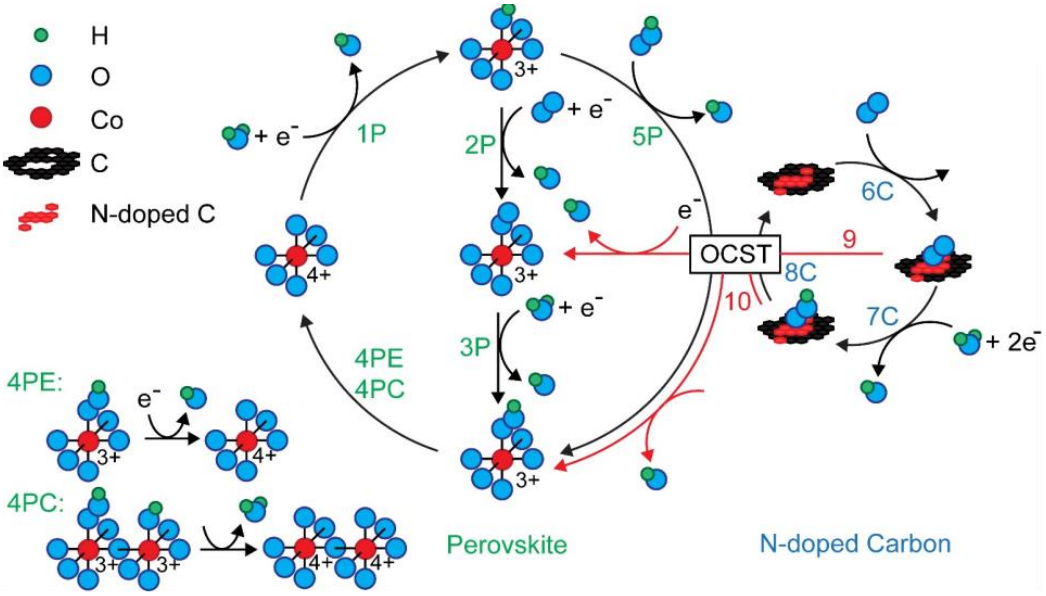

Fig. 20 Suggested mechanism of the oxygen reduction on electrodes made of $La_{1-x}Sr_xCoO_{3-\delta}$ /carbon composite. Reproduced from Ref. [66].

The overall conclusion of this section is that the literature data on the influence of the composition and structure of 3d metal oxides on their electrocatalytic activity in ORR are quite contradictory. This may be due to the choice of experimental conditions, such as catalytic layer thickness, the addition of a carbon binder, its type and percentage, etc. The work of the electrochemistry and energy conversion group at ICPEES UMR7515, which has investigated oxides with different 3d metal cations, has shown that Mn-containing oxides have the highest catalytic activity in the reaction of the oxygen reduction in an alkaline medium. It is in this context that the following section is devoted to the analysis of the structure and electrocatalytic activity of manganese oxides.

1.3 Manganese oxides

ORR electrocatalysis has been investigated on a wide range of manganese oxides with different compositions and crystal structures. One important issue is the determination of the influence of the crystal structure on the electrochemical and electrocatalytic behaviour of oxides. Manganese forms a wide variety of oxide phases, both simple, which can be described by the

formula Mn_xO_y, and complex, with additional to oxygen and manganese atoms, such as the previously considered perovskites ($AMnO_3$) and spinels (AMn_2O_4).

For simple oxides, there is also a variety of structural modifications. For example, the most stable structural modification of MnOOH is γ-MnOOH. The structure of γ-MnOOH (Fig. 21) is similar to that of β-MnO_2 (a structural type of rutile). The only difference is that in MnOOH all the manganese atoms have an oxidation degree of +3, and half of the O^{2-} anions are replaced by OH^- groups. MnOOH crystallises in monoclinic syngony (space group P21/c, Z = 4) and has unit cell parameters a = 5.304(1) Å, b = 5.277(1) Å, c = 5.304(1) Å, β = 114.38(2)°[67].

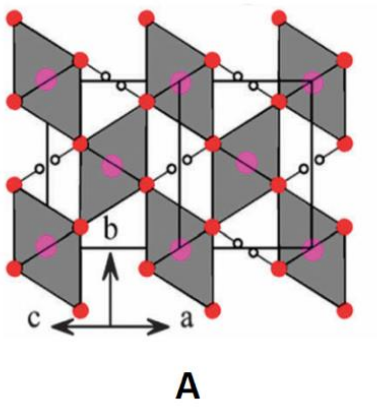

Fig. 21 Crystal structure of γ-MnOOH.

Three structural modifications are known for Mn_2O_3, the most common being α-Mn_2O_3; in nature, this modification occurs in the form of the mineral bixbyite. α-Mn_2O_3 crystallises in cubic syngony (space group $Ia\bar{3}$, Z = 16) and has unit cell parameters a = 9.4091(4) Å [68]. The structure of bixbyite (Fig. 22a) may be considered to be a derivative of fluorite (CaF_2). In contrast to fluorite's structure, however, where the metal cation has a coordination number (CN) equal to 8, for bixbyite CN = 6, due to the absence of two oxygen atoms in the vertices of the cube. This is the case for a quarter of the original fluorite cubes. For the remaining cubes, two vertices are connected not by a solid diagonal within the cube, but by a diagonal of one of its truncated faces (Fig. 22 b). Due to this, the structure of bixbyite is very distorted. Thus, there are two alternating layers in the bixbyite structure. One layer consists of octahedrons formed by truncating fluorite cubes on the diagonal face. In the second layer, half of the octahedrons are formed by the truncation of fluorite cubes on the spatial diagonal, while the other half are formed on the cube diagonal (Fig. 22 c).

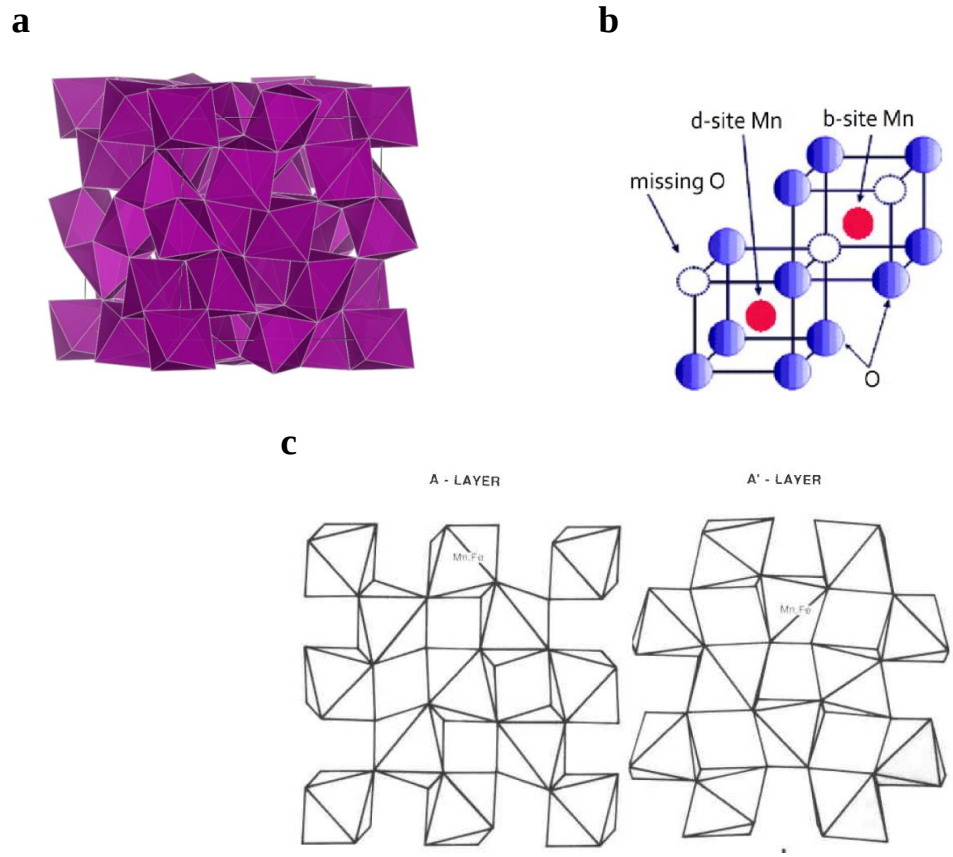

Fig. 22 a) Crystal structure of α-Mn_2O_3, b) formation of octahedrons in the α-Mn_2O_3 structure, c) A and A' layers of α-Mn_2O_3 [68].

MnO_2 is one of the most common manganese oxides in nature. A large number of modifications is known for it (Fig. 23) [69]. The main structural unit in MnO_2 is an octahedron [MnO_6]. Octahedrons are connected by vertices and edges, forming one-dimensional channels of different size. The large variety of structures makes MnO_2 an interesting object for studying the influence of structure on the catalytic activity in various electrochemical processes, in particular the ORR.

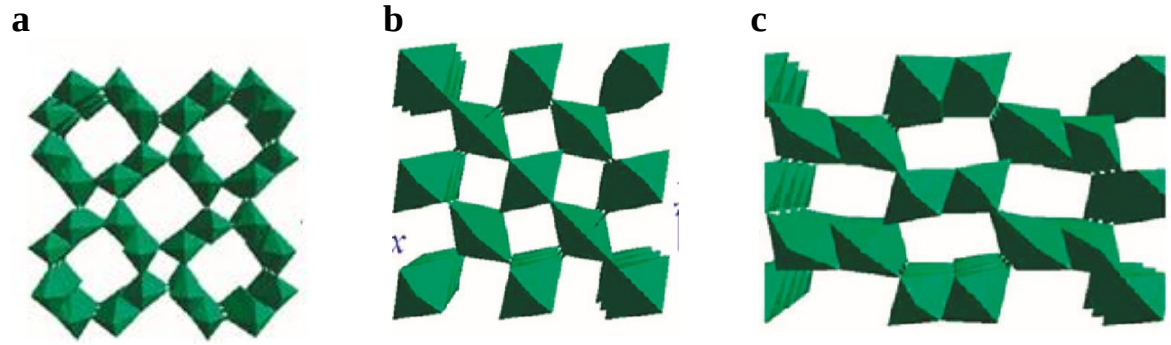

Fig. 23 Crystal structures of α- MnO_2 (a), β-MnO_2 (b), γ-MnO_2 (c) [69].

For manganese oxides, many studies have been carried out to establish a relationship between structure and catalytic activity in the ORR, but when considering the variety of

accumulated data it is difficult to draw a clear conclusion about the influence of composition and structure on the activity in the ORR. It should be noted that, when analysing the literature, there is a problem in that different setting of the electrochemical experiment can lead to significant differences in the kinetic currents, which might be due to the transformation of the oxide surface as a result of its degradation (e.g. because of electrode cycling in a wide potential region; see section 1.4.2.), or due to a suboptimal amount of carbon in the catalytic layer. This may explain why different activity series for manganese-containing oxides were obtained by different scientific groups (Table 1).

In [10], ORR activity of several manganese oxides (Mn_2O_3, Mn_3O_4, $LaMnO_3$, MnO_2, MnOOH) was compared in the potential range corresponding to their electrochemical stability. Activity in ORR was found to decrease in the series Mn_2O_3 > Mn_3O_4 ~$LaMnO_3$ > MnO_2 > MnOOH and correlate with the redox transition potential of Mn(IV)/Mn(III) (Fig. 24). The authors carried out a detailed study of the oxygen reduction kinetics using the rotating disc and the rotating ring electrode methods. It was found that the reduction of oxygen occurred through an intermediate step of hydrogen peroxide formation (2e+2e mechanism). The authors also investigated the electrochemical transformations of hydrogen peroxide on different manganese oxides and found that, for some of them (e.g. MnOOH or Mn_3O_4), a rotation rate-independent cathodic limiting (potential-independent) current was observed, which suggests that the electrocatalytic reduction of hydrogen peroxide occurs through a slow chemical step.

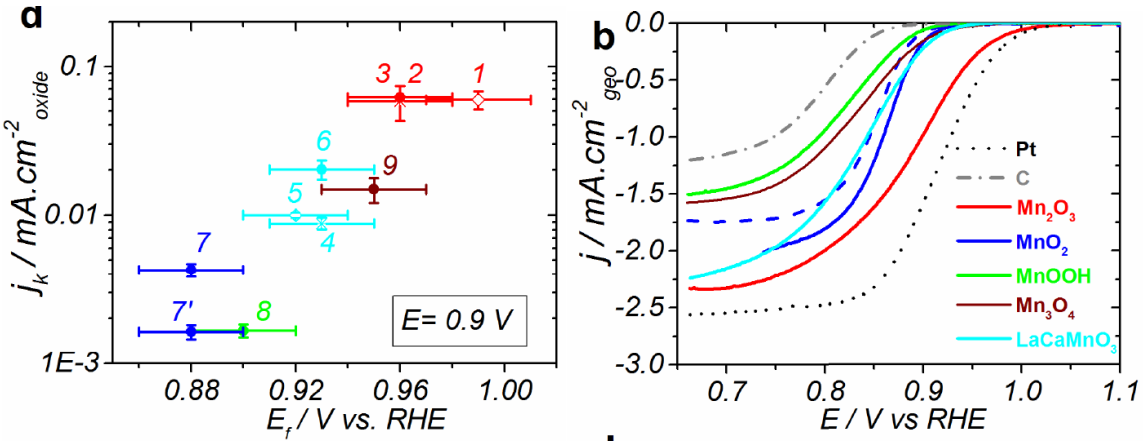

Fig. 24 Dependence of ORR kinetic current densities at 0.9 V vs. RHE on the formal potential (E_f) of the interfacial redox Mn(IV)/Mn(III) transition (a), and ORR polarization curves obtained on a rotating disk electrode in oxygen-saturated 1 M NaOH at 900 rpm and potential scan rate 10 mV/s (b) (numbers 1-3 denote Mn_2O_3 samples obtained according to different synthesis methods and hence specific surface area, 4-6 are manganese perovskites of different compositions, 7 and 7' are MnO_2 samples before and after cathodic degradation, respectively, 8 refers to MnOOH, 9 – to Mn_3O_4). Reproduced from Ref. [10].

Table 1 Representative literature data on the activity of manganese oxides in the ORR

sample	Oxide surface area, $m^2\ g^{-1}$	Oxide/carbon load, $\mu g\ cm^{-2}$	Electrolyte	Potential range vs. RHE	$^1n_{eff}$, e	^2E_i 2%	$^3i_{0.85}$, A g^{-1}	$^3i_{0.85,}$ mA m^{-2} $_{oxide}$	Ref.
Spinel Mn_3O_4.									
50% Mn_3O_4/Vulcan	32	46 μg cm^{-2} oxide/(The amount of carbon given by the synthesis)	1M NaOH	0.43 – 1.23		0.76	0.1	3.40	[70]
34% Mn_3O_4-Vulcan	114*					0.914	13.0		
91% Mn_3O_4/Vulcan	29*					0.8	0.1		
52% Mn_3O_4-S170	95*					0.89	3.3		
14% Mn_3O_4-Monarch900	293*					0.913	14.1		
44% Mn_3O_4-Sibunit	130*					0.902	8.3		
Mn_3O_4/VC		40/200	1M KOH	0.23-1.03	2.4	0.88	6.5		[71]
Mn_3O_4	98	85/0	0.1M KOH	0.17-1.02		0.756	<0.01	<0.01	[72]
Mn_3O_4 with a high concentration of defects		243/48.6	0.1M KOH	0.17 – 1.17	3.96	0.97	1.0		[73]
Mn_3O_4						0.83	0.2		
Mn_3O_4/Sibunit	13	91/91	1M NaOH		2.7	0.93	2.5	190	[10]

Mn_3O_4/pGC			0.1M KOH	0.05-1.1	4	0.81			[74]
Mn_3O_4/NC hybrid		67/33	1M KOH	0.45-1.15	3.9	0.93	23		[75]
Mn_3O_4/NrGO		450	0.1M KOH	-0.04-0.17		0.86	0.44		[76]
Mn_3O_4/Vulcan		40.8/163.2	1M KOH	0.05-1.43	2.4	0.9	12		[77]
Spinels AMn_2O_4 (A = Mg, Li, Zn, Co)									
$MgMn_2O_4$ spherical particles		200/50	0.1 M KOH		4.05	1.08	5.9		[78]
$MgMn_2O_4$ leaf particles					2.65	1.08	1.1		
$MgMn_2O_4$ blocky particles					1.97	0.8	0.2		
$LiMn_2O_4$		92/214	0.1 M KOH	0.45 – 1.05			**1.13**[4]		**[79]**
$Li_{0.74}Mn_2O_4$							**0.92**[4]		
$ZnMn_2O_4$	26	255/51	0.1 M KOH	0.4 – 1.1	3.43	0.87	0.5	17.50	[80]
$ZnMn_{0.2}Co_{1.8}O_4$	28				3.47	0.94	1.8	66.17	
$ZnMn_{0.6}Co_{1.4}O_4$	35				3.98	0.98	6.7	195.3	
$ZnMnCoO_4$	27				3.98	0.98	6	224.9	
$ZnMn_{1.4}Co_{0.6}O_4$	23				3.35	0.97	4.7	205.8	
$ZnMn_{1.8}Co_{0.2}O_4$	21				3.48	0.93	1.8	88.8	
$MnCo_2O_4$/N-rGO		80/20	0.1 M KOH		4	1			[81]
$CoMn_2O_4$	4	30%/70%	0.1 M KOH		2.9	0.884			[82]

$MnCo_2O_4$	7			0.464 – 1.064	3.3	0.897			
$(Co)[Co_{0.1}Mn_{1.9}]O_4$	112				3.4	0.894			
$CoMn_2O_4$		162/243	0.1 M KOH	0.4 – 1		0.91	6.7		[83]
$Co_{1.5}Mn_{1.5}O_4$						0.94	9.1		
$MnCo_2O_4$						0.94	10.2		
MnO_2									
α -MnO_2 (nanowire)		50	0.1 M KOH	0.36-1.16	3.1	0.91			[69]
β -MnO_2 (nanowire)					2.7	0.91			
γ -MnO_2 (nanowire)					2.3	0.91			
α -MnO_2 (nanowire)/Vulcan		50/117			3.8	0.91			
α -MnO_2 (nanospheres)/Vulcan					3.7	0.91			
α -MnO_2 /Vulcan					3.6	0.91			
MnO_2 (nanosheets)	157	82	0.1 M KOH	0.26-1.16	3.4	0.8			[84]
α -MnO_2	70				2.9	0.74			
β -MnO_2	26				2.6	0.74			
Mn_2O_3									

Mn_2O_3/GC			0.1 M KOH	0.05-1.1		0.85	0.4		[74,85]
Mn_2O_3/C		40:20	0.1 M KOH	0.31-1.0	3.9	0.82	26.6	1.66	[86]
Mn_2O_3/ VU	35	40:20	0.1 M KOH	0.4-1.2	4	0.99	5.3 (0.9 V)	0.015 (0.9 V)	[87]
MnOOH									
MnOOH		200	0.1M KOH	0.07-1.37	3.5	0.83			[88]
Mn perovskites									
$LaMnO_{3+\delta}$/AB	0.5	250:50	0.1M KOH	--			0.3 (0.9 V)	0.06 (0.9 V)	[53]
$La_{0.5}Ca_{0.5}MnO_3$/AB	2.1	250:50	0.1M KOH	--			0.2 (0.9 V)	0.01 (0.9 V)	
$La_{0.8}Sr_{0.2}MnO_3$/Sibunit-152	20	91:37	1M NaOH	0.43-1.23	4		2 (0.9 V)	0.01 (0.9 V)	[61]
$LaMnO_3$/VU (autocombustion synthesis of oxide-carbon composites)		46:46	1M NaOH	0.43-1.23	4		1.1	0.08	[89]
$LaMnO_3$/VU (physical mixing)	14	46:46	1M NaOH	0.43-1.23	4		0.4	0.03	[89]

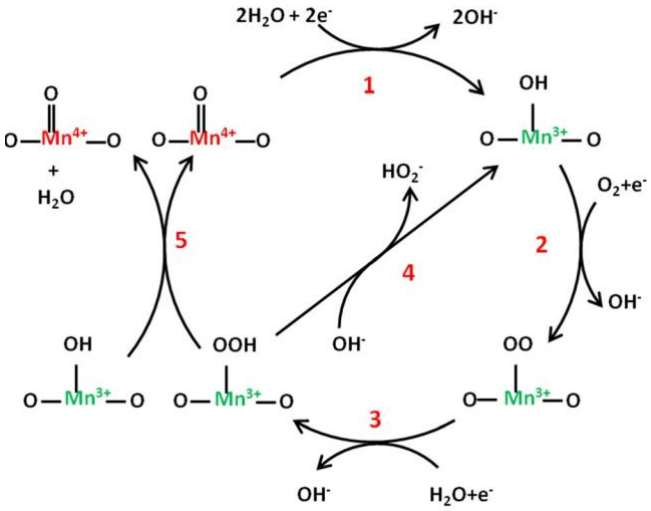

Fig. 25 The mechanism of the oxygen reduction reaction on manganese oxides proposed in Ref. [10].

Based on experimental data and kinetic modelling, the authors of [10] proposed a tentative mechanism of the oxygen reduction shown in Fig. 25. Significant differences can be seen between the mechanisms shown in Fig. 25 and Fig. 17. In the mechanism shown in Fig. 25, a change in the degree of oxidation of the metal occurs only in the first and fifth steps. In this case, step 1 is electrochemical and is accompanied by a single electron transfer, while step 5 is chemical, with no electron transfer to the electrode. It is assumed that oxygen adsorption (step 2) is possible only on the surface Mn(III) centres, which is confirmed by the dependence of the ORR kinetic current on the formal potential of the interfacial redox transition (Fig. 24 a) and supported by kinetic modelling. In step 3, the formation of peroxo- -OOH species occurs at the catalytic centre, which can then be desorbed from the catalyst surface to form peroxide anion HO_2^- (step 4), whose formation was detected by the RRDE. Breaking the bond in the adsorbed hydrogen peroxide occurs in step 5, which is not accompanied by electron transfer (i.e. it does not depend on the applied potential), so this step is called the ‘chemical step’.

To understand the significant differences in the catalytic activity of MnOOH and Mn_2O_3, DFT simulation of the HO_2^- bond breaking step on MnOOH and Mn_2O_3 clusters was performed and reported in [90].

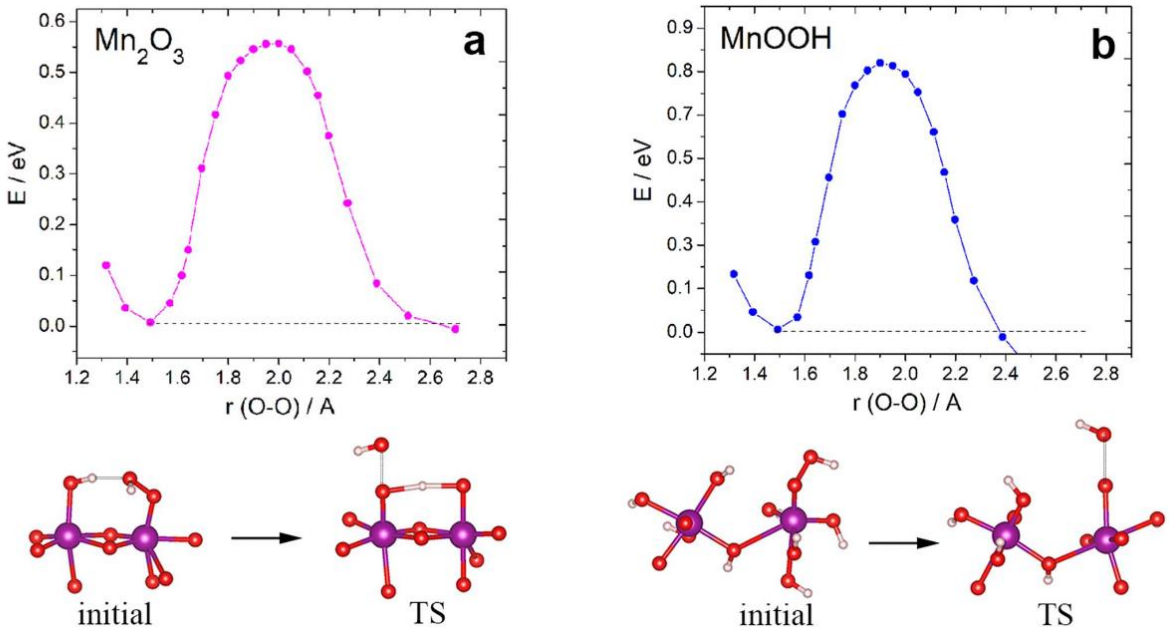

Fig. 26 Energy curves for bond cleavage in HO_2^- on Mn_2O_3 (a) and MnOOH (b) clusters [90].

Fig. 26 shows the respective bond-breaking barriers in HO_2^- adsorbed on Mn_2O_3 and MnOOH clusters, which have been estimated to be approximately 0.5 eV and 0.8 eV, respectively. Transition state geometries show that the smaller distances between neighbouring Mn atoms in Mn_2O_3 allow stabilising interactions to exist between O_{ads} and OH_{ads}, and OH_{ads} and OOH_{ads}, which facilitate OH^- detachment and lower the activation barrier for the O-O bond breaking. For MnOOH, these kinds of interactions are unlikely, as the distance between neighbouring Mn centres is too large.

Further, it was shown that the 'direct' 4e-path on Mn_2O_3 is not possible, due to the very high activation energy (about 2.5 eV) for dissociative adsorption of O_2 and O_2^- on the oxide surface:

$$O_{2ad} + OH_{ad} + e^- \rightarrow 2O_{ad} + OH^- \quad (39)$$

Thus, the origin of the difference in catalytic activity between MnOOH and Mn_2O_3 can be explained by the faster bond breaking in the adsorbed HO_2^- on Mn_2O_3, as well as by the higher formal potential of the interfacial Mn(IV)/Mn(III) redox transition for Mn_2O_3.

Based on rather low values of oxygen adsorption energy on the surface of Mn_2O_3 and MnOOH, the authors [90] suggested that the first steps (steps 2 and 3) of the oxygen reduction reaction may proceed by the outer-sphere mechanism:

$$O_2 + e^- \rightarrow O_2^- \quad (40)$$

$$O_2^- + e^- + H_2O \rightarrow HO_2^- + OH^- \quad (41)$$

The resulting HO_2^- is then adsorbed onto the surface of the oxide:

$$HO_2^- + OH_{ad} + e^- \rightarrow HO_2^-{}_{ad} + OH^- \quad (42)$$

Further, similar to step 5 proposed by the authors [10], the O-O bond is ‘chemically’ broken without electron transfer:

$$HO_2^-{}_{ad} + OH_{ad} \rightarrow O_{ad} + OH_{ad} + OH^- \quad (43)$$

Then the surface is regenerated:

$$O_{2ad} + OH_{ad} + e^- \rightarrow 2O_{ad} + OH^- \quad (44)$$

Thus, despite a large number of studies on the oxygen reduction on various manganese oxides and other 3d metals, there is no consensus on the mechanism of the reaction.

1.4 Degradation (transformation) processes of oxygen reduction electrocatalysts

1.4.1 Degradation processes on platinum surfaces

An important aspect is the study of stability of electrocatalytic materials under operation conditions. The stability of a catalyst can be affected by many factors - temperature, pH, purity of fuel and oxidant in the feed, operating potential and current. As the electrocatalyst gradually degrades, its efficiency can decrease and, consequently, the entire device can gradually fail. Thus, for platinum, which has been the most widely used FC catalyst for a long time, degradation processes have been studied in some detail. However, there remain debates on the mechanisms and key steps of degradation. The possibility of anodic dissolution of platinum was suggested more than a century ago by Tafel (see Ref. [91] and references therein), who warned against using a platinum counter-electrode when investigating cathodic processes at the working electrode. More than 60 years ago, the suggestion of cathodic dissolution of platinum by dissolution from the surface of platinum oxide was suggested by Professor Frumkin, and then confirmed experimentally (see Ref.[92]. and references therein). In addition to the dissolution of the catalyst, other processes occurring during anodic polarisation have been considered, such as agglomeration of platinum particles, Oswald ripening, detachment of particles from the conductive substrate and carbon corrosion (see Refs. [93,94]).

Several approaches are possible when studying the degradation processes of catalysts. Studies can be carried out by electrochemical, structural and spectroscopic methods. Typically, to accelerate degradation, so-called ‘stress testing’ is carried out under conditions harsher than those under which the catalyst normally operates. Usually, the initial electrochemical characteristics of the catalyst are recorded, a constant potential is applied to the working electrode (chronoamperometric measurement) or potential is cycled within a certain potential interval with

a large number of cycles and then the changes occurring to the catalyst are determined by electrochemical and 'post-mortem' physical methods. 'Stress testing' makes it possible to obtain conditions more severe than those under which the catalyst operates in the FC under steady-state conditions, and to reproduce the conditions occurring during start-up and shut-down conditions of the FC. This makes it possible to accelerate the degradation processes occurring with the catalyst, to enable them to be studied in laboratory conditions. Thus, in [95], an ex-situ study of the electrochemical active surface area (EASA) of platinum nanoparticles of different sizes, deposited on different carbon carriers, was performed. The study was carried out after cycling the potential from 0.4 to 1.4 V vs. RHE after 360, 1080, 2160, 3600, 5400, 7200 and 10800 cycles. It was found that, for platinum nanoparticles on a commercially available Vulcan carbon carrier, there was a gradual reduction of the EASA, and after 10800 cycles it decayed by 61% compared to the initial one, decreasing from 77 to 30 m^2 g^{-1}. This behaviour is not, however, the same for all carbon carriers. Thus, for platinum nanoparticles sized 3-4 nm on hollow graphite spheres, a maximum EASA was observed after 1080 cycles, and then the surface of platinum particles started to decrease with further potential cycling. The authors attributed this phenomenon to carbon corrosion, which can lead to greater pore availability as well as improved wettability due to oxidation of the carbon surface. A study of platinum nanoparticles with a size of 1-2 nm showed that, in the first cycles, there was a sharp decrease in EASA, associated with the loss/agglomeration of the smallest platinum nanoparticles. The changes occur primarily with the platinum particles, rather than with the carbon carrier; this has been shown to occur for different substrates.

Electrochemical degradation studies and post-mortem methods are the most accessible and easiest to implement, but they severely limit the information available to researchers. For example, it is extremely difficult to separate the degradation effects of the catalyst itself from the carbon carrier and to understand the degradation mechanism. With the development of hardware capabilities, operando and in situ studies have become more valuable. In particular, works using methods for the analysis of trace amounts of metal cations in solution have made it possible to study the processes associated with the dissolution of platinum [96]. Thus, it has been shown that both cathodic and anodic dissolution of platinum occurs (see Eqs 45 and 46). At the same time, the cathodic dissolution of platinum is 20 times faster than anodic dissolution, and potential cycling in an alkaline environment leads to the formation of more platinum in solution than cycling in an acidic environment.

Anodic dissolution of platinum: $Pt \rightarrow Pt^{2+} + 2e^-$ (45)

Cathodic dissolution of platinum: $PtO_2 + 4H+ + 2e^- \rightarrow Pt^{2+} + 2H_2O$ (46)

Although the dissolution of platinum is one of the possible degradation pathways, we should not forget the presence of the carbon component, which is an integral part of commercially used

catalysts. In this case, oxidation of carbon to form carbonate is possible in an alkaline environment, which contributes to the separation of the platinum particles from the carbon support [103]

Despite significant progress regarding the degradation of carbon-supported Pt catalysts, there are still some debates regarding the degradation mechanisms. In particular, there have been debates about the involvement of platinum oxide in the degradation mechanism of the platinum catalysts [97].

Using in situ X-ray diffraction measurement, however, it has been found that an oxide film predominantly forms on the surface. Interestingly, this effect is not the same for platinum with different facets. Thus, after cycling the Pt (111) planes return to their original state, while the surface of Pt (100) undergoes irreversible changes [98].

1.4.2 Degradation processes on the surface of 3d metal oxides

The issue of electrochemical degradation of oxide compounds is also very urgent, which is associated with the interest of researchers in studying the mechanisms of the ORR and OER on their surfaces, as well as the search for new oxide electrocatalysts.

Degradation processes on oxide materials are not as extensively studied as those for platinum. This is partly due to a large number of different candidate compounds for the role of electrocatalysts for alkaline and anion exchange membrane fuel cells, but also to the relatively recent scientific interest in oxide catalysts for the ORR.

For manganese compounds, oxide stability in an alkaline medium has been investigated at anodic potentials. Results have indicated that the oxides' degradation starts at potentials as low as 1.2 V, which is connected with the formation of permanganate anion [99]. Since the manganese-containing oxides demonstrated catalytic activity in the oxygen reduction reaction, it is most interesting to study their stability in the cathodic region. One approach to determining the cathodic stability and the stability window is cycling with a gradually increasing potential interval [10,100]. Thus, for example, in Ref. [100] stability of Mn, Co containing perovskites was studied using potential cycling by gradually opening the potential window. In Fig. 27 one can see the main electrochemical 'markers' of the degradation, namely (i) characteristic 'tails', which are attributed to irreversible processes, (ii) the disappearance of peaks as it happens for $Sr_{0.5}Gd_{0.5}Mn_{0.25}Co_{0.75}O_{2.87}$ (Fig. 27 d) for the peak at ~0.9 - 1 vs. RHE, or (iii) the appearance of new peaks in the CV curves. The authors of Ref. [100], after each potential cycle in a wide potential interval, recorded a CV in the narrow range of 0.93-1.13 V vs. RHE. Fig. 27 c, f shows the evolution of these CVs and demonstrates how much the imbalance of the cathode and anode parts is modified and how much the charge changes with respect to the original one. The data evidence instability of Co, Mn perovskites at potentials below ~0.65 vs. RHE.

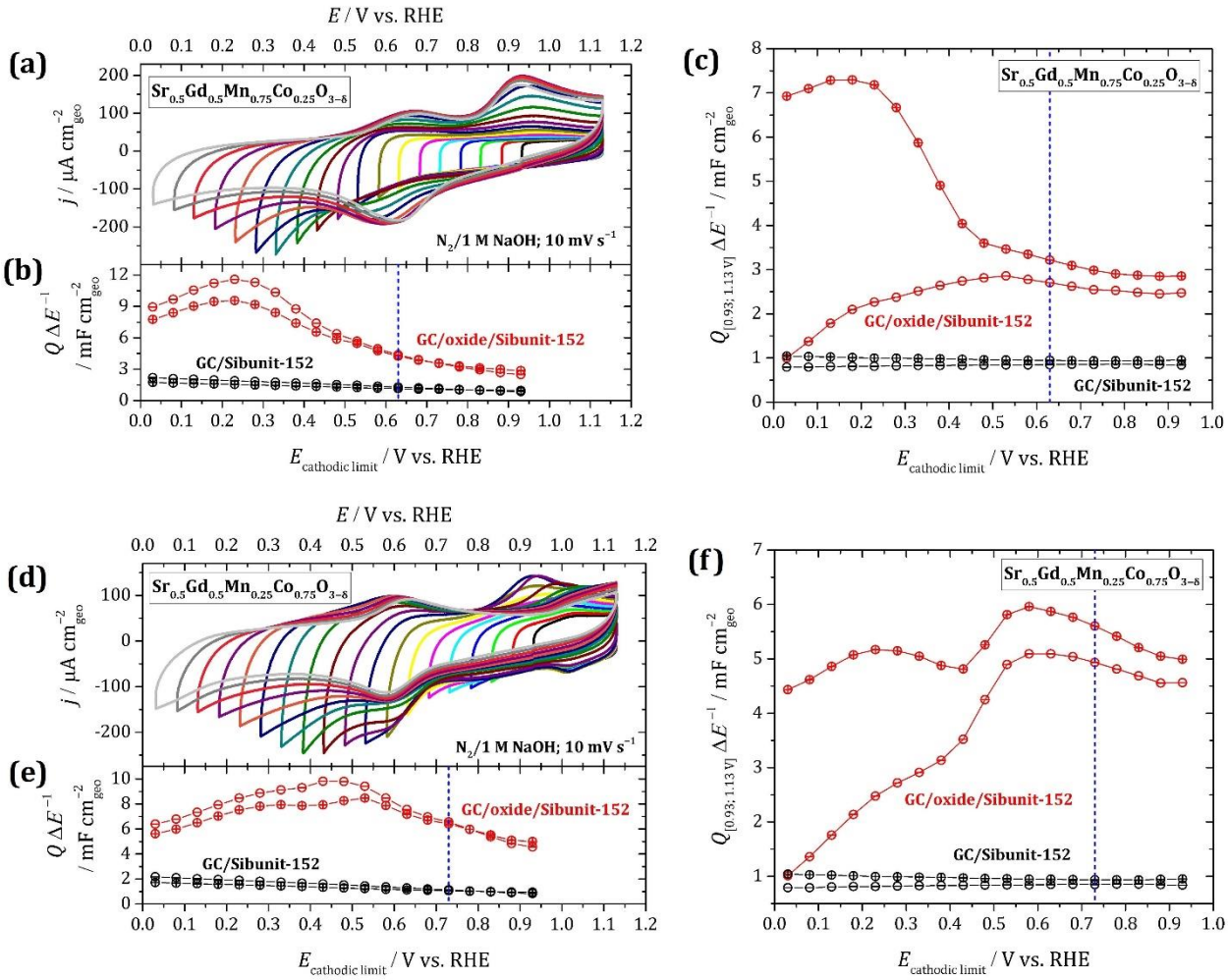

Fig. 27 Study of the cathodic stability of $Sr_{0.5}Gd_{0.5}Mn_{0.75}Co_{0.25}O_{2.98}$ (a-c) and $Sr_{0.5}Gd_{0.5}Mn_{0.25}Co_{0.75}O_{2.87}$ (d-f). CVs with a variable cathodic limit for GC-supported compositions of perovskite oxide and Subunit carbon (loading: 91 μg cm^{-2}_{geo} each) at 10 mV s^{-1} in 1 M NaOH solution saturated with nitrogen (a, d); the corresponding cathodic (⊖) and anodic (⊕) CV charges (b, e); cathodic (⊖) and anodic (⊕) charges extracted from CV obtained in a narrow potential window [0.93; 1.13 V vs. RHE] recorded after applying each cathodic limit (c, f). Reproduced from Ref. [100].

In Ref. [101], the stability of nanosized MnO_x manganese oxide particles was investigated by ex-situ methods. Samples were compared with mild 'ageing' in the air (storing the sample in the air for one year) and 'ageing' under harsh conditions (keeping the oxide in 1M KOH solution purged with oxygen at 80°C). In the latter case, the authors observed significant changes in both the morphology and composition of the sample. The particles agglomerated, their average size exceeding 50 nm, and an impurity phase - manganese hydroxocarbonate - appeared. It is worth noting that the morphology also changed during 'soft ageing' (storage of the sample in the air for one year). The size of agglomerates became approximately 10 nm, but the authors did not observe

significant changes in the electrochemical behaviour of the sample. The authors attributed the change in the activity of the sample subjected to harsh conditions to the loss of effective surface area.

To understand the mechanism of degradation during electrochemical testing, in situ investigation methods are of great interest. Thus, in [102], manganese oxides with different structures were studied using online mass spectroscopy (Fig.28). An important observation was that the dissolution rate of the oxide in a solution was significantly different when saturated with oxygen or deaerated with argon (the red and blue curves in Fig. 28, respectively). The significant rate of manganese dissolution was observed in a limited range of cathodic potentials and was closely related to the formation of hydrogen peroxide. Thus, when the potentials were increased to 0.7-0.8 V relative to RHE, the manganese dissolution rate significantly decreased and became comparable to the rate observed in the solution without oxygen. Conversely, the formation of hydrogen peroxide during the oxygen reduction reaction (proved by the RRDE method) led to a significant increase in the dissolution rate of manganese compared to that measured in a background oxygen-free electrolyte. In this regard, the authors, in order to confirm the high degradation activity of hydrogen peroxide, investigated solutions with initially added H_2O_2 at different concentrations. It was shown that the dissolution rate of manganese under these conditions was significant over the entire potential range investigated, whereas in the solution saturated with oxygen the dissolution occurred only with the in situ formation of hydrogen peroxide. This clearly indicates that it was the peroxide, and not the potential application or the presence of O_2, that caused the enhanced dissolution of Mn.

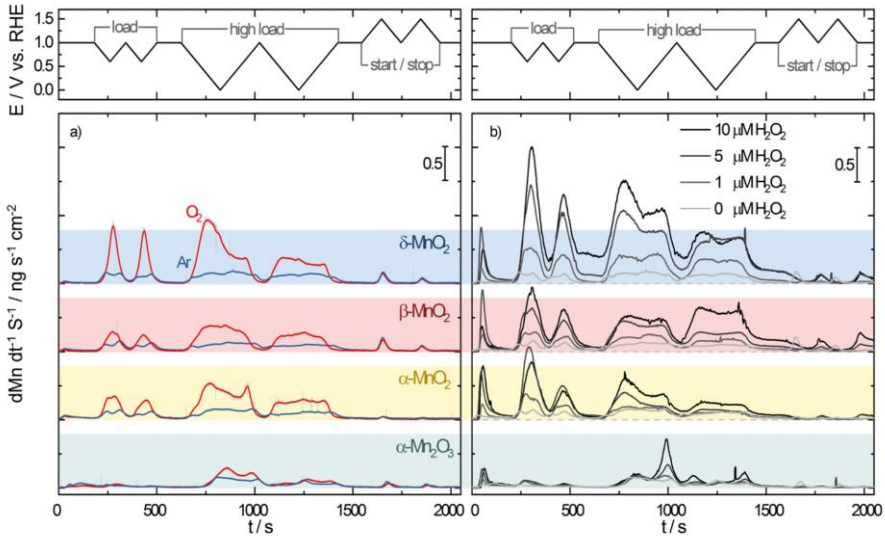

Fig. 28 Dissolution rate of Mn from manganese oxides (α-MnO_2, δ -MnO_2, γ -MnO_2, Mn_2O_3) upon cycling in different potential intervals at 5 mV s^{-1}. (a) Data obtained in 0.05 M NaOH solution purged with oxygen (red) and argon (blue). (b) Dissolution of the oxide in 0.05 M NaOH purified from oxygen with argon for various concentrations of H_2O_2 (0, 1, 5, 10 μM) [102].

To conclude this section, one should keep in mind that transition metal oxides degrade, and that this degradation may be both electrochemical, i.e. induced by the electrode potential (both anodic and cathodic degradation have been documented), and chemical, e.g. induced by the interaction with oxygen or hydrogen peroxide.

1.5 Conclusions

The cost and scarcity of platinum are prompting researchers to find new active and stable catalysts for the oxygen reduction reaction in alkaline media for eventual application in liquid alkaline and anion exchange membrane fuel cells. One of the most promising ways to solve this problem is by switching to 3d metal-based oxide catalysts. Oxides offer great opportunities for researchers, both in terms of the chemical composition and the structural type selection. However, there remain many fundamental questions related to the influence of the composition and structure of 3d metal oxides on their electrocatalytic activity in the ORR, as well as the reaction mechanism. This can be attributed to the fact that the ORR electrocatalysis is influenced by both 'intrinsic factors', that is chemical composition and structure, and 'extrinsic factors' such as electrolyte composition and the presence of carbon additives (the latter applied to improve electrical conductivity of the electrodes). While numerous studies have been devoted to the influence of the structure and composition of 3d metal oxides on their ORR activity, studies on the influence of the electrolyte composition (pH and cation concentration) are scarce. In addition, the stability of 3d metal oxides under electrocatalysis conditions has received insufficient attention in the literature.

The objectives of this thesis were twofold. The first objective was to establish relationship between the composition of Mn oxides and their stability and ORR activity. In order to do so we have chosen manganese oxides with spinel structure of the AMn_2O_4 composition and investigated how the nature of the A element (A - Li, Mg, Mn, Cd) affects speciation of Mn oxidation states, the ensuing stability of the oxide, and its ORR activity. The results are reported in Chapter 3 of the thesis.

The second objective was to unveil the influence of the pH and the cation (Na^+) concentration on the ORR on Mn oxides. For this part of the thesis we have chosen to investigate three Mn oxides (Mn_2O_3, $LaMnO_3$ and MnOOH), which have proven to be active and stable ORR catalysts, and which have shown grossly different ORR kinetics. In chapters 4 and 5, the effect of the electrolyte composition on the interfacial surface recharging (chapter 4) and the electrocatalysis of the oxygen reduction reaction (chapter 5) will be investigated for Mn_2O_3, $LaMnO_3$ and MnOOH oxides.

1.6 References

[1] K.-L. Hsueh, E.R. Gonzalez, S. Srinivasan, Electrolyte effects on oxygen reduction kinetics at platinum: A rotating ring-disc electrode analysis, Electrochimica Acta. 28 (1983) 691–697. https://doi.org/10.1016/0013-4686(83)85066-X.

[2] M.C. Potter, A.D. Waller, Electrical effects accompanying the decomposition of organic compounds, Proceedings of the Royal Society of London. Series B, Containing Papers of a Biological Character. 84 (1911) 260–276. https://doi.org/10.1098/rspb.1911.0073.

[3] B.E. Logan, B. Hamelers, R. Rozendal, U. Schröder, J. Keller, S. Freguia, P. Aelterman, W. Verstraete, K. Rabaey, Microbial Fuel Cells: Methodology and Technology, Environ. Sci. Technol. 40 (2006) 5181–5192. https://doi.org/10.1021/es0605016.

[4] J. Zhang, ed., PEM Fuel Cell Electrocatalysts and Catalyst Layers, Springer London, London, 2008. https://doi.org/10.1007/978-1-84800-936-3.

[5] Z. Zhang, J. Liu, J. Gu, L. Su, L. Cheng, An overview of metal oxide materials as electrocatalysts and supports for polymer electrolyte fuel cells, Energy Environ. Sci. 7 (2014) 2535–2558. https://doi.org/10.1039/C3EE43886D.

[6] X. Ge, A. Sumboja, D. Wuu, T. An, B. Li, F.W.T. Goh, T.S.A. Hor, Y. Zong, Z. Liu, Oxygen Reduction in Alkaline Media: From Mechanisms to Recent Advances of Catalysts, ACS Catal. 5 (2015) 4643–4667. https://doi.org/10.1021/acscatal.5b00524.

[7] M. Pourbaix, H. Zhang, A. Pourbaix, Presentation of an Atlas of Chemical and Electrochemical Equilibria in the Precence of a Gaseous Phase, MSF. 251–254 (1997) 143–148. https://doi.org/10.4028/www.scientific.net/MSF.251-254.143.

[8] B.B. Damaskin, O.A. Petriy, G.A. Tsirlina G. A., Electrochemistry, (2006).

[9] H.S. Wroblowa, Yen-Chi--Pan, G. Razumney, Electroreduction of oxygen: a new mechanistic criteria, J. Electroanal. Chem. 69 (1976) 195–201. https://doi.org/10.1016/S0022-0728(76)80250-1

[10] A.S. Ryabova, F.S. Napolskiy, T. Poux, S.Ya. Istomin, A. Bonnefont, D.M. Antipin, A.Ye. Baranchikov, E.E. Levin, A.M. Abakumov, G. Kéranguéven, E.V. Antipov, G.A. Tsirlina, E.R. Savinova, Rationalizing the Influence of the Mn(IV)/Mn(III) Red-Ox Transition on the Electrocatalytic Activity of Manganese Oxides in the Oxygen Reduction Reaction, Electrochimica Acta. 187 (2016) 161–172. https://doi.org/10.1016/j.electacta.2015.11.012.

[11] J. Suntivich, H.A. Gasteiger, N. Yabuuchi, H. Nakanishi, J.B. Goodenough, Y. Shao-Horn, Design principles for oxygen-reduction activity on perovskite oxide catalysts for fuel cells and metal–air batteries, Nature Chem. 3 (2011) 546–550. https://doi.org/10.1038/nchem.1069.

[12] J.M. Campos-Martin, G. Blanco-Brieva, J.L.G. Fierro, Hydrogen Peroxide Synthesis: An Outlook beyond the Anthraquinone Process, Angewandte Chemie International Edition. 45 (2006) 6962–6984. https://doi.org/10.1002/anie.200503779.

[13] E. Santacesaria, M. Di Serio, R. Velotti, U. Leone, Kinetics, Mass Transfer, and Palladium Catalyst Deactivation in the Hydrogenation Step of the Hydrogen Peroxide Synthesis via Anthraquinone, Ind. Eng. Chem. Res. 33 (1994) 277–284. https://doi.org/10.1021/ie00026a016.

[14] S.C. Perry, D. Pangotra, L. Vieira, L.-I. Csepei, V. Sieber, L. Wang, C. Ponce de León, F.C. Walsh, Electrochemical synthesis of hydrogen peroxide from water and oxygen, Nat Rev Chem. 3 (2019) 442–458. https://doi.org/10.1038/s41570-019-0110-6.

[15] M. Traube, Ueber die elektrolytische Entstehung des Wasserstoffhyperoxyds an der Anode, Ber. Dtsch. Chem. Ges. 20 (1887) 3345–3351. https://doi.org/10.1002/cber.188702002250.

[16] C.M. Sánchez-Sánchez, A.J. Bard, Hydrogen Peroxide Production in the Oxygen Reduction Reaction at Different Electrocatalysts as Quantified by Scanning Electrochemical Microscopy, Anal. Chem. 81 (2009) 8094–8100. https://doi.org/10.1021/ac901291v.

[17] A. Verdaguer-Casadevall, D. Deiana, M. Karamad, S. Siahrostami, P. Malacrida, T.W. Hansen, J. Rossmeisl, I. Chorkendorff, I.E.L. Stephens, Trends in the electrochemical synthesis of H_2O_2: enhancing activity and selectivity by electrocatalytic site engineering, Nano Lett. 14 (2014) 1603–1608. https://doi.org/10.1021/nl500037x.

[18] X. Shi, S. Siahrostami, G.-L. Li, Y. Zhang, P. Chakthranont, F. Studt, T.F. Jaramillo, X. Zheng, J.K. Nørskov, Understanding activity trends in electrochemical water oxidation to form hydrogen peroxide, Nat Commun. 8 (2017) 701. https://doi.org/10.1038/s41467-017-00585-6.

[19] J.S. Jirkovský, I. Panas, E. Ahlberg, M. Halasa, S. Romani, D.J. Schiffrin, Single Atom Hot-Spots at Au–Pd Nanoalloys for Electrocatalytic H_2O_2 Production, J. Am. Chem. Soc. 133 (2011) 19432–19441. https://doi.org/10.1021/ja206477z.

[20] S. Siahrostami, A. Verdaguer-Casadevall, M. Karamad, D. Deiana, P. Malacrida, B. Wickman, M. Escudero-Escribano, E.A. Paoli, R. Frydendal, T.W. Hansen, I. Chorkendorff, I.E.L. Stephens, J. Rossmeisl, Enabling direct H_2O_2 production through rational electrocatalyst design, Nature Mater. 12 (2013) 1137–1143. https://doi.org/10.1038/nmat3795.

[21] S. Chen, Z. Chen, S. Siahrostami, T.R. Kim, D. Nordlund, D. Sokaras, S. Nowak, J.W.F. To, D. Higgins, R. Sinclair, J.K. Nørskov, T.F. Jaramillo, Z. Bao, Defective Carbon-Based Materials for the Electrochemical Synthesis of Hydrogen Peroxide, ACS Sustainable Chem. Eng. 6 (2018) 311–317. https://doi.org/10.1021/acssuschemeng.7b02517.

[22] J. Park, Y. Nabae, T. Hayakawa, M. Kakimoto, Highly Selective Two-Electron Oxygen Reduction Catalyzed by Mesoporous Nitrogen-Doped Carbon, ACS Catalysis, 4 (2014) 3749-3754. https://pubs.acs.org/doi/10.1021/cs5008206

[23] Z. Chen, D. Higgins, H. Tao, R.S. Hsu, Z. Chen, Highly Active Nitrogen-Doped Carbon Nanotubes for Oxygen Reduction Reaction in Fuel Cell Applications, J. Phys. Chem. C. 113 (2009) 21008–21013. https://doi.org/10.1021/jp908067v.

[24] D. Iglesias, A. Giuliani, M. Melchionna, S. Marchesan, A. Criado, L. Nasi, M. Bevilacqua, C. Tavagnacco, F. Vizza, M. Prato, P. Fornasiero, N-Doped Graphitized Carbon Nanohorns as a Forefront Electrocatalyst in Highly Selective O2 Reduction to H2O2, Chem. 4 (2018) 106–123. https://doi.org/10.1016/j.chempr.2017.10.013.

[25] X. Zhao, X. Zou, X. Yan, C.L. Brown, Z. Chen, G. Zhu, X. Yao, Defect-driven oxygen reduction reaction (ORR) of carbon without any element doping, Inorg. Chem. Front. 3 (2016) 417–421. https://doi.org/10.1039/C5QI00236B.

[26] Z.-H. Sheng, H.-L. Gao, W.-J. Bao, F.-B. Wang, X.-H. Xia, Synthesis of boron doped graphene for oxygen reduction reaction in fuel cells, J. Mater. Chem. 22 (2011) 390–395. https://doi.org/10.1039/C1JM14694G.

[27] H.L. Poh, P. Šimek, Z. Sofer, M. Pumera, Sulfur-Doped Graphene via Thermal Exfoliation of Graphite Oxide in H_2S, SO_2, or CS_2 Gas, ACS Nano. 7 (2013) 5262–5272. https://doi.org/10.1021/nn401296b.

[28] J.P. Paraknowitsch, A. Thomas, Doping carbons beyond nitrogen: an overview of advanced heteroatom doped carbons with boron, sulphur and phosphorus for energy applications, Energy Environ. Sci. 6 (2013) 2839. https://doi.org/10.1039/c3ee41444b.

[29] J. Zhang, Z. Xia, L. Dai, Carbon-based electrocatalysts for advanced energy conversion and storage, Science Advances. 1 (2015) e1500564. https://doi.org/10.1126/sciadv.1500564.

[30] A.J. Appleby, J. Marie, Kinetics of oxygen reduction on carbon materials in alkaline solution, Electrochimica Acta. 24 (1979) 195–202. https://doi.org/10.1016/0013-4686(79)80024-9.

[31] I. Morcos, E. Yeager, Kinetic studies of the oxygen—peroxide couple on pyrolytic graphite, Electrochimica Acta. 15 (1970) 953–975. https://doi.org/10.1016/0013-4686(70)80037-8.

[32] M. Appel, A.J. Appleby, A ring-disk electrode study of the reduction of oxygen on active carbon in alkaline solution, Electrochimica Acta. 23 (1978) 1243–1246. https://doi.org/10.1016/0013-4686(78)85080-4.

[33] M.O. Davies, M. Clark, E. Yeager, F. Hovorka, The Oxygen Electrode: I . Isotopic Investigation of Electrode Mechanisms, J. Electrochem. Soc. 106 (1959) 56. https://doi.org/10.1149/1.2427266.

[34] R.J. Taylor, A.A. Humffray, Electrochemical studies on glassy carbon electrodes: II. Oxygen reduction in solutions of high pH (pH>10), Journal of Electroanalytical Chemistry and Interfacial Electrochemistry. 64 (1975) 63–84. https://doi.org/10.1016/S0022-0728(75)80278-6.

[35] E. Yeager, Electrocatalysts for O_2 reduction, Electrochimica Acta. 29 (1984) 1527–1537. https://doi.org/10.1016/0013-4686(84)85006-9.

[36] V.S. Bagotsky, Fuel cell. Problems and solutions., 2009.

[37] V.R. Stamenkovic, B.S. Mun, M. Arenz, K.J.J. Mayrhofer, C.A. Lucas, G. Wang, P.N. Ross, N.M. Markovic, Trends in electrocatalysis on extended and nanoscale Pt-bimetallic alloy surfaces, Nature Mater. 6 (2007) 241–247. https://doi.org/10.1038/nmat1840.

[38] A. Damjanovic, V. Brusic, Electrode kinetics of oxygen reduction on oxide-free platinum electrodes, Electrochimica Acta. 12 (1967) 615–628. https://doi.org/10.1016/0013-4686(67)85030-8.

[39] D.B. Sepa, M.V. Vojnovic, A. Damjanovic, Kinetics and mechanism of O_2 reduction at Pt in alkaline solutions, Electrochimica Acta. 25 (1980) 1491–1496. https://doi.org/10.1016/0013-4686(80)87167-2.

[40] A. Damjanovic, M.A. Genshaw, J.O. Bockris, The Mechanism of Oxygen Reduction at Platinum in Alkaline Solutions with Special Reference to H_2O_2, J. Electrochem. Soc. 114 (1967) 1107. https://doi.org/10.1149/1.2426425.

[41] D.B. Sepa, M.V. Vojnovic, Lj.M. Vracar, A. Damjanovic, Different views regarding the kinetics and mechanisms of oxygen reduction at Pt and Pd electrodes, Electrochimica Acta. 32 (1987) 129–134. https://doi.org/10.1016/0013-4686(87)87021-4.

[42] D.B. Sepa, M.V. Vojnovic, A. Damjanovic, Reaction intermediates as a controlling factor in the kinetics and mechanism of oxygen reduction at platinum electrodes, Electrochimica Acta. 26 (1981) 781–793. https://doi.org/10.1016/0013-4686(81)90037-2.

[43] N.A. Anastasijevic, V. Vesovic, R.R., Determination of the kinetic parameters of the oxygen reduction reaction using the rotation ring-disk electrode, J. Electroanal. Chem. 229 (1987) 305–316.

[44] J.K. Nørskov, J. Rossmeisl, A. Logadottir, L. Lindqvist, J.R. Kitchin, T. Bligaard, H. Jónsson, Origin of the Overpotential for Oxygen Reduction at a Fuel-Cell Cathode, J. Phys. Chem. B. 108 (2004) 17886–17892. https://doi.org/10.1021/jp047349j.

[45] C. Zinola, A.M.C. Luna, W. Triaca, A. Arvia, Kinetics and mechanism of the electrochemical reduction of molecular oxygen on platinum in KOH: influence of preferred crystallographic orientation, (1994). https://doi.org/10.1007/BF00249854.

[46] C. Zhang, F.-R.F. Fan, A.J. Bard, Electrochemistry of Oxygen in Concentrated NaOH Solutions: Solubility, Diffusion Coefficients, and Superoxide Formation, J. Am. Chem. Soc. 131 (2009) 177–181. https://doi.org/10.1021/ja8064254.

[47] N. Ramaswamy, S. Mukerjee, Influence of Inner- and Outer-Sphere Electron Transfer Mechanisms during Electrocatalysis of Oxygen Reduction in Alkaline Media, J. Phys. Chem. C. 115 (2011) 18015–18026. https://doi.org/10.1021/jp204680p.

[48] N.M. Marković, H.A. Gasteiger, P.N. Ross, Oxygen Reduction on Platinum Low-Index Single-Crystal Surfaces in Alkaline Solution: Rotating Ring DiskPt(hkl) Studies, J. Phys. Chem. 100 (1996) 6715–6721. https://doi.org/10.1021/jp9533382.

[49] Q. Zhao, Z. Yan, C. Chen, J. Chen, Spinels: Controlled Preparation, Oxygen Reduction/Evolution Reaction Application, and Beyond, Chem. Rev. 117 (2017) 10121–10211. https://doi.org/10.1021/acs.chemrev.7b00051.

[50] D. Meadowcroft, Low-cost oxygen electrode material, Nature. 226 (1970) 847–848. https://doi.org/10.1038/226847a0.

[51] S. Utara, Trend in Oxygen Reduction Reaction on Transition Metal Oxide Surfaces, 58 (2015) 715–726.

[52] Y.-L. Lee, M.J. Gadre, Y. Shao-Horn, D. Morgan, Ab initio GGA+U study of oxygen evolution and oxygen reduction electrocatalysis on the (001) surfaces of lanthanum transition metal perovskites $LaBO_3$ (B = Cr, Mn, Fe, Co and Ni), Phys. Chem. Chem. Phys. 17 (2015) 21643–21663. https://doi.org/10.1039/C5CP02834E.

[53] J. Suntivich, H.A. Gasteiger, N. Yabuuchi, H. Nakanishi, J.B. Goodenough, Y. Shao-Horn, Design principles for oxygen-reduction activity on perovskite oxide catalysts for fuel cells and metal-air batteries, Nature Chemistry. 3 (2011) 546–550. https://doi.org/10.1038/nchem.1069.

[54] R.F. Savinell, Oxygen-reduction catalysts: Picking perovskites, Nature Chemistry. 3 (2011) 501–502. https://doi.org/10.1038/nchem.1083.

[55] W.T. Hong, M. Risch, K.A. Stoerzinger, A. Grimaud, J. Suntivich, Y. Shao-Horn, Toward the rational design of non-precious transition metal oxides for oxygen electrocatalysis, Energy Environ. Sci. 8 (2015) 1404–1427. https://doi.org/10.1039/C4EE03869J.

[56] J.R. Petrie, V.R. Cooper, J.W. Freeland, T.L. Meyer, Z. Zhang, D.A. Lutterman, H.N. Lee, Enhanced Bifunctional Oxygen Catalysis in Strained $LaNiO_3$ Perovskites, Journal of the American Chemical Society. 138 (2016) 2488–2491. https://doi.org/10.1021/jacs.5b11713.

[57] R. Larsson, L.Y. Johansson, On the catalytic properties of mixed oxides for the electrochemical reduction of oxygen, Journal of Power Sources. 32 (1990) 253–260. https://doi.org/10.1016/0378-7753(90)87018-M.

[58] M. Risch, Perovskite Electrocatalysts for the Oxygen Reduction Reaction in Alkaline Media, Catalysts. 7 (2017) 154. https://doi.org/10.3390/catal7050154.

[59] K.A. Stoerzinger, M. Risch, B. Han, Y. Shao-Horn, Recent Insights into Manganese Oxides in Catalyzing Oxygen Reduction Kinetics, ACS Catal. 5 (2015) 6021–6031. https://doi.org/10.1021/acscatal.5b01444.

[60] K. Nishio, S. Molla, T. Okugaki, S. Nakanishi, I. Nitta, Y. Kotani, Effects of carbon on oxygen reduction and evolution reactions of gas-diffusion air electrodes based on perovskite-type oxides, Journal of Power Sources. 298 (2015) 236–240. https://doi.org/10.1016/j.jpowsour.2015.08.070.

[61] T. Poux, F.S. Napolskiy, T. Dintzer, G. Kéranguéven, S.Ya. Istomin, G.A. Tsirlina, E.V. Antipov, E.R. Savinova, Dual role of carbon in the catalytic layers of perovskite/carbon composites for the electrocatalytic oxygen reduction reaction, Catalysis Today. 189 (2012) 83–92. https://doi.org/10.1016/j.cattod.2012.04.046.

[62] J.T. Mefford, A.A. Kurilovich, J. Saunders, W.G. Hardin, A.M. Abakumov, R.P. Forslund, A. Bonnefont, S. Dai, K.P. Johnston, K.J. Stevenson, Dual role of carbon in the catalytic layers of perovskite/carbon composites for the electrocatalytic oxygen reduction reaction, Phys. Chem. Chem. Phys. 21 (2019) 3327–3338. https://doi.org/10.1039/C8CP06268D.

[63] C.E. Beall, E. Fabbri, T.J. Schmidt, Perovskite Oxide Based Electrodes for the Oxygen Reduction and Evolution Reactions: The Underlying Mechanism, ACS Catal. 11 (2021) 3094–3114. https://doi.org/10.1021/acscatal.0c04473.

[64] A.S. Ryabova, A. Bonnefont, P.A. Simonov, T. Dintzer, C. Ulhaq-Bouillet, Y.G. Bogdanova, G.A. Tsirlina, E.R. Savinova, Further insights into the role of carbon in manganese oxide/carbon composites in the oxygen reduction reaction in alkaline media, Electrochimica Acta. 246 (2017) 643–653. https://doi.org/10.1016/j.electacta.2017.06.017.

[65] G. Kéranguéven, J. Faye, S. Royer, S.N. Pronkin, Electrochemical properties and capacitance of Hausmannite Mn_3O_4 – carbon composite synthesized by in situ autocombustion method., Electrochimica Acta. 222 (2016) 755–764. https://doi.org/10.1016/j.electacta.2016.11.032.

[66] J.T. Mefford, A.A. Kurilovich, J. Saunders, W.G. Hardin, A.M. Abakumov, R.P. Forslund, A. Bonnefont, S. Dai, K.P. Johnston, K.J. Stevenson, Decoupling the roles of carbon and metal oxides on the electrocatalytic reduction of oxygen on $La_{1-x}Sr_xCoO_{3-\delta}$ perovskite

composite electrodes, Phys. Chem. Chem. Phys. 21 (2019) 3327–3338. https://doi.org/10.1039/C8CP06268D.

[67] T. Kohler, Hydrogen bonding and Jahn–Teller distortion in groutite, a-MnOOH, and manganite, g-MnOOH, and their relations to the manganese dioxides ramsdellite and pyrolusite., J. Solid State Chem. 133 (1997) 486–500. https://doi.org/10.1006/jssc.1997.7516.

[68] S. Geller, Structure of α-Mn_2O_3 , $(Mn_{0.983}Fe_{0.017})_2O_3$ and $(Mn_{0.37}Fe_{0.63})_2O_3$ and relation to magnetic ordering, Acta Crystallographica Section B Structural Crystallography and Crystal Chemistry. 27 (1971) 821–828. https://doi.org/10.1107/S0567740871002966.

[69] F. Cheng, Y. Su, J. Liang, Z. Tao, J. Chen, MnO_2-based nanostructures as catalysts for electrochemical oxygen reduction in alkaline media, Chemistry of Materials. 22 (2010) 898–905. https://doi.org/10.1021/cm901698s.

[70] G. Kéranguéven, C. Bouillet, V. Papaefthymiou, P.A. Simonov, E.R. Savinova, How key characteristics of carbon materials influence the ORR activity of $LaMnO_3$- and Mn_3O_4-carbon composites prepared by in situ autocombustion method, Electrochimica Acta. 353 (2020). https://doi.org/10.1016/j.electacta.2020.136557.

[71] F.H.B. Lima, M.L. Calegaro, E.A. Ticianelli, Electrocatalytic activity of manganese oxides prepared by thermal decomposition for oxygen reduction, Electrochimica Acta. 52 (2007) 3732–3738. https://doi.org/10.1016/j.electacta.2006.10.047.

[72] J.S. Lee, G.S. Park, H. Il Lee, S.T. Kim, R. Cao, M. Liu, J. Cho, Ketjenblack carbon supported amorphous manganese oxides nanowires as highly efficient electrocatalyst for oxygen reduction reaction in alkaline solutions, Nano Letters. 11 (2011) 5362–5366. https://doi.org/10.1021/nl2029078.

[73] Y.C. Zhang, S. Ullah, R. Zhang, L. Pan, X. Zhang, J.J. Zou, Manipulating electronic delocalization of Mn_3O_4 by manganese defects for oxygen reduction reaction, Applied Catalysis B: Environmental. 277 (2020) 119247. https://doi.org/10.1016/j.apcatb.2020.119247.

[74] Y. Gorlin, C.J. Chung, D. Nordlund, B.M. Clemens, T.F. Jaramillo, Mn_3O_4 Supported on glassy carbon: An active non-precious metal catalyst for the oxygen reduction reaction, ACS Catalysis. 2 (2012) 2687–2694. https://doi.org/10.1021/cs3004352.

[75] J. Feng, Y. Liang, H. Wang, Y. Li, B. Zhang, J. Zhou, J. Wang, T. Regier, H. Dai, Engineering manganese oxide/nanocarbon hybrid materials for oxygen reduction electrocatalysis, Nano Res. 5 (2012) 718–725. https://doi.org/10.1007/s12274-012-0256-8.

[76] S.K. Bikkarolla, F. Yu, W. Zhou, P. Joseph, P. Cumpson, P. Papakonstantinou, A three-dimensional Mn_3O_4 network supported on a nitrogenated graphene electrocatalyst for efficient oxygen reduction reaction in alkaline media, J. Mater. Chem. A. 2 (2014) 14493–14501. https://doi.org/10.1039/C4TA02279C.

[77] F.H.B. Lima, M.L. Calegaro, E.A. Ticianelli, Investigations of the catalytic properties of manganese oxides for the oxygen reduction reaction in alkaline media, Journal of Electroanalytical Chemistry. 590 (2006) 152–160. https://doi.org/10.1016/j.jelechem.2006.02.029.

[78] C. Liang, H. Wang, K. Huang, S. Lin, W. Liu, K. Bi, M. Lei, Hierarchically Porous - $MgMn_2O_4$ Microspheres Assembled with Nanosheets as High Oxygen Reduction Catalyst, (2019). https://doi.org/10.1007/s10562-019-02760-4.

[79] C. Wei, Z. Feng, G.G. Scherer, J. Barber, Y. Shao-Horn, Z.J. Xu, Cations in Octahedral Sites: A Descriptor for Oxygen Electrocatalysis on Transition-Metal Spinels, Advanced Materials. 29 (2017) 1606800. https://doi.org/10.1002/adma.201606800.

[80] S. Bag, K. Roy, C.S. Gopinath, C.R. Raj, Facile single-step synthesis of nitrogen-doped reduced graphene oxide-Mn_3O_4 hybrid functional material for the electrocatalytic reduction of oxygen, ACS Applied Materials and Interfaces. 6 (2014) 2692–2699. https://doi.org/10.1021/am405213z.

[81] X. Ge, Y. Liu, F.W.T. Goh, T.S.A. Hor, Y. Zong, P. Xiao, Z. Zhang, S.H. Lim, B. Li, X. Wang, Z. Liu, Dual-phase spinel $MnCo_2O_4$ and spinel $MnCo_2O_4$/nanocarbon hybrids for electrocatalytic oxygen reduction and evolution, ACS Applied Materials and Interfaces. 6 (2014) 12684–12691. https://doi.org/10.1021/am502675c.

[82] F. Cheng, J. Shen, B. Peng, Y. Pan, Z. Tao, J. Chen, Rapid room-temperature synthesis of nanocrystalline spinels as oxygen reduction and evolution electrocatalysts, Nature Chemistry. 3 (2011) 79–84. https://doi.org/10.1038/nchem.931.

[83] W. Wang, E. Liu, Y. Hu, L. Jiao, P. Kolla, Y. Liu, M. Tang, J. Luo, Q. Sun, S. Chen, Q. Jia, S. Mukerjee, Understanding the ORR Electrocatalysis on Co–Mn Oxides, The Journal of Physical Chemistry C. 125 (2021) 25470–25477. https://doi.org/10.1021/acs.jpcc.1c00104.

[84] C. Shi, G.-L. Zang, Z. Zhang, G.-P. Sheng, Y.-X. Huang, G.-X. Zhao, X.-K. Wang, H.-Q. Yu, Synthesis of Layered MnO_2 Nanosheets for Enhanced Oxygen Reduction Reaction Catalytic Activity, Electrochimica Acta. 132 (2014) 239–243. https://doi.org/10.1016/j.electacta.2014.03.150.

[85] Y. Gorlin, T.F. Jaramillo, A Bifunctional Nonprecious Metal Catalyst for Oxygen Reduction and Water Oxidation, J. Am. Chem. Soc. 132 (2010) 13612–13614. https://doi.org/10.1021/ja104587v.

[86] F. Cheng, J. Shen, W. Ji, Z. Tao, J. Chen, Selective Synthesis of Manganese Oxide Nanostructures for Electrocatalytic Oxygen Reduction, ACS Appl. Mater. Interfaces. 1 (2009) 460–466. https://doi.org/10.1021/am800131v.

[87] W. Wang, J. Geng, L. Kuai, M. Li, B. Geng, Porous Mn_2O_3: A Low-Cost Electrocatalyst for Oxygen Reduction Reaction in Alkaline Media with Comparable Activity to Pt/C, Chemistry – A European Journal. 22 (2016) 9909–9913. https://doi.org/10.1002/chem.201602078.

[88] W. Sun, A. Hsu, R. Chen, Carbon-supported tetragonal MnOOH catalysts for oxygen reduction reaction in alkaline media, Journal of Power Sources. 196 (2011) 627–635. https://doi.org/10.1016/j.jpowsour.2010.07.082.

[89] G. Kéranguéven, S. Royer, E. Savinova, Synthesis of efficient Vulcan–$LaMnO_3$ perovskite nanocomposite for the oxygen reduction reaction, Electrochemistry Communications. 50 (2015) 28–31. https://doi.org/10.1016/j.elecom.2014.10.019.

[90] V.A. Nikitina, A.A. Kurilovich, A. Bonnefont, A.S. Ryabova, R.R. Nazmutdinov, E.R. Savinova, G.A. Tsirlina, ORR on Simple Manganese Oxides: Molecular-Level Factors Determining Reaction Mechanisms and Electrocatalytic Activity, J. Electrochem. Soc. 165 (2018) J3199. https://doi.org/10.1149/2.0261815jes.

[91] K. Muller, Who was Tafel? J. Res. Inst. Catalysis, Hokkaido Uni., 17 (1969) 54-75

[92] A.N. Chemodanov, Ya.M. Kolotyrkin, M.A. Dembrovski, Dissolution of platinum in acid electrolytes at various polarizations as studied by a radiochemical method, Elekrokhimia. 6 (1970) 460.

[93] J.C. Meier, C. Galeano, I. Katsounaros, J. Witte, H.J. Bongard, A.A. Topalov, C. Baldizzone, S. Mezzavilla, F. Schüth, K.J.J. Mayrhofer, Design criteria for stable Pt/C fuel cell catalysts, Beilstein Journal of Nanotechnology 5:5. 5 (2014) 44–67. https://doi.org/10.3762/BJNANO.5.5.

[94] L. Dubau, L. Castanheira, F. Maillard, M. Chatenet, O. Lottin, G. Maranzana, J. Dillet, A. Lamibrac, J.-C. Perrin, E. Moukheiber, A. ElKaddouri, G. De Moor, C. Bas, L. Flandin, N. Caqué, A review of PEM fuel cell durability: materials degradation, local heterogeneities of aging and possible mitigation strategies, WIREs Energy and Environment. 3 (2014) 540–560. https://doi.org/10.1002/wene.113.

[95] C. Galeano, J.C. Meier, V. Peinecke, H. Bongard, I. Katsounaros, A.A. Topalov, A. Lu, K.J.J. Mayrhofer, F. Schüth, Toward highly stable electrocatalysts via nanoparticle pore confinement, Journal of the American Chemical Society. 134 (2012) 20457–20465. https://doi.org/10.1021/JA308570C/SUPPL_FILE/JA308570C_SI_001.PDF.

[96] S. Cherevko, A.R. Zeradjanin, G.P. Keeley, K.J.J. Mayrhofer, A Comparative Study on Gold and Platinum Dissolution in Acidic and Alkaline Media, Journal of The Electrochemical Society. 161 (2014) H822–H830. https://doi.org/10.1149/2.0881412jes.

[97] S. Cherevko, N. Kulyk, K.J.J. Mayrhofer, Durability of platinum-based fuel cell electrocatalysts: Dissolution of bulk and nanoscale platinum, Nano Energy. 29 (2016) 275–298. https://doi.org/10.1016/J.NANOEN.2016.03.005.

[98] T. Fuchs, J. Drnec, F. Calle-Vallejo, N. Stubb, D.J.S. Sandbeck, M. Ruge, S. Cherevko, D.A. Harrington, O.M. Magnussen, Structure dependency of the atomic-scale mechanisms of platinum electro-oxidation and dissolution, Nature Catalysis. 3 (2020) 754–761. https://doi.org/10.1038/s41929-020-0497-y.

[99] M. Rabe, C. Toparli, Y.-H. Chen, O. Kasian, K.J.J. Mayrhofer, A. Erbe, Alkaline manganese electrochemistry studied by in situ and operando spectroscopic methods – metal dissolution, oxide formation and oxygen evolution, Phys. Chem. Chem. Phys. 21 (2019) 10457–10469. https://doi.org/10.1039/C9CP00911F.

[100] I.S. Filimonenkov, S.Ya. Istomin, B. Rotonnelli, J.-J. Gallet, F. Bournel, E.V. Antipov, E.R. Savinova, G.A. Tsirlina, Interfacial recharging behavior of mixed Co, Mn-based perovskite oxides, Electrochimica Acta. 398 (2021) 139257. https://doi.org/10.1016/j.electacta.2021.139257.

[101] I. Roche, E. Chaînet, M. Chatenet, J. Vondrák, Durability of carbon-supported manganese oxide nanoparticles for the oxygen reduction reaction (ORR) in alkaline medium, J Appl Electrochem. 38 (2008) 1195–1201. https://doi.org/10.1007/s10800-008-9537-z.

[102] F.D. Speck, P.G. Santori, F. Jaouen, S. Cherevko, Mechanisms of Manganese Oxide Electrocatalysts Degradation during Oxygen Reduction and Oxygen Evolution Reactions, J. Phys. Chem. C. 123 (2019) 25267–25277. https://doi.org/10.1021/acs.jpcc.9b07751.

[103] C. Lafforgue, A. Zadick, L. Dubau, F. Maillard, M. Chatenet, Selected Review of the Degradation of Pt and Pd-based Carbon-supported Electrocatalysts for Alkaline Fuel Cells: Towards Mechanisms of Degradation, Fuel Cells. 18 (2018) 229–238. https://doi.org/10.1002/fuce.201700094.

2. Material

2.1. Reagents used

The following reagents were used in the work:

- Cadmium acetate (Reachim, Russia, >99%)
- Hydrochloric acid (Sigma-Aldrich, 30%)
- Hydrogen peroxide (Acros Organics, 35% aqueous solution)
- Hydrogen peroxide (Merck 30 % aqueous solution)
- Lanthanum nitrate (Reachim, Russia, >99%)
- Lithium carbonate (Reachim, Russia, >99%)
- Magnesium oxide (Reachim, Russia, >99%)
- Manganese acetate (Sigma-Aldrich, 99%)
- Manganese nitrate (Sigma-Aldrich, 99%)
- Manganese oxide (II) (Reachim, Russia, >99%)
- Manganese oxide (III) (Reachim, Russia, >99%)
- Manganese oxide (IV) (Reachim, Russia, >99%)
- Manganese sulphate (Sigma-Aldrich, 99%)
- Nitric acid (Sigma-Aldrich)
- Perchloric acid (Sigma-Aldrich, 65%)
- Polyvinyl alcohol (Reachim, Russia)
- Potassium iodide (Reachim, Russia, >98%)
- Potassium permanganate (Prolabo),
- Proton-conducting ionomer Nafion®, 20 wt.% solution in aqueous-alcohol mixture (1.049 g cm^{-1}), eq. weight ≈ 1100 g $mol(H^+)^{-1}$
- Sodium dichromate (Reachim, Russia, >99%)
- Sodium hydroxide (Acros Organics, 50 mas. % aqueous solution)
- Sodium oxalate (Fluka, 0.05 M),
- sodium perchlorate anhydride (ACS, 99%)
- Sodium thiosulphate (Reachim, Russia, >99%)
- Sulphuric acid (Sigma-Aldrich, 95-98%)

The following gases were also used: N_2 (99.99%) и O_2 (99.99%), H_2 (99.99%).

All solutions were prepared using ultra-pure water purified by Millipore Simplicity (USA, 18.2 Mohm cm at 25 °C, TOC < 3 ppb) or ELGA Purelab (UK, 18.2 Mohm cm at 25 °C,

TOC < 1 ppb). The crystallization water content of the crystalline hydrates was determined by thermogravimetric analysis.

Pyrolytic carbon Sibunite-152 used as a conductive additive was provided by the Institute of Hydrocarbon Processing Problems, Siberian Branch of the Russian Academy of Sciences.

2.2. Materials synthesis

Mn_3O_4 and Mn_2O_3 was synthesised by annealing α-MnOOH at 600 °C for 2 hours in Ar and at 550 °C for 12 hours in Air. α-MnOOH was obtained by the method described in [1]. In this method, a solution of $KMnO_4$ (5.89 g) in 200 ml of deionised water was slowly added to a stirred solution of $MnSO_4 \cdot H_2O$ (4.40 g) in 30 ml of water in the presence of sucrose (2.0 g), with addition of 3.0 ml of concentrated HNO_3. The resulting solution was boiled under stirring at 100 °C for 4 hours. Also obtained MnOOH was used for electrochemical experiments.

The synthesis of $LiMn_2O_4$ and $MgMn_2O_4$ was carried out by the modified Pechini method, in accordance with the following procedure. The solutions obtained by dissolving stoichiometric amounts of $Mn(NO_3)_2 \cdot 4H_2O$ in a minimum amount of water, and Li_2CO_3 for $LiMn_2O_4$ or MgO for $MgMn_2O_4$ in a minimum amount of concentrated HNO_3, were mixed together with a 5 % solution of polyvinyl alcohol. After heating under stirring, an excess of citric acid monohydrate was added and heating continued until the formation of a viscous gel. The latter was annealed in air in an open burner flame. The resulting powder was ground in a mortar and then re-annealed in air at a temperature of 300 °C for 12 hours.

$CdMn_2O_4$ was obtained by a modified procedure [2]. A 0.8 M NaOH solution was added dropwise to an aqueous solution containing a stoichiometric mixture of $Cd(CH_3COO_2)$ and $Mn(CH_3COO_2)$. Oxygen was purged into the solution throughout the synthesis. The resulting solution with the precipitate was stirred for 1 hour, then the precipitate was filtered and dried for 24 hours in an oven at 80°C. The obtained powder was finally annealed at 300 °C for 12 hours.

$LaMnO_3$ was synthesised according to the method described in [3]. $La(NO_3)_3 \cdot 5.58H_2O$ (3.5184 g) and $Mn(NO_3)_2 \cdot 3.74H_2O$ (2.0371 g), calculated for 2 g product and an equimolar amount of glycine (1.1257 g) were dissolved in 20 ml distilled water. The solution was evaporated on a hotplate to a constant volume, then poured into a porcelain cup and placed in a furnace heated to 350 °C. The resulting substance was annealed in the oven at 600 °C for 5 hours.

2.3. Characterisation of oxide materials

Phase composition of the samples was determined by X-ray powder diffraction (XRPD) with a Huber G670 imaging-plate Guinier diffractometer ($CuK_{\alpha 1}$ radiation, curved Ge monochromator,

image plate detector). The ICDD PDF2 database was used to perform the phase analysis of the samples. The Jana software was used to carry out calculations according to the Rietveld method.

Scanning electron microscopy (SEM) studies were performed with a Carl Zeiss NVision 40 (accelerating voltage 1-10 kV).

Two sets of X-ray photoelectron spectroscopy (XPS) experiments are presented in this work. The first set of measurements (presented in the main text) was performed with an ultrahigh vacuum laboratory spectrometer Thermo VG-Microtech equipped with a CLAM4 (MCD) hemispherical electron analyser with Al-cathode (excitation energy 1486.6 eV). The Al Kα line (1486.6 eV) of a dual anode X-ray source was used as incident radiation. The second set of measurements was performed at the ISISS beamline (BESSY II synchrotron at the Helmholtz Zentrum, Berlin). If not otherwise stated, Mn3p+Li1s, Mn2p, Cd3d, Mg1s C1s, and O1s spectra were recorded using selected excitation photon energies so that the photoelectrons were emitted at a kinetic energy of ca. 450 eV. The binding energy (BE) values were calibrated using the Au $4f_{7/2}$ set at 84.0 eV peak. The C1s BE of 'graphitic' carbon was equal to 284.0 eV. The spectra were processed using CasaXPS software. The background was described by the Shirley function. The atomic ratio of the elements was determined from the ratio of the integral intensities of the spectral lines normalised by the energy dependent incident photon flux and related to their photoionisation cross section constants [4].

NEXAFS (near edge X-ray absorption fine structure) spectroscopy studies were performed ex-situ at the ISSIS beamline of BESSY-II synchrotron source using a NAP-HE-XPS (Near Ambient Pressure High Energy X-ray Photoelectron Spectroscopy) set-up. Spectra were collected in the interval from 635 to 665 eV corresponding to Mn L_2- and L_3-edges.

The oxidation state of manganese in spinels (chapter 3) was verified with NEXAFS. To do this, the NEXAFS spectra of spinels were described as a linear combination of spectra of reference MnO, Mn_2O_3 and MnO_2 compounds measured with the same set-up. Mn_2O_3 and MnO_2 are commercially available compounds. MnO, which is known to be readily oxidized under ambient conditions, was purposely prepared by heating of MnO_2 in Ar/H_2 (8 vol%) at 1350 ^oC for 48 h and annealed in an Ar/H_2 (8 vol %) flow at 1350 °C for 24 h prior to the measurements. Fitting of the NEXAFS spectra was performed in the energy interval from 635 to 665 eV. The quality of the fitting was evaluated by minimizing the difference between the measured and the calculated spectrum. It should be stressed that such an approach is not rigorous and can only provide an estimate of the Mn oxidation state. Indeed, the shape of L-edge spectra of transition metal oxides is determined by the local electronic structure (which is different e.g. for Mn(II) in MnO and Mn(II) in Mn_3O_4). Thus, quantitative interpretation of L-edge spectra requires multiple-scattering calculations (see e.g. Ref. [5]).

NEXAFS and XPS were performed for oxide powders (or oxide/carbon mixtures), drop-cast on a gold plate from their suspensions and analysed after their exposure to different treatments.

The specific surface area of oxide powders was determined by low temperature N_2 adsorption using an ASAP 2010 analyser (Micromeritics, USA), with the multiple-point Brenauer-Emmett-Teller (BET) approach. In order to remove moisture and adsorbed species from the samples, the latter were evacuated before measurements for 8-12 hours at 200 °C. For MnOOH the degassing temperature was reduced to 80 °C to prevent its decomposition and surface area changes, and the degassing time, in turn, was increased to 24 hours. Afterwards, the exact mass of the oxide sample was determined, and measurements were made at 77 K using liquid nitrogen to achieve adsorption of the introduced gaseous nitrogen on the sample. Adsorption isotherms were processed using the software included with the instrument. The complete isotherm was recorded, but the BET calculation was performed in the standard range of 0.05-0.35 p/p_0.

2.4. Analytical methods of analysis

Hydrogen peroxide decomposes over time, so its concentration must be determined immediately before the electrochemical experiment. The hydrogen peroxide concentration was determined by titration with potassium permanganate. Potassium permanganate is a secondary standard, therefore it was pre-standardised with sodium oxalate**.**

2.4.1. Preparation and standardisation of $KMnO_4$ solution

A solution of $KMnO_4$ with a concentration of approximately 0.02 M was prepared by dissolving 0.64 g $KMnO_4$ in 200 ml of Milli-Q water (18.2 M Ohm-cm Ωcm, Purelab) while heating to 95 °C and stirring for 2 hours. The solution was left to cool to room temperature overnight in a light-protected place.

The standardisation of the permanganate solution obtained was carried out by titration of a 0.006 M $Na_2C_2O_4$ solution acidified with sulphuric acid. The standardisation solution was prepared in a 250 ml volumetric flask. For this purpose, 14 ml of 95-98 % H_2SO_4 (to prepare 1M H_2SO_4), 30 ml of 0.05 M $Na_2C_2O_4$ and Milli-Q water (18.2 M Ωcm, Purelab) were added to the flask, bringing the solution to the mark.

A standard solution of $KMnO_4$ was poured into the titration burette. A 30 mL solution of 0.006 M $Na_2C_2O_4$ was taken into the titration flask and titrated with potassium permanganate under constant stirring at 80 °C until the colour was a stable pink for 30 seconds. The titration was repeated three times. Heating was necessary because of the low reaction rate between $KMnO_4$ and $Na_2C_2O_4$. The reaction followed the following equation:

$$2MnO_4^- + 5C_2O_4^{2-} + 16H^+ \rightarrow 2Mn^{2+} + 10CO_2 + 8H_2O \quad (47)$$

The average volume of potassium permanganate used for the titration was calculated from the results of the three titrations. The concentration of potassium permanganate was calculated using the following formula:

$$C_{MnO_4^-} = \frac{\frac{2}{5} \cdot C_{C_2O_4^{2-}} \cdot V_{C_2O_4^{2-}}}{V_{MnO_4^-}} \quad (48)$$

2.4.2. Titration of H_2O_2 with standardised $KMnO_4$ solution

After standardising the potassium permanganate solution, the concentration of H_2O_2 was determined. For this purpose, 1 ml of 30 % wt. % H_2O_2 was placed in a 250 ml volumetric flask. H_2O_2, 4 ml 95-98 % H_2SO_4 and Milli-Q water (18.2 M Ωcm) were added, bringing the volume to the mark. An aliquot of 20 mL of H_2O_2 solution was taken into a titration flask and titrated with standardised potassium permanganate solution under constant stirring at room temperature until a steady pink colour was obtained for 30 seconds. The reaction between potassium permanganate and hydrogen peroxide is catalysed by Mn^{2+} cations; therefore, the decolouration occurs slowly after adding the first drops of potassium permanganate [7]. As the Mn^{2+} cations accumulate, the reaction accelerates. The reaction followed the following equation:

$$2MnO_4^- + 5H_2O_2 + 6H^+ \rightarrow 2Mn^{2+} + 5O_2 + 8H_2O \quad (49)$$

The average volume of potassium permanganate used for the titration was calculated from the results of the three titrations. The hydrogen peroxide concentration was calculated using the following formula:

$$C_{H_2O_2} = \frac{\frac{5}{2} \cdot V_{MnO_4^-} \cdot C_{MnO_4^-} \cdot}{V_{H_2O_2}} \quad (50)$$

2.4.3. Oxygen stoichiometry in oxide samples

Oxygen stoichiometry in perovskite sample was determined by reverse iodometric titration. First, standardization of sodium thiosulphate was carried out by titration with potassium dichromate. For this purpose a solution of potassium dichromate with a concentration of 0.0002 M as well as a solution of sodium thiosulphate with a concentration of ~0.02 M was prepared. Next, 10 ml of 1 M H_2SO_4 solution, 10 ml of 5% KI and 10 ml of 0.002 M $K_2Cr_2O_7$ were added to the titration flask. The flask was placed in a dark place for 5 minutes. The released iodine was titrated with a sodium thiosulphate solution to a "straw" colour. Then four drops of starch were added and the solution continued to be titrated until the blue colour was completely discoloured.

The titration was repeated three times and the average volume of sodium thiosulphate used for the titration was calculated.

The reactions that take place during titration are given below:

$Cr_2O_7^{2-} + 6I^- + 14H^+ \rightarrow 2Cr^{3+} + 3I_2 + 7H_2O$ (51)

$I_2 + 2S_2O_3^{2-} \rightarrow 2I^- + S_4O_6^{2-}$ (52)

The concentration of sodium thiosulphate was calculated according to the formula:

$$C_{S_2O_3^{2-}} = \frac{6 \cdot C_{Cr_2O_7^{2-}} \cdot V_{Cr_2O_7^{2-}}}{V_{S_2O_3^{2-}}} \quad (53)$$

Oxygen stoichiometry was determined according to the methodology presented below. After the standardisation of sodium thiosulphate a check was carried out for Mn_2O_3 (whose oxygen stoichiometry is well defined). A Mn_2O_3 sample weight containing approximately $3.8*10^{-4}$ mol of Mn^{3+} cations, 20 ml of 20 % KI solution and 2 ml of concentrated HCl solution was added to the titration flask. The flask was placed in a dark place for 5 minutes. Before the titration 50 mL of distilled water was added to the flask. The titration was carried out under constant stirring at room temperature with standardised $Na_2S_2O_3$ solution. Then the titration was carried out similarly to the titration with potassium dichromate. The released iodine was titrated with sodium thiosulphate solution to a "straw" colour. Then 4 drops of starch were added and the solution continued to be titrated until the blue colour was completely discoloured. The titration was repeated three times and the average volume of sodium thiosulphate used for the titration was calculated.

The reactions that take place during titration are given below:

$2Mn^{3+} + 2I^- \rightarrow 2Mn^{2+} + I_2$ (54)

$I_2 + 2S_2O_3^{2-} \rightarrow 2I^- + S_4O_6^{2-}$ (55)

The mass fraction of Mn^{3+} in the sample was calculated according to the formula:

$$W_{Mn^{3+}} = 54{,}94 \cdot \frac{C_{S_2O_3^{2-}} \cdot V_{S_2O_3^{2-}}}{m_{oxide} \cdot 1000} \quad (56)$$

Once the procedure was validated, it was applied for determining oxygen stoichiometry in other oxide samples.

2.5. Electrochemical measurements

2.5.1. Electrode and cell preparation

Electrochemical studies were carried out on an Autolab PGSTAT302N potentiostat / galvanostat with an analogue module to feed a linear potential sweep, using standard GPES and NOVA software. An Autolab Rotator disc electrode was used to perform electrochemical

experiments on a rotating disc electrode (RDE). The data were processed using the Origin 9.0 software package.

Electrochemical measurements were performed in a three-electrode electrochemical cell. All parts of the electrochemical cell in contact with the electrolyte were made of Teflon; the other parts were made of Pyrex glass. In order to remove impurities that could poison the surface of the catalyst, the cell was thoroughly cleaned before measurements were taken. For this purpose, Caro's solution (mixture of H_2O_2 (30 %) and H_2SO_4 (96-98 %) in the ratio 1:1 by volume) was poured inside the cell overnight. Afterwards, the solution was removed and the cell was washed thoroughly with ultrapure water, as traces of H_2O_2 and acid could lead to erroneous results. The obtained Caro's solution was stored in a glass or perfluorinated container in a dark, cool place for a maximum of three months.

All measurements were performed at 25 °C and the temperature was controlled using a JULABO thermostat, model ED. Measurements according to the standard procedure were performed in 1 M NaOH aqueous solution (except for studies on the effect of electrolyte composition on the electrochemical behaviour of oxides described in chapter 4 and chapter 5).

For electrochemical measurements, a suspension containing oxide material and carbon (Sibunit with surface area of 104 $m^2\ g^{-1}$) was immobilised on the glassy carbon (GC) disc electrode. Prior to the measurements, the GC disc was polished with an aqueous suspension of aluminum oxide (with particle sizes of 1.0, 0.3 and 0.05 μm) to obtain a mirror surface, and subsequently cleaned in ethanol and water. To prepare a suspension, the oxide powder was mixed with carbon in a mass ratio 1:1 and ground in an agate mortar where ultrapure water (Milli-Q 18.2 MΩ·cm, < 2 ppb TOC) was added to obtain a 'concentration' of oxide in the suspension of 0.59 g L^{-1}. The suspension was stirred in an ultrasonic bath for 5 minutes to break up agglomerates. An aliquot of the suspension was drop-cast on the GC electrode and dried in a stream of nitrogen, (nitrogen rather than air flow was used to avoid oxidation of Mn during the thin-film drying). This operation was repeated three times in order to obtain a uniform GC coating. The final loading of the oxide (per geometric surface area) was 91 μg cm^{-2}_{geo}. Next, an aqueous solution of Nafion in a Na^+ form with a concentration of 78.6 mg L^{-1} was drop-cast on the electrode surface (to achieve Nafion loading of 2.4 μg cm^{-2}_{geo}) and dried in a nitrogen flow.

Nafion is a polymer in which all hydrogen atoms in the polymer backbone are replaced by fluorine (Fig. 29). When solidified, this polymer forms channel structures through which reagents are supplied and reaction products are removed. The formation of channels occurs due to the fact that there are two parts in the polymer - a polar tail with a $-SO_3H$ group and a non-polar polymer backbone, because of this, during solidification, the polar ends turn to each other, inside the future channel. Ion-exchange of H^+ in the commercial Nafion suspension by Na^+ was performed using

the procedure described in Ref. [6]. 300 µl of the initial 20 % solution was taken and three times as much water (900 µl) was added to it to obtain a 5 % solution. The addition of 625 µl of 0.1M NaOH to the resulting solution was sufficient to neutralise the protons and convert the ionomer to Na^+ form. The resulting solution was left overnight and the next day the pH of the prepared solution was checked (should be 7.2 - 7.6). If the pH of the solution was lower than 7.6, a new batch of NaOH was added to the solution. To obtain a solution with the required concentration of 2.4 µg cm^{-2}, take 10 µl of the previously prepared Na-form of Nafion concentrate and add 4281 µl of water.

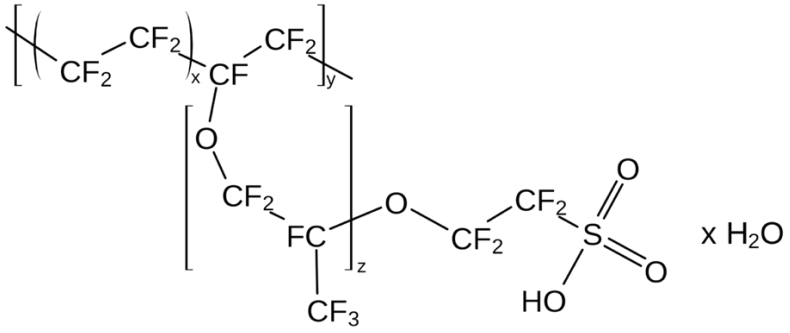

Fig. 29 Nafion's general formula.

A gold wire was used as a counter electrode and a mercury oxide electrode calibrated against a reversible hydrogen electrode (RHE) served as a reference electrode. The detailed electrode calibration procedure is described below.

2.5.2. Electrochemical measurements

Before the experiment, the electrochemical cell filled with background electrolyte was purged with nitrogen for 40 minutes. After that, for each oxide, a potential interval was determined in which no irreversible processes occur (for more details, see section 2.5.1). CVs were obtained for oxides and carbon in oxygen-free solution. The shape of CVs, the formal potential of the Mn(III/IV) interfacial redox transition (E_f) calculated as a half-sum of the potential of the anodic and cathodic peaks in CVs acquired in deaerated supporting electrolyte, and the total charge calculated from CVs (after subtraction of the carbon contribution) were considered as characteristic features of the oxide.

To correct cyclic voltammograms (CVs) for the contribution of carbon, working electrodes were prepared by drop-casting a suspension of carbon (Sibunit) on a GC surface, according to the procedure described above. The carbon loading in this case was also 91 µg cm^{-2}. Then, CVs of carbon were subtracted from the CVs of oxide/carbon compositions (see for example Fig. 30). The

error of such subtractions depends on the true surface of the oxide; the smaller its specific surface, the larger the error and can be up to 10% for the low (~1 m^2 g^{-1}) surface area oxides.

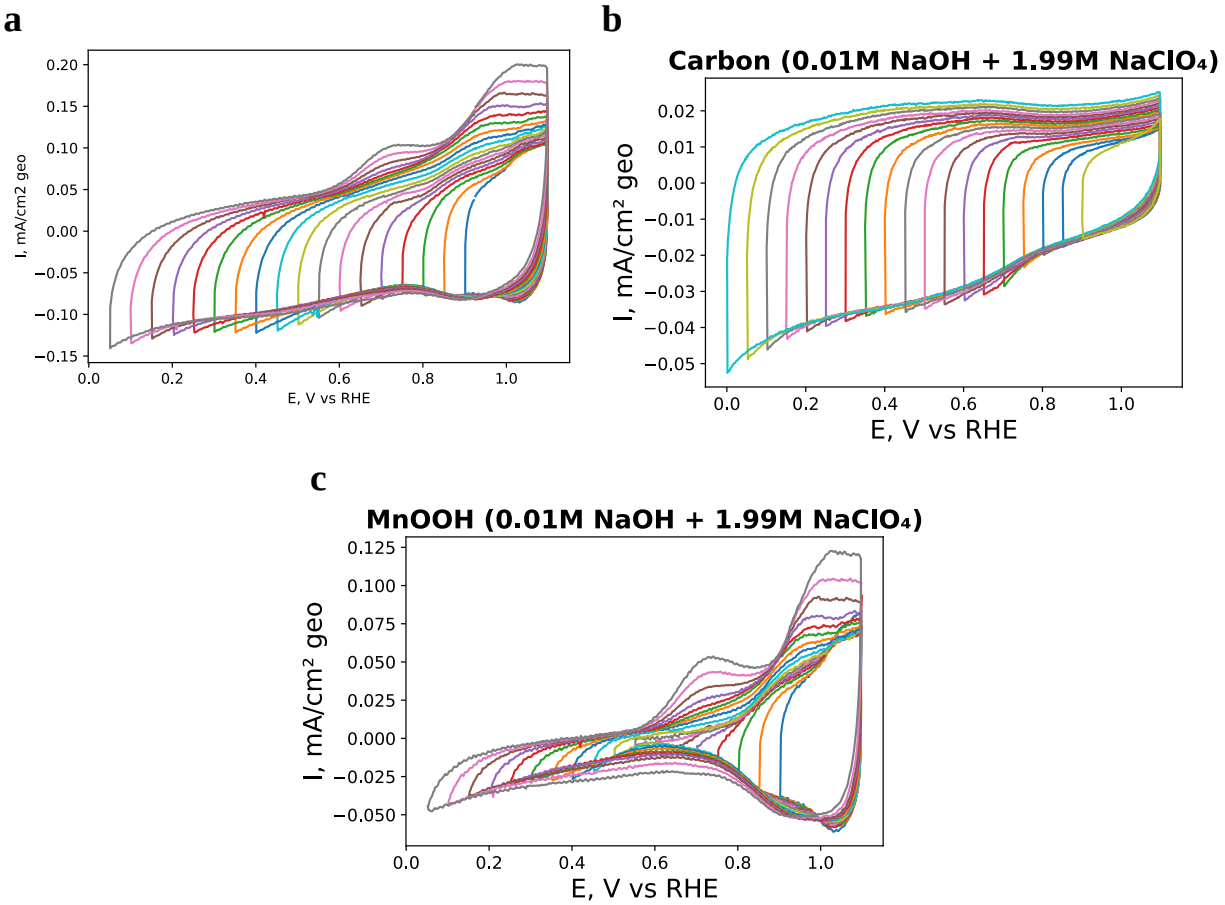

Fig 30 CVs of MnOOH/Sibunit carbon compositions acquired in N_2-purged 0.01 M NaOH + 1.99 M $NaClO_4$ at a scan rate of 10 mV s^{-1} with variable cathodic limit before carbon subtraction (a) and after subtraction of the carbon contribution (c). Oxide loading on the GC surface is 91 μg cm^{-2}, carbon loading is 91 μg cm^{-2}. Current is normalized to the geometric surface of the GC electrode.

Some of the oxides have limited stability in contact with alkaline electrolytes (see chapter 3) and may thus degrade in the course of the measurements. In order to minimise possible degradation effects on the electrochemical characteristics, several precautions were taken. First, the working electrodes with a thin film of studied oxides were placed only in freshly prepared and thoroughly deaerated (40 minutes) solutions, and CVs and rotating disc electrode (RDE) voltammograms were recorded at a scan rate of 10 mV s^{-1} (if not otherwise stated) with a minimum possible number of cycles to obtain stable and reproducible CV (usually stabilisation of a CV required about ten cycles).

To study the oxygen reduction reaction, the electrolyte was saturated with oxygen and RDE voltammograms were measured at rotation rates of 400, 900, 1600 and 2500 rpm, with a scan rate of 10 mV s^{-1}, (three cycles were measured at each rotation rate to obtain a stable and reproducible RDE curve). After the ORR experiments, the electrolyte was deaerated and a CV in the supporting electrolyte was registered again to check its eventual modification.

To study the hydrogen peroxide reduction reaction (HPRR) and the hydrogen peroxide oxidation reaction (HPOR), an H_2O_2 solution standardised with respect to $KMnO_4$ (technique described above) was added to the supporting electrolyte to reach 0.84 mM concentration.

From the ORR and HPOR / HPRR RDE curves, the background cyclic voltammograms obtained in a N_2-purged solution were subtracted. The results of this subtraction are shown in the Fig. 31. It can be seen that hysteresis may occur in some cases. In the case of a hysteresis, an average between the cathodic and anodic scans of the curve was taken.

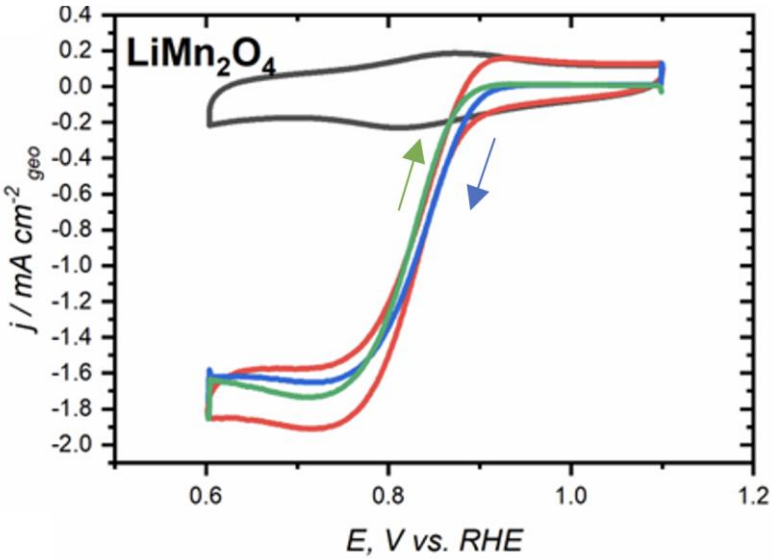

Fig. 31 RDE curves of $LiMn_2O_4$/C in 1 M for the ORR (red), in N_2-saturated solution (grey), blue and green shown after background curves have been subtracted.

Each experiment was repeated at least three times in order to minimise errors associated with the reproducibility of the experiments. In Fig. 32 some examples of RDE voltammograms in O_2-saturated electrolyte are presented to illustrate the reproducibility of the data.

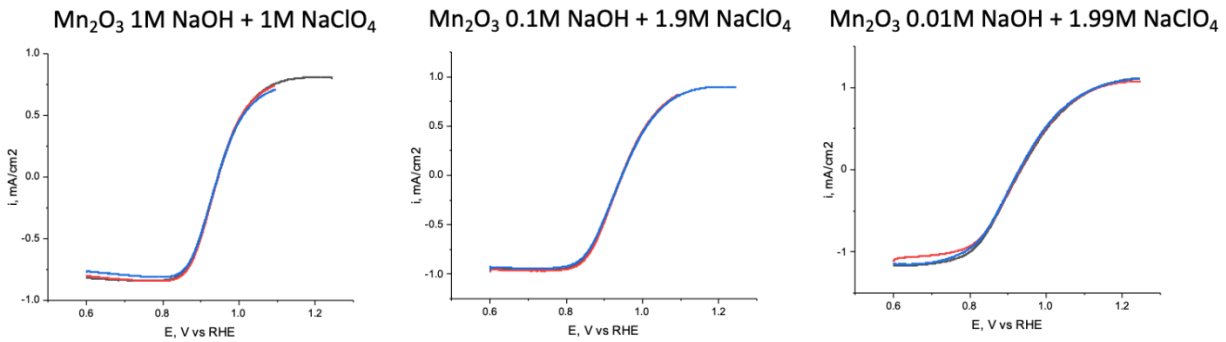

Fig. 32 . Reproducibility of RDE voltammograms acquired for Mn_2O_3 in various electrolytes (as indicated in the panels) at 10 mV s^{-1} and 900 rpm. oxide loading is 91 μg cm^{-2} and carbon loading is 91 μg cm^{-2}. Red, blue and black curves correspond to three independent measurements on newly prepared thin film electrodes.

From the RDE curves of the ORR, the kinetic currents normalised to the BET surface area were determined. First, the diffusion-limited current (I_d) was calculated using the Levich equation:

$$I_d = 0.62nAFD^{2/3}n^{-1/6}Cw^{1/2} \quad (57)$$

where D is the O_2 diffusion coefficient, n is kinematic viscosity, A is geometric area of the electrode surface (in cm^2), C is dissolved oxygen concentration, w is angular rotation rate of the electrode (in rad s^{-1}) and n is the number of electrons (n was taken equal to 2 and 4 for carbon and oxides, respectively). For 1M NaOH D, n and C_{O2} were equal to $1.65 \cdot 10^{-5}$ cm^2 s^{-1}, 0.011 cm^2 s^{-1} and $8.4 \cdot 10^{-7}$ mol cm^{-3}, respectively. Note that D, n and C_{O2} depend on the composition of the supporting electrolyte, as discussed in chapter 4 and chapter 5.

The kinetic current (I_k) was determined from the equation:

$$I_k = \frac{I_d \cdot I}{I_d - I} \quad (58)$$

The carbon contribution to the ORR was corrected as follows:

$$I_{k_{oxide}} = I_{k_{oxide+carbon}} - I_{k_{carbon}} \quad (59)$$

2.5.3. Calibration of the mercury oxide electrode in relation to the reversible hydrogen electrode

Before electrochemical measurements, the mercury oxide reference electrode was calibrated regularly. This was done each time after refilling the reference electrode with electrolyte and every two weeks to confirm stable potential values. The calibration was performed against a reversible hydrogen electrode using platinised platinum.

The platinisation was carried out according to the following procedure. The platinum mesh was fixed on a platinum wire and etched for a short time in boiling aqua regia (a mixture of concentrated hydrochloric and nitric acids in the ratio of 3:1 by volume). The electrode was washed thoroughly in Milli-Q water (18.2 M Ωcm, TOC < 3 ppb) and anodically polarised in 0.1 M HCl with a constant current of 15 mA cm^{-2}, then cathodically polarised in 0.05 M H_2SO_4 at a constant current of 15 mA cm^{-2}. The platinum grid was then washed again thoroughly in Milli-Q water (18.2 M Ωcm, TOC < 3 ppb) and placed in a 1 % H_2PtCl_6 solution. Platinum deposition was carried out at a constant current of 4 mA cm^{-2} for 1 hour. Under these conditions approximately 4 mg Pt per cm^2 of the Pt mesh is deposited. To clean the electrode of adsorbed Cl^-, the electrode was cathodically polarised in 0.05 M H_2SO_4 at a potential slightly below 0 V vs. RHE.

To calibrate the Hg/HgO electrode, a supporting electrolyte of the same composition was placed in the cell for which further electrochemical measurements were to be made and inside the electrode. The working electrode was platinised platinum, the counter electrode was platinum wire and the reference electrode was a Hg/HgO electrode. The electrodes were placed in an electrochemical cell which was then purged with nitrogen for 50 minutes. CVs was recorded in the range of 0.05-1.5 V relative to RHE until stable results were obtained. The cell was then purged with hydrogen, at which time the open circuit potential (OCP) was recorded until its value was stabilized within ± 1 mV. Then, CVs (Fig. 33) was recorded without rotation in the range -0.1-1.5 V relative to the RHE. The zero-current potential (in the case of hysteresis between the anodic and the cathodic scan the potential values were averaged) was used as the calibration value for the reference electrode. The value obtained for the potential of the mercury oxide electrode was generally equal to 0.93 V (which agrees well with the standard potential difference of the Hg/HgO and RHE). The conversion of the potential to the RHE scale was carried out using the formula below:

$$E_{\mathrm{RHE}} = E_{HgO/Hg} + 0.930\ \mathrm{V} \tag{60}$$

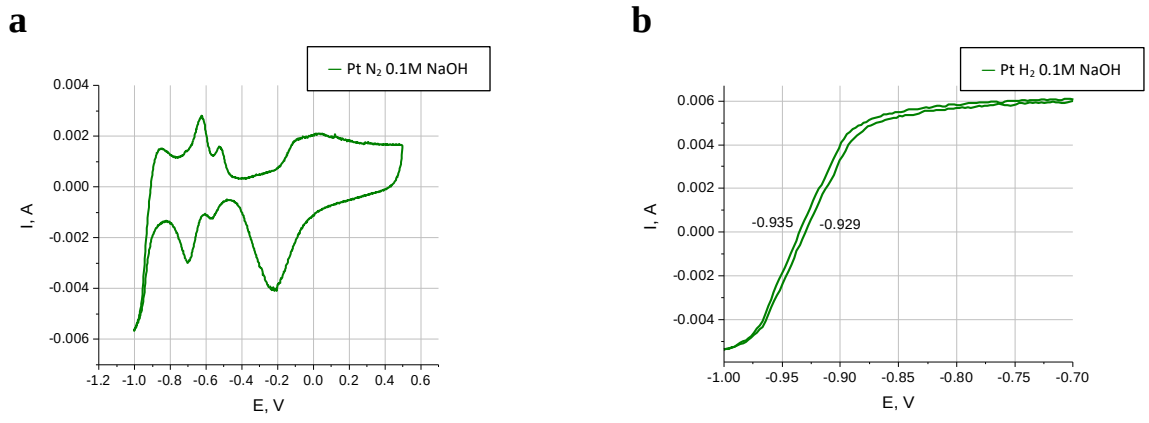

Fig. 33 Example of a CV of a platinised Pt electrode at a scan rate 10 mV s^{-1} in 0.1 M NaOH purged with N_2 (a) and H_2 (b).

To correct the measured potentials E for ohmic drop (E - iR) the value of electrolyte resistance between the working electrode and the reference electrode was used, estimated from the high-frequency cut-off impedance hodographs recorded at a fixed potential in the frequency range from 0.1 Hz to 100 kHz with an amplitude of 5 mV (Fig. 34). The measurement was carried out for each solution and for each electrode.

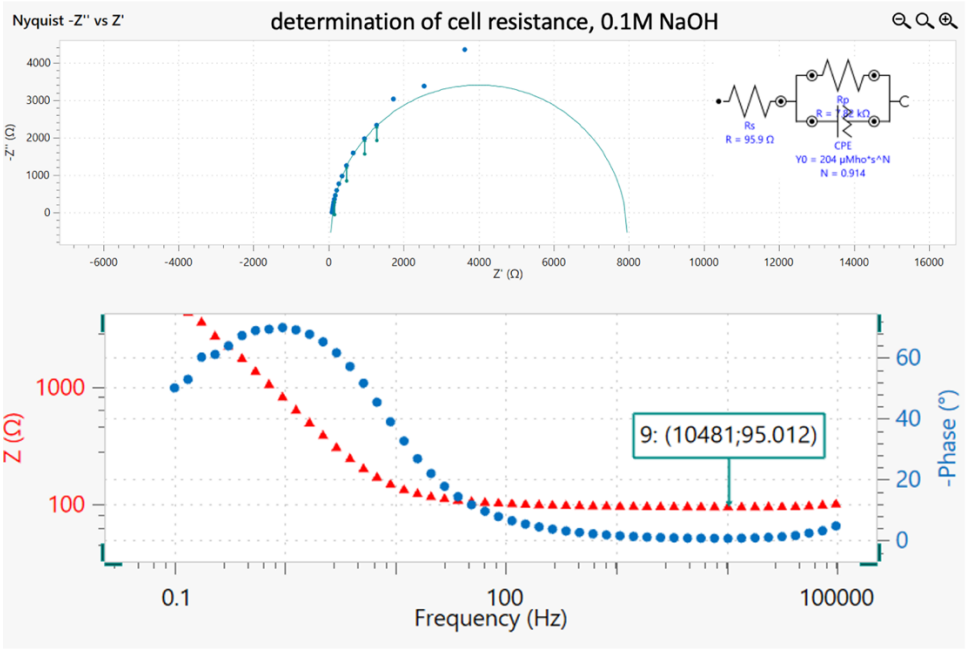

Fig. 34 Nyquist plot of the impedance hodograph (top), described using the presented equivalent circuit and Bode plot - real part of impedance and phase as a function of frequency (bottom). Given for Mn_2O_3/C in 0.1M NaOH.

The resulting impedance curves were processed with the NOVA software. For this purpose the Nyquist plot has been described using an equivalent circuit, which includes a parallel connected (Rp) resistance (charge transfer resistance) and constant phase element (CPE), which in turn are connected in series with the resistance (Rs), which is the sought electrolyte resistance. The second approach, which was used in addition to the first, was to plot the resistance and the phase as a function of frequency (Bode plot). When the phase reaches zero, the required resistance value can be obtained.

Correction for ohmic potential drop was not done in the standard experiments performed at a scan rate 10 mV s^{-1}, as the resulting currents are quite low, and hence the iR drop is negligible. However, in experiments performed at high sweep rates, the recorded currents are much higher than in ORR or HPOR/HPRR studies, so the iR correction was introduced (assuming potential-independent solution resistance).

2.5.4. Methods for electrochemical studies of the effect of electrolyte composition

When investigating the effect of pH on the electrochemical behaviour of the oxides, the following concentrations of NaOH were investigated: 1.00 M, 0.10 M and 0.01 M. Further reduction of the OH^- concentration requires the use of a buffer solution, because in the near-electrode region a change in pH value is possible due to the participation of hydroxide anions in the oxygen reduction reaction. The studies were carried out at a constant ionic strength. This was done to reduce the number of parameters to be varied by decreasing the NaOH concentration, and to avoid increasing the resistance of the solution by using diluted NaOH solutions. For example, Fig. 35 shows RDE voltammograms for the HPRR/HPOR on MnOOH in 0.01M NaOH. The solution resistance was about 1,000 Ohm (as determined by impedance spectroscopy). After the introduction of the IR correction, it was clear (see Fig. 35) that a small error in the value of resistance could lead to large errors in the ohmic-drop-corrected potential.

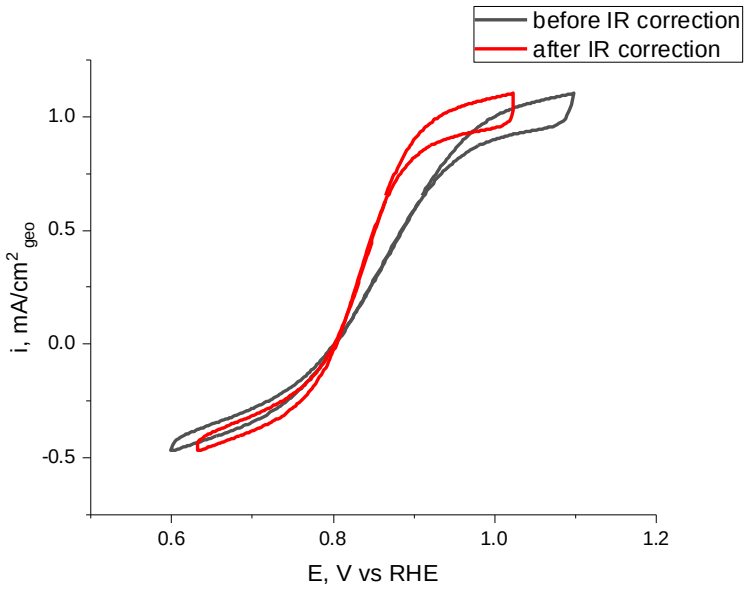

Fig. 35 The polarisation curves of the electrochemical hydrogen peroxide oxidation/reduction reactions (HPOR/HPRR) acquired for MnOOH deposited on a GC RDE in 0.01N NaOH + 0.84 mM H_2O_2 solution before IR correction (black) and after IR correction (red). Rotation rate 900 rpm. Scan rate is 10 mV/s; Loadings are 91 μg cm^{-2} oxide + 91 μg cm^{-2} carbon.

Thus, it was decided to add $NaClO_4$ to the background electrolyte, so that when studying the influence of pH on the electrochemical behaviour of the oxides the ionic strength remained constant at 2 mol L^{-1}, the Na^+ concentration being 2 M.

To investigate the influence of Na^+ on the electrochemical behaviour of the oxides, $NaClO_4$ was added to a NaOH solution with a concentration of 0.1 M to obtain solutions with Na^+ concentrations of 0.1, 0.2, 1.1 and 2.0 M. The composition of the electrolytes used is presented in Table 2.

Table 2. Composition of the supporting electrolytes used to study the influence of the electrolyte on the electrochemical behaviour of the catalysts

Studying the effect of pH	Studying the effect of Na^+ concentration
1M NaOH + 1M $NaClO_4$	0.1M NaOH + 1.9M $NaClO_4$
0.1M NaOH + 1.9M $NaClO_4$	0.1M NaOH + 1M $NaClO_4$
0.01M NaOH + 1.99M $NaClO_4$	0.1M NaOH + 0.1M $NaClO_4$
	0.1M NaOH

The solutions were chosen so that for the first series of experiments (pH effect) the pH could be varied while the ionic strength of the solution and the Na^+ concentration remained constant, and, for the second series of experiments (cation effect), the Na^+ concentration could be varied while the OH^- concentration remained the same (see chapters 4 and 5).

2.6. Investigation of the oxide degradation

2.6.1. Electrochemical measurements

To address cathodic degradation (resulting from reduction of Mn(III) to Mn(II)), a series of CVs was recorded with various cathodic limits. Each series started from the narrow interval [0.9, 1.15] V, and the cathodic limit was subsequently decreased with a 50 mV step. For the widest interval [0.5, 1.15] V, evident features of an irreversible material degradation were observed for all oxides studied. Typically, the cathodic limit in the ORR experiments was 0.6 V or higher, to limit the cathodic degradation.

For some compounds, data on the behaviour of oxides during cycling into the anodic region were also obtained (chapter 4). For this purpose, a series of CVs was obtained with different anodic limits. Each series started with a potential interval of [0.6, 1.1] V vs. RHE after which the anodic limit was increased in steps of 50 mV. The maximum cycling range was [0.6, 1.35].

Figure 36 shows CVs with a variable cyclic limit for $LaMnO_3$ and MnOOH. When analysing these data one should pay attention to "tails" which indicate irreversible processes, as well as to the appearance of new peaks or a strong and large shift of the existing peaks. Thus $LaMnO_3$ does

not exhibit any changes either in the cathodic or anodic regions (within the investigated potential intervals), whereas when MnOOH is cycled into a cathodic region (<0.6 V) its degradation is clearly manifested.

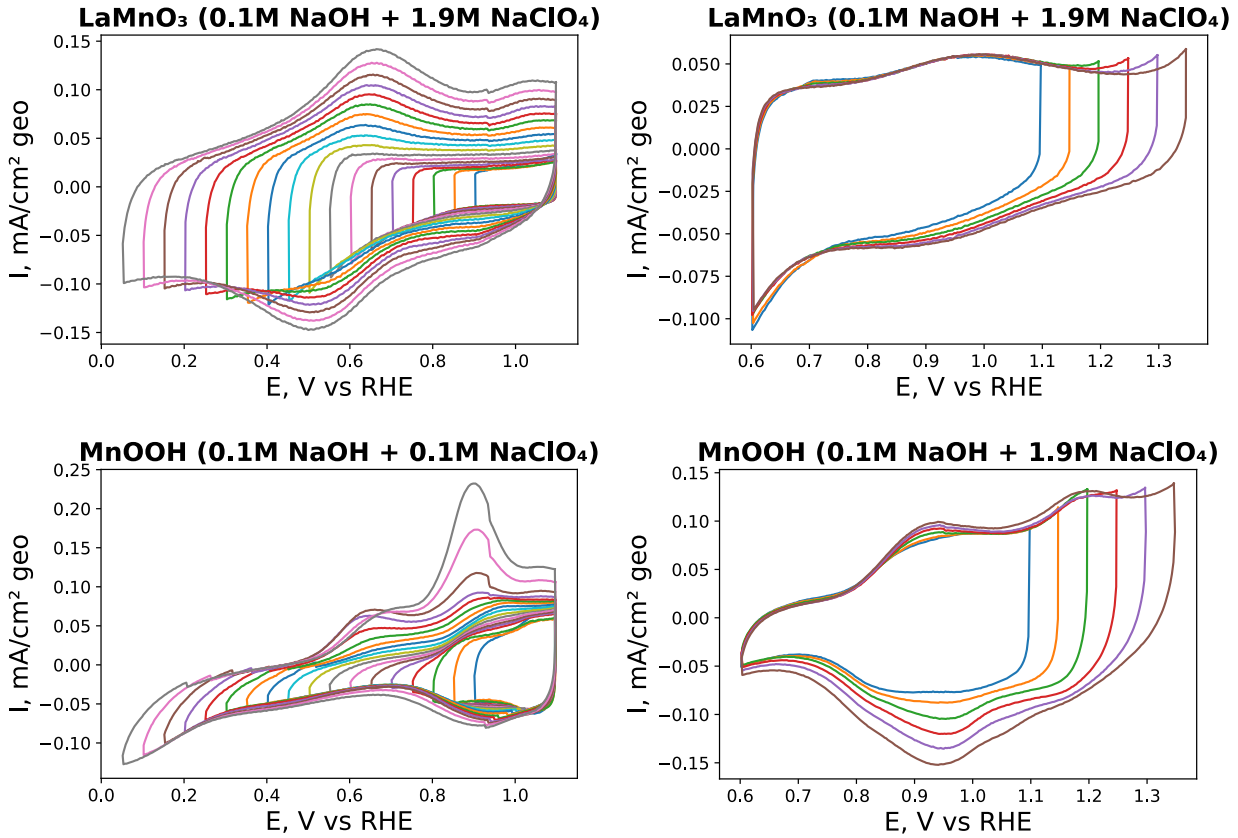

Fig. 36 CVs of $LaMnO_3$/C and MnOOH/C with variable cathodic limit (left) and anodic limit (right) acquired in different electrolytes (as indicated in the panels). Scan rate is 10 mV s^{-1}, oxide loading is 91 μg cm^{-2} and carbon loading is 91 μg cm^{-2}.

Changes in the shape of CV resulting from various treatments (including potential cycling with extended potential limits) were considered as evidence of the materials' surface transformations (typically degradation, as the majority of transformations were found to decrease the ORR activity).

2.6.2. Physicochemical study of oxide degradation

In this work, ex-situ studies of oxide materials after various treatments were carried out. Initially, the stability of the oxides was investigated by long-term incubation in 1 M NaOH at an open circuit potential. For this purpose, the oxide was placed in a plastic test tube with a screw cap, to avoid contamination of the solution with silicates from the glass and to minimise the ingress of CO_2; the cap was also wrapped with parafilm. The oxide was incubated in alkali for two weeks. If no change was observed from powder X-ray diffraction, the powder was placed back into the

alkali solution for a longer period (a year). After contact with alkali, the powder diffraction patterns were examined for the appearance of ether new crystalline phases, or an amorphous halo. The unit cell parameters were also determined and compared with the original samples.

Since X-ray powder diffraction provides information mainly from the volume of the sample, if the oxide transformation occurs in the surface layers this method will not provide information about the changes that have occurred.

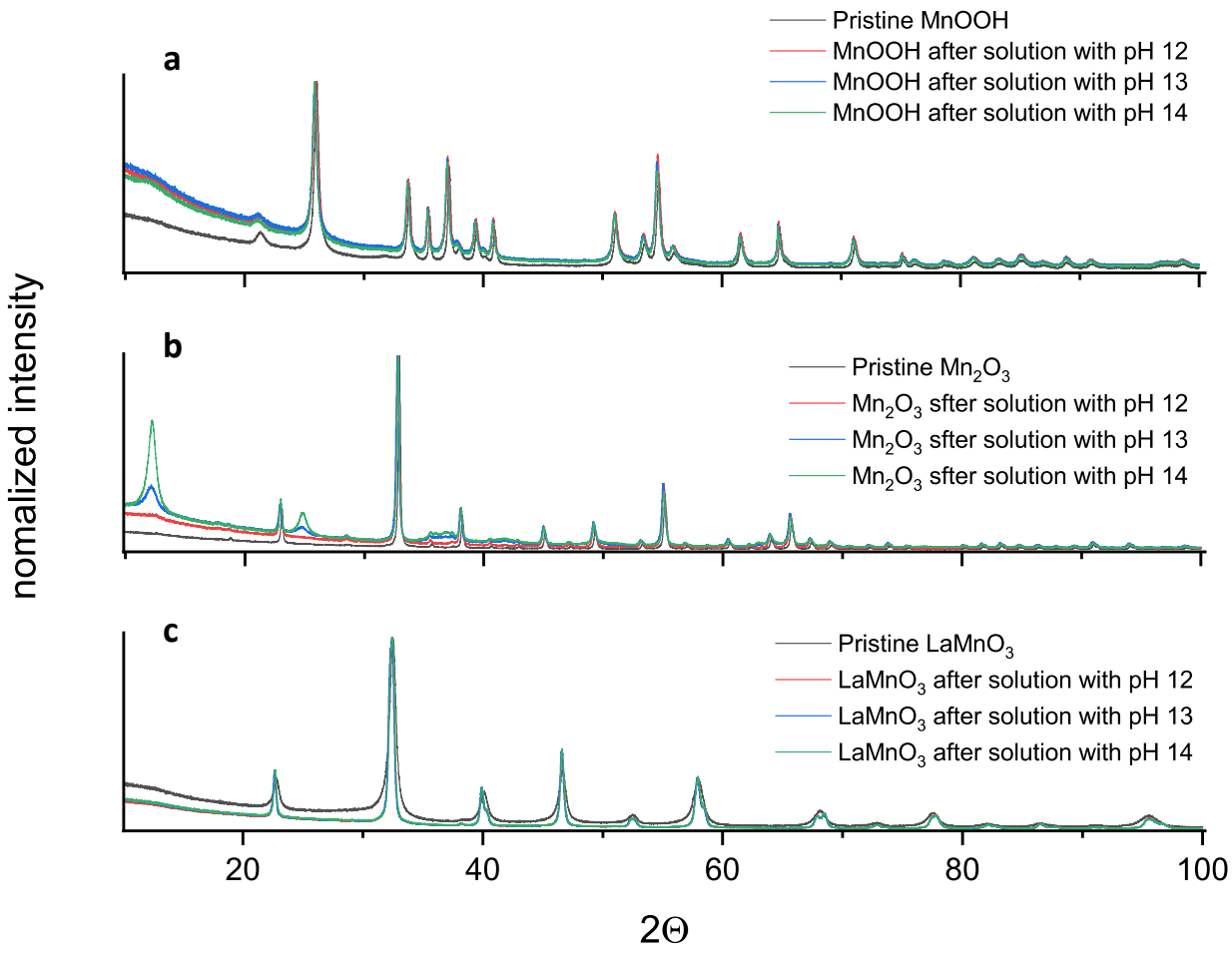

Fig. 37 XRPD patterns for MnOOH (a), Mn_2O_3 (b), $LaMnO_3$ (c) for pristine samples and aged for 1 year in 1 M, 0.1 M and 0.01 M NaOH.

For example, when studying the degradation by powder X-ray diffraction of MnOOH, $LaMnO_3$ and Mn_2O_3, after keeping the corresponding powders in NaOH solutions with different pH for two weeks (not shown here), no changes were found for any of the compounds. Whereas, when keeping the oxides in alkaline solutions for a year, $LaMnO_3$ and MnOOH did not show any changes (Fig. 37). For them, the unit cell parameters were also calculated, which turned out to be constant within the measurement error. The apparent change in the position of the peaks is associated with a zero shift. On the contrary, new peaks were found for Mn_2O_3, which were

attributed to the formation of birnesite - $Na_x(H_2O)_yMnO_2$. It should be noted that its amount increases with increasing pH. We assume however that during short-term experiments discussed in chapters 4 and 5 of this work, Mn_2O_3 does not change. This is justified by the absence of changes in the CV of Mn_2O_3 acquired before and after the electrochemical measurements, and allows us to draw conclusions about the structural factors affecting its electrocatalytic activity in ORR and HPER/HPRR

To detect changes occurring on the surface of oxides as a result of different treatments, the XPS method was used. This method makes it possible to analyse the sample with a depth (evaluated as three times inelastic mean free path) of 2.67 nm for the laboratory instrument and 1.4 nm for measurements performed at 450 eV kinetic energy at the synchrotron. The spectra of (i) original samples as well as samples subjected to different treatments, in particular (ii) after suspending them - treatment with ultrasound in water (inevitable step in the preparation of RDE thin films), (iii) suspended sample applied on a carrier and soaking them in background electrolyte - 1 M NaOH for 6 hours at open circuit potential were studied with this method. XP spectra after electrochemical measurements were also recorded. For this purpose, ten cycles in the potential range from 0.6 to 1.15 V relative to the RHE in 1 M NaOH purged with N_2 were recorded.

2.7 Determination of point of zero charge

The isoelectric point was determined by titrating the oxide (or carbon) dispersion. The titration was performed using a pH electrode (Orion™ 8103 ROSS™ Combination Semi-micro pH Electrode) that was calibrated using commercially available buffer calibration solutions. The following pH points were used for calibration: 1.68, 4.01, 6.86, 9.18 and 12.47. The pH meter was calibrated at the beginning of each day before the measurements were carried out. The resulting calibration curve is shown in Figure 38, reproduced for each calibration.

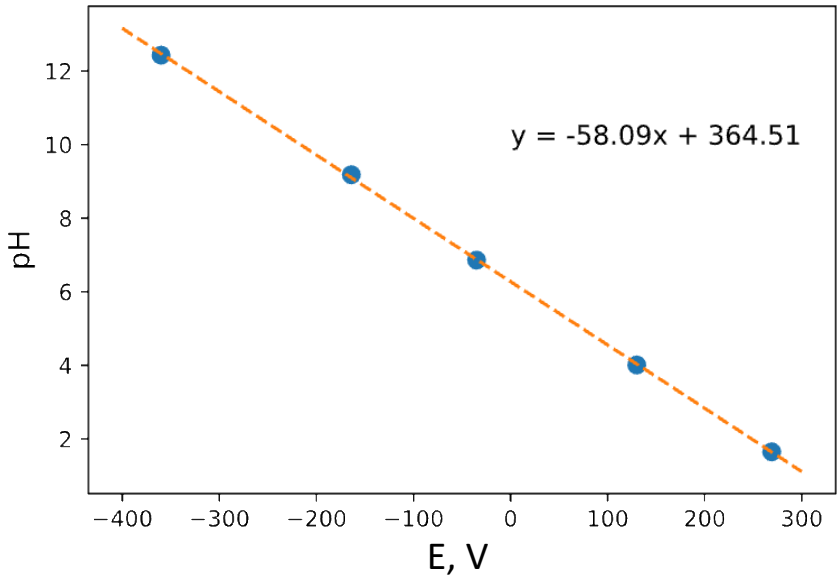

Fig. 38. pH calibration curve. Potential is referred to the Ag/AgCl reference electrode.

After the measurements, a correction for the sodium error was applied to the data obtained, according to the pH meter data sheet, but in all cases it was less than the measurement error of the instrument. Titration was carried out at a constant temperature of 25 °C, with a nitrogen purge to protect the solution from CO_2. The titration cell was made of plastic, to avoid silicate contamination of the electrolyte. The titration was carried out using a Crison Titromatic 2S Universal autotitrator at a constant titrant addition rate (0.1 mL every 15 seconds).

To determine the zero point, a sample of the test substance (~0.1 g) was placed in 5 ml of an aqueous NaOH solution (for the exact electrolyte composition, see Table 3) and incubated overnight under constant stirring. Titration for each compound was performed at three different solution ionic strengths (0.12, 0.03 and 0.021) and constant OH^- concentration. The titration was carried out with perchloric acid solution, with the addition of $NaClO_4$ ($NaClO_4$ concentration being the same as in the test solution) in order to prevent dilution of the solution and the ensuing changes in the ionic strength during titration. In order to obtain correct data for the PZC value, the titration curves were also obtained without the addition of the oxide.

Table 3. Composition of the alkaline solutions in which the test substances were dispersed and composition of the titrant solution.

Background solution	Titrant
0.02M NaOH + 0.1M $NaClO_4$ (BG_1)	0.01M $HClO_4$ + 0.1M $NaClO_4$
0.02M NaOH + 0.01M $NaClO_4$ (BG_2)	0.01M $HClO_4$ + 0.01M $NaClO_4$
0.02M NaOH + 0.001M $NaClO_4$ (BG_3)	0.01M $HClO_4$ + 0.001M $NaClO_4$

From the titration curves for the background solution and the background solution with added oxide or carbon suspension, it was possible to calculate the surface charge (σ) according to the formula:

$$S = \frac{FcDV}{mA}, \tag{61}$$

where F is the Faraday constant, c is the concentration of the acid or base used in the titration, ΔV is the difference in volume of the acid added to obtain the same pH value with the solution without the oxide, m is the mass of the oxide and A is the surface area.

Accordingly, when plotting the σ vs. pH, the point PZC is defined at σ = 0.

When an oxide or carbon is placed in an alkaline solution, part of the OH^- is adsorbed onto the surface of the compound under study. Thus, from the change in pH compared to the control sample (without the dispersible phase), the number of acid/base centres on the surface can be estimated.

2.8. References

[1] A.S. Ryabova, F.S. Napolskiy, T. Poux, S.Ya. Istomin, A. Bonnefont, D.M. Antipin, A. Baranchikov Ye., E.E. Levin, A.M. Abakumov, G. Kéranguéven, E. V. Antipov, G.A. Tsirlina, E.R. Savinova, Rationalizing the Influence of the Mn (IV)/ Mn (III) Red-Ox Transition on the Electrocatalytic Activity of Manganese Oxides in the Oxygen Reduction Reaction, Electrochimica Acta Journa. 187 (2016) 161–172. https://doi.org/10.1016/j.electacta.2015.11.012.

[2] M. Bijelic, Sinteza i strukturne značajka spinelnih nanomaterijala tipa AMn_2O_4(A = Co, Zn, Ni, Cd, Cu), PhD Thesis, Zagreb, (2016).

[3] T. Striker, J.A. Ruud, Effect of Fuel Choice on the Aqueous Combustion Synthesis of Lanthanum Ferrite and Lanthanum Manganite, Journal of the American Ceramic Society. 93 (2010) 2622–2629. https://doi.org/10.1111/j.1551-2916.2010.03799.x.

[4] J.J. Yeh, I. Lindau, Atomic subshell photoionization cross sections and asymmetry parameters: $1 \leqslant Z \leqslant 103$, Atomic Data and Nuclear Data Tables. 32 (1985) 7–9. https://doi.org/10.1016/0092-640X(85)90016-6.

[5] B. Gilbert, B.H. Frazer, A. Belz, P.G. Conrad, K.H. Nealson, D. Haskel, J.C. Lang, G. Srajer, G. De Stasio, Multiple Scattering Calculations of Bonding and X-ray Absorption Spectroscopy of Manganese Oxides, J. Phys. Chem. A. 107 (2003) 2839–2847. https://doi.org/10.1021/jp021493s.

[6] J. Suntivich, H.A. Gasteiger, N. Yabuuchi, Y. Shao-Horn, Electrocatalytic Measurement Methodology of Oxide Catalysts Using a Thin-Film Rotating Disk Electrode, J. Electrochem. Soc. 157 (2010) B1263. https://doi.org/10.1149/1.3456630.

[7] Y.A. Zolotov, Fundamentals of Analytical Chemistry, V.1 (2012)

3. AMn_2O_4 spinels (A - Li, Mg, Mn, Cd) as ORR catalysts: The role of Mn coordination and oxidation state in the catalytic activity and their propensity to degradation

This chapter is based on the article:

"AMn_2O_4 spinels (A - Li, Mg, Mn, Cd) as ORR catalysts: The role of Mn coordination and oxidation state in the catalytic activity and their propensity to degradation" by

K.A. Dosaev, S.Ya. Istomin, D.A. Strebkov, G.A. Tsirlina, E.V. Antipov, E.R. Savinova

published in Electrochimica Acta 428 (2022) 140923; 10.1016/j.electacta.2022.140923

3.1. Introduction

Complex AB_2O_4 oxides with a spinel structure are widely known as noble metal-free catalysts for the oxygen reduction (ORR) and evolution reactions (OER) in alkaline media [1,2]. Numerous studies have been devoted to Mn_3O_4 and substituted AMn_2O_4 spinels, notably to the influence of their composition [3], Mn oxidation state, doping with red-ox "active" and "inactive" cations, vacancy concentration, particle morphology [4], surface crystallography, strain [5–7] etc. on their activity in the ORR (See Refs 1,2 and references therein). However, literature data on their electrocatalytic activity [6,8–20] (see Table 1 in Chapter 1) are rather contradictory, and the structure (composition)-activity relationships are still insufficiently understood. To a large extent, these inconsistencies are caused by the lack of unified measurement protocols (this refers e.g. to the potential limits and the scan rate, catalyst loading on the electrode surface, conductivity of the catalytic layer, etc.), and incorrect data analyses (such as ignorance of the carbon binder contribution, normalizing currents to geometric instead of the real surface area, etc.) [21]. A yet another issue, and the subject of the present study, is related to the stability of the spinel structure/composition under the measurement conditions.

Thermodynamic data [22] demonstrate a limited stability of the Mn_3O_4 spinel to oxidation under standard conditions. The Gibbs formation energies for MnO, Mn_3O_4, Mn_2O_3 (Bixbyite) and MnO_2 (Pyrolusite) are -362.9, -427.73, -440.6 and -465.2 kJ per mole of Mn [22], respectively,

showing that stability of manganese oxides in air under standard conditions increases with the formal Mn oxidation state, MnO_2 being the most stable phase. While considering stability in aqueous alkaline solutions, one should take into account a much wider set of oxides, including hydrated and non-stoichiometric ones. Nevertheless, even a rather rough estimate from the Pourbaix diagram [23] shows that the Mn_3O_4 spinel is prone to oxidation above ~0.6 V RHE, suggesting that it should be unstable either in kinetic or mixed regions of the ORR.

Considering thermodynamic instability of Mn(II) of Mn_3O_4 in the potential interval of the ORR (0.6 – 0.9 V vs RHE), replacing it by red-ox inactive cations appears to be an attractive approach to the design of ORR catalysts with the spinel structure. $LiMn_2O_4$, $CdMn_2O_4$ and $MgMn_2O_4$ oxides are Mn-based spinels containing Mn along with a red-ox inactive cation (Li, Cd, Mg), which does not change its oxidation state under the ORR conditions. Large Mn(II) cation of Mn_3O_4 (r(Mn(II))=0.80 Å [24]) is replaced in these oxides either by larger Cd(II) (r(Cd(II))=0.92 Å [24][2]) or smaller Mg(II) and Li(I) cations (r(Mg(II))=0.71 Å, r(Li(I))=0.73 Å [24]). The average Mn oxidation state should thus increase up to +3 in $CdMn_2O_4$ and $MgMn_2O_4$, and up to +3.5 in $LiMn_2O_4$, compared to +2.67 in Mn_3O_4. According to the available thermodynamic data, $MgMn_2O_4$ is expected to be the most stable compound in this series (at least in what concerns its stability in air), with the standard formation enthalpy of -1570 kJ mol^{-1} [25] (compared to -1250 kJ mol^{-1} for $CdMn_2O_4$ [25], -1380 kJ mol^{-1} for $LiMn_2O_4$ [26] and -1390 kJ mol^{-1} [22] for Mn_3O_4).

To the best of our knowledge, information on the ORR activity and stability of AMn_2O_4 spinel oxides, with a red-ox inactive A-cation, is scarce. The ORR activity of $MgMn_2O_4$ was documented in Ref. [17] (Table 1), but in the absence of the information regarding the real surface area of the oxide the specific activity cannot be estimated. ORR activity of $LiMn_2O_4$ was reported by Wei et al.[27] (Table 1), which in what follows will be compared to this work. No ORR activity data could be found for $CdMn_2O_4$ oxides.

Thus, Mn-containing oxides Mn_3O_4, $LiMn_2O_4$, $CdMn_2O_4$ and $MgMn_2O_4$ have similar spinel crystal structure, possess different thermodynamic stability in air and contain Mn cations with the average oxidation state spanning from +2.67 (Mn_3O_4) to +3.5 ($LiMn_2O_4$). These compounds seem to constitute an informative set of materials to decipher characteristics of the spinel structure essential for its stability in aqueous medium and for electrocatalytic activity in the ORR.

In this work, we study the ORR activity of Mn_3O_4, $LiMn_2O_4$, $CdMn_2O_4$ and $MgMn_2O_4$ using a thin-film rotating-disc (RDE) approach by depositing a thin layer of oxide mixed with carbon (to improve electric conductivity of the catalytic layer) on a glassy carbon disc. Hydrogen peroxide being formed as a stable ORR intermediate [12,21], we also examine electrocatalytic activity of

[2] Note that all r (radius) values are given for coordination number (CN) 4

the above set of materials in the hydrogen peroxide oxidation (HPOR) and reduction reaction (HPRR). In addition to spinels, we have studied also α-MnOOH as a material of different crystal structure with similar Mn oxidation state (3+). Furthermore, we use cyclic voltammetry (CV) to examine the interfacial recharging behavior of spinels. The latter has been extensively studied in view of the development of high capacitance materials for supercapacitor applications [28]. It is important to note that red-ox transitions of surface transition metal cations are also involved in the ORR mechanism [12,29–31]. To find out whether it is worthwhile to correlate the ORR activity with the composition and Mn oxidation state in the pristine materials, the surface state was examined with XPS after different treatments. We demonstrate that the surface of Mn_3O_4 spinel undergoes essential transformation not only under cycling of the electrode potential but also when contacting alkaline solution under the open circuit conditions, and even during the electrode preparation (suspending the oxide in water). Replacement of Mn(II) by red-ox inactive cations results in stabilization of the spinel structure, the highest stability achieved for the $MgMn_2O_4$ spinel.

3.2. Materials and methods

Detailed procedures used for the synthesis of spinels, their characterization with XRPD, BET, SEM, XPS, as well as for their electrochemical studies can be found in Chapter 2.

3.3. Results and discussion

3.3.1. Phase composition and microstructure

XRPD showed the formation of single-phase samples of all studied Mn-containing spinel materials (corresponding XRPD patterns are given in Fig. 39). Except for $LiMn_2O_4$, oxides crystallize in a tetragonal distorted spinel structure due the presence of a high amount of Jahn-Teller Mn(III) cations. According to the SEM data (Fig. 40) all materials, except for $MgMn_2O_4$, contain small slightly aggregated particles. The $MgMn_2O_4$ sample consists of sintered particles of less than 100 nm size. The EDX analysis in SEM was used to determine the composition of cadmium- and magnesium-containing spinels. Their composition corresponds to the formulas $Cd_{1.1\pm0.1}Mn_2O_4$ and $Mg_{1.1\pm0.15}Mn_2O_4$ thus close (within estimated standard deviation) to the expected ones. The BET specific surface areas (Table 4) ranged from 16.5 (for Mn_3O_4) to 39.4 $m^2\ g^{-1}$ (for $LiMn_2O_4$), being similar to manganese oxides studied in previous publications [12,32], and allowing a reasonable comparison of specific charges and catalytic activities.

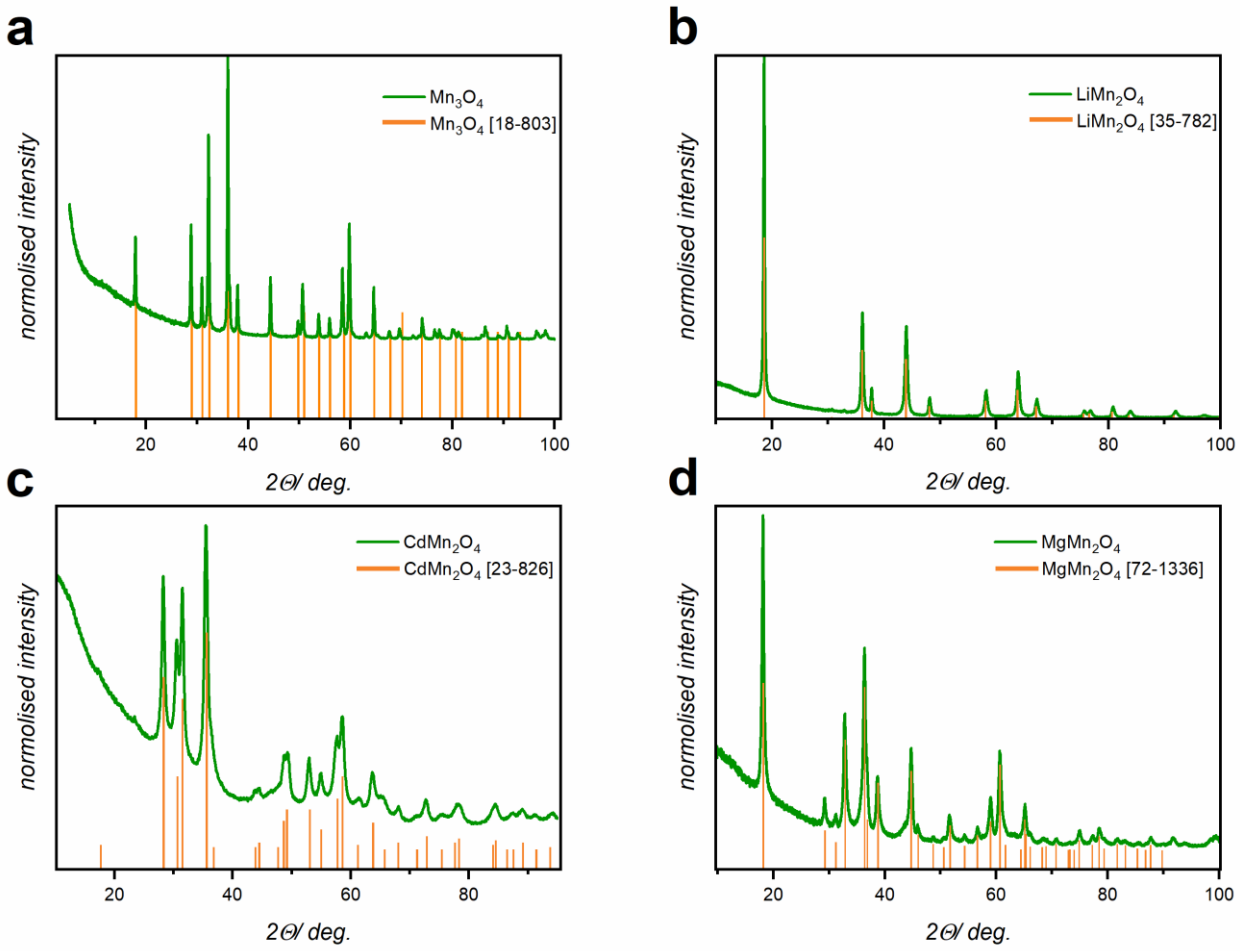

Fig. 39 XRPD patterns of Mn_3O_4 (a), $LiMn_2O_4$ (b), $CdMn_2O_4$ (c), $MgMn_2O_4$ (d) along with the position of reflections (orange vertical lines at the bottom) from the ICDD PDF2 database for Mn_3O_4 (#18-803), $LiMn_2O_4$ (#35-782), $CdMn_2O_4$ (#23-826) and $MgMn_2O_4$ (#72-1336).

For all samples the average Mn oxidation state calculated from NEXAFS was close to the expected one, the latter determined from the stoichiometric composition (Fig. 41). A slightly underestimated average oxidation state of Mn in Mn_3O_4 (Fig. 41) might be attributed to the presence of some admixture of Mn(III) at the surface of our reference MnO sample [33], as confirmed by comparison of our experimental MnO NEXAFS spectrum to the one reported in the literature [34].

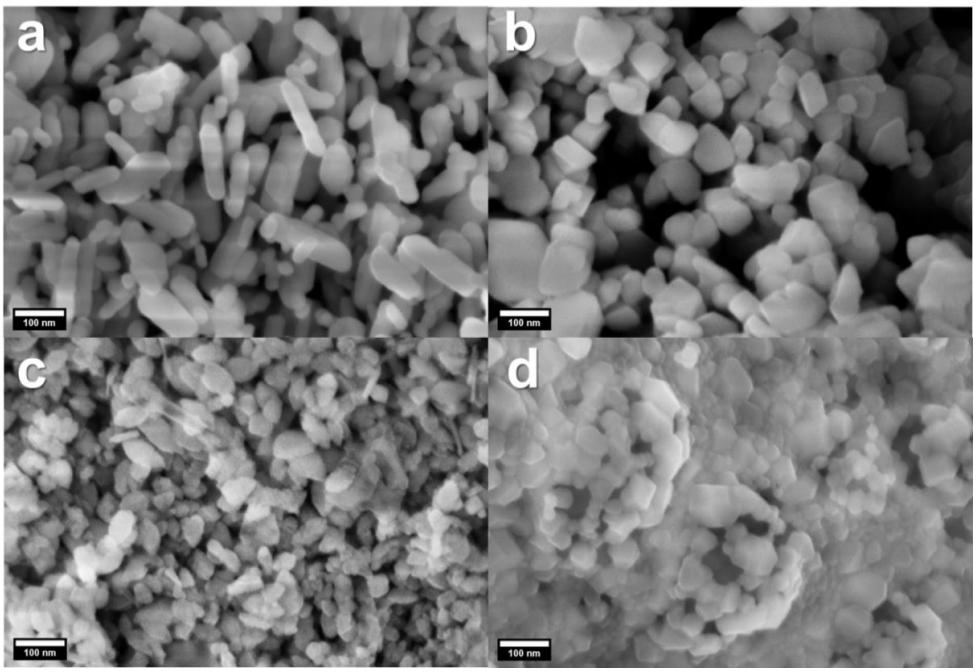

Fig. 40 SEM images of the spinel materials: Mn_3O_4 (a), $LiMn_2O_4$ (b), $CdMn_2O_4$ (c), $MgMn_2O_4$ (d).

Table 4. Unit cell parameters, BET surface area and electrochemical characteristics of Mn-containing spinels.

	Unit cell parameters, Å	**BET surface area, m^2 g^{-1}**	**n_{eff} at 0.65 V**[3]	**E_f**[4]**, V vs RHE**
Mn_3O_4	a = 5.8357(4) c= 9.6824(7)[1]	16.5	2.7	0.93
$LiMn_2O_4$	a=8.247(2) Å[2]	21	2.9	0.83
$CdMn_2O_4$	a = 5.8357(4)[1] c= 9.6824(7)	39.4	2.7	0.89
$MgMn_2O_4$	a = 5.7221(2)[1] c = 9.2929(3)	22	2.8	0.91

[1] space group $I4_1/amd$

[2] space group $Fd\bar{3}m$

[3] Effective number of electrons transferred in the ORR and determined from the slope of Koutecký- Levich plots

[4] Formal potential of the red-ox transition determined from CVs

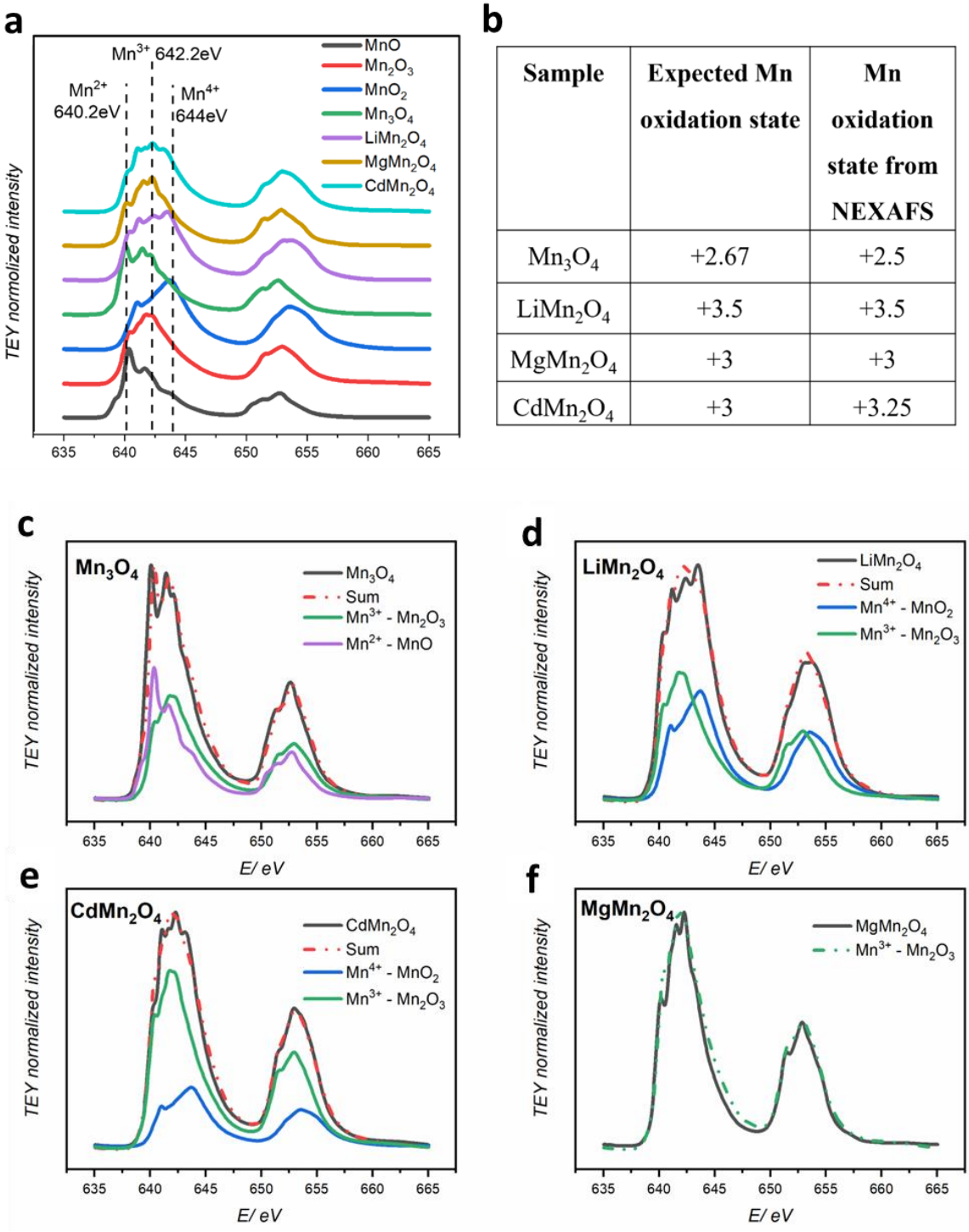

Sample	Expected Mn oxidation state	Mn oxidation state from NEXAFS
Mn_3O_4	+2.67	+2.5
$LiMn_2O_4$	+3.5	+3.5
$MgMn_2O_4$	+3	+3
$CdMn_2O_4$	+3	+3.25

Fig. 41 (a) NEXAFS spectra of Mn_3O_4 (green), $LiMn_2O_4$ (violet), $MgMn_2O_4$ (light brown), $CdMn_2O_4$ (cyan) along with the spectra of the reference samples MnO (black), Mn_2O_3 (red), MnO_2 (blue). (b) Comparison of the Mn oxidation state calculated from stoichiometric composition with the one calculated from NEXAFS data. NEXAFS spectra of (c) Mn_3O_4, (d) $LiMn_2O_4$, (e) $CdMn_2O_4$, (f) $MgMn_2O_4$ and their fitting using a combination of lines for MnO, Mn_2O_3, MnO_2 standard samples.

3.3.2. Electrochemical characterization of the spinels

3.3.2.1. Interfacial recharging behavior

3.3.2.1.1. Influence of the cathodic limit

We start our analysis of the interfacial recharging behavior of spinel oxides by analyzing a series of CVs with a variable cathodic limit obtained by the so-called potential opening method, where the negative cathodic limit is shifted in –50 mV increments for each subsequent CV (Fig. 42). First, we note that all samples demonstrate a pair of anodic and cathodic peaks, which, following previous publications, could be attributed to Mn(IV/III) redox transition [12,35]. The corresponding formal potentials (E_f) calculated as a half-sum of the respective anodic and cathodic peak potentials from the 10th cycle of CVs acquired in the potential interval from 0.6 to 1.15 V vs. RHE, are reported in Table 4. $LiMn_2O_4$ showed the lowest E_f of 0.83 V while for Mn_3O_4 this value (0.94 V) is the highest in the series, in satisfactory agreement with Ref. [12] (0.95 V). For $CdMn_2O_4$ and $MgMn_2O_4$ rather close E_f values of 0.89 V and 0.91 V, respectively, are observed. However, these values tend to change slightly in the course of a prolonged potential cycling (see Fig. S1 in the ANNEX). It should be noted that CVs for Mn_3O_4 in the literature are rather contradictory, often demonstrating multiple peaks [7,36,37], which may be attributed to potential cycling in a much wider potential interval (compared to this work), sometimes the cathodic limit being extended to as low potential as 0.2 V vs. RHE.

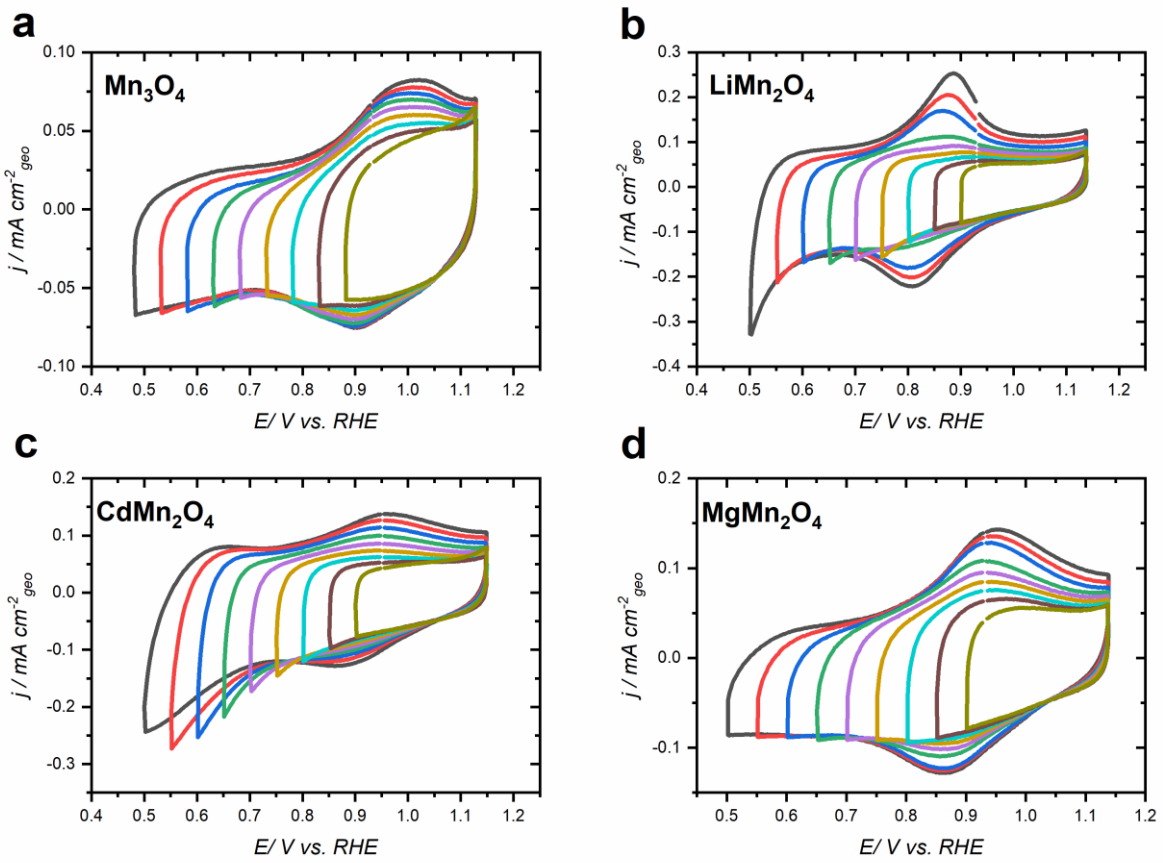

Fig. 42 CVs with a decreasing cathodic potential limit for GC-supported thin films of oxide/carbon composites in N_2-purged 1 M NaOH at 10 mV s^{-1} registered for Mn_3O_4 (a) $LiMn_2O_4$ (b), $CdMn_2O_4$ (c) and $MgMn_2O_4$ (d). Currents are normalized to the geometric area of the electrode. For each cathodic limit the third CV is shown. Loadings are 91 μg cm^{-2} oxide + 91 μg cm^{-2} carbon.

Furthermore, one may see that the reversibility of the interfacial recharging of AMn_2O_4 spinels strongly depends on the nature of the A-cation. Indeed, for $CdMn_2O_4$ (and probably also $LiMn_2O_4$), once the cathodic limit is extended beyond 0.8 V, a cathodic 'tail' shows up suggesting occurrence of some irreversible transformations (Fig. 42 b, c). In the meantime, the shape of CVs for Mn_3O_4 and $MgMn_2O_4$ (Fig. 42 a, d) does not demonstrate obvious signs of such irreversible degradation even when the cathodic limit is extended to 0.5 V vs. RHE. The observed differences correlate with our approximate thermodynamic stability estimates (see Introduction in this chapter). In what follows the irreversibility of CVs will be corroborated by the XPS analysis of the surface composition, see section 3. 3.3.

3.3.2.1.2. Influence of the scan rate

Studying the influence of the scan rate (n) on the interfacial recharging allows one to distinguish 'fast' and 'slow' charging processes [38,39]. The former correspond to recharging of the cations located at the 'outer' surface, while the latter may comprise recharging processes occurring in the pores ('inner' surface according to Trasatti) as well as intercalation processes. Fig. 43 presents CVs with currents normalized to the scan rate. For all studied materials, increase of the scan rate results in a significant decrease of the charge as well as in a change in the CV shape, both suggesting possible contribution of intercalation processes (e.g. protons from water and/or sodium cations from NaOH) in the interfacial recharging. Note that the corresponding specific capacity values are much lower than those reported for spinel-carbon composite materials specially designed for supercapacitors and usually studied in neutral Na_2SO_4 electrolytes [28].

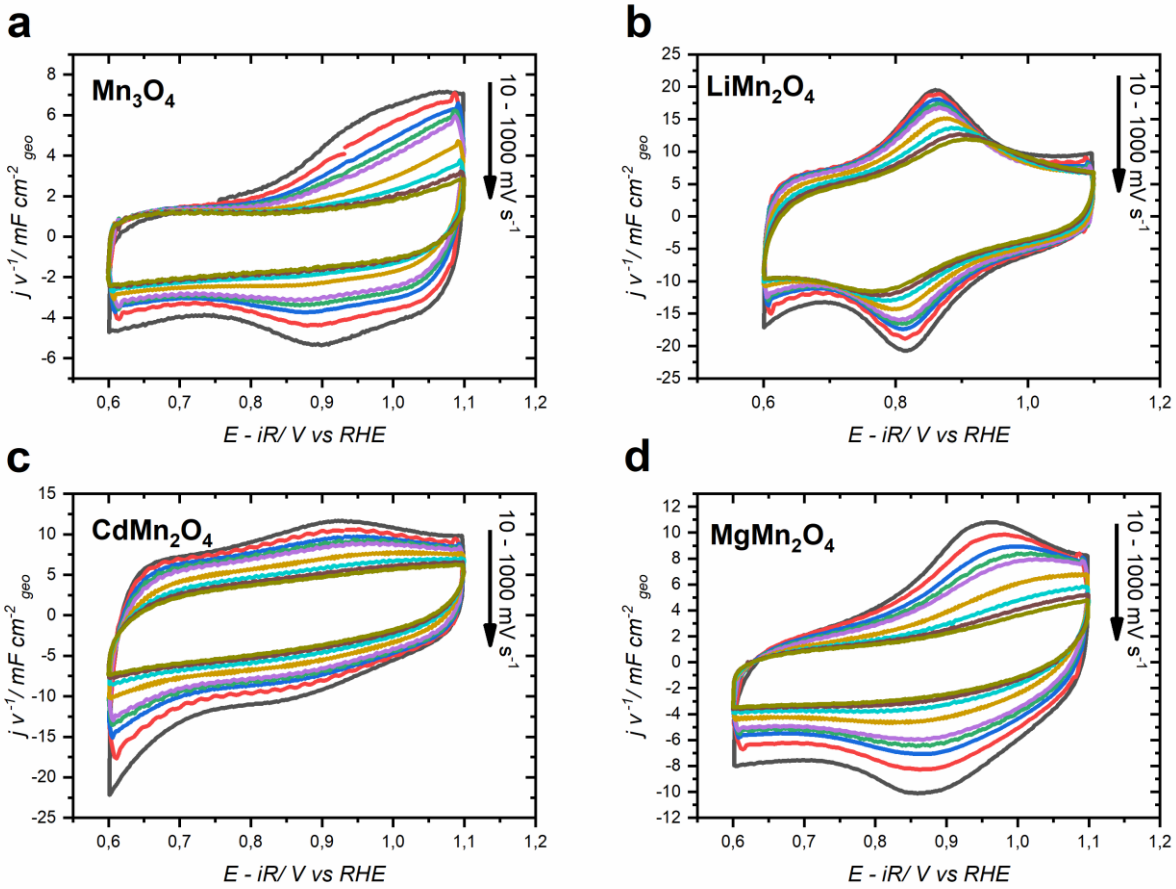

Fig. 43 Cyclic voltammograms with variable scan rate (from 10 to 1000 mV s^{-1}) for GC-supported thin films of oxide/carbon composites in N_2-purged 1 M NaOH at 10 mV s^{-1} registered for Mn_3O_4 (a) $LiMn_2O_4$ (b), $CdMn_2O_4$ (c) and $MgMn_2O_4$ (d). Currents are normalized to the scan rate and to the geometric area of the electrode. Loadings are 91 μg cm^{-2} oxide + 91 μg cm^{-2} carbon.

Following the approach introduced by Trasatti [39], charges calculated from CVs at different scan rates were plotted in the coordinates (i) Q vs. $n^{-½}$ and (ii) Q^{-1} vs. $n^{½}$ (Fig. 44) Extrapolating (i) to 'infinitely high' and (ii) to 'infinitely low' scan rates allows one to estimate Q_{min}, which can be attributed to 'fast' recharging, and Q_{max} corresponding to the sum of 'fast' and 'slow' recharging (Table 5), the latter including intercalation processes and/or slow interfacial discharge. For all samples, except for $LiMn_2O_4$, Q_{min} is comparable or smaller than the expected Mn monolayer charge, independently of the choice of the linear regression interval. In contrast, Q_{max} for all samples except for $CdMn_2O_4$ significantly exceeds the 'monolayer' value. We thus conclude that for all spinels (probably with the exception of $CdMn_2O_4$), intercalation processes non-negligibly contribute to the interfacial recharging, with the highest contribution observed for $LiMn_2O_4$. We will discuss intercalation phenomena in section 3.3.3. while considering stability of spinel oxides under different treatments.

Table 5 Specific surface area of the spinels, the charge determined from the CVs of the spinels at a scan rate of 10 mV s^{-1}, the minimum and maximum charge (Q_{min} and Q_{max}) determined from extrapolation of the dependences $Q(n^{-½})$ and $Q^{-1}(n^{½})$. In case of non-linear plots the curves are described by two linear segments (Fig. 44) resulting in two values of Q_{min} and Q_{max}. The calculated charge ($Q_{monolayer}$) corresponds to the average densities of Mn atoms at the surfaces of polycrystalline oxides (see Ref. [12] for details).

Compound	**S_{BET} $m^2 g^{-1}$**	***Q*** **at 10 mV s^{-1}** **µC cm^{-2} oxide**	***Q_{min}*** **µC cm^{-2} oxide**		***Q_{max}*** **µC cm^{-2} oxide**		***$Q_{monolayer}$*** **µC cm^{-2} oxide**
			(1)	**(2)**	**(1)**	**(2)**	
$MgMn_2O_4$	22	189	40	90	230		142
$LiMn_2O_4$	21	290	153	214	318	265	152
$CdMn_2O_4$	39.4	129	33	83	147		134
Mn_3O_4	16.5	238	135	168	267	191	180*/139**
MnOOH	31	112	--		--		153

* Considering Mn cations both in octahedral and tetrahedral sites
** Considering only Mn in octahedral sites

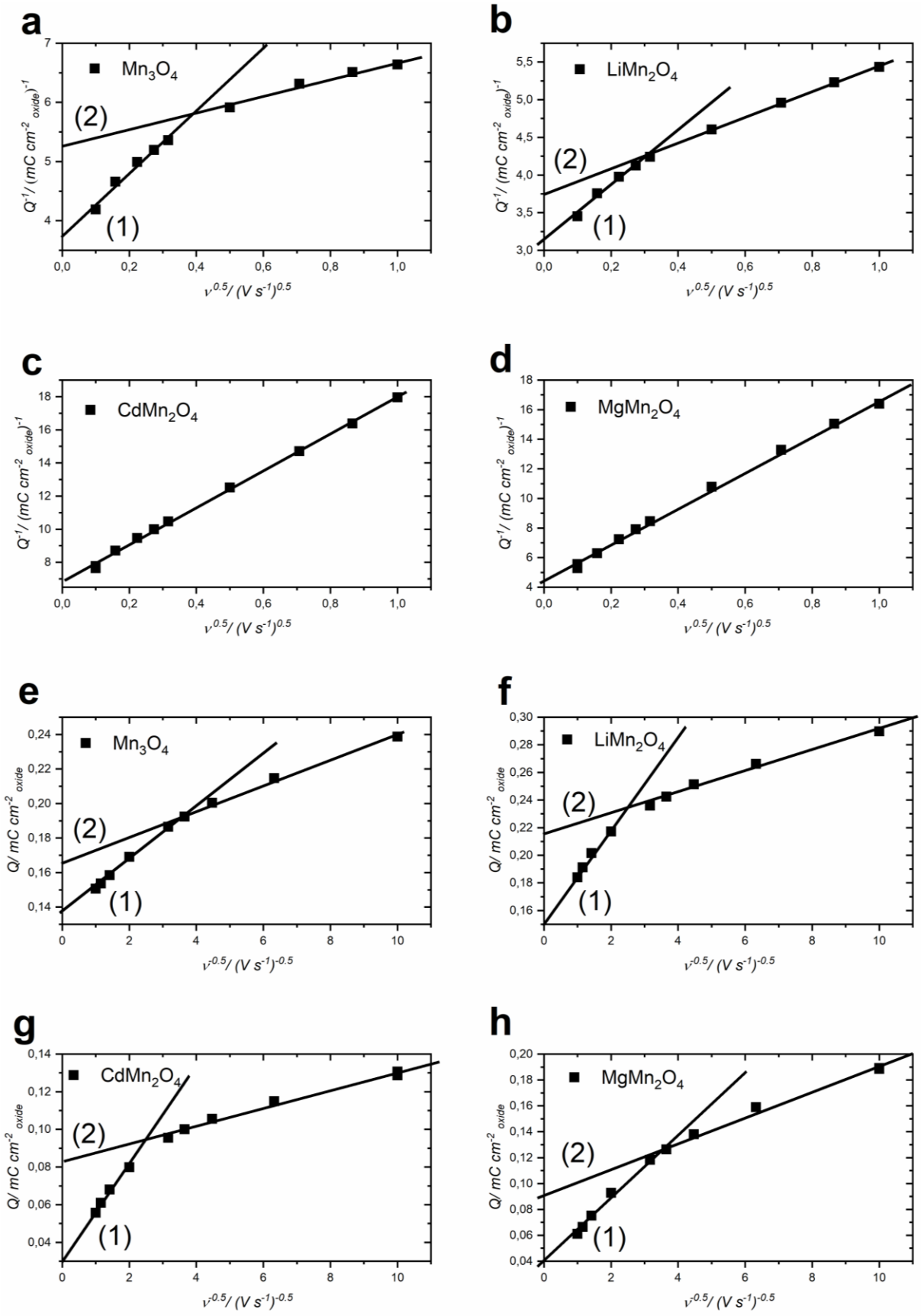

Fig. 44 Dependencies of the reciprocal value of the cathodic charge(Q^{-1}) for the spinel samples on the square root of the potential scan rate ($n^{½}$) (a-d) and Q on $n^{-½}$ (e-h). Q is calculated from the CVs in Figure 43.

Not only the value of the charge but also the shape of CV is affected by the scan rate. For all samples except for the $LiMn_2O_4$, increase of the scan rate up to 500 mV s^{-1} (cyan traces in Fig. 43) leads to a disappearance of the red-ox peaks. Such a behavior may be attributed to a faster interfacial Mn(IV)/Mn(III) red-ox transition in $LiMn_2O_4$ compared to other spinels. We will come back to this assumption in the next section in connection with the ORR activity of spinels.

3.3.2.2. Oxygen reduction reaction (ORR) and hydrogen peroxide reduction and oxidation reactions (HPRR/HPOR) on spinels

Data presented in subsection 3.3.2.1 suggest that potential cycling even in a rather narrow potential interval may not be innocent and might result in modification of the surface structure and/or composition (as clearly seen from the influence of the cathodic limit on the shape of CV of $CdMn_2O_4$). While influence of different treatments on the surface composition will be discussed in section 3.3.3, herewith we present data on the ORR and HPRR/HPOR activity of AMn_2O_4 oxides in the frames of a standardized protocol intended to minimize surface transformations during the measurements. The RDE voltammograms in an O_2-saturated electrolyte were collected in the potential interval from 0.6 to 1.15 V vs. RHE at rotation rates from 400 to 2500 rpm after 10 cycles in the oxygen-free supporting electrolyte (in the same potential interval) and 30 minutes exposure to the open circuit potential during saturation of solution with oxygen. For more details the reader is referred to Chapter 2.

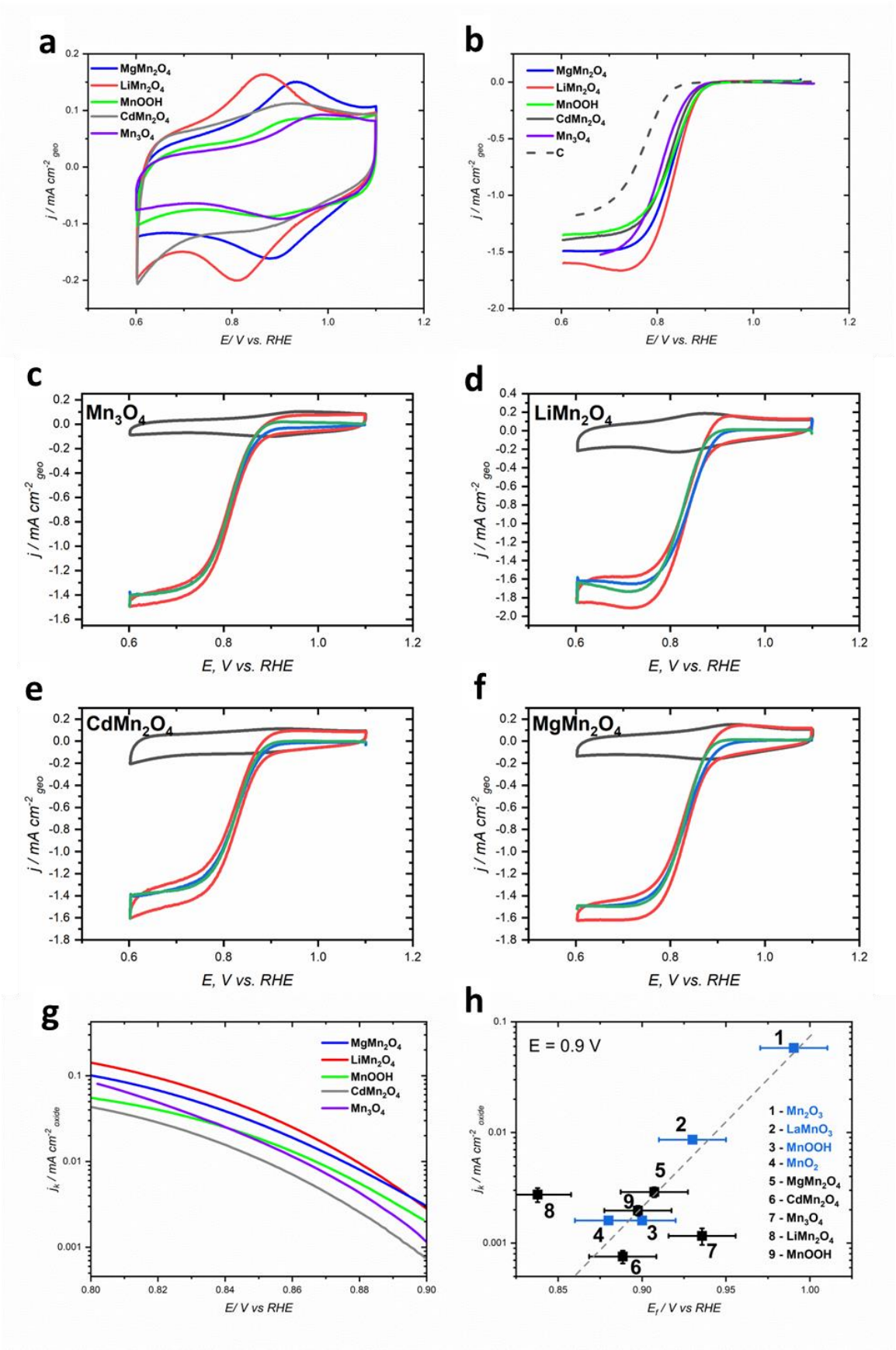

Fig. 45 (a) CVs in N_2-saturated 1 M NaOH (the tenth cycle is shown for each sample), and (b) RDE voltammograms in O_2-saturated 1 M NaOH at 900 rpm for $MgMn_2O_4$, Mn_3O_4, $LiMn_2O_4$, $CdMn_2O_4$ and α-MnOOH. (c, d) CVs in N_2-saturated (black) and RDE voltammograms in O_2-

saturated 1 M NaOH (red) for Mn_3O_4, (c) $LiMn_2O_4$ (d), $MgMn_2O_4$ (e), $CdMn_2O_4$ (f). Blue and green traces correspond to the cathodic and anodic traces, respectively, of RDE voltammograms obtained after subtraction of the background CV in O_2-free supporting electrolyte. (g) The corresponding Tafel plots, and (h) kinetic ORR currents at 0.90 V vs. RHE plotted against the formal potential (E_f) of the Mn(IV/III) red-ox transition, with black symbols - data from this work, blue symbols - data taken from Ref. [12]. Loadings are 91 μg cm^{-2} oxide + 91 μg cm^{-2} carbon. Currents in panels (g, h) are normalized to the BET surface area of the oxides.

CVs in N_2-saturated electrolyte for the studied series of AMn_2O_4 spinels along with RDE curves acquired in O_2-saturated 1 M NaOH at 900 rpm are given in Fig. 45 a and b, respectively (RDE voltammograms acquired at different rotation rates are shown in Fig. 46). One may see that the peaks of the Mn(IV/III) red-ox transition (and hence the formal potential E_f, see Fig. 45 a and Table 4) for $LiMn_2O_4$ are significantly shifted negative compared to other samples. This low value of E_f (0.83 V vs RHE) may be attributed to the flexibility of the $LiMn_2O_4$ structure which is known to withstand rather wide range of the cation and oxygen vacancies [40–42]. Such behavior results in the easiness of the red-ox transition in agreement with Ryabova et al. [12].

For all spinels ORR currents become observable below ca. 0.9 V vs. RHE (Fig. 45 b). Comparison of RDE voltammograms in O_2-saturated and CVs in O_2-free electrolyte (see Fig. 45 a, b) confirms, in agreement with the previous publications [12], that the ORR requires the presence of Mn(III) sites and cannot occur when all interfacial Mn cations are in the Mn(IV) state. Hence, the ORR activity is closely related to the interfacial Mn(IV/III) transition, as discussed in what follows. Note that any comparison of the so-called ORR 'onset' to the literature values is meaningless, unless the catalyst loadings and specific surface areas of materials are similar. Instead, in Fig. 45 g we compare kinetic currents (j_k) calculated from RDE voltammograms (see chapter 2), normalized to the BET surface areas of oxides and plotted against the electrode potential (Tafel plots). Data for α-MnOOH (S_{BET}=31 m^2 g^{-1}) are given for comparison and are in a reasonable agreement with the previously published data [12].

It is instructive to compare ORR activities of this work with the literature data. As mentioned in the introduction, ORR activity values for Mn_3O_4 are very disparate, some authors reporting higher, while other – lower specific and mass activities (*cf.* Table 1 in Chapter 1). For example, Ryabova et al. documented significantly higher specific activity of Mn_3O_4 under the same experimental conditions [12]. This may be due to some differences either in the composition/structure of the samples (e.g. small impurity of a highly active Mn_2O_3 phase was detected in Ref. [12]) or their surface state (regarding the influence of different treatments on the surface composition the reader should refer to section 3.3.3). For $Li_xMn_2O_4$ (x = 1 and 0.74) Wei

et al. [27] reported significantly lower ORR activity than observed in this work. Indeed, potential required to achieve 25 μA per cm^2 (per unit of the BET surface area of the $LiMn_2O_4$ oxide), was equal to 0.77 V in Ref. [27] against 0.86 V in this work. This difference may be attributed to different electrolytes (0.1 M KOH in Ref. [27] against 1 M NaOH in this work) as well as to the different cathodic potential limits (0.45 V vs. RHE in Ref. [27] against 0.6 V vs. RHE in this work) and the ensuing cathodic degradation. This emphasizes the necessity of a unified measurement protocol for comparing ORR activities.

In earlier studies of Ryabova et al. [12,32] it was demonstrated that the ORR specific activity of various Mn-oxides correlates with the formal potential of the interfacial Mn(IV/III) red-ox transition (E_f) confirming the above-mentioned redox-mediated ORR mechanism. Since E_f may be considered as an *in situ* characteristics of the materials surface (the catalytic reaction layer), in Fig. 45 h we plot kinetic currents at 0.90 V normalized to the BET surface area of oxides against E_f. Previous data for Mn_2O_3 and other Mn oxides from Ref. [12] are included for the sake of comparison. Analysis of Fig. 45 h allows one to make the following conclusions. First, all studied Mn spinel samples demonstrate specific ORR activity inferior of either Mn_2O_3 or manganese-containing perovskites. Second, except for the $LiMn_2O_4$ spinel, the data fit reasonably well the dependence of the logarithm of activity on the E_f. Possible reasons for the higher activity of $LiMn_2O_4$ will be discussed below in connection to its electrocatalytic activity in the HPRR/HPOR (this section) and its transformation under the reaction conditions (section 3.3.3).

The effective number of electrons n_{eff} transferred in the ORR was calculated from the slope of Koutecký–Levich (K-L) plots (typical KL plots are shown in Fig. 46 e) at 0.6 V and listed in Table 4. For all spinel samples n_{eff} is below 3, suggesting (in agreement with the previous studies [43]) that the ORR on Mn oxides occurs through an intermediate formation of H_2O_2. Considering this, we studied activity of Mn spinels in the oxidation and reduction reactions of H_2O_2. In passing we wish to emphasize that the value of n_{eff} as well as the amount of H_2O_2 produced during the ORR depend on the catalyst loading on the electrode surface [44,45].

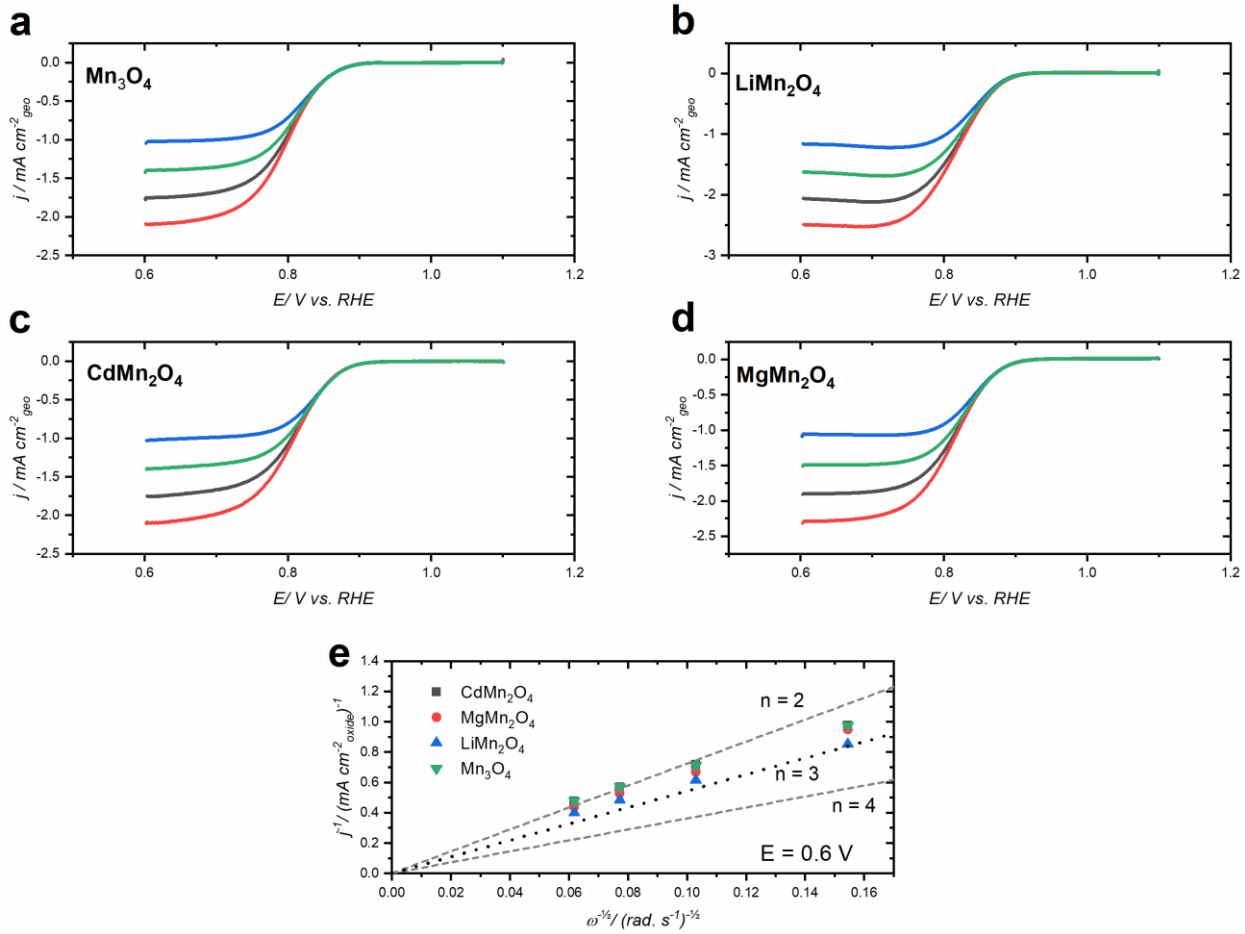

Fig. 46 RDE voltammograms in O_2-saturated 1M NaOH at 10 mV s^{-1} for GC supported thin films of Mn_3O_4 (a), $LiMn_2O_4$ (b), $CdMn_2O_4$ (c), $MgMn_2O_4$ (d). Loadings are 91 μg cm^{-2} oxide + 91 μg cm^{-2} carbon. Color codes: 400 (black), 900 (red), 1600 (blue), 2500 (green) rpm. Currents are normalized to the electrode geometric area and corrected to the background currents measured in the N_2 atmosphere. Koutecky–Levich plots for currents at 0.6 V vs RHE (e) extracted from RDE voltammograms in O_2-saturated 1 M NaOH for Mn_3O_4 (green), $LiMn_2O_4$ (blue), $MgMn_2O_4$ (red), $CdMn_2O_4$ (black). Dashed and dotted lines show the slopes calculated for a $2e^-$, $3e^-$ and $4e^-$ ORR.

Fig. 47 represents RDE voltammograms acquired for the spinel oxides in the presence of H_2O_2 (a comparison of the curves with each other can be found in Fig. S2 of the ANNEX). For all samples the anodic HPOR currents demonstrate an expectable rotation-rate dependence (reaching diffusion-limited plateau might require incursions into potentials above 1.15 V vs. RHE which we wish to avoid in order to limit the extent of the anodic oxide degradation) [46]. In the meantime, for all samples except for the $LiMn_2O_4$, cathodic HPRR currents demonstrate a rotation-rate independent plateau (see Fig. 47 a-d) suggesting the absence of mass-transport limitations (*cf*. no dependence on the rotation rate). Cathodic current observed in this region is also potential-independent below ca. 0.8 V vs. RHE which means that the process is limited by a chemical step.

In previous studies this step was identified with a chemical O-O bond breaking in an adsorbed hydrogen peroxide intermediate (step 5 in the reaction mechanism represented in Figure 25 of Chapter 1) [43]. Such a behavior was previously documented for α-MnOOH [43] and attributed to a high activation barrier of the O-O bond breaking step [44]. The mixed potential values for $MgMn_2O_4$ (0.85 V vs. RHE), Mn_3O_4 (0.85 V vs RHE) and $CdMn_2O_4$ (0.85 V vs RHE) are also very close to that observed for α-MnOOH (0.84 V vs. RHE [43]).

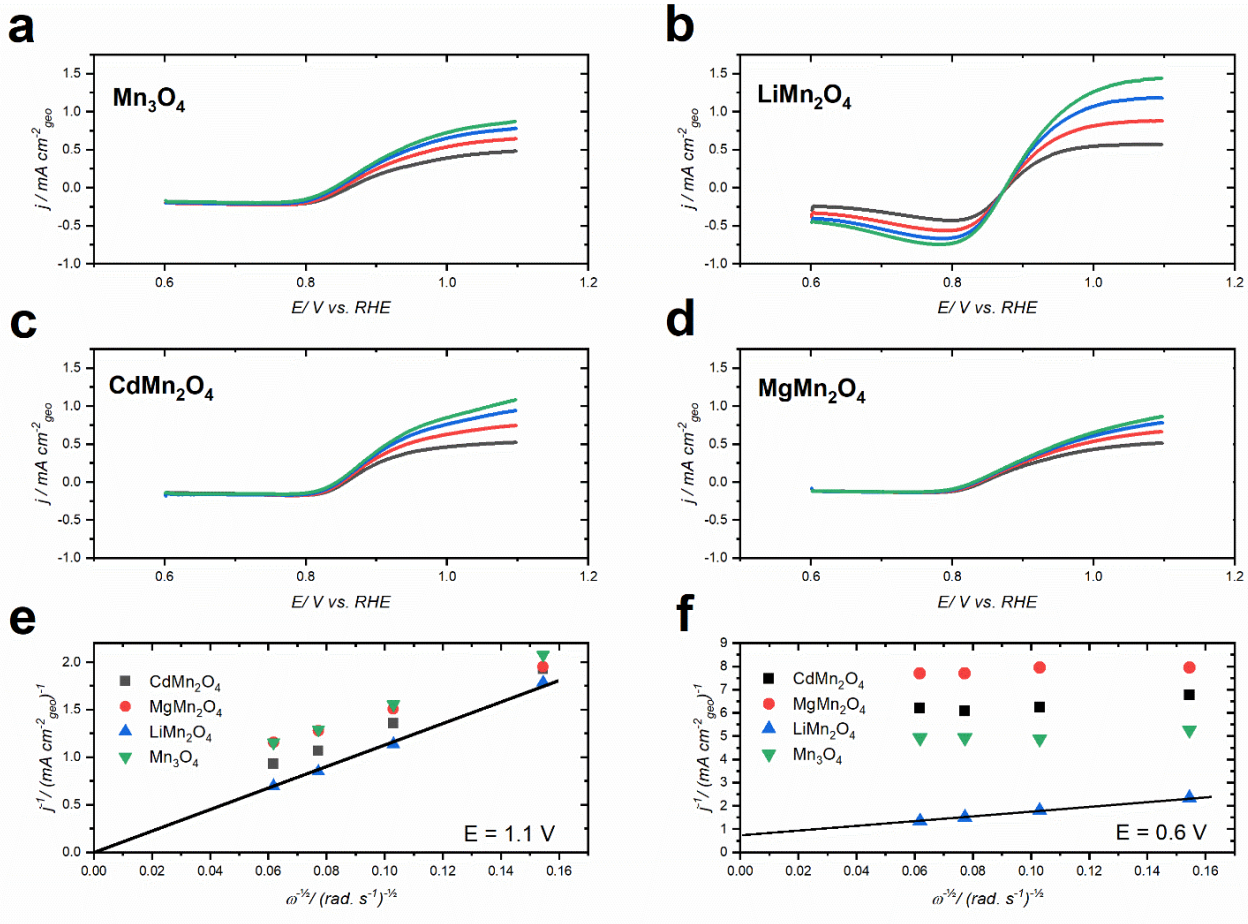

Fig. 47 RDE voltammograms in N_2-saturated 1 M NaOH + 0.84 mM H_2O_2 at 10 mV s^{-1} for GC supported thin films of Mn_3O_4, $LiMn_2O_4$, $CdMn_2O_4$, $MgMn_2O_4$ (a-d). Loadings are 91 μg cm^{-2} oxide + 91 μg cm^{-2} carbon. Color codes: 400 (black), 900 (red), 1600 (blue), 2500 (green) rpm. Currents are normalized to the electrode geometric area and corrected to the background currents measured in the H_2O_2-free electrolyte. Koutecký–Levich plots of the (e) anodic (at 1.1 V vs RHE) currents and (f) cathodic (at 0.6 V vs RHE) currents extracted from RDE voltammograms in N_2-purged 1 M NaOH with 0.84 mM H_2O_2 for Mn_3O_4 (green), $LiMn_2O_4$ (blue), $MgMn_2O_4$ (red), $CdMn_2O_4$ (black).

Interestingly, for $LiMn_2O_4$, cathodic HPRR currents increase slightly with the electrode rotation rate, suggesting an improvement in the kinetics of the above-mentioned chemical step compared to other spinels. The mixed potential exhibits higher value (0.88 V vs RHE) than other

spinel samples studied in this work. Moreover, instead of a plateau, cathodic currents exhibit a maximum at potentials slightly below that of the red-ox transition (cf. CVs in Fig. 45 a). From this we conclude that the higher ORR kinetic currents may be attributed to the improvement in the kinetics of the chemical O–O bond breaking step on the $LiMn_2O_4$ surface and probably also to a faster Mn(IV/III) interfacial red-ox transition. We will come back to this in section 3.3.3 when analyzing the surface state of spinels.

3.3.3. Post-mortem XPS study of AMn_2O_4 spinels after various treatments

Very distinct behavior of $LiMn_2O_4$ in the ORR and especially in the HPRR along with its significantly more negative E_f value are suggestive of its rather different surface state compared to other AMn_2O_4 samples. In this section we will analyze XPS spectra of (i) pristine samples along with those subjected to various treatments, notably (ii) suspending and sonicating them in water (an imminent step in the thin RDE film preparation), (iii) after suspending, immobilization on the support and soaking them in the supporting 1 M NaOH for 6 hours under the open-circuit conditions (open-circuit potentials for Mn_3O_4, $MgMn_2O_4$, $CdMn_2O_4$, $LiMn_2O_4$, were close to each other and equal to 0.90, 0.92, 0.93, and 0.93 V vs RHE, correspondingly), and (iv) after suspending, immobilization on the support and application of 10 potential cycles in the interval from 0.6 to 1.15 V vs. RHE (for comparison of the 1st and the 10th cycle the reader is referred to Fig. S1 in the ANNEX). The XPS study was complemented with electrochemical measurements to detect eventual changes in the ORR activity following 6h soaking in 1M NaOH (for comparison of the ORR polarization curves before and after 6h soaking the reader is referred to Fig. 48). In addition, changes in the shape of CVs were analyzed in the course of 20 hours soaking in 1M NaOH (Fig. 49).

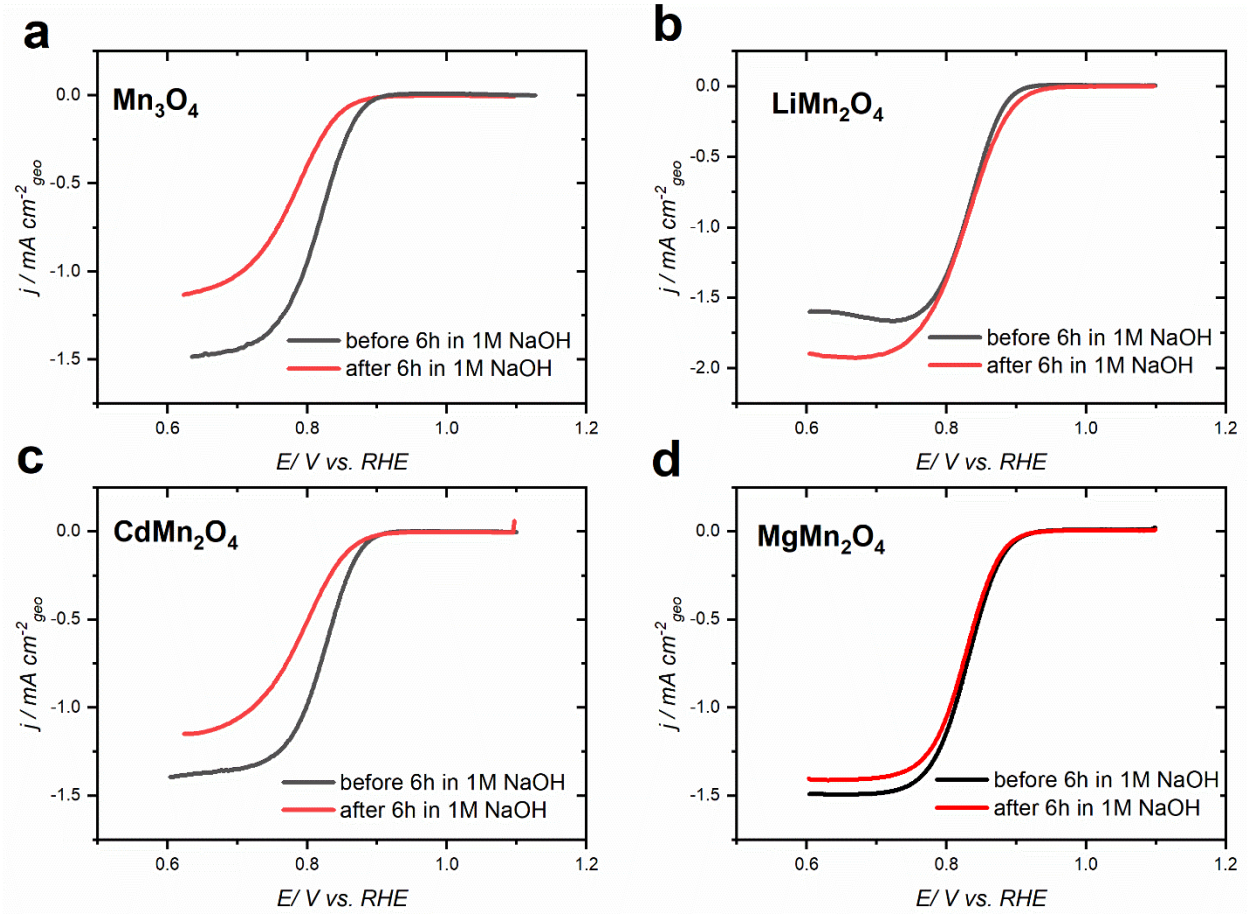

Fig.48. RDE voltammograms acquired in O_2-saturated 1 M NaOH at 900 rpm and 10 mV s^{-1} for Mn_3O_4, $LiMn_2O_4$, and $CdMn_2O_4$ and $MgMn_2O_4$ samples before (black curve) and after (red curve) 6 h soaking in 1M NaOH. Loadings are 91 μg cm^{-2} oxide + 91 μg cm^{-2} carbon. Currents are normalized to the electrode geometric area and corrected to the background currents measured in the N_2 atmosphere.

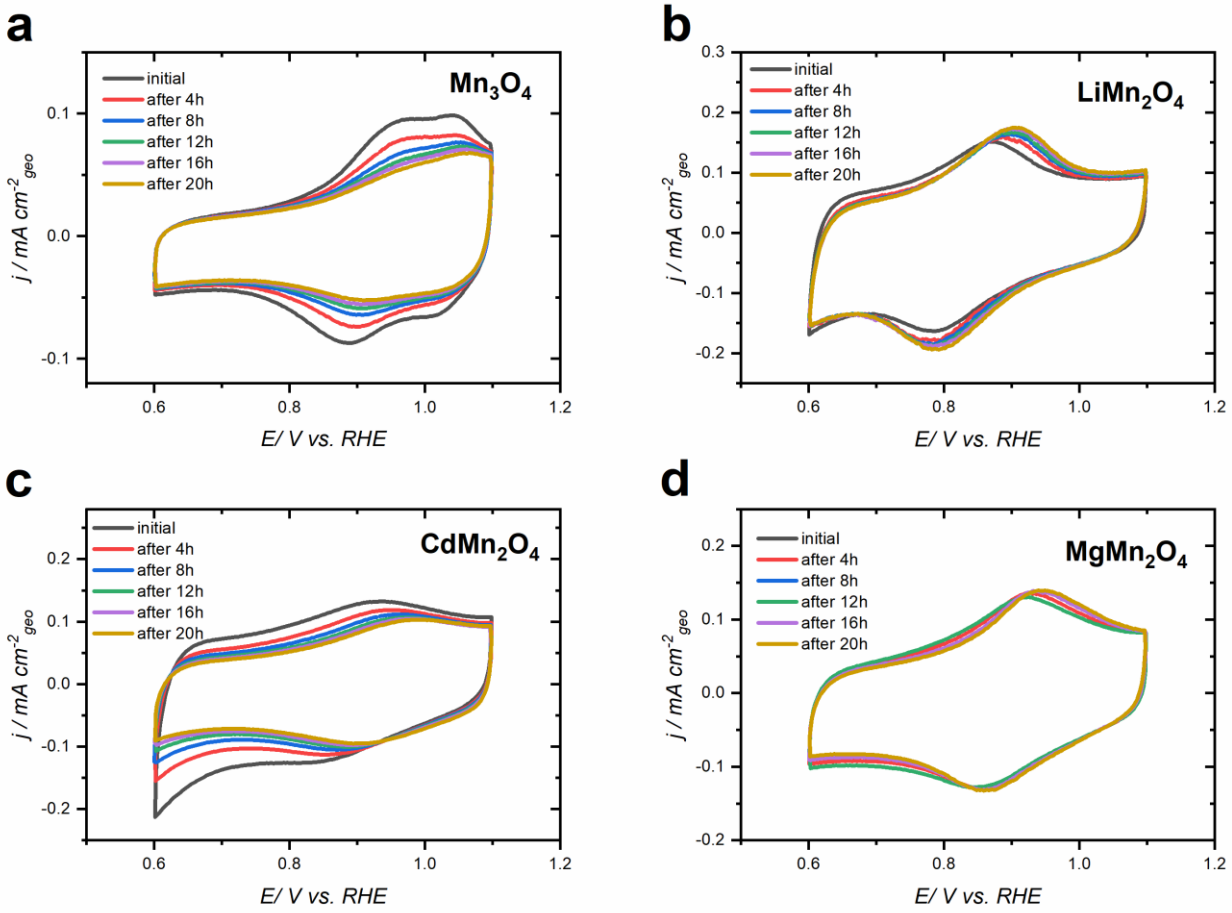

Fig. 49 CVs of Mn_3O_4 (a), $LiMn_2O_4$ (b), $CdMn_2O_4$ (c) and $MgMn_2O_4$ (d) measured at 10 mV s^{-1} every 4 hours during the day. Electrodes between the measurements were kept in 1M NaOH at OCP (open circuit potential) conditions. Loadings are 91 µg cm^{-2} oxide + 91 µg cm^{-2} carbon. CVs corrected to the background currents measured on Sibunit carbon under the same conditions.

Table 6 Peak position and charges for the cathodic and anodic parts of the CVs for oxide/carbon compositions measured at 10 mV s^{-1} before (initial) and after soaking in 1 M NaOH solution for 20 h.

	E_c V vs. RHE		***E_a V vs. RHE***		**Q_c µC cm^{-2} oxide**		**Q_a µC cm^{-2} oxide**	
	Initial	**After 20 h**	**initial**	**After 20 h**	**initial**	**After 20 h**	**initial**	**After 20 h**
Mn_3O_4	--[1]	--[1]	--[1]	--[1]	187	162	183	117
$LiMn_2O_4$	0.79	0.79	0.87	0.91	260	294	254	268
$CdMn_2O_4$	0.85	0.91	0.93	0.99	156	99	148	99
$MgMn_2O_4$	0.84	0.86	0.92	0.94	229	214	215	209

We now turn to the discussion of XP spectra after various treatments. Mn3s and Mn3p lines are known to be the most sensitive to the oxidation state of Mn [47]. However, Mn3s line overlaps with the Au4f peak (note that gold foil was used as the support for the powder samples for spectroscopic studies), so we limit the analysis of spectra to the Mn3p line. Representative Mn3p XP spectra acquired with a laboratory spectrometer are shown in Fig. 50, while the surface composition calculated from the XPS analyses is represented in Table 7. XP spectra acquired at ISSIS station of Bessy-II synchrotron facility are shown in Fig. S3 of the Annex.

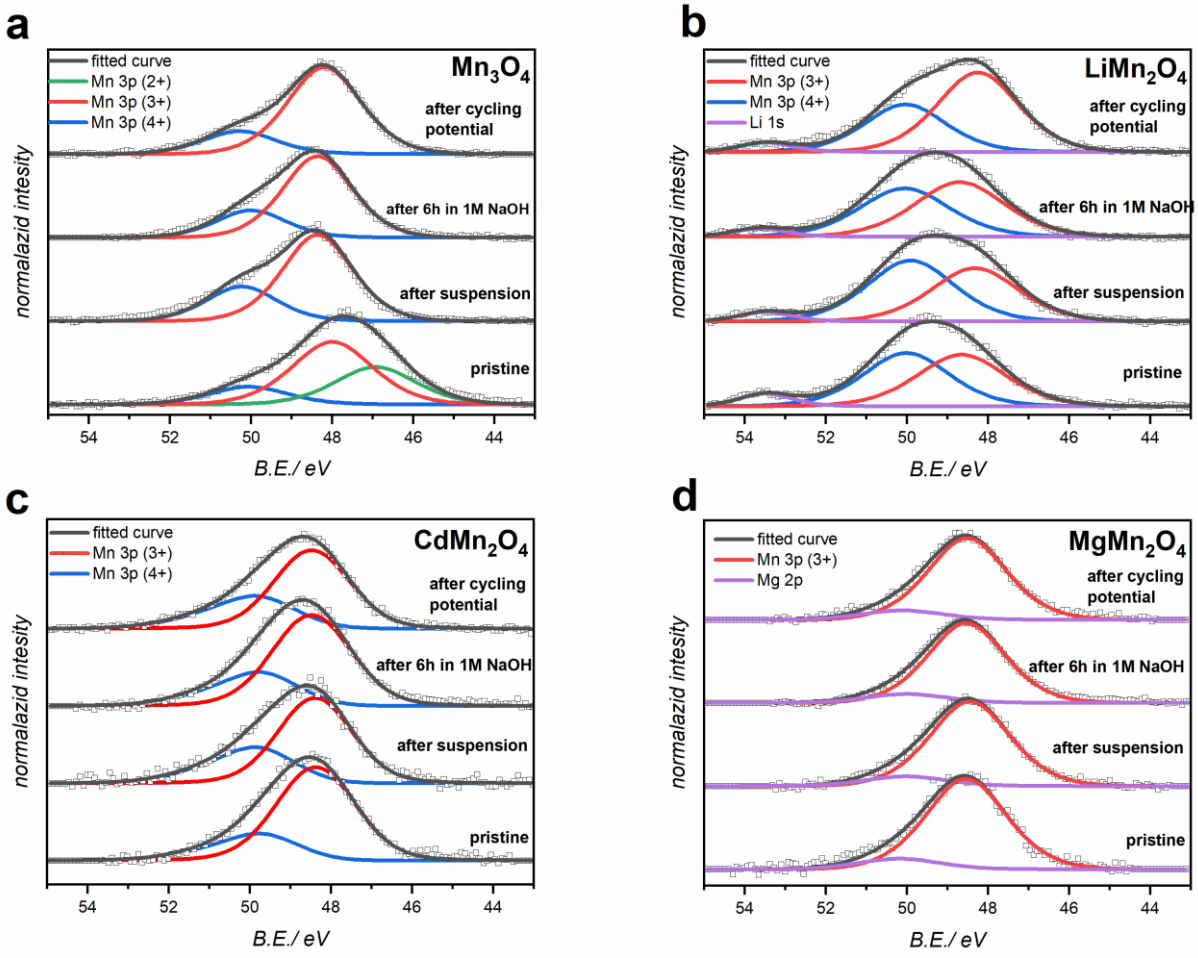

Fig. 50 Mn3p XP spectra for Mn_3O_4 (a), $LiMn_2O_4$ (b), $CdMn_2O_4$ (c) and $MgMn_2O_4$ (d) (pristine samples and after preparation of aqueous suspension using ultrasound, soaking in 1M NaOH for 6 h and after 10 cycles of CV in the potential interval from 0.6 to 1.15 V vs. RHE. Black solid line corresponds to deconvolution of the spectra assuming the presence of Mn(II) (green), Mn(III) (red) and Mn(IV) (blue). Spectra are collected with a laboratory Thermo VG-Microtech spectrometer with Al-cathode (excitation energy 1486.6 eV).

Table 7. The fractions of Mn in different oxidation states, the average oxidation state of Mn calculated from these values, and the A-cation content (x in $A_xB_2O_4$) in the near-surface layer calculated from the laboratory XP spectra.

Oxide	**Treatment**	**A-cation content**	**Fraction of Mn^{z+}**			**Average Mn oxidation state**
			Mn^{2+}	**Mn^{3+}**	**Mn^{4+}**	
Mn_3O_4	(i) pristine	--	0.3 ± 0.05	0.5 ± 0.05	0.2 ± 0.05	+2.9 ± 0.1
	(ii) suspension	--	--	0.7 ± 0.05	0.3 ± 0.05	+3.3 ± 0.1
	(iii) 6h in 1M NaOH	--	--	0.75 ± 0.05	0.25 ± 0.05	+3.25 ± 0.1
	(iv) CV	--	--	0.8 ± 0.05	0.2 ± 0.05	+3.2 ± 0.1
$MgMn_2O_4$	(i) pristine	1 ± 0.1	--	1.0 ± 0.1	--	+3.0 ± 0.1
	(ii) suspension	1 ± 0.1	--	1.0 ± 0.1	--	+3.0 ± 0.1
	(iii) 6h in 1M NaOH	0.95 ±0.1	--	1.0 ± 0.1	--	+3.0 ± 0.1
	(iv) CV	1.0 ± 0.1	--	1.0 ± 0.1	--	+3.0 ± 0.1
$LiMn_2O_4$	(i) pristine	0.9 ± 0.15	--	0.50 ± 0.05	0.5 ± 0.05	+3.5 ± 0.1
	(ii) suspension	0.6 ± 0.1	--	0.47 ± 0.05	0.53 ± 0.05	+3.53 ± 0.1
	(iii) 6h in 1M NaOH	0.5 ± 0.1	--	0.53 ± 0.05	0.47 ± 0.05	+3.47 ± 0.1

	(iv) CV	0.6 ± 0.1	--	0.63 ± 0.05	0.37 ± 0.05	+3.37 ± 0.1
$CdMn_2O_4$	(i) pristine	1.0 ± 0.1	--	0.8 ± 0.05	0.2 ± 0.05	+3.2 ± 0.1
	(ii) suspension	0.9 ± 0.1	--	0.7 ± 0.05	0.3 ± 0.05	+3.3 ± 0.1
	(iii) 6h in 1M NaOH	1.1 ± 0.1	--	0.75 ± 0.05	0.25 ± 0.05	+3.25 ± 0.1
	(iv) CV	0.36 ± 0.1	--	0.7 ± 0.05	0.3 ± 0.05	+3.3 ± 0.1

We start our discussion with the analysis of the Mn_3O_4 sample. Already for the pristine sample, the surface composition significantly deviates from the Mn(II):Mn(III)=1:2 expected for Mn spinel, with the average Mn oxidation state +2.9 against the expected +2.67 and the appearance of Mn(IV). This result suggests that the surface of Mn_3O_4 exposed to air is oxidized resulting in a decrease of the ratio of Mn(II) and Mn(III), and in the formation of Mn(IV) in the near-surface layer. The latter is not surprising since Mn_3O_4 is known to oxidize through the formation of Mn_5O_8 [48,49], which contains Mn(II) and Mn(IV) cations only [50]. Noticeable change of the oxidation state of Mn at the surface is further confirmed by synchrotron-based XP spectra, where Mn(II) could not be detected at all (Fig. S3 of the Annex). This is explained by the significantly smaller analysis depth in the latter case. Indeed, the mean-free path is 2.67 nm for laboratory spectrometer and 1.40 nm for synchrotron-based XPS at kinetic energy of 450 eV. Contact of Mn_3O_4 with either water (in the course of the suspension preparation) or 1 M aqueous NaOH solution leads to complete disappearance of Mn(II) in the near-surface region (in Fig. 50 a this can be seen from a significant shift of the Mn3p line maximum to the higher energies for Mn_3O_4). The observed changes are related to the instability of Mn(II) at the surface, in agreement with the Pourbaix diagram. This is also seen from the open circuit potential (note that 0.90 V vs RHE for Mn_3O_4 is above the stability interval of Mn_3O_4 according to Pourbaix diagram [51]). Potential cycling in the interval from 0.6 to 1.15 V results in no further change of the Mn oxidation state (Table 7). To sum up, XPS data evidence significant deviation of the Mn_3O_4 surface composition compared to the stoichiometric one. This surface transformation is accompanied by changes in the shape of CVs (Fig. 51 a), by a pronounced disbalance of cathodic and anodic charges (Q_c/Q_a) calculated

from CVs (Table 8), and a decrease of the ORR activity (*cf*. RDE voltammograms acquired in O_2-saturated 1M NaOH before and after 6 h soaking in 1M NaOH (Fig. 48).

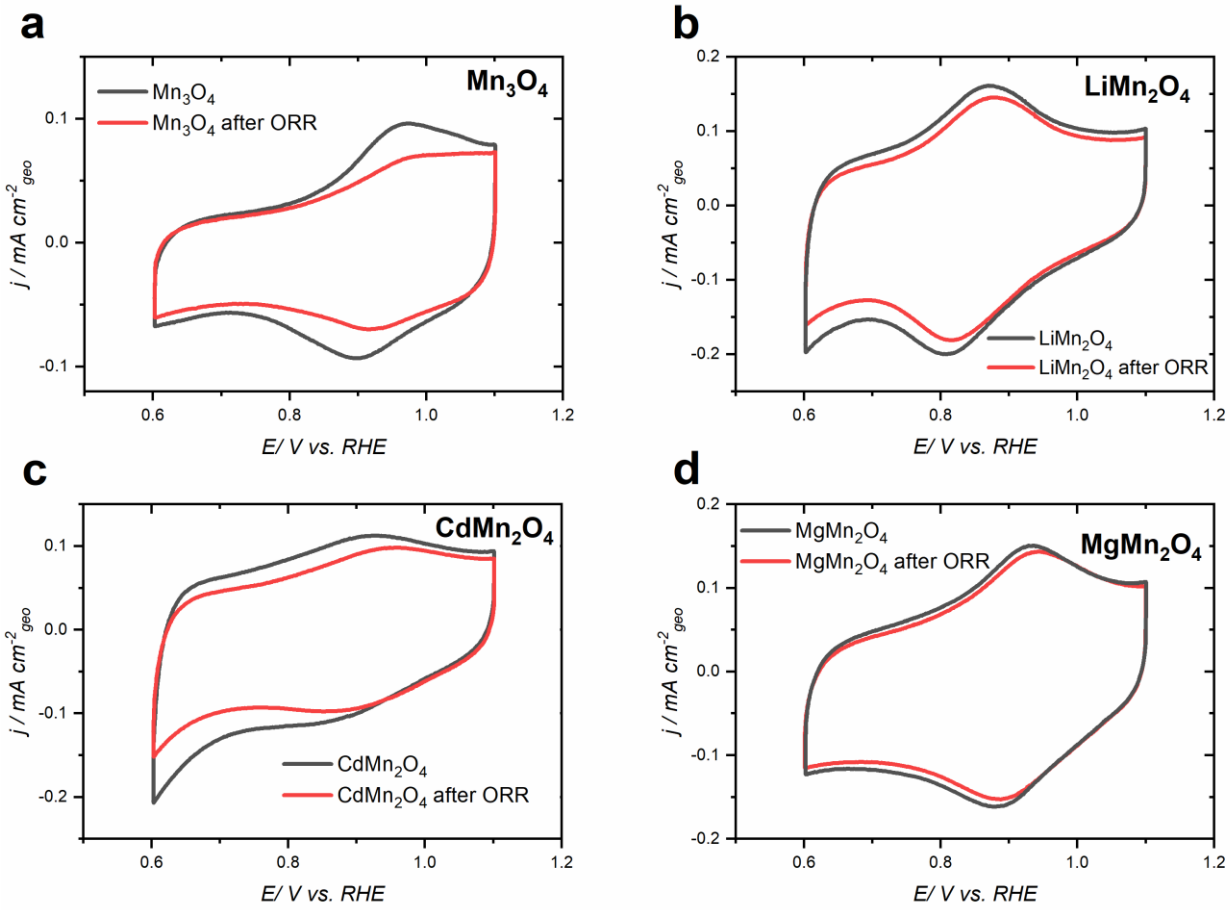

Fig. 51 CVs in N_2-saturated 1 M NaOH in the potential interval from 0.6 to 1.15 V vs. RHE for Mn_3O_4, $LiMn_2O_4$, $CdMn_2O_4$ and $MgMn_2O_4$ samples before (black curve) and after (red curve) ORR experiments. Loadings are 91 μg cm^{-2} oxide and 91 μg cm^{-2} carbon. Currents are normalized to the electrode geometric area. In each case the last CV acquired after ten subsequent cycles is shown.

Table 8 Ratio of cathodic (Q_c) and anodic (Q_a) charges and variation ($\Delta Q_a/Q_a$ and $\Delta Q_c/Q_c$, in %) of anodic and cathodic parts of CVs obtained by integration of CVs and formal potential (E_f) for samples before and after ORR measurements (Fig. 51).

	E_f V vs. RHE before ORR	**E_f V vs. RHE after ORR**	**Q_c/Q_a before ORR**	**Q_c/Q_a after ORR**	**$\Delta Q_a/Q_a$ %**	**$\Delta Q_c/Q_c$ %**
Mn_3O_4	0.93	0.95	1.03	1.07	20.4	17.1
$LiMn_2O_4$	0.83	0.84	1.03	1.03	12.1	12.0
$CdMn_2O_4$	0.89	0.91	1.05	1.09	18.2	15.5
$MgMn_2O_4$	0.91	0.91	1.01	1.02	5.8	4.9

In order to reveal the structure of the surface layer, XRPD analysis was performed after soaking a Mn_3O_4 powder in 1 M NaOH for 2 weeks. XRPD patterns (not shown) did not evidence any new phase formation after two weeks of the NaOH soaking suggesting that the bulk Mn_3O_4 spinel structure was preserved. However, after 1 year soaking in 1M NaOH peaks corresponding to $Na_xMnO_2 \cdot yH_2O$ birnessite phase could be clearly observed in the XPRD pattern, while other studied Mn spinels show no signs of degradation (Fig. 52).

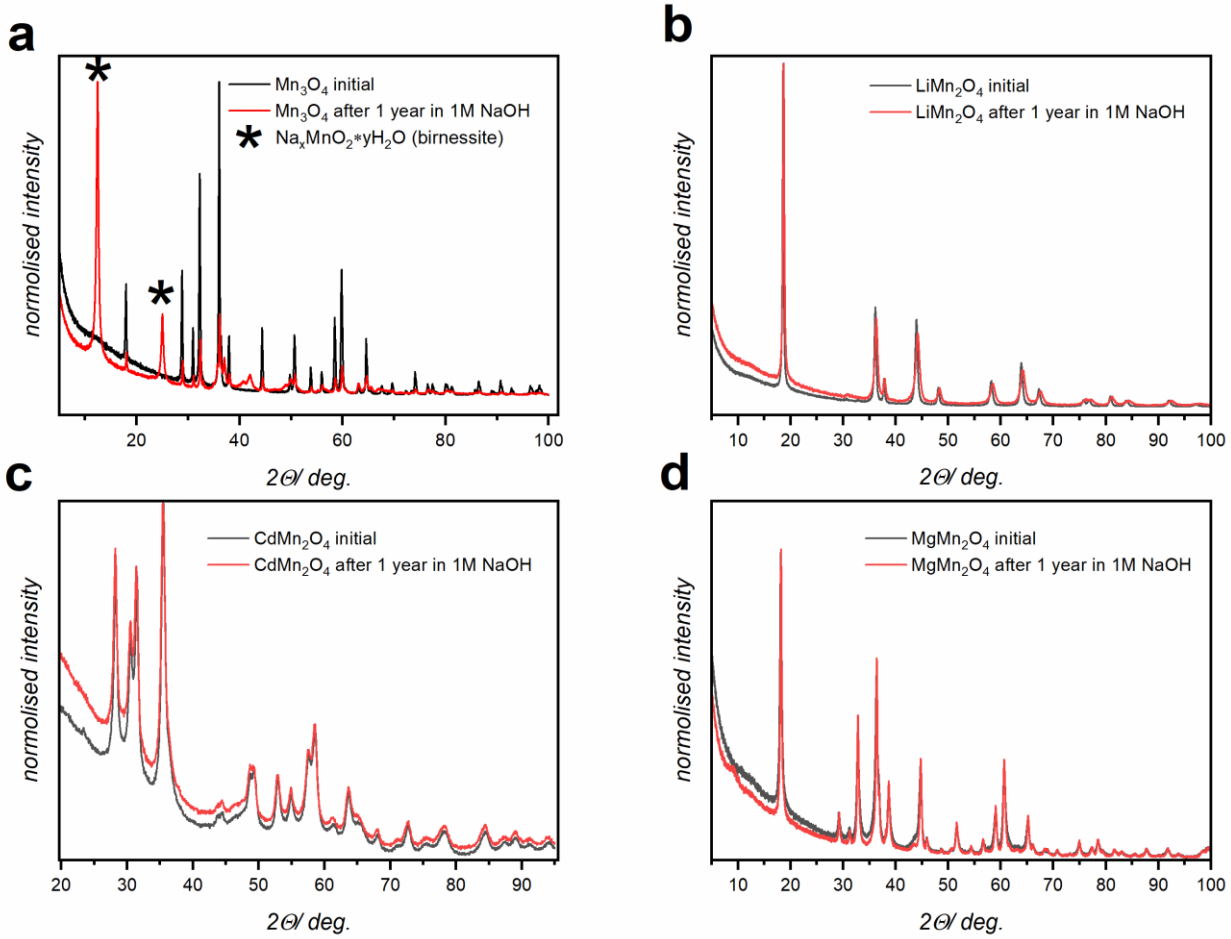

Fig. 52 XRPD of patterns Mn_3O_4 (a), $LiMn_2O_4$ (b), $CdMn_2O_4$ (c), $MgMn_2O_4$ (d) before (black) and after (red) soaking in 1 M NaOH for 1 year.

Combined evidence from XPS (disappearance of Mn(II) from the near-surface region), electrochemistry (changes in the CV following either Mn_3O_4 soaking at OCP or potential cycling in 1 M NaOH), and XRPD (after prolonged soaking in 1 M NaOH) allows us to conclude that the near-surface layers of Mn_3O_4 experience phase transformation in alkaline electrolyte (in the presence of oxygen) and upon potential cycling (in the interval from 0.6 to 1.15 V vs RHE). Indeed, recent publications evidenced spinel-birnessite phase transition occurring during aqueous battery cycling [52–54]. Literature data suggest formation of a layered birnessite structure induced by Mn(II) dissolution and Mn(III) oxidation to Mn(IV) and occurring through crystal water

intercalation. Absence of Na1s in the XP spectra of Mn_3O_4 after different treatments (not shown) suggests that early stages of spinel degradation occur through water rather than sodium ion intercalation. This significant structural transformation accounts for the observed decay of the ORR activity and indicates that Mn_3O_4 cannot be considered as a viable ORR catalyst.

Isovalent replacement of Mn(II) cations by Mg(II) greatly increased stability of the spinel structure. Indeed, XPS spectra did not show any changes either in the Mn oxidation state (which did not deviate from the expected Mn(III)) or in the Mg stoichiometric ratio following various treatments (Fig. 50, Table 7). The spectroscopic data are corroborated by the electrochemical experiments which did not evidence any decrease of the ORR activity after 6h soaking in 1 M NaOH (Fig. 48 d). Changes in the shape of CV upon 20 h soaking in NaOH, albeit noticeable (Fig. 49 d), were much smaller than for any other sample examined in this work (see formal potentials and charges in Table 6). Charge disbalance between the anodic and cathodic branch of CV (Table 8) was negligible (not exceeding 5 %), all of the above confirming that replacement of Mn(II) by red-ox inactive Mg(II) is a pertinent approach for stabilizing Mn spinel against degradation. This is in accordance with the highest thermodynamic stability of this spinel mentioned above. XRPD data confirm high stability of $MgMn_2O_4$ after 1 year soaking in 1 M NaOH (Fig. 52. d).

In contrast, isovalent replacement of Mn(II) with a larger Cd(II) cation destabilizes the spinel structure. Indeed, based on the thermodynamic data $CdMn_2O_4$ has the smallest standard formation enthalpy among the studied AMn_2O_4 spinels (see Introduction, section 3.1). This is not surprising since from the spinel crystal structure stability map it follows that $CaMn_2O_4$ with the next largest after cadmium cation calcium (r_{Cd2+}=1.09 Å, r_{Ca2+}= 1.14 Å for CN=6), does not have the spinel structure [55]. According to XPS, the surface composition of $CdMn_2O_4$ does not show noticeable changes when the sample is exposed either to water or to 1 M NaOH. However, potential cycling in the interval from 0.6 to 1.15 V vs RHE results in the loss of Cd cations from the surface. The asymmetry of CVs (*cf.* cathodic 'tails' discussed in section 3.3.2.1), lets us suppose that deintercalation of Cd from the tetrahedral sites of the spinel is concomitant to the redox transition of Mn cations. These compositional changes lead to significant changes in the CV (Fig. 51 c) and to a decrease of the ORR activity (Fig. 48 c). According to Table 7, the chemical composition of the near-surface layers after the potential cycling corresponds to the formula $Cd_{0.36}Mn_2O_4$. It can be noted that if the spinel crystal structure is preserved, Cd removal from the lattice should lead to an increase of the average Mn oxidation state. However, XPS data do not evidence noticeable change of the oxidation state of Mn cations (Table 7). Even if Cd is replaced by protons from water (note that we did not observe Na1s line in the XP spectra suggesting that sodium cation is not intercalated in $CdMn_2O_4$), Mn(III) cations must be partly oxidized to Mn(IV) to preserve the spinel structure. Since this is not the case (see Table 7), we assume that the spinel structure in the near-

surface region degrades and transforms into another structure. However, the available data does not allow us to identify this new surface phase. Note that even after 1 year soaking in 1 M NaOH we were unable to observe any new phase formation with XRPD (Fig. 52 c).

Heterovalent replacement of Mn(II) by lithium cation resulted in an increase of Mn formal oxidation state in $LiMn_2O_4$ up to +3.5. NEXAFS (Fig. 41) and XPS data (Fig. 50, Table 7) for the pristine $LiMn_2O_4$ sample are in excellent agreement suggesting 50% Mn(III) + 50%Mn(IV) on the surface, even if one cannot exclude small contribution Mn(II) suggested in Ref. [56]. It is interesting to note that Schönewald et al. [57], using EELS, observed formation of a thin (below 3 nm thick) shell of reduced oxide (Mn average oxidation state 2.93) surrounding an oxidized core (Mn average oxidation state 3.82) for a commercial $LiMn_2O_4$ material. The authors attributed this to the presence of tetrahedral defects in the shell. However, our XPS data (both acquired with laboratory spectrometer and synchrotron-based XPS) allow us to exclude formation of an anomalously reduced oxide layer on $LiMn_2O_4$ synthesized in this work.

Li content on the surface of the pristine and differently treated $LiMn_2O_4$ was estimated from the Li1s peak observed at 53.7±0.2 eV. This Li1s BE value is in good agreement with Refs. [58] where the BE scale was calibrated against the Au4f line (87.6 eV), but lower than in Ref. [59], where calibration was performed against the C1s peak (set at 285.0 eV[3]). It should be kept in mind that low photoionization cross section of the Li1s line as well as its overlap with the Mn3p line result in a significant analysis error. Nevertheless, both laboratory and synchrotron-based XPS data[4] (acquired in two series of independent measurements) provide evidence regarding washing of lithium out from the near-surface layers after all treatments, even after the preparation of suspension (Fig. 50, Fig. S3 of the Annex and Table 7). This is not surprising since $LiMn_2O_4$ is known to be a candidate cathode material for lithium-ion batteries due to fast diffusion of lithium cations in a three-dimensional spinel structure. Delithiation of $LiMn_2O_4$ has been reported in previous publications. For example, delithiation in acid (0.1 M HNO_3 solution) was used by Wei et al. [27] to obtain $Li_{0.74}Mn_2O_4$ from $LiMn_2O_4$ under open circuit after 2 h sonication. More or less reversible cathodic lithiation was observed in alkaline LiOH solutions above 0 V vs. RHE [61], while anodic delithiation was reported below the 'onset' of the OER [62].

Instability of $LiMn_2O_4$ in an aqueous solution is likely to be related to a very high solvation energy of Li^+ in the aqueous media. Under all treatments Li content at the surface stabilizes at x=0.5-0.6 (Table 7). Note however that loss of Li only leads to small changes in the Mn oxidation state (Fig. 50, Table 7 and Fig. S3 b in the Annex). For example, after CV the Mn oxidation state

[3] In this work the C1s peak was at 284.0 eV.

[4] Note that the ratio of the ionization cross sections of Li1s and Mn2p (the ionization cross-sections were retrieved from Ref. [60]) increases by a factor of two when the excitation energy changes from 1486.6 eV (laboratory XPS spectrometer) to 500 eV (synchrotron-based XPS)

slightly decreases down to +3.37. A simultaneous decrease of Li content and Mn oxidation state can happen either in case of a complete change of the structure of the near-surface layers (as assumed above for $CdMn_2O_4$) or in case of the lithium ion replacement by protons resulting in a $Li_{1-x}Mn_2O_{4-y}OH_y$ near-surface composition (with x~0.5) with a partial replacement of oxygen by OH^-. There are several examples of compounds with a replacement of oxygen by OH^- including well-known orthorhombic modification of Cu-based mineral atacamite $Cu_2Cl(OH)_3$ with a spinel-related structure, where all tetrahedral sites are empty [63,64]. Another example is β-MnO_2 (Pyrolusite) and α-MnOOH (Manganite) both having a rutile crystal structure. Given minor changes of either CVs in O_2-free electrolyte (see Fig. 51 b) or the ORR activity after different treatments (Figure 48 b) we conclude that the spinel structure of $LiMn_2O_4$ is likely to be preserved and the loss of lithium ions to be compensated by the proton intercalation. This hypothesis is supported by the literature data, evidencing that Li^+ can be easily exchanged with proton not only in acidic but also in neutral and alkaline aqueous electrolytes [65,66]. Proton intercalation may account for the changes observed in CVs of $LiMn_2O_4$ upon scan rate variation (Fig. 43). Rapid proton intercalation/deintercalation is likely to account for fast Mn(IV/III) transition at the surface and in the near-surface layers and high CV charge observed for $LiMn_2O_4$ even at high scan rates (see Table 5). Faster Mn(IV/III) red-ox transition (compared to other spinel oxides studied in this work) may also explain faster HPRR/HPOR on $Li_{1-x}Mn_2O_{4-y}OH_y$ and relatively high ORR kinetics despite its low formal potential. This hypothesis is supported by comparison of Fig. 45 d and f showing that for $MgMn_2O_4$ the ORR current becomes noticeable at potential corresponding to the redox peak, while for $Li_{1-x}H_xMn_2O_4$ the ORR begins at potential positive of the redox peak. Finally, it is worth mentioning that even after 1 year soaking of $LiMn_2O_4$ in 1 M NaOH we were unable to observe any new phase formation with XRPD (Fig. 52 b).

3.4. Conclusions

Using the rotating disk electrode (RDE) and cyclic voltammetry (CV) techniques, we studied electrochemical behavior, including activity in the oxygen reduction reaction (ORR) in an alkaline solution, of different AMn_2O_4 (A=Mn(II), Mg(II), Li(I) and Cd(II)) oxides with the spinel structure. With the help of post-mortem XPS characterization we demonstrate that the surface of the studied spinels (except for $MgMn_2O_4$) undergoes essential modification not only under potential cycling but also after contacting alkaline solution under open circuit conditions, and even during the electrode preparation.

The widely studied Mn_3O_4 spinel demonstrates the strongest surface modifications. We conclude that Mn(II) at the Mn_3O_4 surface is unstable in the presence of oxygen and is oxidized into Mn(III) and Mn(IV). This transformation is observed already for the dry sample exposed to air and is further enhanced upon its contact with either water or with NaOH electrolyte. Oxidation of Mn(II) results in dramatic catalyst degradation, likely leading to the loss of the spinel structure in the near-surface layers in short-term experiments and complete structure collapse in the long run. Hence, it is risky to include spinel Mn_3O_4 oxide (as well as other Mn(II)-containing oxides) in any structure/composition/ORR activity correlation. This brings us to a conclusion that evaluation of the materials stability must be included as an essential part of the measurement protocol for comparing ORR activities of different materials.

We demonstrated that replacement of Mn(II) in Mn_3O_4 spinel by redox inactive cations is a viable strategy to enhance the stability of Mn spinels during the ORR. However, among the three substituted AMn_2O_4 spinel oxides (A=Li, Cd and Mg), only the $MgMn_2O_4$ spinel has proven to be stable during the ORR [67], while $LiMn_2O_4$ loses lithium ions from the near-surface layers but is likely to preserve its spinel structure through lithium replacement by protons resulting in a $Li_{1-x}Mn_2O_{4-y}OH_y$ composition.

All studied AMn_2O_4 oxides are ORR active, with the $LiMn_2O_4$ and $MgMn_2O_4$ showing the highest activity. However, it should be noticed that specific ORR activity of AMn_2O_4 spinels, being similar to that of the α-MnOOH oxide, is significantly lower than that of α-Mn_2O_3. For all studied spinel oxides the H_2O_2 reduction occurs through a slow chemical step as confirmed by the potential- and rotation-rate independent current in the potential interval from 0.6 to 0.8 V vs RHE. $LiMn_2O_4$ exhibits faster kinetics of the chemical step and higher HPRR activity, which we tentatively attribute to lithium replacement by proton and formation of $Li_{1-x}Mn_2O_{4-y}OH_y$ spinel in the near-surface region.

In agreement with the previous publications [12] this conforms that Mn(IV/III) transition is an essential step of the ORR mechanism. However, its formal potential is not the only parameter determining the ORR activity. The rate of this red-ox transition also likely influences the ORR activity. Another essential factor is the rate constant of the O-O bond breaking [43]. Also important is the number of sites available for electrocatalysis, which can be estimated from the Q_{min} value determined by Trasatti's procedure [38] divided by the charge necessary for recharging of an oxide monolayer. However, for dispersed oxides, such estimates are rough due to their irregular surface faceting. Further advances are expected from studies of model crystallographically orientated oxide films.

3.5. References

[1] Q. Zhao, Z. Yan, C. Chen, J. Chen, Spinels: Controlled Preparation, Oxygen Reduction/Evolution Reaction Application, and beyond, Chemical Reviews. 117 (2017) 10121–10211. https://doi.org/10.1021/acs.chemrev.7b00051.

[2] X.-M. Liu, X. Cui, K. Dastafkan, H.-F. Wang, C. Tang, C. Zhao, A. Chen, C. He, M. Han, Q. Zhang, Recent advances in spinel-type electrocatalysts for bifunctional oxygen reduction and oxygen evolution reactions, Journal of Energy Chemistry. 53 (2021) 290–302. https://doi.org/10.1016/j.jechem.2020.04.012.

[3] J. Kim, W. Ko, J.M. Yoo, V.K. Paidi, H.Y. Jang, M. Shepit, J. Lee, H. Chang, H.S. Lee, J. Jo, B.H. Kim, S.-P. Cho, J. van Lierop, D. Kim, K.-S. Lee, S. Back, Y.-E. Sung, T. Hyeon, Structural Insights into Multi-Metal Spinel Oxide Nanoparticles for Boosting Oxygen Reduction Electrocatalysis, Advanced Materials. 34 (2022) 2107868. https://doi.org/10.1002/adma.202107868.

[4] J. Liu, L. Jiang, T. Zhang, J. Jin, L. Yuan, G. Sun, Activating Mn_3O_4 by Morphology Tailoring for Oxygen Reduction Reaction, Electrochimica Acta. 205 (2016) 38–44. https://doi.org/10.1016/j.electacta.2016.04.103.

[5] Y. Hao, S. Sun, X. Du, J. Qu, L. Li, X. Yu, X. Zhang, X. Yang, R. Zheng, J.M. Cairney, Z. Lu, Boosting Oxygen Reduction Activity of Manganese Oxide Through Strain Effect Caused By Ion Insertion, Small. 18 (2022) 2105201. https://doi.org/10.1002/smll.202105201.

[6] W. Wang, E. Liu, Y. Hu, L. Jiao, P. Kolla, Y. Liu, M. Tang, J. Luo, Q. Sun, S. Chen, Q. Jia, S. Mukerjee, Understanding the ORR Electrocatalysis on Co–Mn Oxides, J. Phys. Chem. C. 125 (2021) 25470–25477. https://doi.org/10.1021/acs.jpcc.1c00104.

[7] Y. Yang, Y. Xiong, M.E. Holtz, X. Feng, R. Zeng, G. Chen, F.J. DiSalvo, D.A. Muller, H.D. Abruña, Octahedral spinel electrocatalysts for alkaline fuel cells, Proceedings of the National Academy of Sciences. 116 (2019) 24425–24432. https://doi.org/10.1073/pnas.1906570116.

[8] G. Kéranguéven, C. Bouillet, V. Papaefthymiou, P.A. Simonov, E.R. Savinova, How key characteristics of carbon materials influence the ORR activity of $LaMnO_3$- and Mn_3O_4-carbon composites prepared by in situ autocombustion method, Electrochimica Acta. 353 (2020) 136557. https://doi.org/10.1016/j.electacta.2020.136557.

[9] F.H.B. Lima, M.L. Calegaro, E.A. Ticianelli, Electrocatalytic activity of manganese oxides prepared by thermal decomposition for oxygen reduction, Electrochimica Acta. 52 (2007) 3732–3738. https://doi.org/10.1016/j.electacta.2006.10.047.

[10] J.S. Lee, G.S. Park, H. Il Lee, S.T. Kim, R. Cao, M. Liu, J. Cho, Ketjenblack carbon supported amorphous manganese oxides nanowires as highly efficient electrocatalyst for oxygen reduction reaction in alkaline solutions, Nano Letters. 11 (2011) 5362–5366. https://doi.org/10.1021/nl2029078.

[11] Y.-C. Zhang, S. Ullah, R. Zhang, L. Pan, X. Zhang, J.-J. Zou, Manipulating electronic delocalization of Mn_3O_4 by manganese defects for oxygen reduction reaction, Applied Catalysis B: Environmental. 277 (2020) 119247. https://doi.org/10.1016/j.apcatb.2020.119247.

[12] A.S. Ryabova, F.S. Napolskiy, T. Poux, S.Ya. Istomin, A. Bonnefont, D.M. Antipin, A. Baranchikov Ye., E.E. Levin, A.M. Abakumov, G. Kéranguéven, E. V. Antipov, G.A. Tsirlina, E.R. Savinova, Rationalizing the Influence of the Mn (IV)/ Mn (III) Red-Ox Transition on the Electrocatalytic Activity of Manganese Oxides in the Oxygen Reduction Reaction, Electrochimica Acta Journa. 187 (2016) 161–172. https://doi.org/10.1016/j.electacta.2015.11.012.

[13] Y. Gorlin, C.-J. Chung, D. Nordlund, B.M. Clemens, T.F. Jaramillo, Mn_3O_4 Supported on Glassy Carbon: An Active Non-Precious Metal Catalyst for the Oxygen Reduction Reaction, ACS Catal. 2 (2012) 2687–2694. https://doi.org/10.1021/cs3004352.

[14] J. Feng, Y. Liang, H. Wang, Y. Li, B. Zhang, J. Zhou, J. Wang, T. Regier, H. Dai, Engineering manganese oxide/nanocarbon hybrid materials for oxygen reduction electrocatalysis, Nano Research. 5 (2012) 718–725. https://doi.org/10.1007/S12274-012-0256-8.

[15] S.K. Bikkarolla, F. Yu, W. Zhou, P. Joseph, P. Cumpson, P. Papakonstantinou, A three-dimensional Mn3O4 network supported on a nitrogenated graphene electrocatalyst for efficient oxygen reduction reaction in alkaline media, Journal of Materials Chemistry A. 2 (2014) 14493–14501. https://doi.org/10.1039/c4ta02279c.

[16] F.H.B. Lima, M.L. Calegaro, E.A. Ticianelli, Investigations of the catalytic properties of manganese oxides for the oxygen reduction reaction in alkaline media, Journal of Electroanalytical Chemistry. 590 (2006) 152–160. https://doi.org/10.1016/j.jelechem.2006.02.029.

[17] C. Liang, H. Wang, K. Huang, S. Lin, W. Liu, K. Bi, M. Lei, Hierarchically Porous - MgMn 2 O 4 Microspheres Assembled with Nanosheets as High Oxygen Reduction Catalyst, (2019). https://doi.org/10.1007/s10562-019-02760-4.

[18] S. Bag, K. Roy, C.S. Gopinath, C.R. Raj, Facile Single-Step Synthesis of Nitrogen-Doped Reduced Graphene Oxide-Mn_3O_4 Hybrid Functional Material for the Electrocatalytic Reduction of Oxygen, ACS Appl. Mater. Interfaces. 6 (2014) 2692–2699. https://doi.org/10.1021/am405213z.

[19] X. Ge, Y. Liu, F.W.T. Goh, T.S.A. Hor, Y. Zong, P. Xiao, Z. Zhang, S.H. Lim, B. Li, X. Wang, Z. Liu, Dual-Phase Spinel $MnCo_2O_4$ and Spinel $MnCo_2O_4$ /Nanocarbon Hybrids for

Electrocatalytic Oxygen Reduction and Evolution, ACS Appl. Mater. Interfaces. 6 (2014) 12684–12691. https://doi.org/10.1021/am502675c.

[20] F. Cheng, J. Shen, B. Peng, Y. Pan, Z. Tao, J. Chen, Rapid room-temperature synthesis of nanocrystalline spinels as oxygen reduction and evolution electrocatalysts, Nature Chem. 3 (2011) 79–84. https://doi.org/10.1038/nchem.931.

[21] A. Bonnefont, A.S. Ryabova, T. Schott, G. Kéranguéven, S.Y. Istomin, E. V. Antipov, E.R. Savinova, Challenges in the understanding oxygen reduction electrocatalysis on transition metal oxides, Current Opinion in Electrochemistry. 14 (2019) 23–31. https://doi.org/10.1016/J.COELEC.2018.09.010.

[22] J.A. Dean, Lange's Handbook of Chemistry, 1999. https://doi.org/10.5370/JEET.2015.10.6.2348.

[23] M. Pourbaix, Atlas of Electrochemical Equilibria in Aqueous Solutions, 1974. https://doi.org/10.4028/www.scientific.net/msf.251-254.143.

[24] R.D. Shannon, Revised effective ionic radii and systematic studies of interatomic distances in halides and chalcogenides, Acta Cryst. A32 (1976) 751–767. https://doi.org/10.1107/S0567739476001551.

[25] A. Navrotsky, O.J. Kleppa, Thermodynamics of formation of simple spinels, Journal of Inorganic and Nuclear Chemistry. 30 (1968) 479–498. https://doi.org/10.1016/0022-1902(68)80475-0.

[26] M. Wang, A. Navrotsky, Thermochemistry of Li1+xMn2−xO4 ($0 \leqslant x \leqslant 1/3$) spinel, Journal of Solid State Chemistry. 178 (2005) 1182–1189. https://doi.org/10.1016/J.JSSC.2004.12.007.

[27] C. Wei, Z. Feng, G.G. Scherer, J. Barber, Y. Shao-Horn, Z.J. Xu, Cations in Octahedral Sites: A Descriptor for Oxygen Electrocatalysis on Transition-Metal Spinels, Advanced Materials. 29 (2017) 1606800. https://doi.org/10.1002/adma.201606800.

[28] J. Zhu, Q. Wu, J. Li, Review And Prospect of Mn_3O_4-Based Composite Materials For Supercapacitor Electrodes, ChemistrySelect. 5 (2020) 10407–10423. https://doi.org/10.1002/slct.202002544.

[29] A.R.C. Bredar, M.D. Blanchet, A.R. Burton, B.E. Matthews, S.R. Spurgeon, R.B. Comes, B.H. Farnum, Oxygen Reduction Electrocatalysis with Epitaxially Grown Spinel $MnFe_2O_4$ and Fe_3O_4, ACS Catal. 12 (2022) 3577–3588. https://doi.org/10.1021/acscatal.1c05172.

[30] K. Bradley, K. Giagloglou, B. E. Hayden, H. Jungius, C. Vian, Reversible perovskite electrocatalysts for oxygen reduction/oxygen evolution, Chemical Science. 10 (2019) 4609–4617. https://doi.org/10.1039/C9SC00412B.

[31] N. Ramaswamy, S. Mukerjee, Fundamental Mechanistic Understanding of Electrocatalysis of Oxygen Reduction on Pt and Non-Pt Surfaces: Acid versus Alkaline Media, Advances in Physical Chemistry. 2012 (2012) e491604. https://doi.org/10.1155/2012/491604.

[32] A.S. Ryabova, S.Y. Istomin, K.A. Dosaev, A. Bonnefont, J. Hadermann, N.A. Arkharova, A.S. Orekhov, R.P. Sena, V.A. Saveleva, G. Kéranguéven, E. V. Antipov, E.R. Savinova, G.A. Tsirlina, Mn_2O_3 oxide with bixbyite structure for the electrochemical oxygen reduction reaction in alkaline media: Highly active if properly manipulated, Electrochimica Acta. 367 (2021) 137378. https://doi.org/10.1016/J.ELECTACTA.2020.137378.

[33] R. Qiao, T. Chin, S.J. Harris, S. Yan, W. Yang, Spectroscopic fingerprints of valence and spin states in manganese oxides and fluorides, Current Applied Physics. 13 (2013) 544–548. https://doi.org/10.1016/j.cap.2012.09.017.

[34] Y. Suzuki, H. Hino, M. Kotsugi, K. Ono, Automated estimation of materials parameter from X-ray absorption and electron energy-loss spectra with similarity measures, Npj Computational Materials. 5 (2019) 1–7. https://doi.org/10.1038/s41524-019-0176-1.

[35] M. Risch, K.A. Stoerzinger, B. Han, T.Z. Regier, D. Peak, S.Y. Sayed, C. Wei, Z. Xu, Y. Shao-Horn, Redox Processes of Manganese Oxide in Catalyzing Oxygen Evolution and Reduction: An in Situ Soft X-ray Absorption Spectroscopy Study, J. Phys. Chem. C. 121 (2017) 17682–17692. https://doi.org/10.1021/acs.jpcc.7b05592.

[36] G. Kéranguéven, J. Faye, S. Royer, S.N. Pronkin, Electrochemical properties and capacitance of Hausmannite Mn_3O_4 – carbon composite synthesized by in situ autocombustion method., Electrochimica Acta. 222 (2016) 755–764. https://doi.org/10.1016/j.electacta.2016.11.032.

[37] T. Tsumura, K. Tsumori, G. Shimizu, M. Toyoda, Electrochemical properties of spinel-type manganese oxide/porous carbon nanocomposite powders in 1M KOH aqueous solution, Journal of Physics and Chemistry of Solids. 73 (2012) 237–244. https://doi.org/10.1016/j.jpcs.2011.10.036.

[38] S. Trasatti, O.A. Petrii, Real surface area measurements in electrochemistry, Pure and Applied Chemistry. 63 (1991) 711–734. https://doi.org/10.1351/pac199163050711.

[39] S. Ardizzone, G. Fregonara, S. Trasatti, "Inner" and "outer" active surface of RuO_2 electrodes, Electrochimica Acta. 35 (1990) 263–267. https://doi.org/10.1016/0013-4686(90)85068-X.

[40] P. Strobel, F. Le Cras, L. Seguin, M. Anne, J.M. Tarascon, Oxygen Nonstoichiometry in Li–Mn–O Spinel Oxides: A Powder Neutron Diffraction Study, J. of Solid State Chemistry. 135 (1998) 132–139. https://doi.org/10.1006/jssc.1997.7611.

[41] P. Strobel, G. Rousse, A. Ibarra-Palos, C. Masquelier, Disproportionation of stoichiometric $LiMn_2O_4$ on annealing in oxygen, Journal of Solid State Chemistry France. 177 (2004) 1–5. https://doi.org/10.1016/S0022-4596(03)00189-0.

[42] J.M. Tarascon, F. Coowar, T.N. Bowmer, G. Amatucci, W.R. McKinnon, D. Guyomard, Synthesis conditions and oxygen stoichiometry effects on Li insertion into the spinel $LiMn_2O_4$, Journal of the Electrochemical Society; (United States). 141:6 (1994). https://doi.org/10.1149/1.2054941.

[43] A.S. Ryabova, A. Bonnefont, P. Zagrebin, T. Poux, R. Paria Sena, J. Hadermann, A.M. Abakumov, G. Kéranguéven, S.Y. Istomin, E.V. Antipov, G.A. Tsirlina, E.R. Savinova, Study of Hydrogen Peroxide Reactions on Manganese Oxides as a Tool To Decode the Oxygen Reduction Reaction Mechanism, ChemElectroChem. 3 (2016) 1667–1677. https://doi.org/10.1002/celc.201600236.

[44] V.A. Nikitina, A.A. Kurilovich, A. Bonnefont, A.S. Ryabova, R.R. Nazmutdinov, E.R. Savinova, G.A. Tsirlina, ORR on Simple Manganese Oxides: Molecular-Level Factors Determining Reaction Mechanisms and Electrocatalytic Activity, J. Electrochem. Soc. 165 (2018) J3199. https://doi.org/10.1149/2.0261815jes.

[45] T. Poux, A. Bonnefont, G. Kéranguéven, G.A. Tsirlina, E.R. Savinova, Electrocatalytic Oxygen Reduction Reaction on Perovskite Oxides: Series versus Direct Pathway, ChemPhysChem. 15 (2014) 2108–2120. https://doi.org/10.1002/cphc.201402022.

[46] F.D. Speck, P.G. Santori, F. Jaouen, S. Cherevko, Mechanisms of Manganese Oxide Electrocatalysts Degradation during Oxygen Reduction and Oxygen Evolution Reactions, J. Phys. Chem. C. 123 (2019) 25267–25277. https://doi.org/10.1021/acs.jpcc.9b07751.

[47] E.S. Ilton, J.E. Post, P.J. Heaney, F.T. Ling, S.N. Kerisit, XPS determination of Mn oxidation states in Mn (hydr)oxides, Applied Surface Science. 366 (2016) 475–485. https://doi.org/10.1016/j.apsusc.2015.12.159.

[48] S. Fritsch, J. Sarrias, A. Rousset, G.U. Kulkarni, Low-temperature oxidation of Mn_3O_4 hausmannite, Materials Research Bulletin. 33 (1998) 1185–1194. https://doi.org/10.1016/S0025-5408(98)00108-1.

[49] W. Feitknecht, Einfluss der Teilchengrösse auf den Mechanismus von Festkörperreaktionen, Pure and Applied Chemistry. 9 (1964) 423–440. https://doi.org/10.1351/pac196409030423.

[50] H.R. Oswald, M.J. Wampetich, Die Kristallstrukturen von Mn_5O_8 und $Cd_2Mn_3O_8$, Helvetica Chimica Acta. 50 (1967) 2023–2034. https://doi.org/10.1002/hlca.19670500736.

[51] M. Pourbaix, H. Zhang, A. Pourbaix, Presentation of an Atlas of Chemical and Electrochemical Equilibria in the Precence of a Gaseous Phase, MSF. 251–254 (1997) 143–148. https://doi.org/10.4028/www.scientific.net/MSF.251-254.143.

[52] E. Yang, H. Kim, S. Kim, I. Kim, J. Kim, H. Ji, J.W. Choi, Y. Jung, Origin of unusual spinel-to-layered phase transformation by crystal water, Chem. Sci. 9 (2018) 433–438. https://doi.org/10.1039/C7SC04114D.

[53] J. Hao, J. Mou, J. Zhang, L. Dong, W. Liu, C. Xu, F. Kang, Electrochemically induced spinel-layered phase transition of Mn_3O_4 in high performance neutral aqueous rechargeable zinc battery, Electrochimica Acta. 259 (2018) 170–178. https://doi.org/10.1016/j.electacta.2017.10.166.

[54] S. Kim, K.W. Nam, S. Lee, W. Cho, J.-S. Kim, B.G. Kim, Y. Oshima, J.-S. Kim, S.-G. Doo, H. Chang, D. Aurbach, J.W. Choi, Direct Observation of an Anomalous Spinel-to-Layered Phase Transition Mediated by Crystal Water Intercalation, Angewandte Chemie International Edition. 54 (2015) 15094–15099. https://doi.org/10.1002/anie.201505487.

[55] C.D. Ling, J.J. Neumeier, D.N. Argyriou, Observation of Antiferromagnetism in Marokite $CaMn_2O_4$, Journal of Solid State Chemistry. 160 (2001) 167–173. https://doi.org/10.1006/jssc.2001.9214.

[56] D. Tang, Y. Sun, Z. Yang, L. Ben, L. Gu, X. Huang, Surface Structure Evolution of LiMn2O4 Cathode Material upon Charge/Discharge, Chem. Mater. 26 (2014) 3535–3543. https://doi.org/10.1021/cm501125e.

[57] F. Schönewald, M. Eckhoff, M. Baumung, M. Risch, P.E. Blöchl, J. Behler, C.A. Volkert, A criticial view on e_g occupancy as a descriptor for oxygen evolution catalytic activity in $LiMn_2O_4$ nanoparticles, (2020). https://doi.org/10.48550/arXiv.2007.04217.

[58] J. Tsuji, M. Fujita, Y. Haruyama, K. Kanda, S. Matsui, N. Ozawa, T. Yao, K. Taniguchi, Excitation Energy Dependence for the Li 1s X-ray Photoelectron Spectra of $LiMn_2O_4$, Anal. Sci. 21 (2005) 779–781. https://doi.org/10.2116/analsci.21.779.

[59] C.V. Ramana, M. Massot, C.M. Julien, XPS and Raman spectroscopic characterization of $LiMn_2O_4$ spinels, Surface and Interface Analysis. 37 (2005) 412–416. https://doi.org/10.1002/sia.2022.

[60] J.J. Yeh, I. Lindau, Atomic subshell photoionization cross sections and asymmetry parameters: $1 \leqslant Z \leqslant 103$, Atomic Data and Nuclear Data Tables. 32 (1985) 7–9. https://doi.org/10.1016/0092-640X(85)90016-6.

[61] W. Li, W.R. McKinnon, J.R. Dahn, Lithium Intercalation from Aqueous Solutions, J. Electrochem. Soc. 141 (1994) 2310. https://doi.org/10.1149/1.2055118.

[62] M. Baumung, L. Kollenbach, L. Xi, M. Risch, Undesired Bulk Oxidation of LiMn2O4 Increases Overpotential of Electrocatalytic Water Oxidation in Lithium Hydroxide Electrolytes, ChemPhysChem. 20 (2019) 2981–2988. https://doi.org/10.1002/cphc.201900601.

[63] A.F. Wells, The crystal structure of atacamite and the crystal chemistry of cupric compounds, Acta Cryst. 2 (1949) 175–180. https://doi.org/10.1107/S0365110X49000461.

[64] J.B. Parise, B.G. Hyde, The structure of atacamite and its relationship to spinel, Acta Crystallogr C Cryst Struct Commun. 42 (1986) 1277–1280. https://doi.org/10.1107/S0108270186092570.

[65] C. Cachet-Vivier, S. Bach, J.-P. Pereira-Ramos, Electrochemical proton insertion in manganese spinel oxides from aqueous borate solution, Electrochimica Acta. 44 (1999) 2705–2709. https://doi.org/10.1016/S0013-4686(98)00377-6.

[66] M. Jayalakshmi, M. Mohan Rao, F. Scholz, Electrochemical Behavior of Solid Lithium Manganate ($LiMn_2O_4$) in Aqueous Neutral Electrolyte Solutions, Langmuir. 19 (2003) 8403–8408. https://doi.org/10.1021/la0340448.

[67] I. Roche, E. Chaînet, M. Chatenet, J. Vondrák, Durability of carbon-supported manganese oxide nanoparticles for the oxygen reduction reaction (ORR) in alkaline medium, J Appl Electrochem. 38 (2008) 1195–1201. https://doi.org/10.1007/s10800-008-9537-z.

4. Investigation of the oxide/electrolyte interface

4.1. Introduction

The processes in heterogeneous electrocatalysis proceed at the electrode/electrolyte interface. Oxygen reactions (reactions of oxygen reduction to water or hydrogen peroxide, oxygen evolution reaction) occur at the interface of the solid and liquid phases, thus they are affected by both the properties of the solid phase (chemical composition, crystal structure, structural defects, etc.) and properties of the liquid phase - electrolyte (pH, concentrations of cations and anions, etc.). However, despite the fact that the interface plays crucial role in electrocatalysis, its influence on the kinetics of electrocatalytic processes is often greatly simplified, and some factors are not considered. For oxide catalysts, the effect of the oxide/electrolyte interface on the kinetics of electrocatalytic processes is much less studied in the literature compared to the metal/electrolyte interface, which may be due to the more complex organization of the former [1]. Processes occurring at the oxide/electrolyte interface include charging of the electrical double layer, redox transitions of interfacial cations, acid–base equilibria, and, in some cases, also intercalation processes [2–4]. Thus, it is very important to distinguish various types of equilibria occurring at the transition metal oxide/electrolyte: (i) acid-base equilibria involving OH^-/H^+ adsorption from the electrolyte, which occur without redox transitions, and (ii) oxidation/reduction equilibria, accompanied by a redox transition of the metal cation or oxide anion (for example, Mn(III)/Mn(IV). The catalytic properties of the oxide are generally considered in connection with the second type of equilibria (redox) separately from its acid-base characteristics. However, Trassati [3] noted that the acid-base properties are determined by the strength of the interaction between the metal cation on the surface of the oxide and the oxygen of the surface OH group. Similarly, oxygen-containing reaction intermediates are bound to active surface sites (metal ions), so the activation energy is expected to depend on the strength of the M-OH bond.

Thus, a comprehensive characterization of the oxide interface, including both its acid-base characteristics and surface recharging, is important for a complete understanding of the electrocatalytic processes. This chapter consists of the Introduction and literature review (4.1), Experimental (4.2) and Results and Discussion (4.3). Section 4.1.1 provides a brief review of the literature, which will first consider surface recharging depending on both the composition and structure of the catalyst and the composition of the electrolyte. In Section 4.1.1.1 and 4.1.1.2, electrochemical approaches to the separation of recharging processes on the surface and in the bulk of the electrode will be briefly considered, and in Section 4.1.1.3 the acid-base properties of the surface and the determination of the point of zero charge will be considered.

4.1.1. Literature review

4.1.1.1. Surface recharging

Experimental data on the surface recharging have been obtained for many transition metal oxides, including manganese oxides, but its effect on the electrocatalytic properties is often not considered. Nevertheless, at the moment there are both a number of assumptions and a number of proven hypotheses regarding the effect of the recharge of transition metal cations on the surface of transition metal oxides on their electrocatalytic activity. For example, it was shown that the Mn(III)/Mn(IV) redox transition (eq. 54) is involved in the oxygen reduction reaction, which was confirmed by spectroscopic data [5,6]. For example, Mn(III)/Mn(IV) and Mn(II)/Mn(III) transitions (at 1.13 and 0.63 V, respectively) were observed for Mn_2O_3 by the in situ XANES (X-ray absorption near edge spectroscopy) in Ref. [6]. V. Celorrio et al [7] analyzed potential-dependent Mn(II), Mn(III) and Mn(IV) speciation in $LaMnO_3$ using in situ hard X-ray absorption and emission spectroscopies (see Figure 53).

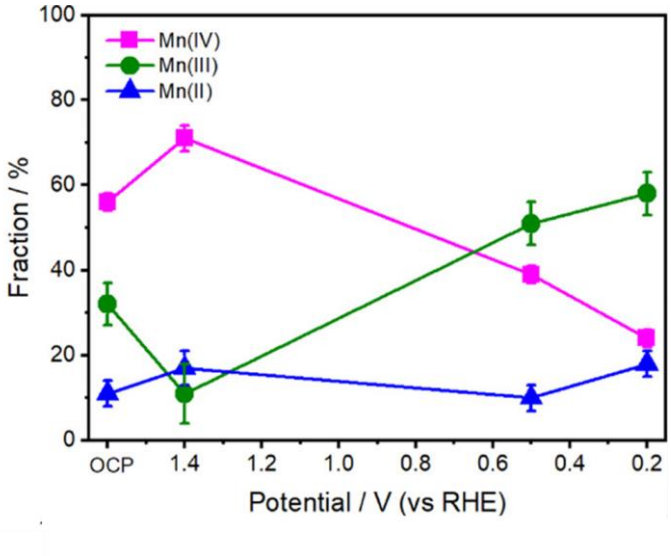

Fig. 53 Mn(II), Mn(III) and Mn(IV) speciation in $LaMnO_3$ depending on the electrode potential determined with in situ hard X-ray absorption and emission spectroscopies (XAS and XES). From [7].

Since the participation of the redox transition (eq. 54) in the oxygen reduction reaction is unambiguous ([8]), the question arises of how the position of the peaks in cyclic voltammogram measured in the supporting electrolyte (See Fig. 54), the peaks which correspond to the redox transitions of manganese, is related to the electrocatalytic activity.

$$Mn(IV)=O + H_2O + e^- \rightarrow Mn(III)\text{-}OH + OH^- \quad (54)$$

This question was studied by Ryabova in her works [8,9]. The position of the peaks was characterized by the formal potential $E_{f,}$ which is calculated as the half-sum of the potential of the cathodic and anodic peaks. Fig. 54, which shows CV curves for a number of manganese oxides, shows that the formal potential of the redox transition depends on the composition and structure of the oxide.

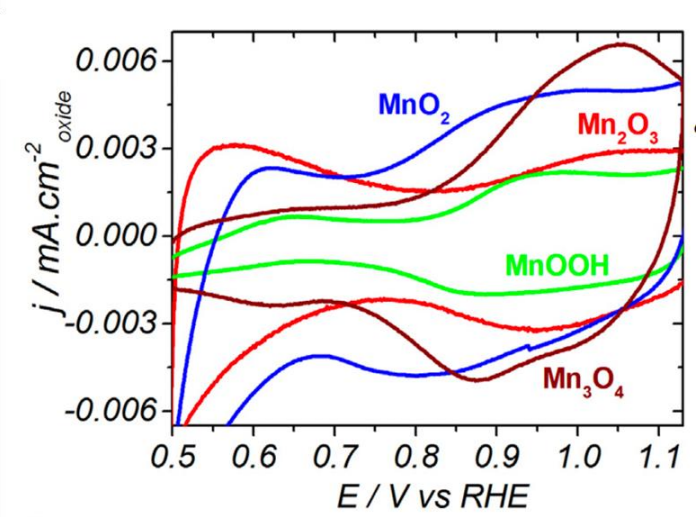

Fig. 54 CVs MnO_2/C, Mn_2O_3/C, Mn_3O_4/C, MnOOH/C в N_2-saturated 1 M NaOH measured at 10 mV s^{-1}. From Ref. [10].

Ryabova et al. ([8]) documented the dependence of the specific electrocatalytic activity, calculated as the kinetic current of the ORR per unit oxide surface, on E_f (Fig. 24 a). This dependence was interpreted by Ryabova et al. within the framework of a kinetic model in which oxygen adsorption is possible only on Mn(III) centers.

Integration of CV curves makes it possible to determine the number of redox centers on the oxide surface. Therefore, it can be expected that the total measured catalytic activity will correlate with the charge spent on recharging the surface of the oxide (while the specific catalytic activity does not depend on the surface area, as can be seen from the close values of the specific activity of Mn_2O_3 oxide with different specific surface areas, Fig 24 a). A similar correlation is discussed in Ref. [9,11] for Mn_2O_3 with various conductive additives [11], and for Mn_2O_3 obtained by various synthesis methods and having different BET surface areas [9].

A large amount of work on the recharging of oxides has been carried out in the framework of supercapacitor research and development. For example, MnO_2 has been extensively studied as a material for supercapacitors. The following redox equilibrium involving the electrolyte cation M^+ (62) was proposed in Ref. [12]:

$$MnO_{2(surface)} + M^+ + e^- \rightarrow MnO_2{}^-M^+{}_{(surface)} \quad (62)$$

Redox transitions also occur in the oxide subsurface/bulk, and are accompanied by intercalation of either an alkali metal cation from the electrolyte (63):

$$MnO_2 + M^+ + e^- \rightarrow MnOOM \quad (63)$$

or a proton (64):

$$MnO_2 + H^+ + e^- \rightarrow MnOOH \quad (64)$$

For MnO_2, a number of crystal structures (α, δ, γ, λ, β) with tunnels of various sizes within the crystal structure were studied [13]. The authors studied oxide materials with various specific surface areas: 5 (for λ- MnO_2), 31 (for γ- MnO_2), and 123 $m^2 g^{-1}$ (for α-MnO_2 obtained by the microemulsion synthesis method, which is further referred to as α(m)-MnO_2). Specific capacitance values have been shown to decrease in the series α(m) > α ≅ δ > γ > λ > β. β-MnO_2 demonstrated the lowest specific capacitance, which is associated with the presence of extremely small (1×1) tunnels in the structure, whose small size does not allow metal cations from the electrolyte to be accommodated in them during the charge/discharge cycle. However, this oxide also has some capacity due to the adsorption of cations on the surface.

The influence of the composition of the electrolyte has also been studied for MnO_2. Since intercalation of the electrolyte cations makes a significant contribution to the intrinsic capacity of MnO_2, some studies have been devoted to the selection of the optimal electrolyte cation allowing to enhance the capacitance [12,14–16]. Thus, in [14], operando Raman experiments have been performed to investigate the recharging of MnO_2 in a solution of nitrates of alkali cations (Li, Na, K) with a concentration of 2 M. It was shown that reversible intercalation is observed for all cations. The highest capacity is observed for the Li-containing solution, which the authors attribute to the higher mobility of this cation. It should be noted however that the differences between the CVs are not very significant (Fig. 55).

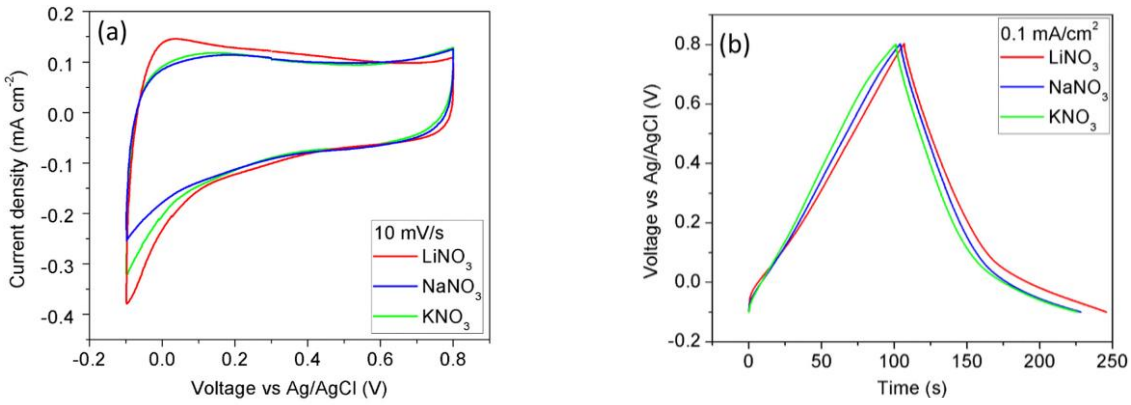

Fig. 55. CVs of a thin-film MnO_2 electrode in an aqueous electrolyte of 2 M $LiNO_3$, 2 M $NaNO_3$, and 2 M KNO_3. Scan rate 10 mV s^{-1}. (b) Charge-discharge curves [14].

Another important factor influencing the oxide charge/discharge is the concentration of the supporting electrolyte. In Ref. [17] the effect of the KCl concentration on the MnO_2 recharging was shown. In the same work, for RuO_2, in addition to the influence of the KCl concentration, the influence of the electrolyte pH was also investigated (Fig. 56).

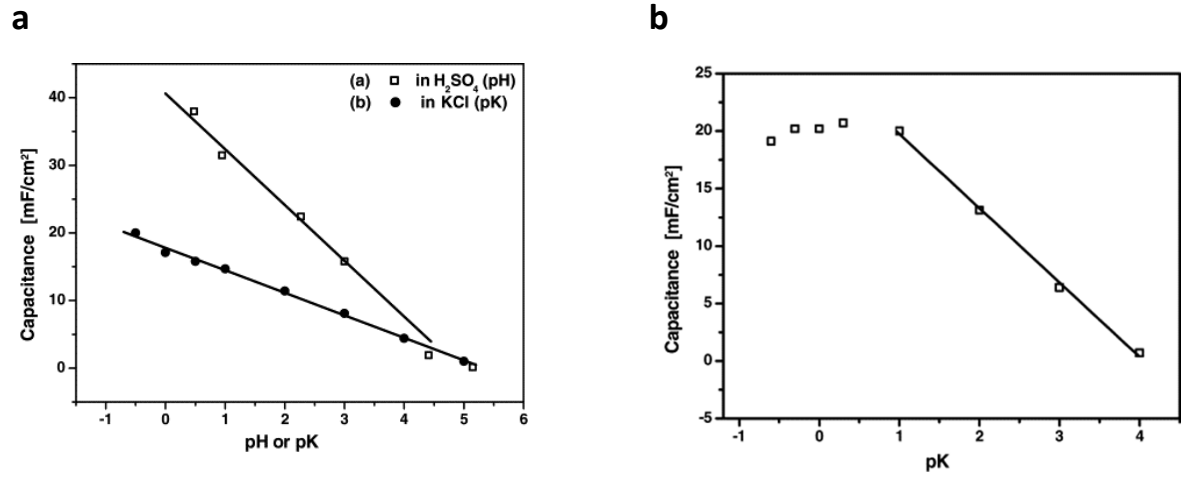

Fig. 56. Capacity versus pH and pK ($-\log C_{KCl}$) for RuO_2 (a) and capacity versus pK for MnO_2 (b)[17].

From these dependences (Fig. 56), we can conclude that since the capacities have a linear dependence on pH and pK, the charge/discharge processes are first-order reactions in proton and potassium concentration. The mechanism of the charge/discharge of ruthenium oxide electrodes includes the intercalation of protons in an acid solution and the intercalation of potassium ions in a KCl solution. There is a larger slope in the dependence of capacitance on pH in an acidic electrolyte solution than on pK in a KCl solution. The capacitance of the MnO_2 electrodes increases with the concentration of the KCl electrolyte and demonstrates a linear dependence on the pK. However, as the KCl concentration exceeds 100 mM, the capacity reaches a plateau.

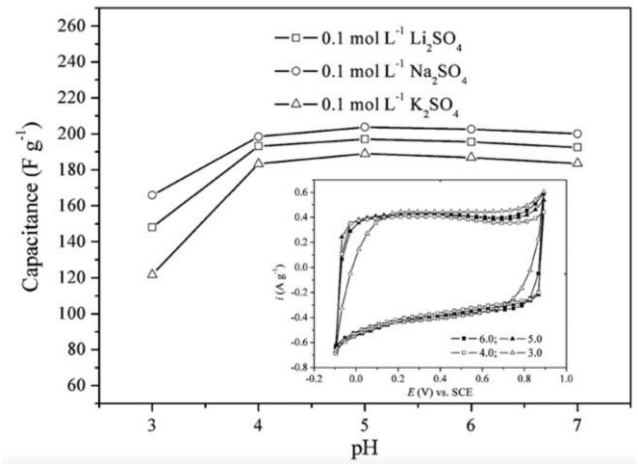

Fig. 57. Capacity versus pH in Li_2SO_4, Na_2SO_4 and K_2SO_4. The inset shows cyclic voltammograms of MnO_2 in Li_2SO_4 electrolyte with a concentration of 0.1 mol L^{-1} at various pH values. pH was set by adding H_2SO_4 [16].

In Ref. [16] the effect of pH on the recharging of MnO_2 was studied. Fig. 57 shows that as the pH decreases from 7 to 4, the capacitance practically does not change, from which the authors conclude that there are no intercalation processes involving a proton. At pH less than 4, manganese is likely to dissolve into the electrolyte.

$LaMnO_3$ as a supercapacitor with anion intercalation was studied by the authors of [18]. In this work, two $LaMnO_3$ samples with different oxygen stoichiometry were investigated. One sample was oxygen-rich, the second was oxygen-deficient ($LaMnO_{3.09}$ and $LaMnO_{2.91}$, respectively). In Fig. 58 CVs of $LaMnO_3$ are given at various NaOH concentrations. The authors attribute peaks in the CVs to oxygen intercalation, with the first peak (at –0.4 V vs Hg/HgO) related to the Mn(II)/Mn(III) transition, and the second peak (at 0 V vs Hg/HgO) to the Mn(III)/Mn(IV) transition.

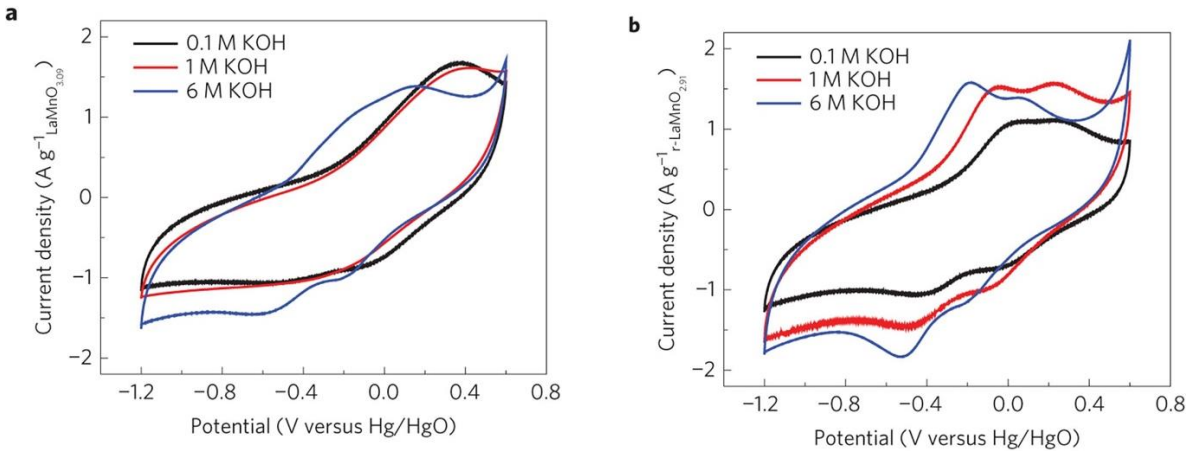

Fig. 58. CVs of $LaMnO_{3.09}$ (a) and $LaMnO_{2.91}$ (b) at a sweep rate of 40 mV/s at various NaOH concentrations [18].

From the shape of CVs for $LaMnO_{3.09}$, and its evolution with the NaOH concentration, the authors conclude that even for an anion-rich oxide, there are oxygen vacancies on the surface. The following intercalation equilibrium was proposed:

$$La\left[Mn_{2\delta}^{2+}; Mn_{1-\delta}^{3+}\right]O_{3-\delta} + 2\delta OH^- \leftrightarrow LaMn^{3+}O_3 + 2\delta e^- + \delta H_2O \quad (65)$$

4.1.1.2. Separation of 'fast' and 'slow' recharging processes

The brief review of the literature presented in the previous section showed that both surface processes and processes of intercalation into the bulk occur at the oxide/electrolyte interface. Their contributions can be separated by examining the dependence of CVs on potential scan rate v. Trasatti in his study of RuO_2 [2] proposed to separate the processes occurring on the so-called 'outer' and 'inner' surfaces by extrapolating the dependencies Q ($n^{-½}$) and Q^{-1} ($n^{½}$) to "infinitely" high and "infinitely" small sweep rate, which will correspond to fast and slow processes occurring, respectively, on the 'outer' and 'inner' surfaces (Fig. 59). The original version of Trasatti 's approach assumed the "slow" charging to occur on surface areas shielded in pores or cracks, but slow intercalation into the oxide volume leads to a qualitatively similar behavior.

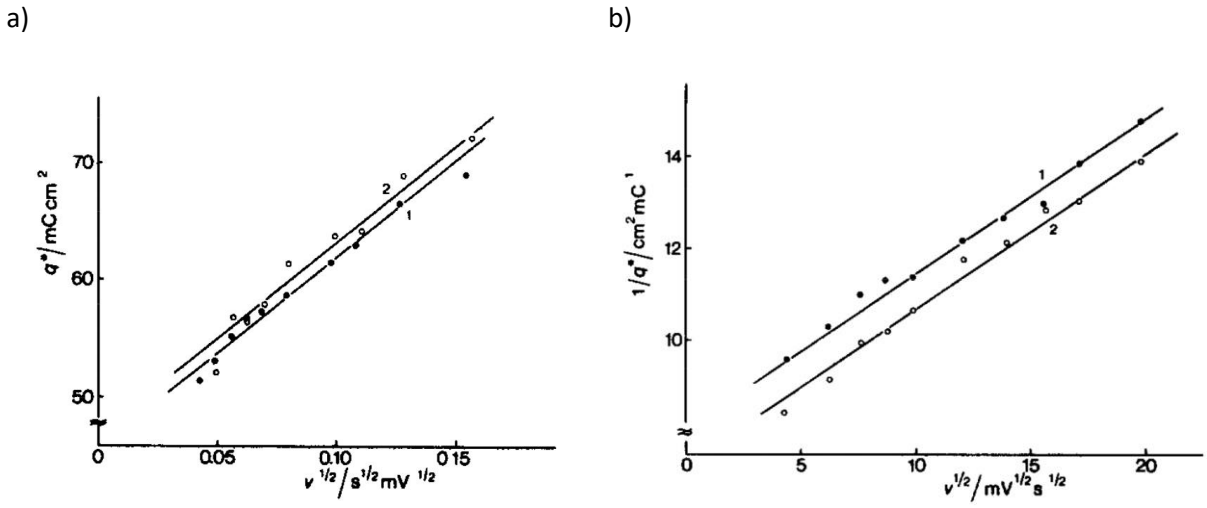

Fig. 59. Typical plot of charge q at scan rate v as a function of ($n^{-½}$) (a) and 1/q vs. $n^{½}$(b) for (1) $HClO_4$ (2) KOH solution [2].

However, it should be noted that the Trasatti's coordinates were proposed for the analysis of diffusion-limited rather than "fast" surface recharging processes. For a more accurate analysis of "fast" processes, it is possible to use the approach described by Conway [19,20]. In this case, the

interfacial recharging current at a given potential is represented as j = an^b, where a and b are constants. If the current corresponds to a fast pseudocapacitive recharging process, the value of b should be close to 1, and if it is caused by a slow diffusion process (either in the pores of the electrode or in the bulk of the solid), the value of b should be close to 0.5. Thus, with the simultaneous occurrence of "fast" and "slow" processes, the value of b will vary from 0.5 to 1 and can be estimated as the slope of the dependence of logj on log$n$ In this case, the total current can be considered as the sum of the "fast" and "slow" contributions: j = $a_1 n + a_2 n^{½}$, where a_1 and a_2 are constants representing, respectively, the slope and the intercept on the j$n^{-½}$on $n^{½}$, dependence. It should be kept in mind that possible parasitic Faraday processes (such as the cathodic reduction of trace O_2 or anodic oxidation of electrode components) can contribute to the total current as a third term independent of n, increasing the error of the described data analysis method.

The authors of [21] applied both of the above approaches to study the interfacial recharging behavior of various Mn and Co containing perovskites. Fig. 60 shows an example of the Conway's analysis for $Sr_{0.5}Gd_{0.5}Mn_{0.75}Co_{0.25}O_{2.98}$ и $Sr_{0.5}Gd_{0.5}Mn_{0.25}Co_{0.75}O_{2.87}$ perovskites.

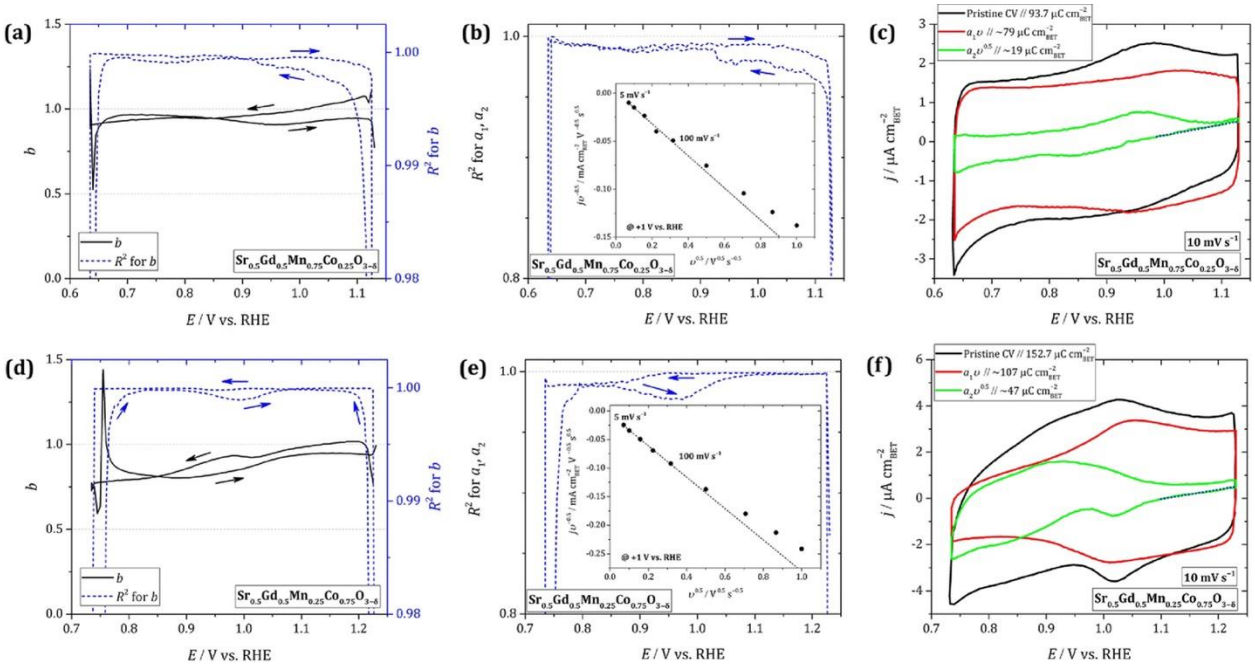

Fig. 60. Analysis of the j-n dependences for $Sr_{0.5}Gd_{0.5}Mn_{0.75}Co_{0.25}O_{2.98}$ (a-c) and $Sr_{0.5}Gd_{0.5}Mn_{0.25}Co_{0.75}O_{2.87}$ (d-f) according to the Conway's approach: (a, d) slope b of the log j vs. log n dependence and the corresponding Pearson correlation coefficient R^2; (b, e) $jn^{-½}$ vs. $n^{½}$ dependence at 1 V vs. RHE and the corresponding Pearson correlation coefficient R^2; (c, f) pristine CV at 10 mV $s^{-1}$and CVs corresponding to 'fast' ($a_1 n$) and 'slow' ($a_2 n^{-½}$) processes. Parameters a_1 and a_2 represent the slope and the intercept of the $jn^{-½}$ vs. $n^{½}$dependence, respectively. Dashed plots indicate parts with a high calculation error formally corresponding to b > 1. [21]

The authors of Ref. [21] came to the conclusion that the Trasatti's approach does not work at very high scan rates and it is preferable to use the Conway's approach. However, it should be noted that at scan rates of more than 100 mV s^{-1}, the dependence $jn^{-½}$ ($n^{½}$) linearizes with a much lower correlation coefficient, which the authors attribute to ohmic effects. Using the Conway approach, the authors managed to separate the process of intercalation into the perovskite lattice from the surface recharge processes (Fig. 60) and show that the contribution of intercalation processes increases with increase in the cobalt content in mixed manganese-cobalt perovskites.

4.1.1.3. Acid-base properties of oxides. Determination of the point of zero charge

When studying the acid-base characteristics of oxides, researchers are usually interested in such a characteristics as $pH_{0.}$ At this pH value, the surface becomes electrically neutral. When the oxide is placed in a solution with a given pH value, its surface charge is determined by the position of pH relative to $pH_{0.}$ If the pH value is above $pH_{0,}$ then the surface is charged negatively, due to the dissociation of surface hydroxyl groups, if pH is below $pH_{0,}$ then the surface is positively charged. The absolute value of the surface charge increases with an increase in pH and an increase in the concentration of electrolyte cations [22].

There are two approaches to determine pH_0, and these are based on electrokinetic and titrimetric methods. In electrokinetic analysis, the determined quantity is the zeta potential (ζ). The zeta potential is the potential difference between a dispersion medium and a fixed layer of liquid, relative to a dispersed particle. This potential is quite easy to determine experimentally and it depends on the nature of the material under study and the composition of the electrolyte. By varying the concentration of the solution (in the particular case pH), one can determine the value of pH_0 at which ζ=0. Such a pH_0 point, determined by electrokinetic methods, is called the isoelectric point (IEP). The main approach for determining the IEP is electrophoresis - the movement of colloidal particles in an electric field. This method is only suitable for stable dispersions, it is not possible to use it for large particles, since they can settle before the end of the measurement. Another method of measurement ζ is electroosmosis, often considered as a phenomenon that accompanies electrophoresis. In this case, the solid phase is fixed (for example, in the form of a capillary, membrane, or porous plug), and the electric field induces a fluid flow. This method is suitable for large particles or fibers. The opposite effect is that if a liquid flow is forced to pass through a fixed solid phase, then an electric field is induced, which can be measured and used to determine the potential ζ.

Another approach for determining pH_0 is to titrate an oxide suspension. In this case, due to the fact that the surface is charged, part of the H^+ / OH^- from the electrolyte (depending on the surface charge) is adsorbed on the surface, due to which the titration curve deviates from its counterpart measured for a solution without dispersed particles (Fig. 61). The intersection of the curves is the sought pH_0 point, in this case it is called the point of zero charge (PZC). From the shift of the titration curves (ΔV), the surface charge (σ) can be calculated using the equation (61)

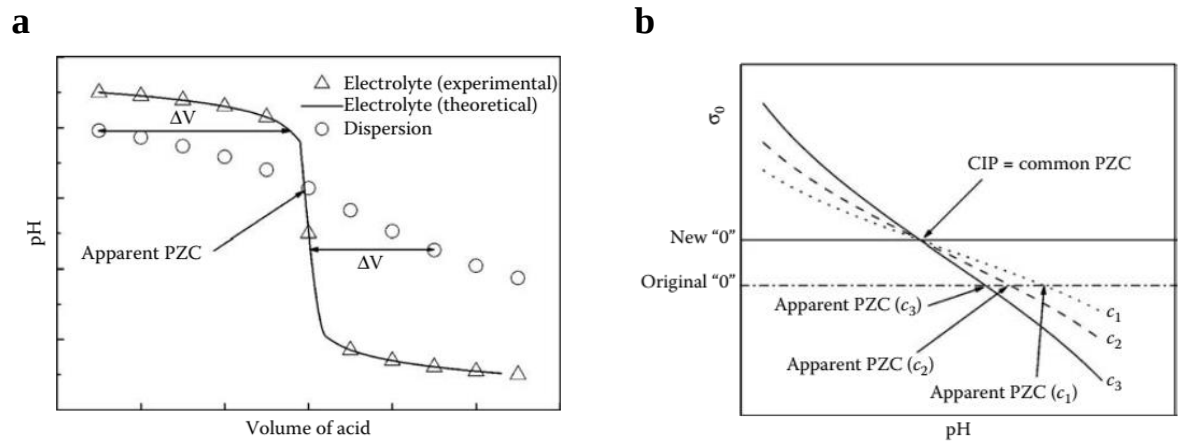

Fig. 61 a) Variant of the titration curve for suspension (marked with circles) and blank solution (marked with triangles), b) apparent and true PZC points obtained from a titrimetric experiment using solutions with different ionic strength [23].

Often titration of a suspension provides an apparent rather than the true PZC value, which is due to the fact that some acid or base may be present in the powder after synthesis. To solve this problem and refine the PZC value, it is necessary to carry out a series of experiments with different ionic strengths of the supporting electrolyte solution. This point is also referred to as the common intersection point (CIP) in the literature.

PZC and IEP points can take the same value, but this is possible only in the absence of specific adsorption of ions on the surface of dispersed particles. The determination of PZC and IEP makes it possible to obtain information regarding the charge of the ions adsorbed on the surface of the oxide in contact with the electrolyte. In a number of works, an assumption is made about the processes occurring on the surface of the oxide. Thus, there are two points of view regarding acid sites on the surface, namely assuming one or two types of acid-base equilibria on the surface [22,24,25]:

$$S\text{-}OH + OH^- \rightarrow S\text{-}O^- + H_2O \quad (66)$$

$$S\text{-}(OH)_2 + OH^- \rightarrow HO\text{-}S\text{-}O^- + H_2O \quad (67)$$

$$HO\text{-}S\text{-}O^- + OH^- \rightarrow {}^-O\text{-}S\text{-}O^- + H_2O \quad (68)$$

For example, the authors of Ref. [26] used the approach described in Ref. [24], and from the titration of a suspension of Mn_2O_3 determined the acidity constants for two consecutive equilibria (K_{a1}, K_{a2}), and the formation constants of $S\text{-}O^-Na^+$ complexes (pK_{Ct}) and $S\text{-}OH_2^+Cl^-$ (pK_{Cl}).

Table 9 Acidity constants (pK_a) and complexation constants (pK_{Cl} and pK_{Ct}) of surface hydroxyl groups for the Mn_2O_3/Ct system (Ct = Li, Na, Cs) [26].

Constant	Electrolyte		
	LiCl	NaCl	CsCl
pKa1	4.77±0.01	5.02±0.20	4.97±0.07
pKa2	7.85±0.08	7.80±0.22	8.28±0.08
pKCl	4.99±0.06	5.02±0.35	5.54±0.32
pKCt	7.50±0.01	7.52±0.28	8.15±0.09

Table 10. PZC and IEP values reported in the literature for Mn_2O_3, MnOOH, $LaMnO_3$

	PZC	IEP
Mn_2O_3	6.5 [26]; 6 [27]; 4.7 [28]	3.8 [26]; 7.5 [29]
MnOOH	7.4 [30];	
$LaMnO_3$	7.4 [31], 7.5 [32]	

As can be seen, for all of the studied oxides, the IEP and PZC values reported in different works differ greatly. This may be due to many factors, including the microstructure of the oxide, which depends on the method of its synthesis, the history of the sample (for example, its calcination, etc.), as well as the experimental technique used for determining PZC/IEP. Thus, it is known that the results obtained can be strongly influenced by purging the solution with an inert gas to protect the supporting electrolyte from carbon dioxide [33,34]. Furthermore, the use of special plastic cups inert with respect to alkali may improve the results, which is associated with the dissolution of silicates and their redeposition on the oxide surface [35,36].

An important but little-studied issue is the dependence of the charge on the oxide surface on the electrode potential. In the works of the Russian Electrochemical School [4], it was shown that, compared to metals, oxides are characterized by an 'inverted' dependence of the surface charge on the electrode potential. Indeed, for oxides the surface charge (at constant pH) does not increase, but rather decreases when the electrode potential is shifted positive.

4.1.2. Conclusions and problem statement

When the surface of transition metal oxides is recharged, the processes may occur both on the surface and subsurface/bulk (intercalation). The latter are fundamental to the operation of a number of supercapacitors, so the study of the interface for oxide systems has been carried out to a large extent within the framework of materials development and the study of the charge accumulation mechanism of supercapacitors. Although the state of the oxide/electrolyte interface (surface charge, surface composition, adsorption of ions from the electrolyte, etc.) has a crucial impact on electrocatalytic systems, the influence of the surface state on the electrocatalytic phenomena has been studied in a much lesser extent.

Recently, many studies documented very significant influence of the electrolyte composition on the rates of electrocatalytic processes occurring on the surface of catalysts based on noble metals. As far as electrocatalysis on transition metal oxides is concerned, there are still very few works on the influence of electrolyte composition (see literature review of Chapter 5). Meanwhile, the surface of oxides differs to a large extent from the surface of metals, the processes of recharging on it are more complex, as is the interface itself, and one can expect a significant effect of both pH and cation concentration on electrocatalysis.

In this work, we study influence of pH and Na^+ concentration on the surface charge and on the interfacial recharging for selected Mn oxides. To this end, we have chosen previously studied ([8,10]) stable manganese compounds - Mn_2O_3, $LaMnO_3$, MnOOH. These compounds have different crystal structures and demonstrated significant differences in the ORR kinetics.

Table 11. Rate constants for steps k_2, k_3, k_5 of the proposed ORR mechanism (see Fig. 25) estimated by microkinetic modeling (see Ref. [8]) for MnOOH, $LaMnO_3$ and Mn_2O_3

Catalyst	**Rate constants of individual reaction steps**		
	k_2 **[10^{13} $cm^3 mol^{-1} s^{-1}$]**	**k_3** **[10^{10} s^{-1}]**	**k_5** [s^{-1}]
Mn_2O_3	1.5	5.1	50
$LaMnO_3$	0.03	0.1	10
MnOOH	0.15	0.5	0.05

Thus, in Ref. [10], the highest rates of steps 2, 3, and 5 were found by kinetic modeling for Mn_2O_3 (Fig. 25) and, accordingly, the ORR on this oxide proceeds at the highest rate. MnOOH is characterized by a significantly lower value of the rate constant of the chemical (does not depend

on the applied potential) step 5 involving O-O bond breaking in the adsorbed hydrogen peroxide intermediate (Fig. 25). As a result, when studying the electrochemical transformations of the hydrogen peroxide for MnOOH, the cathodic currents limited by the chemical reaction were observed (see Chapter 1). For MnOOH, the rate of this step is the slowest among the investigated Mn oxides, and for this compound the overall ORR rate is the slowest. On the other hand, the rate constants of steps 2 and 3 are the lowest for $LaMnO_3$, while step 5 is fast, indicating different limiting steps in the ORR mechanism for these three oxide materials.

In addition to the above-mentioned Mn oxides, carbon (pyrolytic carbon of the Sibunit family) was also investigated. Carbon is a necessary component for electrochemical studies of poorly conducting catalysts, for example oxides. However, as mentioned earlier, carbon also acts as a cocatalyst of the ORR reaction, so changes occurring at the carbon/electrolyte interface upon variation in the composition of the electrolyte can also affect the electrochemical behavior of oxides.

Thus, the influence of Na^+ concentration and pH was studied for Mn_2O_3, $LaMnO_3$, MnOOH and carbon of the Sibunit family. Two series of experiments were carried out. In the first series of experiments, to unveil the effect of pH, the ionic strength of the solution was kept constant by fixing the concentration of Na^+ at 2 M. In the second set of experiments, to determine the effect of the concentration of Na^+, the concentration of OH^- was fixed at was 0.1 M. The Na^+ concentration was controlled by adding $NaClO_4$. We used various methods to study the interface. Thus, classical cyclic voltammetry was used to study the interfacial recharging behavior. To study the "fast" and "slow" processes occurring during the interface recharging, CVs were recorded at different scan rates. In addition to electrochemical analysis of the interface, acid-base equilibria were studied; for this, oxides were titrated from an alkaline medium.

4.2. Materials and methods

For all oxide samples and carbon, the surface area was determined by the BET method (Table 12). The largest specific surface area among the oxides was obtained for MnOOH (33 $m^2 g^{-1}$), while specific surface areas of Mn_2O_3 and $LaMnO_3$ were similar (15 and 16 $m^2 g^{-1}$, respectively).

Table 12. Investigated materials and their BET surface area

Materials	**S_{BET} $m^2 g^{-1}$**
Mn_2O_3	15
MnOOH	33
$LaMnO_3$	16
Sibunit	105

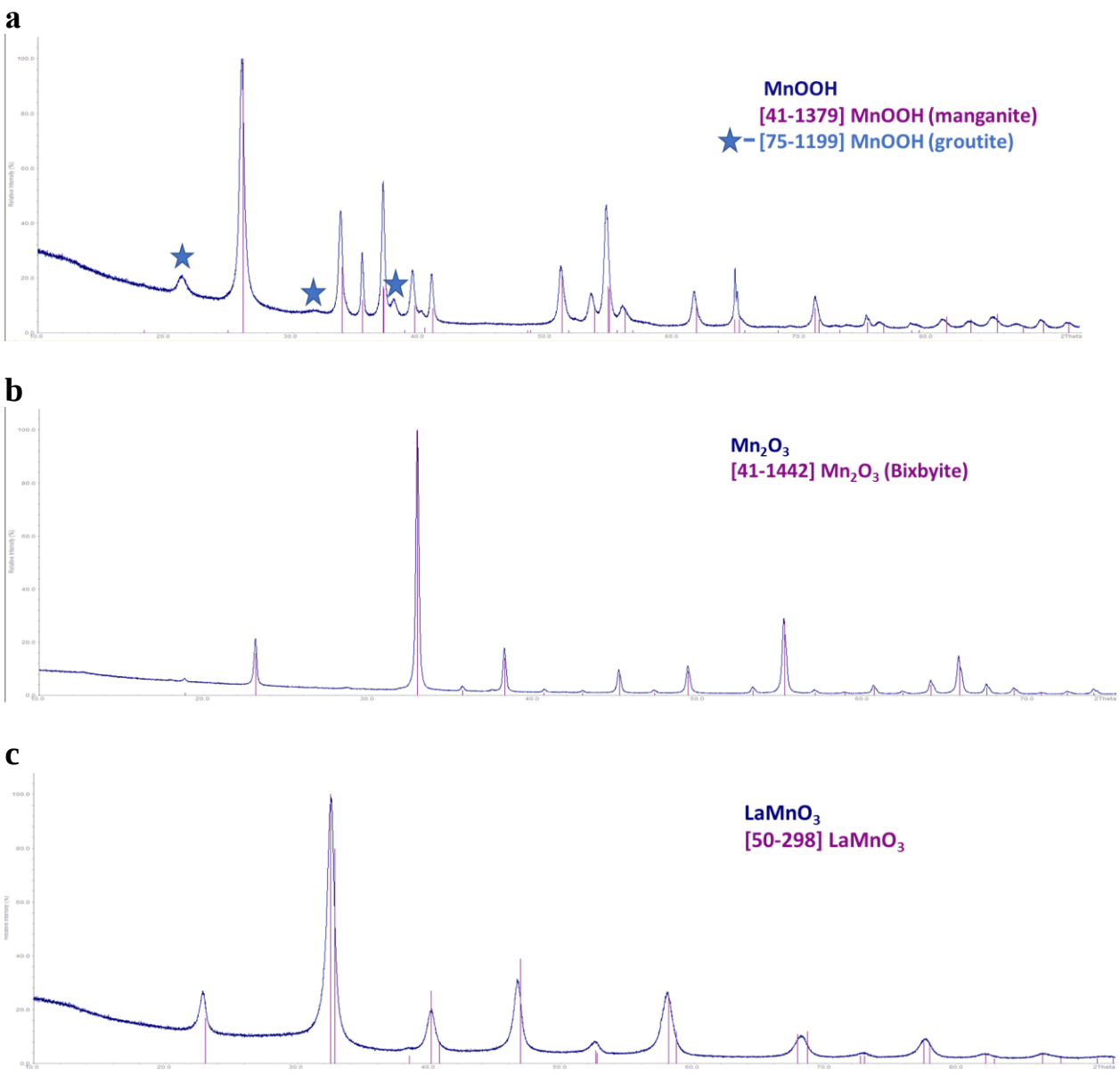

Fig. 62 X-ray diffraction patterns of samples a) MnOOH, b) Mn_2O_3, c) $LaMnO_3$, Bar diagrams correspond to the position of reflections from the ICDD PDF2 database #41-1349 and #75-1199 for MnOOH with manganite and groutite structures, respectively (a), #41- 1442 bixbyite - Mn_2O_3 (b), #50-298 $LaMnO_3$ (c).

The phase composition of the obtained samples was confirmed by powder X-ray diffraction (Fig. 62). The samples of Mn_2O_3 and $LaMnO_3$ are single-phase, MnOOH is a mixture of two modifications - manganite (~90%) and groutite (~10%).

Experimental procedures utilized for electrochemical measurements and acid-base titrations are detailed in Chapter 2.

4.3. Results and discussion

4.3.1. Influence of pH and cations

We start by the discussion of the influence of the pH (OH^- concentration) on CVs of MnOOH, Mn_2O_3 and $LaMnO_3$ oxides studied at a constant ionic strength. CVs of Sibunit carbon in the same electrolytes are shown for comparison. Fig. 63 shows that while CVs of the Sibunit carbon are similar in all studied electrolytes, CVs of Mn oxides demonstrate significant changes. It is interesting to note that each of the three studied oxides responds differently to the change of the OH^- concentration. Considering this, we will discuss them sequentially and begin our discussion with $LaMnO_3$.

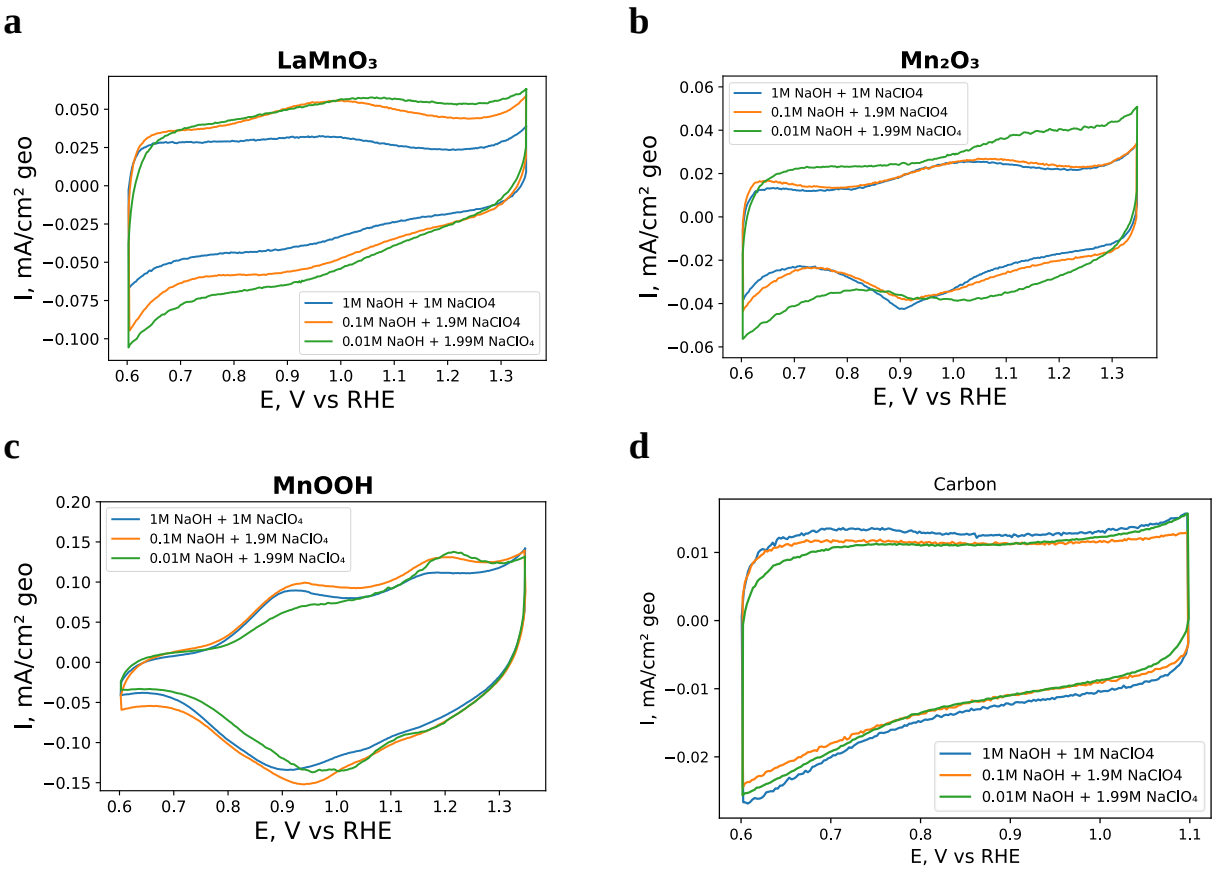

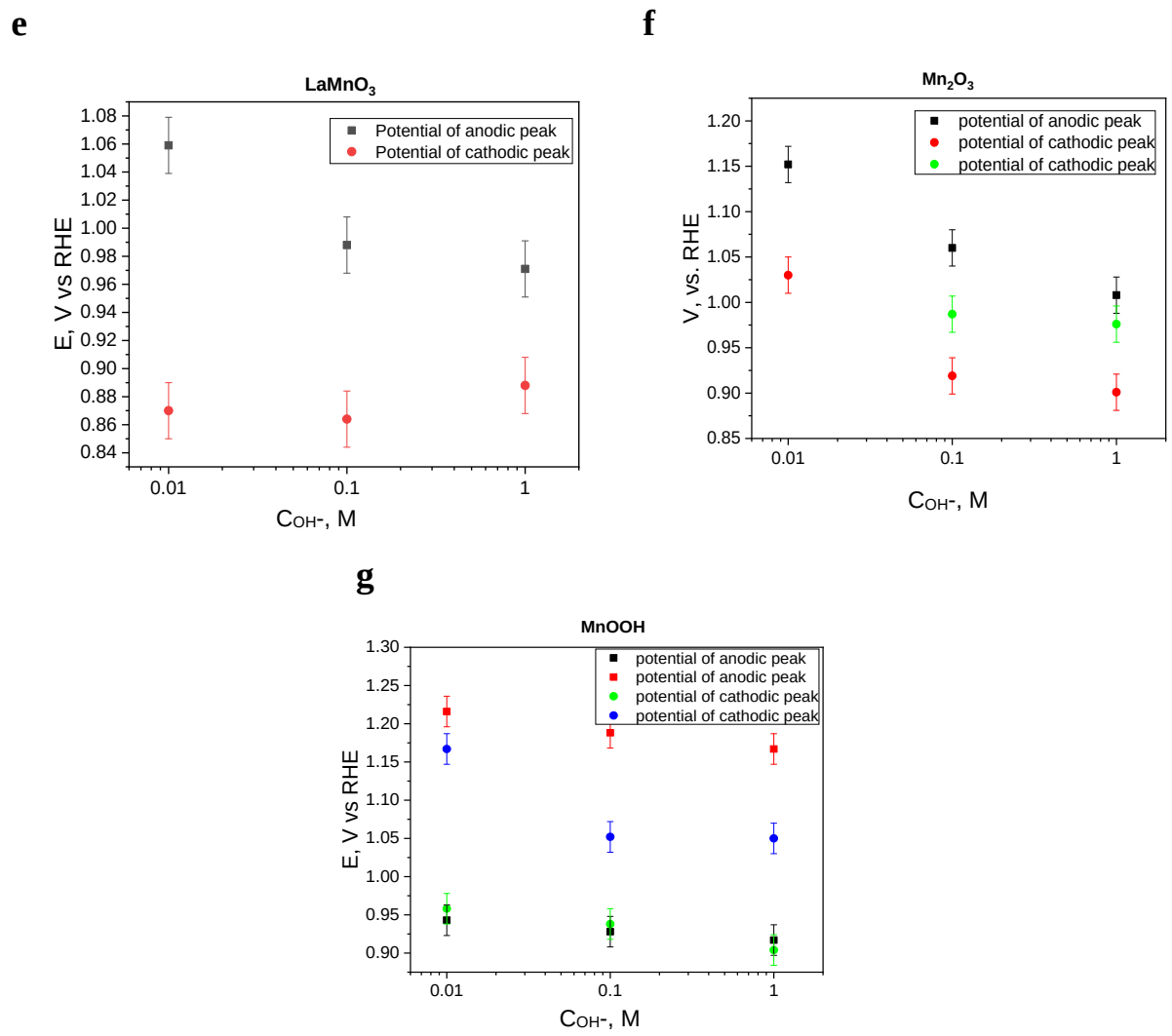

Fig. 63. CVs in N_2-saturated alkaline solutions for $LaMnO_3$ (a), Mn_2O_3 (b), MnOOH (c) and Sibunit carbon (d) at different OH^- concentrations and constant ionic strength (as indicated in the panels). Evolution of the cathodic and anodic peak positions (*cf*. panels a-c) with the OH^- concentration for $LaMnO_3$ (e), Mn_2O_3 (f), MnOOH (g). Scan rate 10 mV s^{-1}, oxide loading is 91 μg cm^{-2} and carbon loading is 91 μg cm^{-2}.

In the interval from 0.6 to 1.35 V vs. RHE $LaMnO_3$ shows a pair of broad anodic and cathodic peaks, which in the previous studies were attributed to the Mn(III)/Mn(IV) redox transition. While the anodic peak shifts negatively with the increase of the OH^- concentration, the potential of the cathodic peak stays unchanged within the error bar of the measurements. The resulting formal potential of the red-ox transition is practically independent of the OH^- concentration (within the experimental error) and equal to 0.94±0.15 V vs. RHE. We thus conclude that for $LaMnO_3$ the pH dependence of the E_f is close to Nerstian and (considering that the pH dependence of the RHE potential scale) on the SHE (standard hydrogen electrode scale) can be expressed as follows:

$$E_f(\text{vs. SHE}) = \text{const} - 0.059\text{pH} \quad (69)$$

Eq. 69 corresponds to the equilibrium (Eq 70)

$$\text{-Mn(IV)=O} + e^- + H_2O \rightarrow \text{-Mn(III)-OH} + OH^- , \quad (70)$$

which agrees with the hypothesis made in previous publications ([8]).

The Mn(III)/Mn(IV) equilibrium at the $LaMnO_3$ /electrolyte interface can also be represented through (70') :

$$\text{Mn(IV)}\begin{matrix}\text{-OH}\\\text{-OH}\end{matrix} + e^- \rightarrow \text{Mn(III)-OH} + OH^- \quad (70')$$

Yet, the observed shift of the anodic peak potential (as well as the noticeable decrease of the pseudocapacitance with the concentration of OH^-) indicates that Eqs. 70/70' may be oversimplified and phenomena occurring at the $LaMnO_3$/electrolyte interface may be more complex.

As to Mn_2O_3, it also demonstrates a pair of anodic peaks . However, the cathodic peak splits into two, which is especially clearly seen at high OH^- concentrations. Contrary to $LaMnO_3$, for Mn_2O_3 both the anodic and the cathodic peak shift negative with the OH^- concentration (Fig 63 f) thus demonstrating a non-Nerstian dependence of the following type:

$$E_f(\text{vs. SHE}) = \text{const} - 0.11\text{pH} \quad (71)$$

Eq. 71 suggests that Mn(III)/Mn(IV) redox transition involves transfer of about two OH^- anions, which does not agree with equilibrium of type (70/71') and calls for further analyses. We will present them below when discussing the influence of the Na^+ concentration on the CVs.

MnOOH demonstrates the most peculiar OH^- concentration dependence. CVs show two anodic peaks at grossly different potentials, and a broad cathodic peak accompanied by a shoulder (likely arising from an overlap of two cathodic peaks). The high-potential peak demonstrates stronger dependence on the pH (with about 20 mV per pH) compared to the low-potential counterpart. Moreover, the ratio between the intensities of the two anodic peak is also OH^- -concentration dependent. We hypothesize that the surface comprises of two types of surface redox centers, and their surface coverage is pH-dependent. This will be discussed in more detail below when we present the dependence of the CV on the Na^+ concentration.

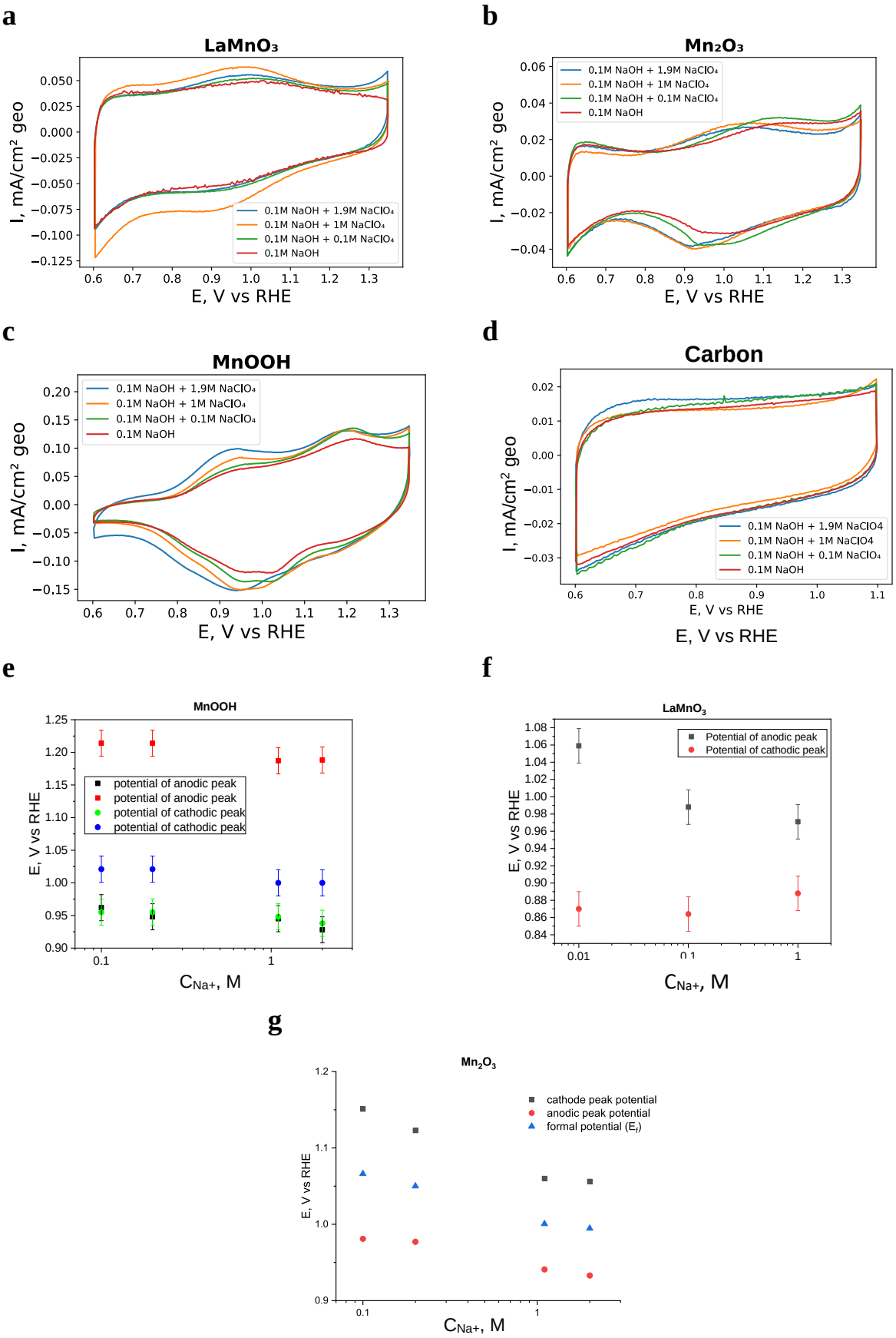

Fig. 64. CVs in N_2-saturated alkaline solutions at different concentration of Na^+ and constant pH for $LaMnO_3$ (a), Mn_2O_3 (b), MnOOH (c), and Carbon (d). Potentials of the anodic and cathodic peaks plotted against the Na^+ concentration for $LaMnO_3$, Mn_2O_3, MnOOH (e-g).

We now move to the discussion of the influence of the Na^+ concentration (measured at a constant OH^- concentration) on the CVs. For MnOOH, again, we observe two pairs of anodic/cathodic peaks, their relative intensity depending on the Na^+ concentration, but their potentials being weakly dependent on the cation concentration. Based on this we assume that two types of Mn red-ox centers are present on the MnOOH surface. The first type of redox centers, which is nearly Na^+-independent may be characterized by the following equilibrium:

$$Mn(IV)=O + e^- + H_2O \rightarrow Mn(III)\text{-}OH + OH^- \quad (72)$$

Or, alternatively:

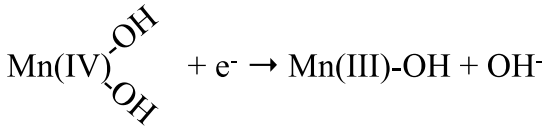

(72')

The second type of redox centers involves Na^+:

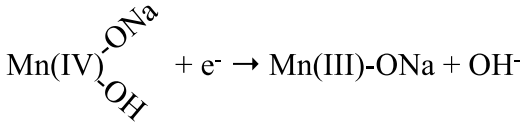

(73)

Interestingly, the Mn(IV)=O (Mn(OH)OH) and Mn(IV)(OH)ONa sites show grossly different recharging behavior. The recharging of the Mn(OH)ONa sites occurs at lower electrode potentials and demonstrates higher reversibility (smaller difference between the potentials of the anodic and cathodic peaks). This potential difference between the two types of redox centers on the MnOOH surface may arise from Na^+ cations stabilizing Mn(IV) sites, resulting in a decrease of the formal potential of the interfacial Mn(III)/Mn(IV) redox transition. Relative coverage of the two types of centers depends on the Na^+ concentration due to the occurrence of the equilibria:

$$Mn(III)OH + Na^+ + OH^- \rightarrow Mn(III)ONa + H_2O \quad (74)$$

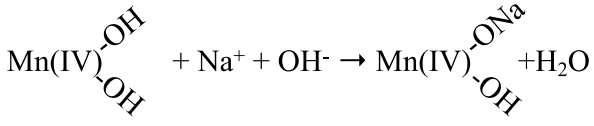

(75)

For $LaMnO_3$ the shift of the Mn(III)/Mn(IV) peaks with the Na^+ concentration is small, E_f shifting by about -20 mV per pNa, suggesting that cations exert minor influence on the oxide/electrolyte interface. For Mn_2O_3 both the anodic and the cathodic peaks shift negative with an increase of the Na^+ concentration, suggesting that Na^+ cations enter the equilibrium of the red-ox transition. The E_f follows the dependence:

$$E_f = \text{const} - 0.058 \log (C_{Na^+}) \quad (76)$$

The observed cumulative effect of OH^- and Na^+ concentration could be tentatively attributed to the following interfacial equilibrium at the Mn_2O_3/electrolyte interface:

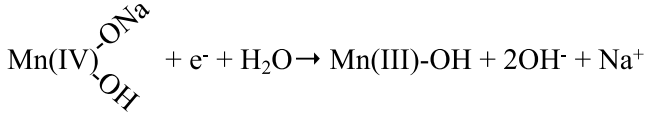

(77)

On the other hand, the cation effect for Mn_2O_3 may be similar to that of MnOOH. That is, there are two pairs of broad overlapping anodic/cathodic peaks with close Ef values, which do not shift with the cation concentration, but it is rather the ratio of their intensities which changes resulting in the observed apparent peak shift. Unfortunately, it is impossible to reliably confirm or discard this assumption based on the available dataset due to the large width.

Similar to what has been discussed above for the OH^- concentration effect, the concentration of Na^+ does not lead to noticeable change in the CV of the Sibunit carbon.

Finally, it is interesting to analyse the evolution of the so-called open circuit potential with the pH and pNa. Indeed, when an oxide is placed in contact with an oxygen-free supporting electrolyte, a steady-state is established at the interface resulting in a certain value of the interfacial drop, the latter defining the open circuit potential (OCP). The OCPs for $LaMnO_3$, Mn_2O_3 and MnOOH in N_2-purged solutions with varying pH (OH^- concentration) and in solutions with varying Na^+ concentration (at constant pH) are shown in Fig. 65. First of all, we note that for all studied materials the OCP value lies either at the 'onset' or within the potential interval of the Mn(III)/Mn(IV) redox transition suggesting that both Mn(III) and Mn(IV) centers are present at the interface under steady-state OCP conditions. In what concerns the influence of the OH^- concentration, for all oxides the OCP first increases (when C_{OH^-} is increased from 0.01 to 0.1 M) and then decreases (when C_{OH^-} is increased from 0.1 to 1 M), with the largest change observed for the MnOOH oxide. Similarly, when the concentration of Na^+ in solution is varied, the largest changes in the OCP can be observed for MnOOH, with OCP increasing from 0.86 to 0.98 V vs RHE when the Na^+ concentration increases by an order of magnitude. The OCP also increases for Mn_2O_3 with the Na^+ concentration, but to a much lesser extent than for MnOOH. On the contrary, for $LaMnO_3$ practically no change in the OCP is observed with the cation concentration. To conclude, the observed dependence of the OCP on the pH is in agreement with the CV data suggesting that the interfacial equilibria are pH-dependent for all studied oxides. As to the Na^+ concentration, its influence on the MnOOH/electrolyte interface is the strongest. This will be further corroborated in Chapter 5, where the influence of the electrolyte composition on the ORR electrocatalysis will be discussed.

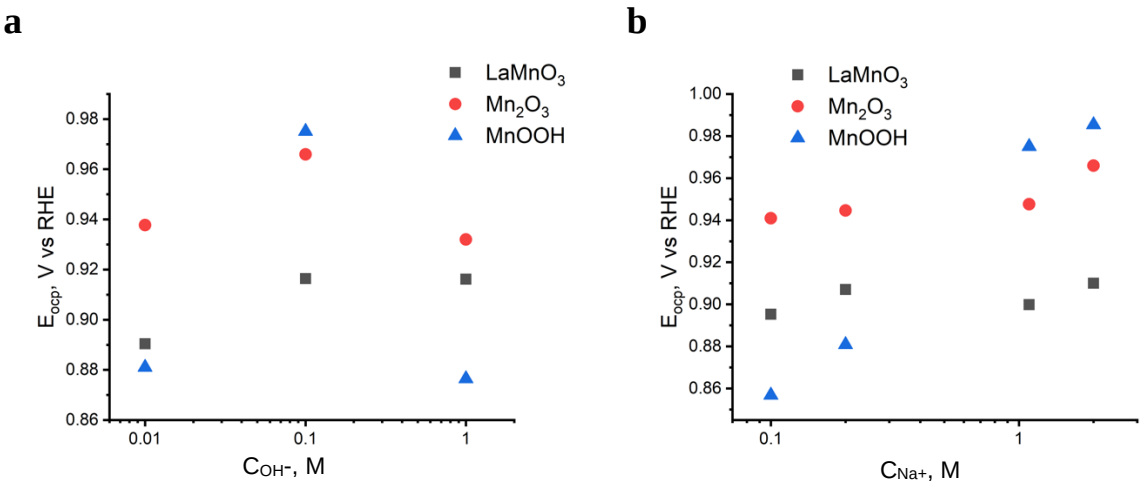

Fig. 65. Open-circuit potential for $LaMnO_3$, Mn_2O_3 and MnOOH in N_2-purged solutions with varying pH and constant Na^+ concentration (a) and in solutions with varying Na^+ concentration at constant pH (b).

4.3.2. Influence of the scan rate on the interfacial recharging

Study of the influence of the scan rate on the CV is a useful tool for delineating 'slow' and 'fast' electrochemical steps. Analysis of Fig. 66 leads us to conclude that for $LaMnO_3$ and Mn_2O_3 the interfacial Mn(IV)/Mn(III) red-ox transition is fast in any of the electrolytes investigated (*cf.* little influence of the scan rate on the CV shape and on the pseudocapacitance)[5]. In the meantime, for MnOOH the charge under the CV and thus pseudocapacitance strongly decrease with the scan rate suggesting contribution of some slow interfacial recharging steps. This may be tentatively attributed to the Na^+ intercalation in the subsurface and the bulk of the MnOOH oxide. Furthermore, decrease of the OH^- concentration leads to slowing down of the interfacial redox transition (step 1 of the ORR mechanism in Figure 25 of Chapter 1). This information will be useful for the analysis of the pH and Na^+ concentration on the kinetics of the ORR.

[5] Changes observed in 0.1 M NaOH (without the $NaClO_4$ addition) may be attributed to ohmic losses increasing with the scan rate.

$LaMnO_3$

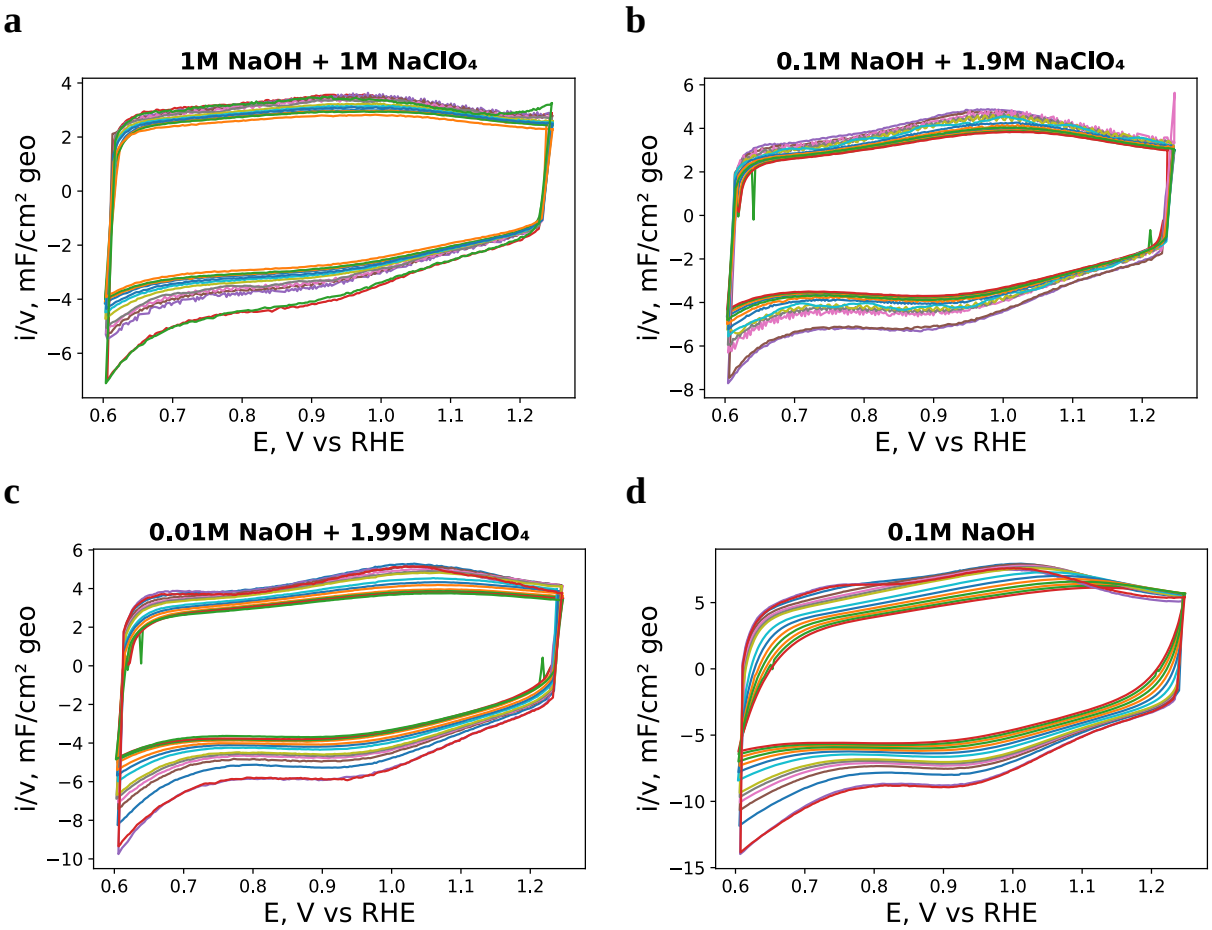

Mn_2O_3

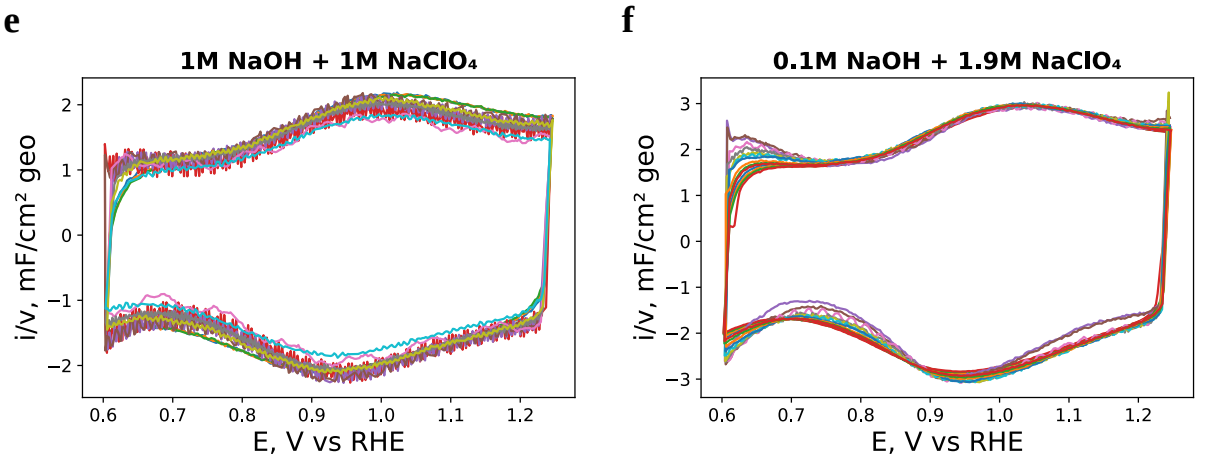

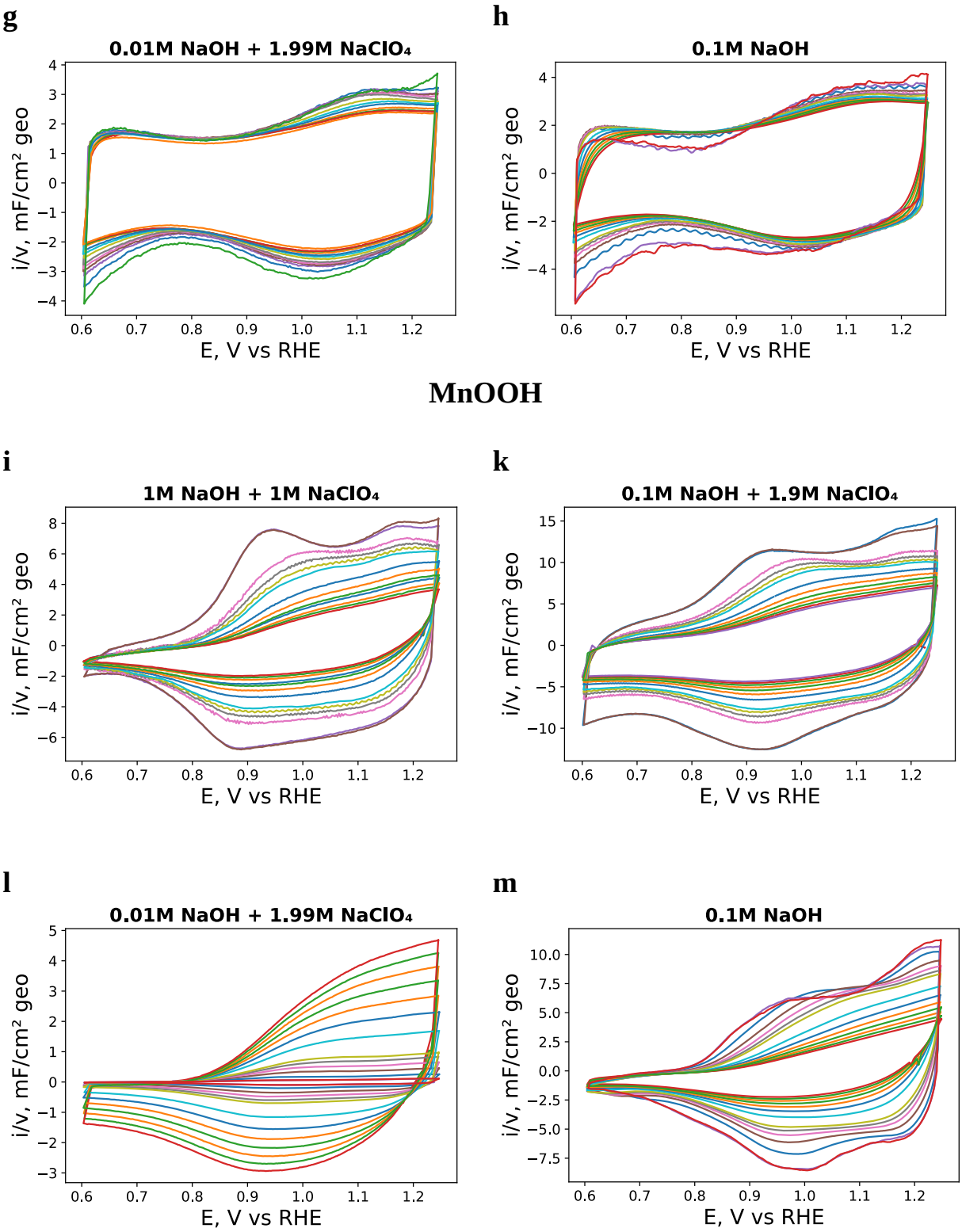

Fig. 66. Cyclic voltammograms with variable scan rate (from 10 to 1000 mV s^{-1}) for GC-supported thin films of oxide/carbon composites in N_2-purged electrolytes of different composition for $LaMnO_3$ (a-d), Mn_2O_3 (e-h), MnOOH (i-m).Currents are normalized to the scan rate and to the geometric area of the electrode. Loadings are 91 μg cm^{-2} oxide and 91 μg cm^{-2} carbon.

4.3.3. Acid-base titrations

In this section we study acid-base properties of the Mn oxides, that is surface acid-base equilibria, which do not involve changes in the Mn oxidation state. These could be expressed as follows in acidic medium:

$$Mn(III)OH_2 \rightarrow Mn(III)OH + H^+ \text{ and} \quad (78)$$

$$Mn(III)OH \rightarrow Mn(III)O^- + H^+, \quad (79)$$

or, alternatively, in base:

$$Mn(III)OH_2 + OH^- \rightarrow Mn(III)OH + H_2O \quad (80)$$

$$Mn(III)OH + OH^- \rightarrow Mn(III)O^- + H_2O \quad (81)$$

Titration curves for $LaMnO_3$, Mn_2O_3, MnOOH and Sibunit carbon in different standard solutions (0.02 M NaOH + x M $NaClO_4$) are presented in Figures 67. For all studied materials the titration curves differ from the background (BG) curves measured in the absence of oxide (or carbon) suspension, confirming that dispersed particles interact with the electrolyte through acid-base equilibria (*cf.* Eqs. 80, 81) and this interaction affects the electrolyte pH.[6]

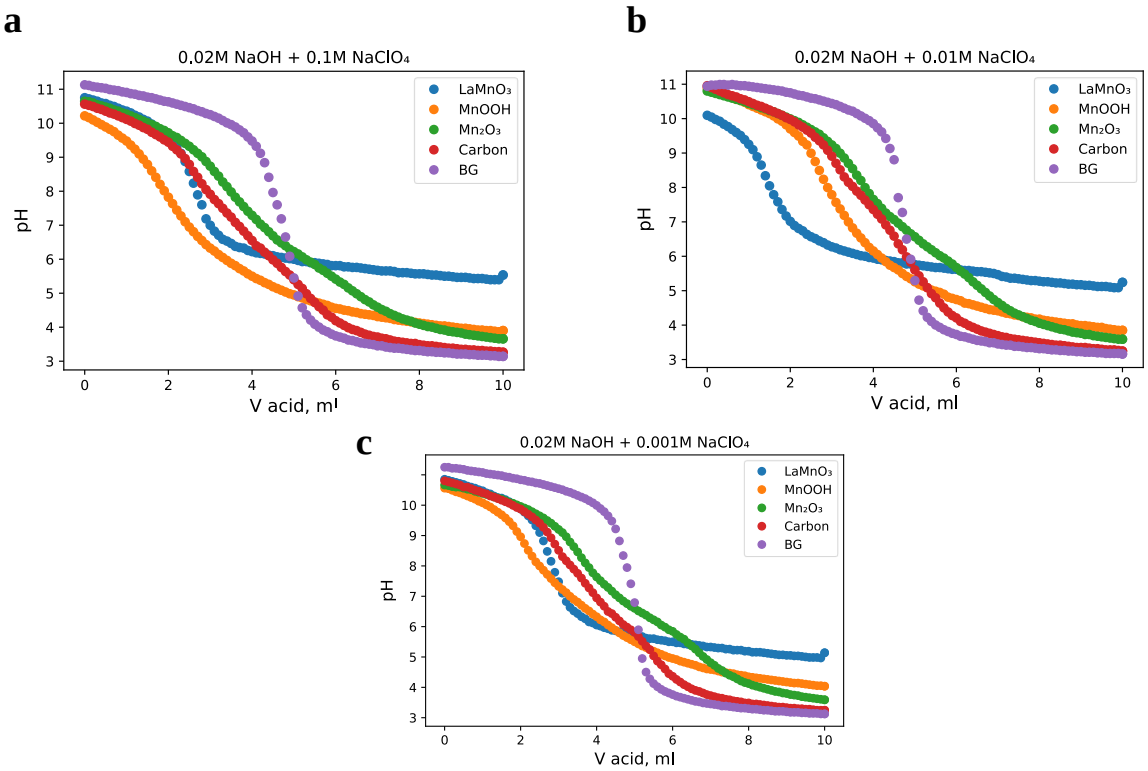

[6] Note that the NaOH concentration of the standard solution has been chosen such as to make the deviation from the background curve observable.

Fig. 67. Titration curves for $LaMnO_3$, MnOOH, Mn_2O_3, Sibunit carbon, and oxide-free solution (background - BG) for various background solution (constant pH, different ionic strength).

It is interesting to note that in titration curves for all studied materials (Fig. 67), with the exception of $LaMnO_3$, two inflection points can be observed, which is probably due to the occurrence of several acid-base equilibria on the catalyst surface [24].

By comparing the titration curves for the background solution and the background solution with dispersed oxide (or carbon), the surface charge (σ) was calculated using equation 61 of section 2.6 Chapter 2. In Figure 68 the surface charge determined from the titration curves is plotted against the electrolyte pH. The point PZC can be determined from the surface charge plots (Figure 68) at σ = 0. These values are tabulated in Table 13.

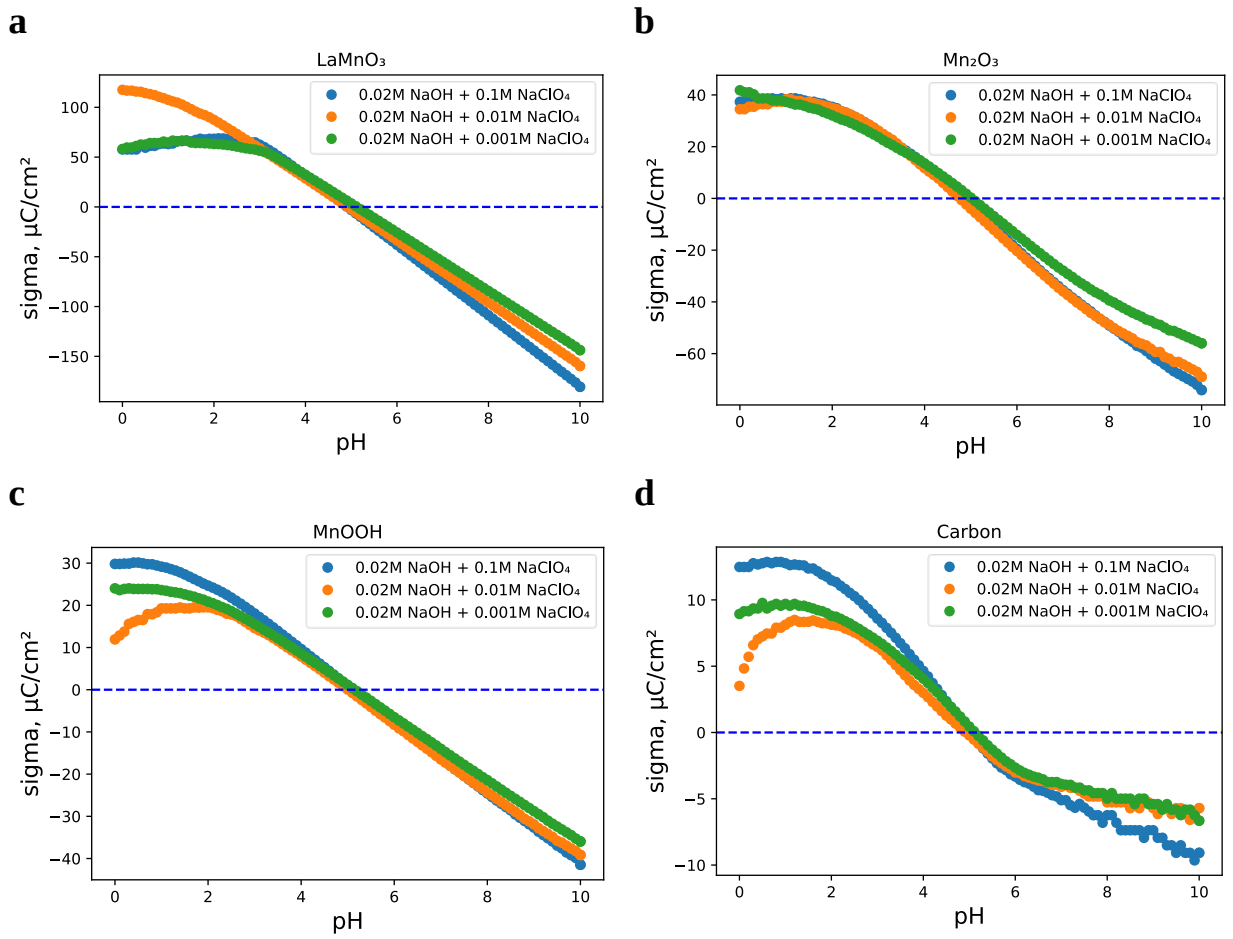

Fig. 68. Surface charge versus pH determined from titration curves for $LaMnO_3$ (a), Mn_2O_3 (b), MnOOH (c), and Sibunit carbon (d).

One may see that for all studied oxides the isoelectric point is below 7. This means that in alkaline media all of them are negatively charged and thus interact with Na^+. Adsorption of Na^+ on MnOOH was confirmed by low temperature XPS studies in Refs [37,38].

Table 13. Point of zero charge (PZC) determined from titration curves

Solution	**$LaMnO_3$**	**Mn_2O_3**	**MnOOH**	**Sibunit carbon**
0.02M NaOH + 0.1M $NaClO_4$	6.01	6.34	4.90	5.38
0.02M NaOH + 0.01M $NaClO_4$	5.77	6.80	5.25	5.78
0.02M NaOH + 0.001M $NaClO_4$	5.67	6.58	5.40	5.63
Average	**5.82**	**6.57**	**5.18**	**5.38**

By analysing the charge curves (Fig. 68) derived from the titration curves, strong differences in the sigma value at pH = 10 can be observed for the studied materials. This charge corresponds to the number of acid centres capable of participating in acid-base equilibria. It can be noticed that the highest value of the surface charge is observed for $LaMnO_3$ and is about 160 μC cm^{-2}, followed by Mn_2O_3 with a charge of 70 μC cm^{-2}, the lowest value among the oxides is 40 μC cm^{-2}, for MnOOH. For carbon a value of 10 μC cm^{-2} is obtained.

The concentration of acid sites was calculated from the amount of OH^- reacted (pH change compared to the solution without the oxide) with the acid sites on the oxide surface after dispersing it in the initial solution of NaOH. These values are listed in Table 14. It should be noted that the concentration of centers correlates with the charge determined from the titration curves. The highest concentration of acid sites among the oxides was determined for $LaMnO_3$, the lowest for MnOOH. In this case, if we compare the concentration of acid sites with the surface concentration of Mn on the surface (defined as the volume concentration of Mn to the power of 2/3), then we can notice a strong difference for MnOOH and Mn_2O_3 and a fairly good correlation between these values for $LaMnO_3$. Such strongly underestimated concentrations of acid sites for Mn_2O_3 and MnOOH may be associated with low acidity constants, due to which, at pH = 10, most of them remain protonated.

Table 14. Concentration of acid sites on the surface of the studied compounds, calculated from titration curves and compared to the Mn surface density estimated from the volume density of Mn cations in the corresponding oxides.

Materials	Concentration of the acid centers (10^{18} m^{-2})	Mean surface density of Mn cations n_s^*, (10^{18} m^{-2})
$LaMnO_3$	5.37	6.4
Mn_2O_3	2.75	11
MnOOH	1.51	9.6
Sibunit	0.93	--

* Estimated from the volume concentration of Mn in the corresponding crystal structure to the power of 2/3.

On the other hand, the difference between the calculated number of acid-base centers and that determined experimentally may have a different nature. For MnOOH and Mn_2O_3, when studying the red-ox centers, it was suggested that the both -OH and -ONa centers are present on the oxide surface. In this regard, if some of the protons are replaced by Na^+, then they are inaccessible for the acid/base titration.

4.4. Conclusions

The effect of the electrolyte composition on the state of the solid/liquid interface was studied for $LaMnO_3$, Mn_2O_3, MnOOH and carbon. The acid-base phenomena were studied by acid-base titrations of materials' powders in dilute NaOH electrolyte, while and redox properties were investigated with cyclic voltammetry in electrolytes with different OH^- concentration (at a constant ionic strength) and different Na^+ concentration (at a constant pH).

The results of the cyclic voltammetry measurements indicate that both the OH^- concentration (at a constant ionic strength) and Na^+ concentration (at a constant pH) affect the interfacial Mn(III)/Mn(IV) redox transition, and the effects are not the same for different oxides. Thus, when changing pH, the position of the $LaMnO_3$ redox peaks remained practically unchanged on the RHE scale, which agrees with the first step of the previously proposed (see Ref. [8]) ORR mechanism ($Mn(IV)=O + H_2O + e^- \rightarrow Mn(III)\text{-}OH + OH^-$). For MnOOH and Mn_2O_3 the influence of pH is different suggesting more complex phenomena occurring at the interface. So, for Mn_2O_3 a shift of ~110 mV/pH was found which may be due to the participation of more than one OH^- in

the interfacial redox process. For MnOOH the presence of two pairs of peaks with different pH dependence was demonstrated, which may be related to the presence of two types of active centers on the surface, namely Mn(III)OH or Mn(III)ONa. When studying the effect of the Na^+ concentration, it was shown that the ratio of these two peaks for MnOOH changes with variations in the Na^+ concentration. This can be attributed to the H^+/Na^+ substitution occurring on the MnOOH/electrolyte interface resulting in the equilibrium shift between Mn(III)OH or Mn(III)ONa centers. The position of the Mn_2O_3 redox peaks also changes with changes in the Na+ concentration. From this we conclude that Na^+ is directly involved in the interfacial recharging, which is supposed to be the first step of the ORR mechanism:

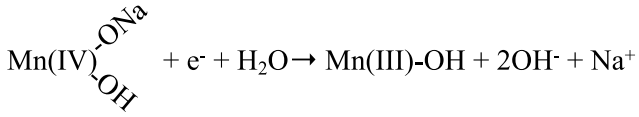

(82)

Cyclic voltammetry experiments performed with different scan rates indicate that the interfacial Mn(III)/Mn(IV) recharging is fast for Mn_2O_3 and $LaMnO_3$. Different behavior was observed for MnOOH, with an important contribution of slow processes, which may be attributed to the H^+/Na^+ intercalation. These processes of Na^+ intercalation/deintercalation can lead to structural changes, in particular to the change of unit cell parameters at the oxide/electrolyte interface.

Titration experiments have shown that the point of zero charge for all of the studied oxides is lower than 7, from which it can be concluded that in alkaline electrolytes they are all negatively charged. For Mn_2O_3, MnOOH and carbon the concentration of acid-base centres on the surface is shown to differ strongly from the one calculated from the crystallographic density of Mn cations, which is probably due to their low acidity constants.

The information gathered in Chapter 4 regarding redox and acid-base equilibria will be applied in Chapter 5 in order to understand the influence of pH and cation concentration on the ORR kinetics.

4.5. References

[1] N.M. Markovic, Interfacing electrochemistry, Nature Mater. 12 (2013) 101–102. https://doi.org/10.1038/nmat3554.

[2] S. Ardizzone, G. Fregonara, S. Trasatti, “Inner” and “outer” active surface of RuO_2 electrodes, Electrochimica Acta. 35 (1990) 263–267. https://doi.org/10.1016/0013-4686(90)85068-X.

[3] S. Ardizzone, S. Trasatti, Interfacial properties of oxides with technological impact in electrochemistry, Advances in Colloid and Interface Science. 64 (1996) 173–251. https://doi.org/10.1016/0001-8686(95)00286-3.

[4] O.A. Petrii, Surface electrochemistry of oxides: Thermodynamic and model approaches, Electrochimica Acta. 41 (1996) 2307–2312. https://doi.org/10.1016/0013-4686(96)00060-6.

[5] F.H.B. Lima, M.L. Calegaro, E.A. Ticianelli, Electrocatalytic activity of manganese oxides prepared by thermal decomposition for oxygen reduction, Electrochimica Acta. 52 (2007) 3732–3738. https://doi.org/10.1016/j.electacta.2006.10.047.

[6] Y. Gorlin, B. Lassalle-Kaiser, J.D. Benck, S. Gul, S.M. Webb, V.K. Yachandra, J. Yano, T.F. Jaramillo, In Situ X-ray Absorption Spectroscopy Investigation of a Bifunctional Manganese Oxide Catalyst with High Activity for Electrochemical Water Oxidation and Oxygen Reduction, J. Am. Chem. Soc. 135 (2013) 8525–8534. https://doi.org/10.1021/ja3104632.

[7] V. Celorrio, A.S. Leach, H. Huang, S. Hayama, A. Freeman, D.W. Inwood, D.J. Fermin, A.E. Russell, Relationship between Mn Oxidation State Changes and Oxygen Reduction Activity in (La,Ca)MnO_3 as Probed by In Situ XAS and XES, ACS Catal. 11 (2021) 6431–6439. https://doi.org/10.1021/acscatal.1c00997.

[8] A.S. Ryabova, F.S. Napolskiy, T. Poux, S.Ya. Istomin, A. Bonnefont, D.M. Antipin, A.Ye. Baranchikov, E.E. Levin, A.M. Abakumov, G. Kéranguéven, E.V. Antipov, G.A. Tsirlina, E.R. Savinova, Rationalizing the Influence of the Mn(IV)/Mn(III) Red-Ox Transition on the Electrocatalytic Activity of Manganese Oxides in the Oxygen Reduction Reaction, Electrochimica Acta. 187 (2016) 161–172. https://doi.org/10.1016/j.electacta.2015.11.012.

[9] A.S. Ryabova, S.Ya. Istomin, K.A. Dosaev, A. Bonnefont, J. Hadermann, N.A. Arkharova, A.S. Orekhov, R.P. Sena, V.A. Saveleva, G. Kéranguéven, E.V. Antipov, E.R. Savinova, G.A. Tsirlina, Mn_2O_3 oxide with bixbyite structure for the electrochemical oxygen reduction reaction in alkaline media: Highly active if properly manipulated, Electrochimica Acta. 367 (2021) 137378. https://doi.org/10.1016/j.electacta.2020.137378.

[10] A.S. Ryabova, A. Bonnefont, P. Zagrebin, T. Poux, R. Paria Sena, J. Hadermann, A.M. Abakumov, G. Kéranguéven, S.Y. Istomin, E.V. Antipov, G.A. Tsirlina, E.R. Savinova, Study of Hydrogen Peroxide Reactions on Manganese Oxides as a Tool To Decode the Oxygen Reduction Reaction Mechanism, ChemElectroChem. 3 (2016) 1667–1677. https://doi.org/10.1002/celc.201600236.

[11] A.S. Ryabova, A. Bonnefont, P.A. Simonov, T. Dintzer, C. Ulhaq-Bouillet, Y.G. Bogdanova, G.A. Tsirlina, E.R. Savinova, Further insights into the role of carbon in manganese

oxide/carbon composites in the oxygen reduction reaction in alkaline media, Electrochimica Acta. 246 (2017) 643–653. https://doi.org/10.1016/j.electacta.2017.06.017.

[12] M. Toupin, T. Brousse, D. Bélanger, Charge Storage Mechanism of MnO_2 Electrode Used in Aqueous Electrochemical Capacitor, Chem. Mater. 16 (2004) 3184–3190. https://doi.org/10.1021/cm049649j.

[13] S. Devaraj, N. Munichandraiah, Effect of Crystallographic Structure of MnO_2 on Its Electrochemical Capacitance Properties, J. Phys. Chem. C. 112 (2008) 4406–4417. https://doi.org/10.1021/jp7108785.

[14] D. Chen, D. Ding, X. Li, G.H. Waller, X. Xiong, M.A. El-Sayed, M. Liu, Probing the Charge Storage Mechanism of a Pseudocapacitive MnO_2 Electrode Using in Operando Raman Spectroscopy, Chem. Mater. 27 (2015) 6608–6619. https://doi.org/10.1021/acs.chemmater.5b03118.

[15] H.Y. Lee, J.B. Goodenough, Supercapacitor Behavior with KCl Electrolyte, Journal of Solid State Chemistry. 144 (1999) 220–223. https://doi.org/10.1006/jssc.1998.8128.

[16] C. Xu, C. Wei, B. Li, F. Kang, Z. Guan, Charge storage mechanism of manganese dioxide for capacitor application: Effect of the mild electrolytes containing alkaline and alkaline-earth metal cations, Journal of Power Sources. 196 (2011) 7854–7859. https://doi.org/10.1016/j.jpowsour.2011.04.052.

[17] S. Wen, J.-W. Lee, I.-H. Yeo, J. Park, S. Mho, The role of cations of the electrolyte for the pseudocapacitive behavior of metal oxide electrodes, MnO_2 and RuO_2, Electrochimica Acta. 50 (2004) 849–855. https://doi.org/10.1016/j.electacta.2004.02.056.

[18] J.T. Mefford, W.G. Hardin, S. Dai, K.P. Johnston, K.J. Stevenson, Anion charge storage through oxygen intercalation in $LaMnO_3$ perovskite pseudocapacitor electrodes, Nature Mater. 13 (2014) 726–732. https://doi.org/10.1038/nmat4000.

[19] T.-C. Liu, W.G. Pell, B.E. Conway, S.L. Roberson, Behavior of Molybdenum Nitrides as Materials for Electrochemical Capacitors: Comparison with Ruthenium Oxide, J. Electrochem. Soc. 145 (1998) 1882. https://doi.org/10.1149/1.1838571.

[20] J. Wang, J. Polleux, J. Lim, B. Dunn, Pseudocapacitive Contributions to Electrochemical Energy Storage in TiO_2 (Anatase) Nanoparticles, J. Phys. Chem. C. 111 (2007) 14925–14931. https://doi.org/10.1021/jp074464w.

[21] I.S. Filimonenkov, S.Ya. Istomin, B. Rotonnelli, J.-J. Gallet, F. Bournel, E.V. Antipov, E.R. Savinova, G.A. Tsirlina, Interfacial recharging behavior of mixed Co, Mn-based perovskite oxides, Electrochimica Acta. 398 (2021) 139257. https://doi.org/10.1016/j.electacta.2021.139257.

[22] S.M. Ahmed, Studies of the double layer at oxide-solution interface, The Journal of Physical Chemistry. 73 (1969) 3546–3555. https://doi.org/10.1021/j100845a004.

[23] M. Kosmulski, Surface charging and point of zero charge, CRC Press, 2009.

[24] J.A. Davis, R.O. James, J.O. Leckie, Surface ionization and complexation at the oxide/water interface: I. Computation of electrical double layer properties in simple electrolytes, Journal of Colloid and Interface Science. 63 (1978) 480–499. https://doi.org/10.1016/S0021-9797(78)80009-5.

[25] A. Daghetti, G. Lodi, S. Trasatti, Interfacial properties of oxides used as anodes in the electrochemical technology, Materials Chemistry and Physics. 8 (1983) 1–90. https://doi.org/10.1016/0254-0584(83)90020-2.

[26] A.G. W. Janusz, Electrical double layer, Physicochemical Problems of Mineral Processing. 35 (2001) 31–41.

[27] K. Akhtar, S. Sajjad, A. Shah, M. Gul, I.U. Haq, N. Zubair, Synthesis and characterization of uniform fine particles of manganese oxide and its morphological stability towards calcination rates Synthesis and Characterization of uniform Fine particles of Manganese Oxide and its Morphological Stability towards Calci, (2018).

[28] A. Khan, K. Zhang, P. Sun, H. Pan, Y. Cheng, Y. Zhang, High performance of the A-Mn_2O_3 nanocatalyst for persulfate activation: Degradation process of organic contaminants via singlet oxygen, Journal of Colloid and Interface Science. 584 (2021) 885–899. https://doi.org/10.1016/j.jcis.2020.10.021.

[29] S.D. Škapin, V. Čadež, D. Suvorov, I. Sondi, Formation and properties of nanostructured colloidal manganese oxide particles obtained through the thermally controlled transformation of manganese carbonate precursor phase, Journal of Colloid and Interface Science. 457 (2015) 35–42. https://doi.org/10.1016/j.jcis.2015.06.041.

[30] D.A. Shaughnessy, H. Nitsche, C.H. Booth, D.K. Shuh, G.A. Waychunas, R.E. Wilson, H. Gill, K.J. Cantrell, R.J. Serne, Molecular Interfacial Reactions between Pu(VI) and Manganese Oxide Minerals Manganite and Hausmannite, Environ. Sci. Technol. 37 (2003) 3367–3374. https://doi.org/10.1021/es025989z.

[31] A.A. Souza, J.B.R. Fernandes, J.F.S. Ribeiro, M.J.B. Souza, A.M. Garrido Pedrosa, Development of $LaMnO_3$ and $LaNiO_3$ type materials with calcium doping by the modified proteic method and evaluation for the dye removal efficiency, Cerâmica. 67 (2021) 406–413. https://doi.org/10.1590/0366-69132021673843146.

[32] É.V. Nascimento, A.M. Garrido Pedrosa, M.J.B. Souza, Development of $La_xCa_{1-x}MnO_3$ materials for Bezaktiv Blue removal in aqueous media, Water Science and Technology. 83 (2021) 2793–2808. https://doi.org/10.2166/wst.2021.174.

[33] C. Appel, L.Q. Ma, R. Dean Rhue, E. Kennelley, Point of zero charge determination in soils and minerals via traditional methods and detection of electroacoustic mobility, Geoderma. 113 (2003) 77–93. https://doi.org/10.1016/S0016-7061(02)00316-6.

[34] C. Su, D.L. Suarez, In Situ Infrared Speciation of Adsorbed Carbonate on Aluminum and Iron Oxides, Clays Clay Miner. 45 (1997) 814–825. https://doi.org/10.1346/CCMN.1997.0450605.

[35] R. Beckwith, R. Reeve, Studies on soluble silica in soils. I. The sorption of silicic acid by soils and minerals, Soil Res. 1 (1963) 157. https://doi.org/10.1071/SR9630157.

[36] U. Schwertmann, H. Fechter, The point of zero charge of natural and synthetic ferrihydrites and its relation to adsorbed silicate, Clay Minerals. 17 (1982) 471–476. https://doi.org/10.1180/claymin.1982.017.4.10.

[37] M. Ramstedt, B.M. Andersson, A. Shchukarev, S. Sjöberg, Surface Properties of Hydrous Manganite (γ-MnOOH). A Potentiometric, Electroacoustic, and X-ray Photoelectron Spectroscopy Study, Langmuir. 20 (2004) 8224–8229. https://doi.org/10.1021/la0496338.

[38] M. Ramstedt, A.V. Shchukarev, S. Sjöberg, Characterization of hydrous manganite (γ-MnOOH) surfaces—an XPS study, Surface and Interface Analysis. 34 (2002) 632–636. https://doi.org/10.1002/sia.1376.

5. Effect of the Electrolyte Composition on the ORR Kinetics on Mn oxides

5.1 Introduction

As a rule, the study of the oxygen reduction reaction on transition metal oxides is carried out in alkali solutions of high concentration (usually 1 or 0.1 M), which is associated with the instability of many of the transition metal oxides in acidic solutions, as well as with the fact that with a decrease in the concentration of the background electrolyte, the ohmic resistance of the cell increases greatly. In addition, when approaching neutral pH values, the local concentration of OH^- anions in the vicinity of the electrode may change, due to their formation during the oxygen reduction reaction (see equation 2) [1]. Despite the fact that the concentration of OH^- may have a significant impact on the kinetics of the ORR, targeted research in this area has not yet been carried out for transition metal oxides. The small number of studies of the ORR as a function of pH is all the more surprising since electrolyte pH is one of the most important factors that can significantly affect the rate of reactions in electrocatalysis in general, and in ORR electrocatalysis in particular. As shown in Chapter 1, studying the effect of pH on the rate of the ORR on carbon and platinum provided some evidence regarding the most likely key steps in the ORR mechanism.

On the other hand, Chapter 4 shows that not only pH affects the electrochemical behavior of oxide catalysts, but also the cationic composition of the electrolyte (both cation type and concentration). The effect of cations on the kinetics of the ORR on oxide catalysts is considered in the literature to an even lesser extent than the effect of pH. Meanwhile, for the reverse reaction, namely the OER, a number of studies have been published that consider the effect of electrolyte on the reaction kinetics for oxide catalysts. Although OER is beyond the scope of this work, often the OER mechanism (or its elementary steps) is considered as the reverse of the ORR mechanism, which makes it useful to be considered in the literature review of this chapter.

Thus, in this chapter, we will consider possible factors that influence electrocatalytic behavior of oxides and metals (Pt, Au) in the reactions of the oxygen reduction and evolution upon variation of the pH and cationic composition of the electrolyte.

5.1.1 Literature review

5.1.1.1 Role of pH in electrocatalysis

Electrolyte pH can have a multifaceted effect on electrode processes. First, pH can affect thermodynamic equilibrium (as for the ORR and OER, for example). Second, pH can influence the mechanism of the process. Third, the products/intermediates can undergo acid–base dissociation, which, in turn, can affect their interaction with the electrode surface. And, finally, with a change in pH, the charge of the electrode surface and, accordingly, the composition of the adsorption layer may change.

Isolation of thermodynamic effects

Important in studying the effect of pH on electrocatalytic systems is the separation of kinetic and thermodynamic effects. While thermodynamic effects are easy to predict because they obey the Nernst equation (for a step involving the same number of electrons and protons, the potential shifts by 59 mV per unit change in pH), kinetic effects are the subject of much research on the kinetics of electrochemical processes. When choosing a potential scale, one can either take into account the thermodynamic contribution (by choosing, for example, the RHE scale) or, vice versa, reveal it (by choosing, for example, the SHE scale), as shown in Fig. 69 for electrochemical transformations of hydrogen peroxide on a single crystal of platinum. Hydrogen peroxide can be either the end product of the oxygen reduction or an intermediate. Therefore, the study of peroxide reactions makes it possible to answer many questions regarding the processes occurring on the catalyst surface during the ORR.

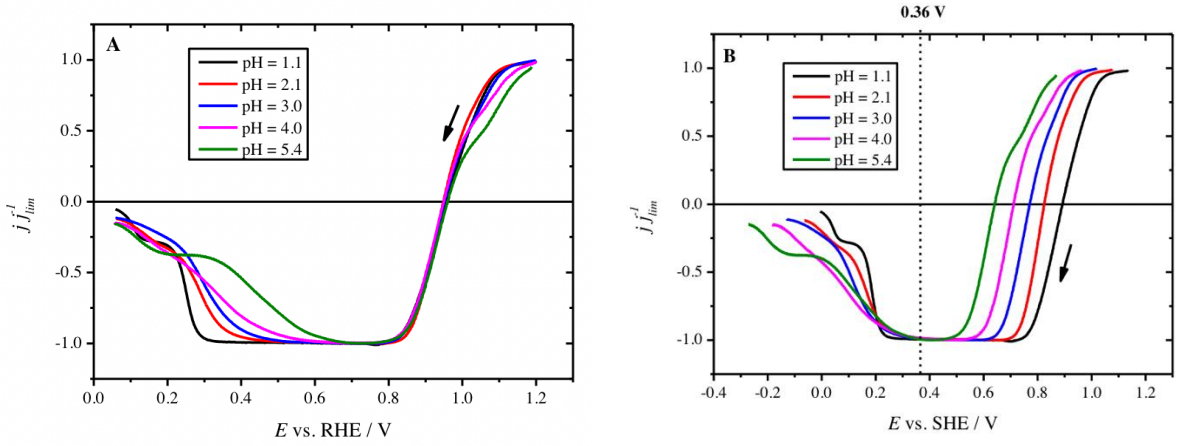

Fig. 69 Normalized polarization curves for the HPRR and HPOR on Pt(111) in 1.7 mM H_2O_2 with pH ≤ 5.4 prepared with NaF/$HClO_4$ mixtures on the RHE scale (A) and on the SHE scale (B). Reproduced from Ref. [2].

The effect of pH on the reaction kinetics and the mechanism

On the other hand, for each individual step, it is also possible to theoretically determine the kinetic potential shift with a change in pH. Thus, Koper in his work [3] analyzes in detail how a change in pH affects an electrode reaction comprised of the steps involving a proton and an electron transfer. Elementary steps can proceed either through simultaneous proton and electron transfer (proton-coupled or concerted electron transfer) or via sequential transfer of an electron and a proton (non-concerted transfer), Fig. 70.

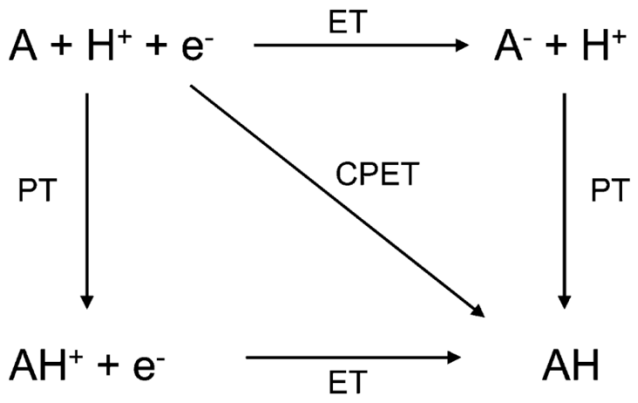

Fig. 70 Square scheme for proton-coupled electron transfer. ET - electron transfer, PT - proton transfer, CPET - concerted proton–electron transfer. Reproduced from Ref. [3].

Separate proton and electron transfer has been shown to result in a strong dependence of the electrocatalytic reaction rate on pH. The results obtained were compared with experimental examples of proton-electron transfer in heterogeneous electrocatalysis, and it was shown that the coupled process is more likely when there is a strong interaction between the catalyst surface and the key reaction intermediate. Such an interaction occurs, for example, for Pt in the process of the oxygen reduction. The absence of an effect of pH on the catalytic activity of Pt in the electroreduction of oxygen (on the RHE scale) [4]confirms the occurrence of a coupled process of proton-electron transfer. In the case of a weak interaction between the catalyst surface and the key intermediate, the interaction of the catalyst with the electrolyte begins to play a more important role. In this case, electrolyte ions are stabilized on the catalyst surface, and the pH of the medium has a greater effect on the reaction rate. This situation is realized on a catalyst such as Au [5], which is practically inactive in the ORR in an acidic media, but active in an alkaline one. It has been demonstrated that for polycrystalline gold the ‘onset’ of the ORR is strongly pH-dependent on the RHE potential scale but practically pH-independent on the SHE scale (see Ref. [5] and references therein). Such a behavior was attributed to the $O_2+e^- \rightarrow O_2^-$ being the rds. Thus, plotting

ORR voltammograms on the RHE and on the SHE scales has been instrumental in distinguishing the proton-coupled (pH-independent on the RHE-scale) and decoupled (pH-independent on the SHE scale) electron transfer steps (for a multi-electron reaction such as ORR this applies to the rds). However, such a view neglects the EDL (electric double layer effects) and may thus be oversimplified.

Indeed, Huang et al [6] performed a computation modeling that integrates density-functional theory (DFT) calculations for elementary reaction steps, microkinetic modeling for multistep kinetics, and continuum modeling for the EDL structure, and found that EDL effects may cause significant dependence of the OER kinetics even within the framework of a proton-coupled electron transfer mechanism. They documented the so-called ‘cation overcrowding’ effect whereby at a high negative electrode charge there is cation accumulation and anion depletion, the latter being pH and cation-dependent.

In the field of electrocatalytic oxygen evolution on metal oxides, the study of the influence of pH is a common practice in establishing the reaction mechanism [7–9]. Currently, two main mechanisms of the oxygen evolution on perovskites (but also on other transition metal oxides) are proposed: with and without the participation of lattice oxygen (Fig. 71).

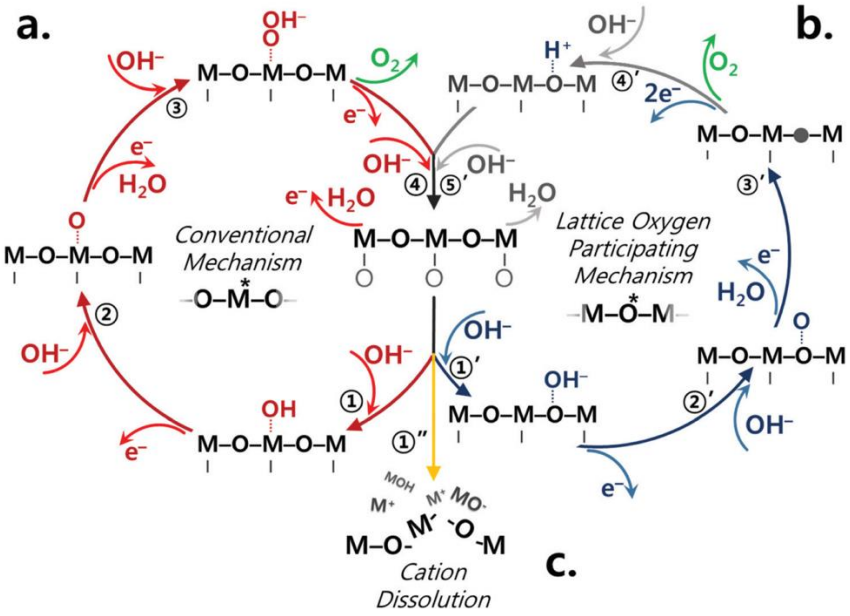

Fig. 71 Conventional adsorbate (a) and lattice oxygen participating (b) oxygen evolution mechanisms on perovskite catalysts. Reproduced from Ref. [9].

It has been demonstrated that in the case of the participation of lattice oxygen, the catalytic activity significantly changes with the pH. On the contrary, with the conventional adsorbate (without the participation of lattice oxygen) OER mechanism, there is no dependence on pH (Fig.

72). The use of pH dependence for decoupling the lattice and surface mechanisms of the OER was proposed by Grimaud, citing studies using labeled oxygen (O^{18}) as an evidence.

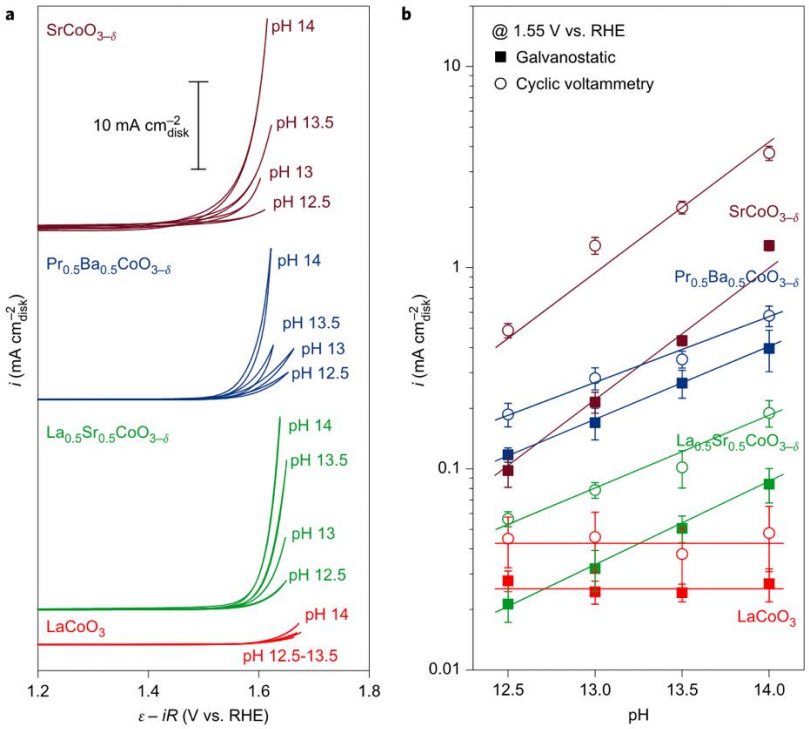

Fig. 72 pH dependence of the OER activity on the RHE scale. (a) CV measurements from O_2-saturated 0.03 M KOH (pH 12.5) to 1 M KOH (pH 14) recorded at 10 mV s^{-1}. (b) Specific OER activity (current normalized by oxide BET surface area) at 1.55 V versus RHE after iR correction as a function of pH. The nominal oxide loading is 0.25 mg_{oxide} cm_{disk}^{-2}. Error bars represent standard deviation of three measurement results. Reproduced from Ref. [8].

Whereas the effect of pH on the reaction of the oxygen evolution on oxide materials has been studied in sufficient detail, only a few works are devoted to the reaction of the oxygen reduction on transition metal oxides. For example, Roche et al. investigated nanosized MnO_x oxides deposited on carbon [10,11]. From the XRD data, it was determined that the obtained samples contain MnO_2 as the main phase, however, their low degree of crystallinity does not allow one to make an unambiguous conclusion about their single-phase nature. It was found that the potential shift per unit pH is 33 mV on the SHE scale. A mechanism for the oxygen reduction reaction was proposed, including Mn(IV) reduction to Mn(III) coupled with the intercalation of a proton (see Chapter 4) into the structure of manganese oxide, followed by adsorption and electroreduction of oxygen.

$$MnO_2 + H_2O + e^- \rightarrow MnOOH + OH^- \quad (83)$$

$$2MnOOH + O_2 \rightarrow (MnOOH)_2\text{---}O_{2\ ads} \quad (84)$$

$$(MnOOH)_2\text{---}O_{2\ ads} + e^- \rightarrow MnOOH\text{---}O_{ads} + OH^- + MnO_2\ (rds) \quad (85)$$

$$MnOOH\text{---}O_{ads} + e^- \rightarrow MnO_2 + OH^- \quad (86)$$

It is also important to mention the effect of pH on the electrocatalytic activity of carbon, since carbon is an integral part of the composite mixture. Carbon was studied in early publications, and studies of the effect of pH made it possible to propose a mechanism of the oxygen reduction reaction without resorting to complex physicochemical methods of analysis that were not available at that time. The bulk of such work has been discussed in Chapter 1. It has been shown that the mechanism of the oxygen reduction reaction strongly depends on the type of carbon material. For example, the catalytic activity of a GC electrode is pH independent both in acid and in base (Fig. 73) [12].

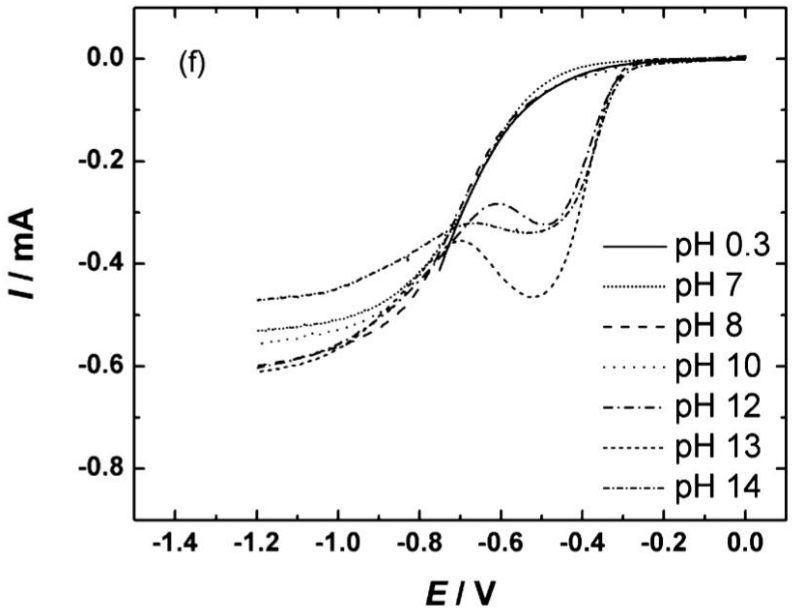

Fig. 73 RDE voltammetry curves for O_2 reduction on bare GC electrodes in O_2 saturated solutions of various pH. The potential is given on the SCE scale. Reproduced from Ref. [12].

Influence of pH on the form of the intermediate

A change in pH can affect not only the reaction mechanism, but also the form of the electrochemically active components and reaction intermediates in solution. Hydrogen peroxide, being an intermediate in the oxygen reduction reaction, can exist in protonated (H_2O_2) or

deprotonated (HO_2^-) forms ($pK_a = 11.65$). In the Pourbaix diagram (Fig. 74) one can see that there is a change in the slope of the two-electron oxygen reduction potential (O_2 / H_2O_2) versus pH near pK_a.

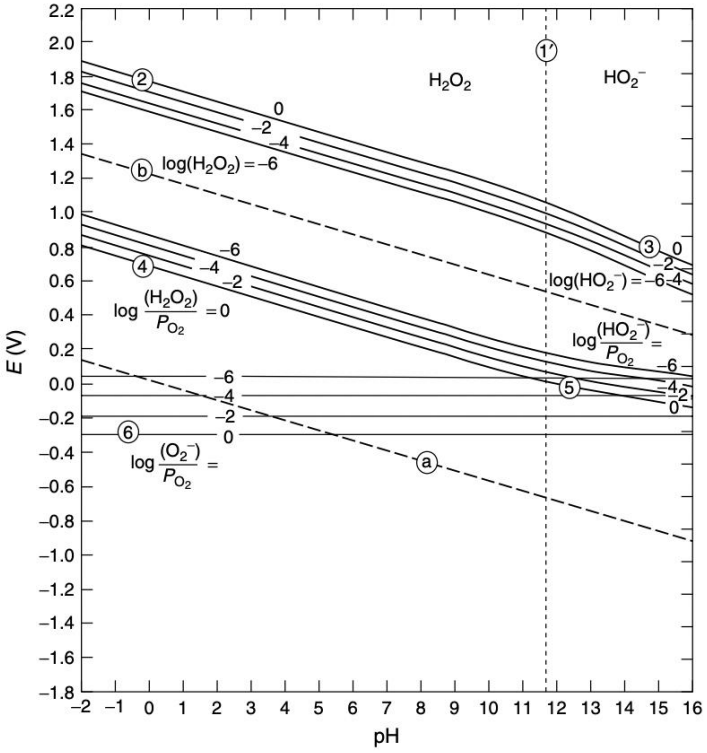

Fig. 74 Pourbaix diagram for oxygen and hydrogen peroxide equilibria also including the equilibrium for the superoxide/oxygen reaction [13].

The negative charge of HO_2^- should promote adsorption on the positively charged surface of the electrode. Thus, when studying the reactions of the hydrogen peroxide electrochemical conversion on the surface of Au(111) Fig. 75, the authors [14] found an increase in the rate of the anodic reaction of hydrogen peroxide oxidation with increasing pH (note that Au(111) is not active in the reduction of hydrogen peroxide). The authors primarily associated this effect with a change in the ratio of two equilibrium forms of hydrogen peroxide - protonated and deprotonated H_2O_2 and HO_2^-, respectively. With an increase in pH, the concentration of the anionic form of hydrogen peroxide naturally increases. The authors assume that the interaction of H_2O_2 with the Au(111) surface is very weak. In an alkaline media, due to the fact that Au has a positive surface charge, the electrostatic interaction promotes the adsorption of the HO_2^- anion and due to this, there is a gain in the activation energy of the reaction. Studying the oxygen reduction reaction on Au, the authors of [5] also concluded that the high catalytic activity of Au in the oxygen reduction reaction in an alkaline medium is associated with the stabilization of negatively charged intermediates on the catalyst surface.

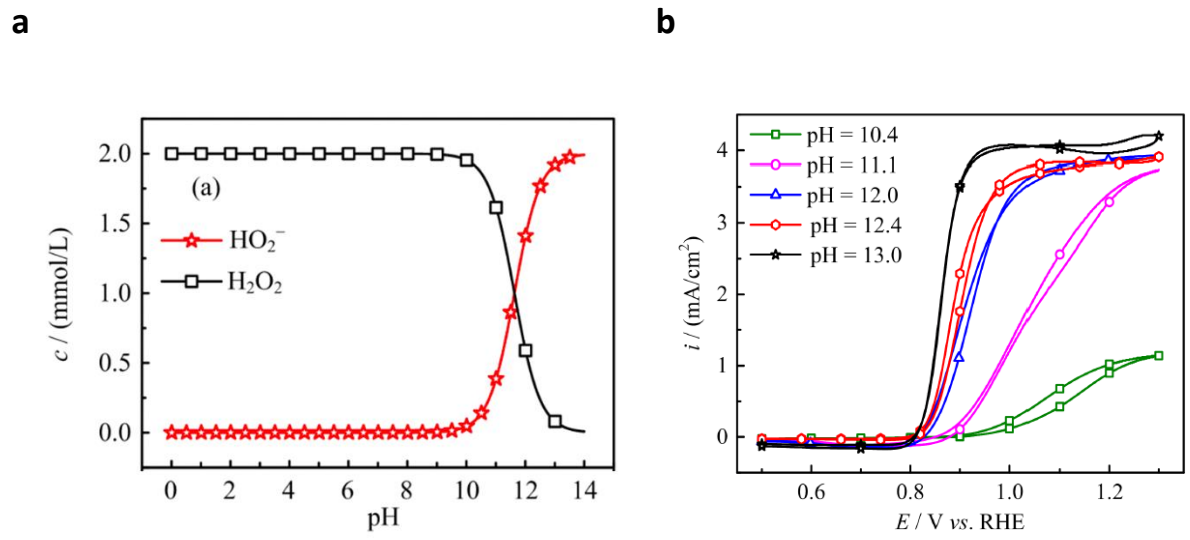

Fig. 75 (a) Concentration the protonated (H_2O_2) and deprotonated (HO_2^-) forms of the hydrogen peroxide as a function of solution pH. The total concentration of the hydrogen peroxide is 2 mmol L^{-1}. (b) Polarization curves for the oxidation of H_2O_2 or HO_2^- on Au(111) in 0.5 mol L^{-1} $NaClO_4$+2 mmol L^{-1} H_2O_2 +x mmol L^{-1} NaOH. pH values are indicated in the figure. Electrode rotation speed: 2500 r min^{-1}, scan rate: 50 mV s^{-1}. Reproduced from Ref. [14].

5.1.1.2 Effect of the cation identity and cation concentration on the electrocatalytic properties

The influence of cations on the kinetics of oxygen reduction is not so obvious, since their direct participation is not reflected in the hypothesized mechanisms of oxygen reactions (oxygen reduction, oxygen evolution, electrochemical conversion of hydrogen peroxide). However, this does not mean that electrolyte cations do not take part in individual elementary steps, and also that they do not have any additional effects on the electrochemical behavior of catalysts. In this work the type of electrolyte cation (Na^+) was kept constant, while its concentration was varied. In this section, we will also consider the influence of the identity of electrolyte cation on the kinetics of electrochemical processes, which recently attracted much attention. Some of the effects that influence the interfacial equilibria were already discussed in Chapter 4, in this part they will be partly repeated in conjunction with their influence on the kinetics of electrochemical processes.

In recent years, much attention has been drawn to the influence of the concentration and composition of the supporting electrolyte on the structure of the electrical double layer at the electrode/electrolyte interface, and, accordingly, on the kinetics of electrode reactions, such as the ORR/OER or HOR/HER. In the meantime, the influence of the supporting electrolyte on the rates

of electrode reactions has already been discussed in early publications by Frumkin, Parsons, Fawcett and others. The influence of the electrolyte concentration on the peroxodisulfate reduction at a mercury electrode can be explained within the so-called Frumkin correction factor. It has been discovered that not only the concentration but also the nature of the cations of the supporting electrolyte strongly affect the electrode kinetics. Indeed, the rate of the peroxodisulfate reduction on a mercury electrode strongly increased in the following sequence: NaF< KF< CsF [15].

Various phenomena have been invoked to explain the influence of the cation concentration and type on the electrode kinetics, among them (i) a cation-dependent potential distribution in the electric double layer and hence the effective potential at the plane where the electron transfer occurs [16], (ii) the ensuing redistribution of the electron density of the adsorbate species [17], (iii) formation of ion pairs (associates) and cation-bridge assisted charge transfer at the interface [18,19], (iv) adsorbate and/or transition state stabilization [20,21], (v) surface blocking due to cation adsorption [22], and (vi) cation-dependent structure and dynamics of interfacial water [17]. Some of these will be discussed below.

When considering the influence of ions on the interface, it is impossible not to consider the effects associated with the structuring of water. So ions are classified as kosmotropes (structure) and chaotropes (destructure) depending on their influence on the structuring of water. The degree of structuring of water is determined mainly by two types of quantities: a change in the viscosity of water due to the addition of salts and the entropy of solvation of ions [23]:

$$\left[\frac{\eta}{\eta*} - 1\right] = A_\eta c^{1/2} + B_\eta c + = \ldots \quad (87)$$

where η_0 is the viscosity of pure water at the same temperature. A is a constant independent of the concentration c; its physical meaning can be explained by the Debye-Hückel theory as a result of screening of counterions at low ionic strengths. The constant B, called the Jones- Dole B coefficient, is the quantity of interest to us, which determines the degree of structuring of water. B > 0 for kosmotropic ions and B < 0 for chaotropic ions (Table 15).

Table 15. The values of the B coefficient at 25 ^{0}C for the most common cations and anions that are part of the background electrolyte in electrocatalysis [24].

Anion	B value	Cation	B value
OH^-	0.122	Li^+	0.146
ClO_4^-	-0.058	Na^+	0.085
F^-	0.107	K^+	-0.009
Cl^-	-0.005	Cs^+	-0.047
Br^-	-0.033		
I^-	-0.073		
NO_3^-	-0.043		
SO_4^{2-}	0.206		

Several effects of cations and anions on the electrocatalyst / electrolyte interface are considered in the literature. So, for example, Marković [25], studying the electrochemical behavior of platinum in solutions of Li, Na, K, Cs hydroxides, demonstrated the importance of non-covalent interactions between cations (and their hydration shell) of the supporting electrolyte and OH species adsorbed on the surface of the catalysts, while stabilizing them. In this case, the strength of interaction decreases in the series Li >> Na > K > Cs, which corresponds to an increase in the energy of hydration of cations and an increase in the concentration of clusters $OH_{ad} – M^+(H_2O)_x$ or $OH_{ad} – H_2O - M^+(H_2O)_x$ Fig. 76. Then, a similar phenomenon was also found for gold, although not as pronounced as for platinum, which the authors attribute to a lower concentration of adsorbed OH on the surface [22]

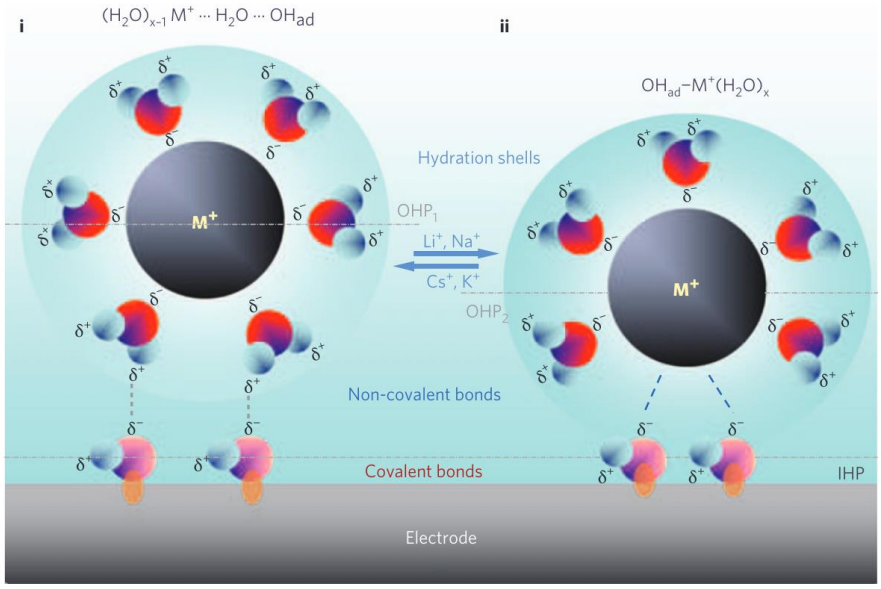

Fig. 76 Model of non-covalent interactions on the electrode surface proposed in Ref. [25].

The authors observed an influence of electrolyte cations on the electrocatalytic activity of platinum and gold in the ORR, which was considered from the point of view of surface blocking by adsorbed cations and a decrease in the availability of catalytic centers for oxygen adsorption. In all cases, the presence of Li^+ initiating hydroxide formation at lower potentials and shifting irreversible oxide formation to even higher electrode potentials compared to Na^+. These effects can be associated with the adsorption energy of OH_{ad}, which arises both due to the oxophilicity of the surface (covalent surface interactions) and due to the stabilization of the associate $OH_{ad}^-M^+(H_2O)$ (non-covalent interactions) [25,26].

It should be noted that the authors [27] suggest a different explanation of the cation influence on the ORR. In Ref. [27], the authors studied perovskites $Ba_{0.5}Sr_{0.5}Co_{0.8}Fe_{0.2}O_{3-\delta}$ and $LaMnO_3$ in the reactions of oxygen reduction and evolution in an alkaline medium. The studies were carried out at pH = 13 using LiOH, NaOH, KOH. A strong effect of the dependence of the kinetic current on the chosen cation was found, the ORR activity decreases with decreasing the cation size ($Li^+ < Na^+ < K^+$), where the activity in KOH is about an order of magnitude higher than in LiOH. The authors also suggest the formation of clusters with the Li cation involved in the elementary steps of the ORR/OER:

$$B^{m+}\text{-}OH^- + O_2 + e^- \rightarrow B^{m+1}\text{-}O_2^{2-} + OH^- \quad (88)$$

$$B^{m+}\text{-}OH^- - Li^+(H_2O)_x + O_2 + e^- \rightarrow B^{m+1}\text{-}O_2^{2-} - Li^+(H_2O)_y + OH^- \quad (89)$$

$$B^{m+1}\text{-}O_2^{2-} + H_2O + e^- \rightarrow B^{m+}\text{-}OOH^- + OH^- \quad (90)$$

$$B^{m+1}\text{-}O_2^{2-}\,Li^+(H_2O)_{x'} + H_2O + e^- \rightarrow B^{m+}\text{-}OOH^-\,Li^+(H_2O)_{y'} + OH^- \quad (91)$$

A similar effect was found by Moureaux et al. [28] where nanosized carbon-supported MnOx was investigated as an ORR catalyst in highly concentrated KOH and LiOH. The authors attribute this to two factors: i) The strong interaction of Li with oxygen stabilizes Mn(III), which prevents the electrochemical transition of Mn(III) to Mn(IV). ii) Also, Li stabilizes the peroxide anions formed during the reaction, which makes the $2e^-$ reaction pathway preferable.

Another factor that can affect the electrocatalytic activity is the specific adsorption of cations. For example, for Pt (553) a number of experiments were carried out with varying the concentration of cations, pH, and the type of cation in the electrolyte. A strong shift of the peak corresponding to OH adsorption was found. DFT calculations of the peak position was carried out

to support the experimental data (Fig. 77) [29]. It has been found that the peak shifts towards more positive potentials as the concentration of alkali cations increases, and that the magnitude of the shift increases with increasing cation size. DFT calculations show that cation adsorption destabilizes ∗OH, which explains the shift of the CV peak towards more positive potentials, and the source of destabilization is the surface dipole created by cation adsorption. This dipole changes the hydrogen bond between adsorbed water and OH_{ad}.

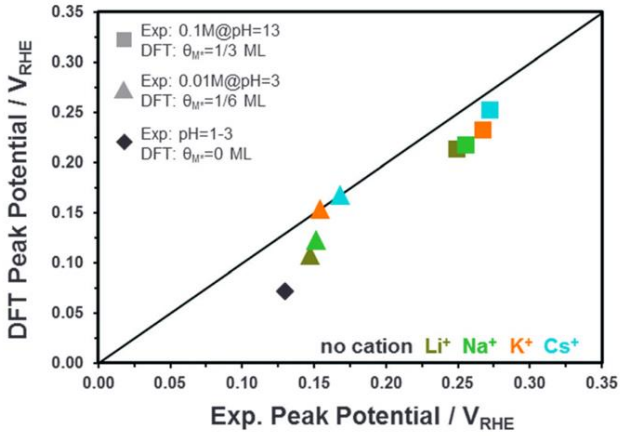

Fig. 77 Potential of the OH adsorption/desorption peak calculated by the DFT method at different cationic composition of the electrolyte and different pH plotted against the experimental peak position. Reproduced from Ref. [29].

It is also interesting to consider the influence of the cationic composition on the reverse process, the evolution of oxygen. On the one hand, in the field of oxygen evolution, more work has been carried out related to the study of the effect of electrolyte on the catalytic behavior of oxides, on the other hand, the effects presented may have a similar nature in the electrocatalysis of the oxygen reduction.

For example, the authors of [20] carried out experiments using LiOH, NaOH, KOH, CsOH hydroxides or the corresponding perchlorates with a constant concentration during the study of the OER on the NiOOH electrocatalyst [30]. Research was carried out, in particular, by *in situ* Raman spectroscopy, and it was shown that for the NiOOH samples placed in solutions of various alkalis, the Ni-O bond length changes (Fig. 78). The largest bond length is observed when CsOH is used as an electrolyte, and in this case the highest activity in the oxygen evolution reaction is observed. For a sample placed in LiOH, the situation is opposite. The data obtained are in good agreement with earlier studies, which state that catalyst activity correlates with the M-O bond length. The Cs^+ cation in this case, being the largest among the alkali metal cations, stabilizes the NiOO--M^+ intermediate.

It is worth noting that the influence of the electrolyte cation identity on the OER has also been observed by Moureaux et al. [31], who reported significantly higher activity of the 'activated' 316L stainless steel in a KOH compared to a LiOH electrolyte (5M in both cases). Note that the electrochemical 'activation' of the steel anode resulted in a formation of a Ni-rich layer (also containing Cr and Fe).

In this context one may also recall the above-mentioned publication of Huang et al [6], whereby the authors performed calculations specifically for a NiOOH electrode, and which explains the influence of the type of electrolyte cation on the OER kinetics within the EDL effects ('cation overcrowding').

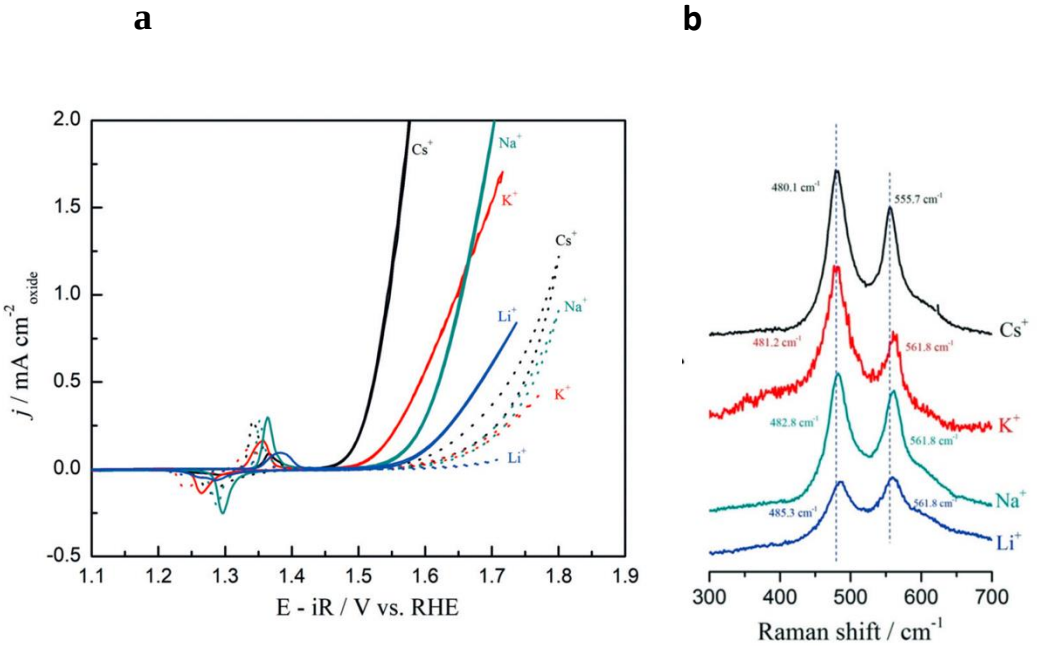

Fig. 78 a) Cyclic voltammograms of NiOOH at pH 13 in the region of oxygen evolution in different electrolytes. (Solid lines: as received electrolytes; dotted lines: electrolytes purified from iron) b) In situ Raman spectra of NiOOH obtained at 1.7 V at pH 13 in the presence of different electrolyte cations. Reproduced from Ref. [30].

5.1.2 Conclusions

The effects of pH and cations on electrocatalysis are multifactorial. First, pH affects both thermodynamics and kinetics of the electrode reactions, and to single out the thermodynamic and kinetic effects, plotting RDE voltammograms on both RHE and SHE scales is instrumental. Second, pH may change the form of intermediate formed during the ORR due to acid/base dissociation (for the ORR one must consider protonated and deprotonated forms of the hydrogen

peroxide). Third, both pH and cation type/concentration affect the EDL at the electrode/electrolyte interface and hence the reaction kinetics. In addition, cations may intercalate in oxide materials. All these effects combined may complicate interpretation of the experimental data.

Despite the complexities, investigation of pH and cation effects has recently attracted much attention of the scientific community. Such studies help in elucidation of the reaction mechanisms and the dependence of the reaction kinetics on the so-called 'local reaction environment'. It became clear that fundamental advances in electrocatalysis are impossible without the understanding of the electrolyte effect (pH and cations) on the kinetics of electrochemical reactions. Several experimental and computational studies have been performed for metal electrodes, but much less has been done for transition metal oxides, in particular in what concerns the ORR.

In this chapter we discuss the influence of the supporting electrolyte on the ORR and on the hydrogen peroxide reactions on MnOOH, Mn_2O_3, and $LaMnO_3$ oxides, their choice being described in Chapter 4. Similarly to the procedure utilized for studying the effect of electrolyte on the interface (Chapter 4), two series of background electrolyte solutions were prepared - solutions with constant ionic strength (constant Na^+ concentration) and variable pH, and solutions with constant OH^- concentration (constant pH) and variable Na^+ concentration. Thus, the discussion of the results of this chapter is divided into two main parts - the influence of pH and the influence of Na^+ concentration. In each of the parts, the reactions of the electrochemical hydrogen peroxide oxidation/reduction and the reduction of oxygen are considered. Hydrogen peroxide being the reaction intermediate, at the end of this chapter, a comparison of the RDE curves for the ORR and HPRR / HPOR is given in order to better understand the influence of the electrolyte on the ORR kinetics.

5.2 Experimental

A description of the synthesis of selected oxides and a detailed procedure for the electrochemical experiment can be found in Chapter 2.

Electrochemical measurements were performed in electrolyte solutions with variable NaOH and $NaClO_4$ concentration. When studying the ORR one must keep in mind that with the addition of $NaClO_4$ and with a change in the concentration of NaOH, several parameters of the Levich equation, which describes the limiting diffusion current, may change, mainly the viscosity of the solution, the diffusion coefficient, and the solubility of oxygen. It is important to determine the parameters most sensitive to the electrolyte change, since the first two (viscosity and diffusion coefficient) affect only the limiting diffusion current, while oxygen solubility also affects the

kinetic current. In the meantime, when studying the electrochemical transformation of the H_2O_2, the concentration of the hydrogen peroxide is set (we used 0.84 mM hydrogen peroxide), the changes in the limiting current only originate from the changes of the diffusion coefficient and viscosity. Thus, if variation of pH or Na^+ concentration does not entail changes in the diffusion coefficient and viscosity, the limiting current must be constant. To this end, combined investigation of the ORR and HPRR/HPORR is useful for separating influence of the electrolyte on diffusion-limited and kinetic-limited currents.

The solubility of oxygen can be estimated using Henry's law, which describes the dependence of the solubility of a gas on its partial pressure and Henry's constant (H), which depends on the nature of the gas and solvent at a constant temperature. An approach was also proposed with an assessment of the solubility of gases based on the cationic and anionic composition of the electrolyte according to the following formula:

$$\log \frac{C_0}{C} = \sum_{k=0}^{n} H_n I_n \quad (92)$$

where C_0 is the solubility of oxygen in pure water, C is the solubility of oxygen in the studied solution, H_n is the salting out constant for the corresponding ion (see table 16), I_n is the contribution of the ion to the total ionic strength of the solution, determined by the formula below.

$$I_n = \frac{1}{2} C_n z_n^2 \quad (93)$$

Table 16. Ion Specific Constants for Salting-Out Oxygen at 25°C

Ion	H_n
Na^+	-0.550
OH^-	0.888
ClO_4^-	0.941

In what follows we will use Eq. 92 and constants of Table 16 to calculate oxygen solubility in different electrolyte solutions and compare with the measured limiting currents.

5.3 Results and discussion

5.3.1 Influence of pH on the ORR and electrochemical hydrogen peroxide reactions

As already stated above, changes in the electrolyte composition may not only influence the ORR kinetics (which is the focus of this chapter) but also affect oxygen solubility and the rate of its diffusion from the bulk to the interface. Considering these overlapping effects, we start this chapter from the discussion of the hydrogen peroxide reactions. Since the concentration of the hydrogen peroxide is fixed, changes in the diffusion-limited currents will provide information regarding the influence of the electrolyte composition on the diffusion coefficients and electrolyte viscosity. Once the hydrogen peroxide reactions are discussed, we will move to the analysis of the ORR kinetics. The same structure will be followed for the discussion of the cation effect (section 5.4.2).

RDE voltammograms $LaMnO_3$, Mn_2O_3, and MnOOH are presented in Fig. 79 for electrolytes with different pH and constant ionic strength. One may see that for Mn_2O_3 and $LaMnO_3$ the limiting anodic and cathodic currents, in all studied electrolytes, increase with the electrode rotation rate as expected for diffusion-limited currents (see Fig. 80 a,b). These anodic and cathodic diffusion-limited currents decrease with the NaOH concentration in the same manner. This may be attributed to the increase of viscosity and concomitant decrease of the diffusion coefficient. In what follows we will see similar behavior for the ORR limiting currents. Analyzing the Koutecký–Levichdependences for $LaMnO_3$ and Mn_2O_3 (Fig. 80 c- f), one can see a similar linear dependence of the reverse current on the rotation speed both in the cathodic and anodic regions with the slope corresponding to the transfer of 2 electrons. This confirms that the currents are limited by diffusion. In 1M NaOH + 1M $NaClO_4$ solution the slope of the Levich - Koutecky plots are retained, however, the line does not cross the origin (0.0), which may be due to the failure to reach the limiting current values (RDE curves at different rotation speeds for different NaOH concentration are presented in the ANNEX).

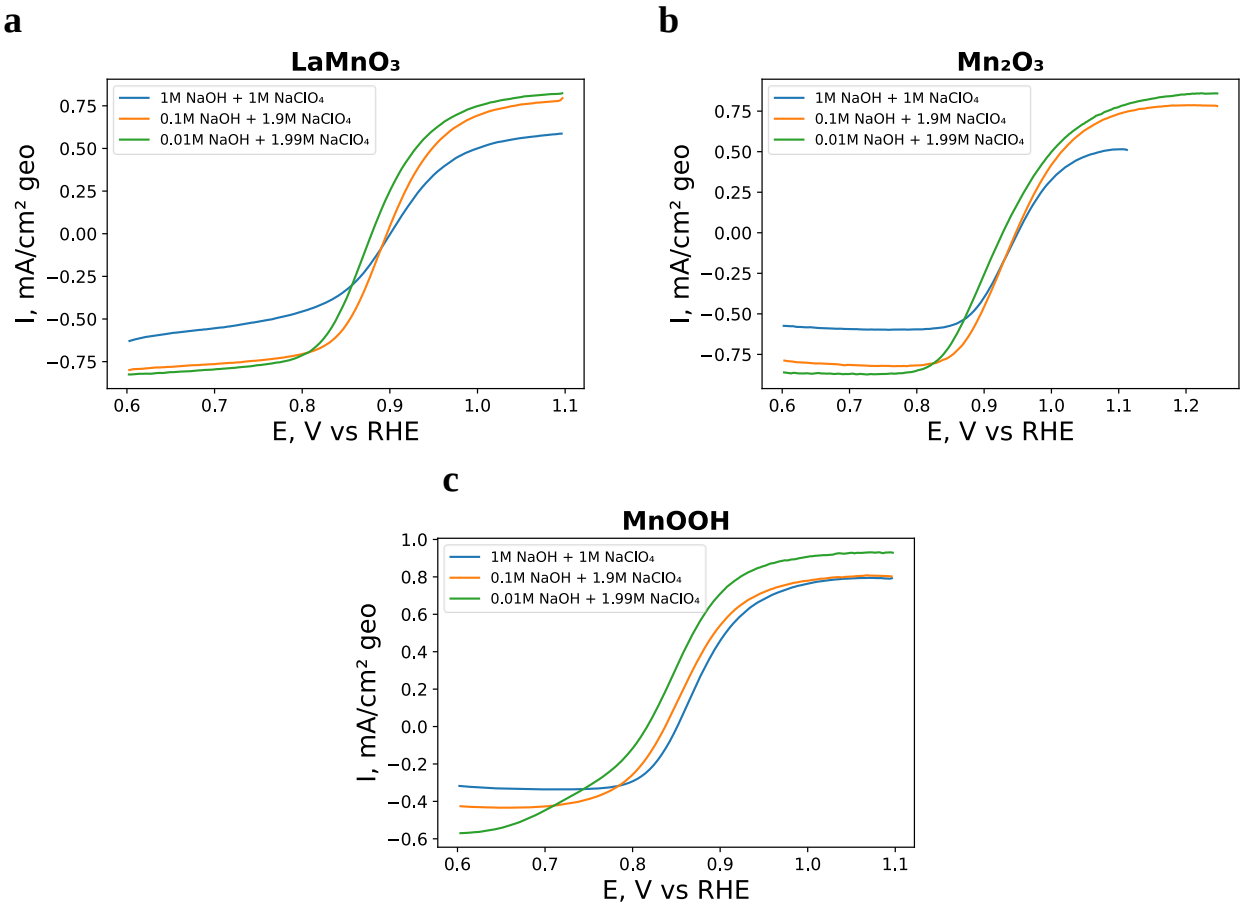

Fig. 79 RDE voltammograms in N_2-purged alkaline solution (at different pH and constant ionic strength) in the presence of 0.84 mM H_2O_2 at 10 mV s^{-1} for GC supported thin films of $LaMnO_3$ (a), Mn_2O_3 (b), MnOOH (c). Catalyst loadings are 91 µg cm^{-2} oxide + 91 µg cm^{-2} carbon. Currents are normalized to the electrode geometric area and corrected to the background currents measured in the N_2 atmosphere.

For MnOOH a different behavior is observed. Indeed, the cathodic limiting current is smaller than the anodic (Fig. 79 c), which is in agreement with the chemical limiting step of the O-O bond breaking in HO_2^- intermediate adsorbed on the oxide surface. This chemical step manifests itself in rotation rate-independent cathodic plateau observed at low potentials in 0.1 M NaOH (see Fig. 81). Such a behavior is in agreement with previous publications [32], where it was attributed to a slower kinetics of step 5 on MnOOH compared to $LaMnO_3$ or Mn_2O_3. It is remarkable that when the NaOH concentration decreases, the cathodic limiting current for MnOOH becomes somewhat rotation rate-dependent, which points to a faster kinetics of step 5 (*cf.* ORR mechanism shown in Fig. 25 of Chapter 1) at lower OH^- concentrations (Fig. 81).

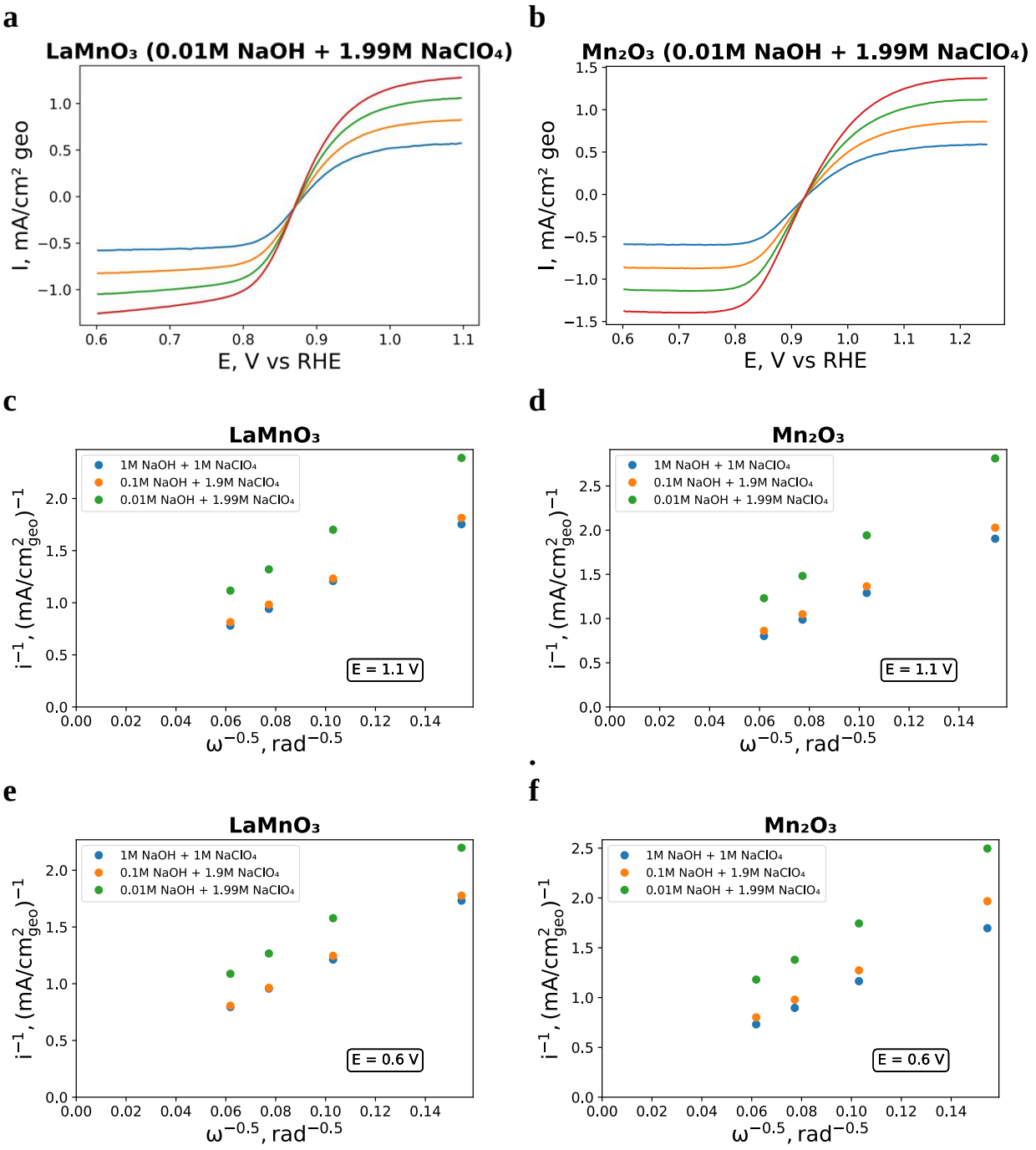

Fig. 80 RDE voltammograms in N_2-purged solutions of 0.84 mM H_2O_2 in 0.01M NaOH + 1.99 M $NaClO_4$ for GC-supported thin films of $LaMnO_3$ (a) and Mn_2O_3 (b) Panels c) and d) show Koutecký–Levichplots of anodic and cathodic currents for $LaMnO_3$ (c and e respectively) and Mn_2O_3 (d and f respectively). The oxide and carbon loadings are 91 μg cm^{-2} each. Color codes: 400 (blue), 900 (orange), 1600 (green), 2500 (red) rpm. Currents are normalized to the electrode geometric area and corrected to the background currents measured in the N_2 atmosphere.

Levich - Koutecky plots for MnOOH confirm strong differences in the values and in the rotation rate dependence of the cathodic and anodic limiting currents. While the anodic currents, similar to $LaMnO_3$ and Mn_2O_3, demonstrate diffusion-controlled behavior, the cathodic currents are smaller and are much less influenced by the rotation rate as expected for a kinetically-

controlled reaction. Levich - Koutecky plots for MnOOH also confirm that decrease of the NaOH concentration (at constant Na^+ concentration) not only results in an increase of the cathodic limiting current but also amplifies its sensitivity to the rotation rate. Both are in agreement with the conclusion that decrease of pH enhances the kinetics of the chemical step on MnOOH. One may also notice that decrease of the pH changes the shape of the RDE voltammogram for MnOOH, whereby at lower pH one may notice two cathodic waves. Such a behavior might be attributed to an increase of the concentration of the protonated form (H_2O_2) of hydrogen peroxide, which may be more reactive on a negatively charged electrode surface. In addition, the negative charge at the MnOOH/electrolyte is expected to increase with the OH^- concentration (cf. Figure 68 of chapter 4), thus disfavoring adsorption and reaction of the deprotonated form of hydrogen peroxide on the oxide surface (HO_2^-). The fact that the two cathodic waves are observed for MnOOH but not for either Mn_2O_3 or $LaMnO_3$ is in agreement with the fast kinetics of step 5 of the ORR mechanism (see Figure 25 of Chapter 1) for Mn_2O_3 and $LaMnO_3$ and slow – for MnOOH (Table 11 of Chapter 4).

Finally one may notice that increase of the NaOH concentration results in a positive shift of the mixed potential for all studied oxides, the amplitude of this shift being the highest for MnOOH. Note that positive shift is expected upon increase of the rate of HPRR compared to HPOR, and, vice versa, negative shift occurs when the rate of the HPOR increases more than the rate of HPRR. This will be discussed in more detail in section 5.4.3.

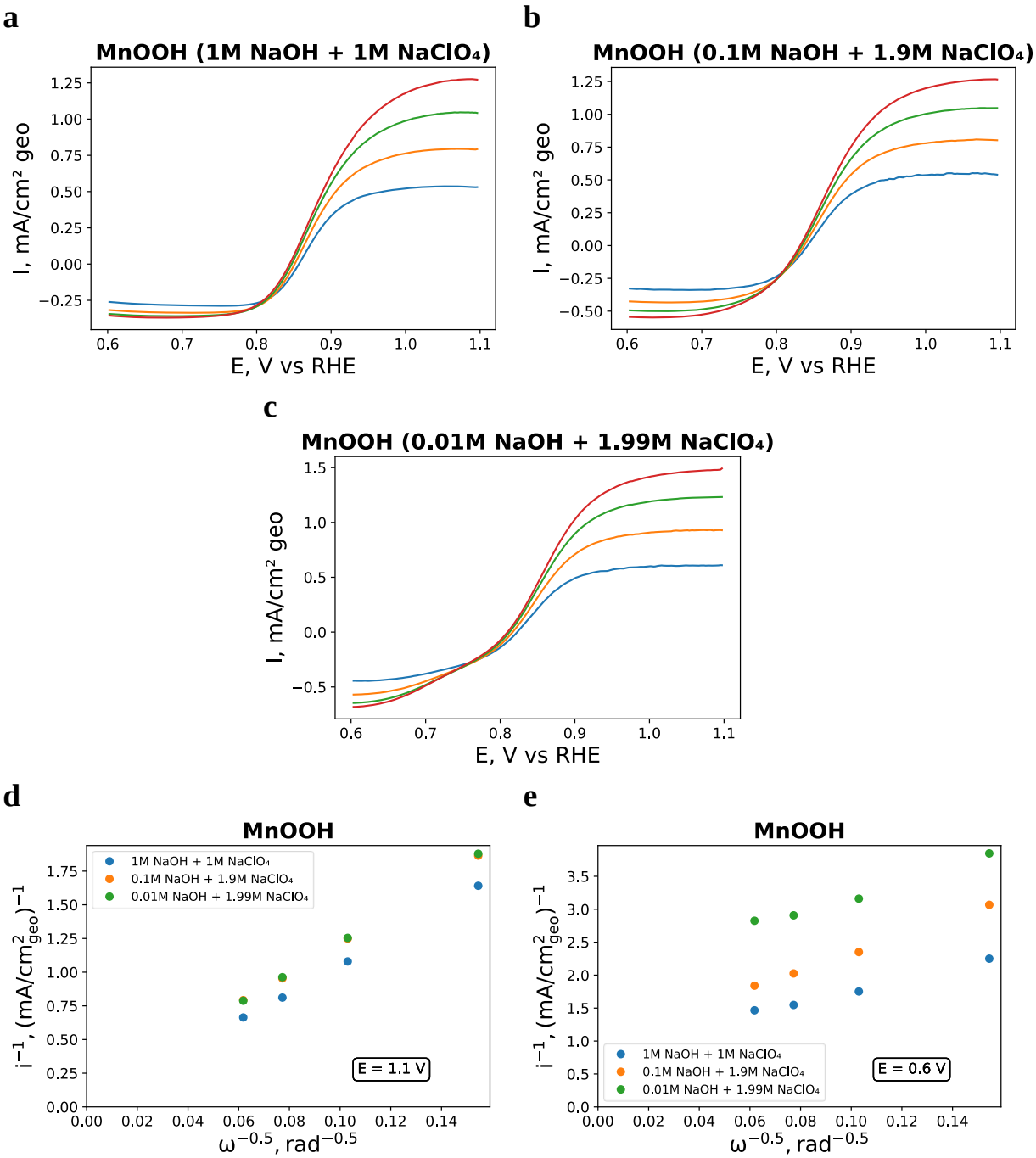

Fig. 81 RDE voltammograms in N_2-purged solutions of 0.84 mM H_2O_2 for GC-supported thin films of MnOOH at different OH^- concentrations and constant ionic strength: 1M NaOH + 1M $NaClO_4$ (a), 0.1M NaOH + 1.9 M $NaClO_4$ (b), and 0.01M NaOH + 1.99 M $NaClO_4$ (c). Panel d shows Koutecký–Levichplots of anodic (e) and cathodic (d) currents. MnOOH and carbon loadings are 91 μg cm^{-2} each. Color codes: 400 (blue), 900 (orange), 1600 (green), 2500 (red) rpm. Currents are normalized to the electrode geometric area and corrected to the background currents measured in the N_2 atmosphere.

We now move to the discussion of the influence of the OH^- concentration on the ORR (Fig. 82). As mentioned above, changes in the NaOH concentration entail changes in the diffusion-

limiting currents for the hydrogen peroxide reaction, which indicates a change in the viscosity of the solution and diffusion coefficients. We expect similar effects on the diffusion-limited currents in the study of the ORR. Indeed, RDE voltammograms acquired for the ORR (Fig. 82) demonstrate similar decrease of the diffusion-limited current with the NaOH concentration. To confirm that the solubility of oxygen is not affected, the latter was calculated using the method described in the experimental part (section 5.2).

Table 17. Concentration of dissolved oxygen in solutions with variable NaOH concentration and constant ionic strength calculated according to Henry's law along with the cathodic limiting ORR current measured for Sibunit carbon at an electrode rotation speed of 900 rpm

Solution	**Calculated O_2 solubility (mM)**	**Cathodic limiting ORR current for Sibunit carbon (mA cm^{-2} geo)***
1M NaOH + 1M $NaClO_4$	0.53	0.90
0.1M NaOH + 1.9M $NaClO_4$	0.56	1.09
0.01M NaOH + 1.99M $NaClO_4$	0.56	1.12

*Data taken from Figure 82.

It can be seen that the solubility of oxygen remains constant within ±3%, while the limiting ORR current for Sibunit carbon (for which the number of transferred electrons is constant and equal to 2) increases by ~20%, which confirms the assumption made above, and let us neglect variation of the O_2 solubility in this set of experiments.

Analysis of Fig. 82 shows that for all studied materials (including carbon) increase of pH results in a shift of the ORR voltammograms to higher potentials on the RHE scale. However, the amplitude of this shift is smaller than 60 mV. Since the RHE scale itself is pH dependent (shifting 60 mV negative per pH unit), to help the understanding, in Fig. S9 the ORR voltammogramms are also plotted on the SHE scale. Fig. S9 demonstrates that the ORR 'onset' is pH-dependent also on the SHE scale. For Sibunit carbon, the shift of the ORR voltammograms is ~ +30 mV/pH on the RHE and ~ –30 mV/pH on the SHE scale, which is in agreement with the thermodynamic Nernst potential (see Figure 69) for the O_2/HO_2^- equilibrium.

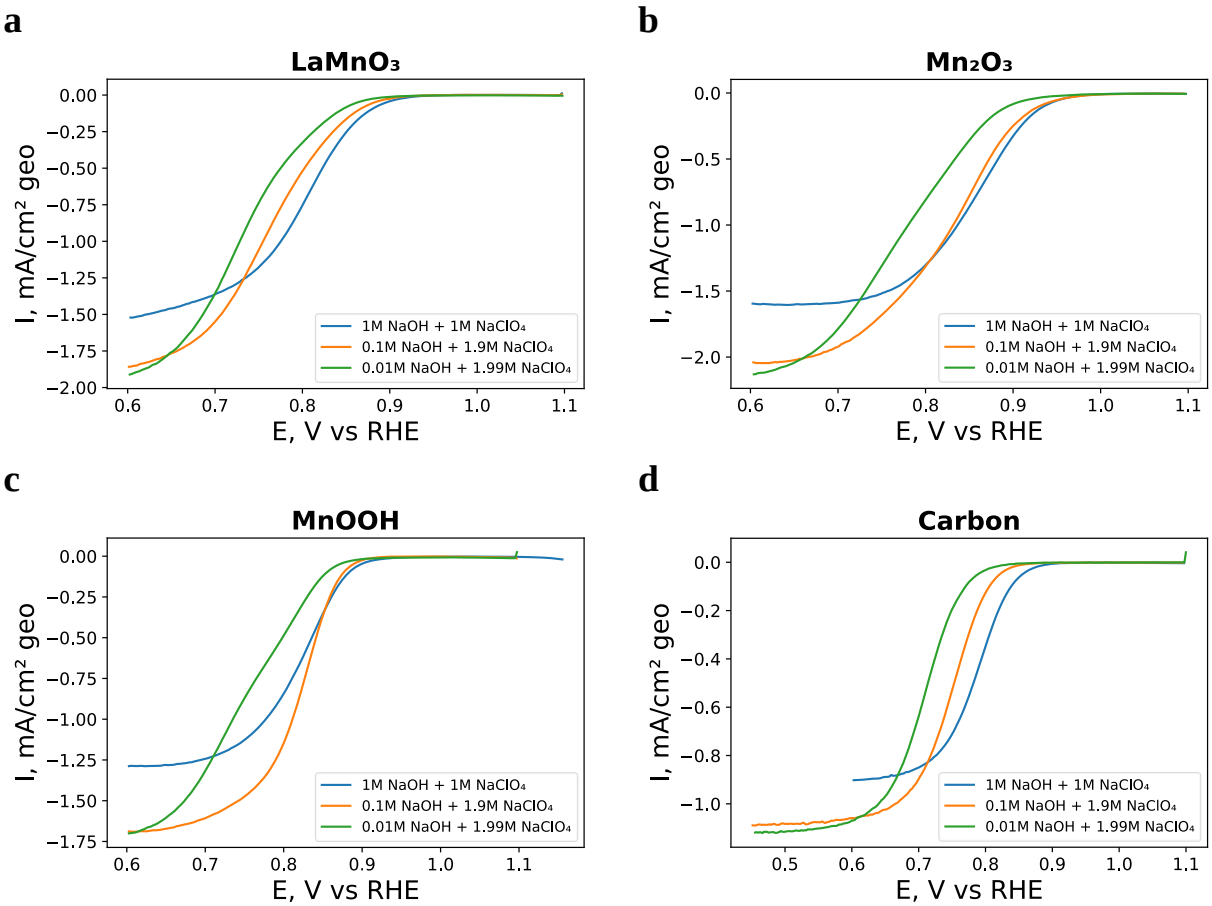

Fig. 82 RDE voltammograms in O_2-saturated alkaline solution (at different pH and constant ionic strength) at 10 mV s^{-1} and 900 rpm for GC supported thin films of $LaMnO_3$ (a), Mn_2O_3 (b), MnOOH (c), and Sibunit carbon (d). Currents are normalized to the electrode geometric area and corrected to the background currents measured in the N_2 atmosphere. Oxide and carbon loadings are 91 μg cm^{-2} each.

Table. 18. Tafel slopes (V/dec) defined for carbon, $LaMnO_3$*, Mn_2O_3*, MnOOH*

	Carbon	**$LaMnO_3$**		**Mn_2O_3**		**MnOOH**
linearization interval (V vs RHE):	0.78 - 0.82	0.84 - 0.9	0.82-0.78	0.84 - 0.9	0.82-0.78	0.88 - 0.9
1M NaOH + 1M $NaClO_4$	0.05	0.06	0.09	0.06	0.115	0.053
0.1M NaOH + 1.9M $NaClO_4$	0.05	0.06	0.1	0.063	0.12	0.042
0.01M NaOH + 1.99M $NaClO_4$	0.056	0.05	0.1	0.07	0.121	0.054

*Without correction for the carbon contribution

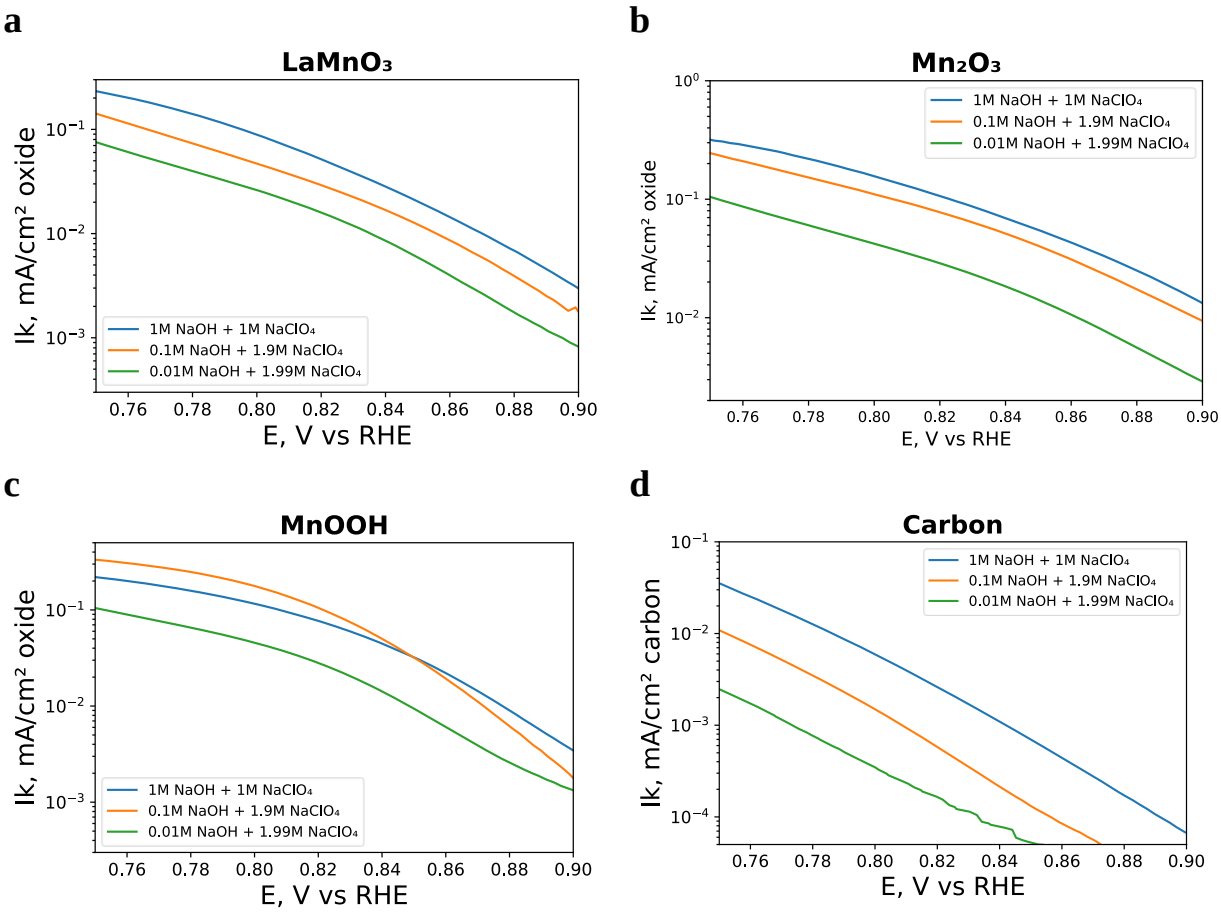

Fig. 83 Tafel plots for the ORR on $LaMnO_3$ (a), Mn_2O_3 (b), MnOOH (c), and Sibunit carbon (d) at different NaOH concentration and constant ionic strength. Currents are normalized to the BET surface area of materials. The currents are given without subtracting the contribution of carbon.

For oxides and carbon, Tafel curves were constructed - the dependence of the kinetic current on the potential. The first thing worth paying attention at is the presence of two slopes on the Tafel curves for oxides at high potentials (0.84 - 0.9 V vs RHE) and hence low overpotentials ~60 mV / dec, and at low potentials (0.82-0.78 V vs RHE) and high overpotentials ~90-120 mV / dec. As discussed in Chapter 1, for Pt, the presence of two Tafel slopes had been attributed to a change in the adsorption layer. At high overpotential, the oxygen coverage on the surface of Pt is low and it is assumed that there is no interaction between adsorbed oxygen atoms (adsorption obeys Langmuir isotherm), and the Tafel slope is in agreement with 'theoretical' 118 mV/dec (at 298 K) slope for an electron-transfer rds. At low overpotential, the oxygen coverage on the Pt surface is high, and adsorbate-adsorbate interaction cannot be neglected (adsorption obeys Frumkin isotherm). This potential-dependent oxygen coverage on Pt leads to a decrease of the Tafel slope. The presence of two slopes on the Tafel plots was previously noticed also for oxides in the work of Efremov and Tarasevich [33], in which they studied cobalt spinels and found Tafel slopes of 40

and 120 mV/dec in the region of low and high overpotential, respectively. It is also important to consider Ref. [34] in which microkinetic modeling was used to describe the experimental ORR data for Mn oxides. In this simulation, the Frumkin isotherm was used to describe the adsorption layer, in which the Frumkin interaction parameter (γ) was varied from 0 (no adsorbate-adsorbate interaction, Langmuir isotherm) to 10 (strong adsorbate-adsorbate interaction-repulsion). The simulation showed good agreement with the experimental data and a change in the Tafel slope was demonstrated from 120 mV/decade for E < 0.85 V to 30-50 mV/decade for E >0.95 V. The Tafel slope change occurred between 0.85 and 0.95 V depending on the formal potential of the Mn(III)/Mn(IV) interfacial transition. The authors explain the presence of two slopes by the following reasons: a decrease in the proportion of Mn (III) centers available for O_2 and HO_2^- adsorption on the surface with an increase in the electrode potential. It should be noted that at high overpotential, when the surface coverage with Mn(III) sites is high, the Tafel slope is close to 120 mV/decade, regardless of the value of the Frumkin interaction parameter. On the contrary, the Tafel slope at low overpotentials depends significantly on repulsive interactions in the O_{ad} layer, the slope increases from 30 to about 50 mV/decade as γ increases from 0 to 6. It is worth noting that the Tafel slope in the region of low overpotential depends not only on the adsorbates on the catalyst surface, but also on the values of the rate constants k_2 and k_3 (see ORR mechanism in Fig. 25 of Chapter 1).

Returning to the obtained experimental data, one can note that for Mn_2O_3 and $LaMnO_3$ Tafel slope at high overpotentials varies from ~90 to 120 mV/dec, in a good agreement with the literature data, including those confirmed by theoretical calculations, which is suggestive of an electron transfer rds. The Tafel slopes at low overpotentials vary from 40 to 60 mV/decade for the investigated materials.

In Fig. 83 we compare the pH-dependent potential shift at a fixed kinetic current density. The latter was chosen separately for each material in such a way as to avoid either excessively high overpotentials (where diffusion dominates) or too low overpotentials (where the currents are too low and hardly distinguishable from the background). For all studied materials the potential at a fixed kinetic current increases with the pH, the most systematic shift (~30 mV/pH as already discussed above) being observed for carbon (Fig. 83). For MnOOH the curves at different potentials cross, which will be discussed later in this chapter.

5.3.2 Effect of the Na^+ Concentration on the ORR and electrochemical hydrogen peroxide reactions

As in the previous section, we will begin our discussion with the RDE data for the hydrogen peroxide transformations (HPRR/HPOR). For Mn_2O_3 and $LaMnO_3$ changes in the composition of the solution do not affect limiting anodic and cathodic currents (some deviation of the cathodic currents from the plateau for $LaMnO_3$ may be related to the quality of the catalyst layer on the GC support). In this case, it can be concluded that the viscosity of the solution remains constant, as does the diffusion coefficient of H_2O_2. Below, we will see that the limiting ORR currents change strongly with a change in the composition of the electrolyte, which we attribute to a change in the solubility of oxygen.

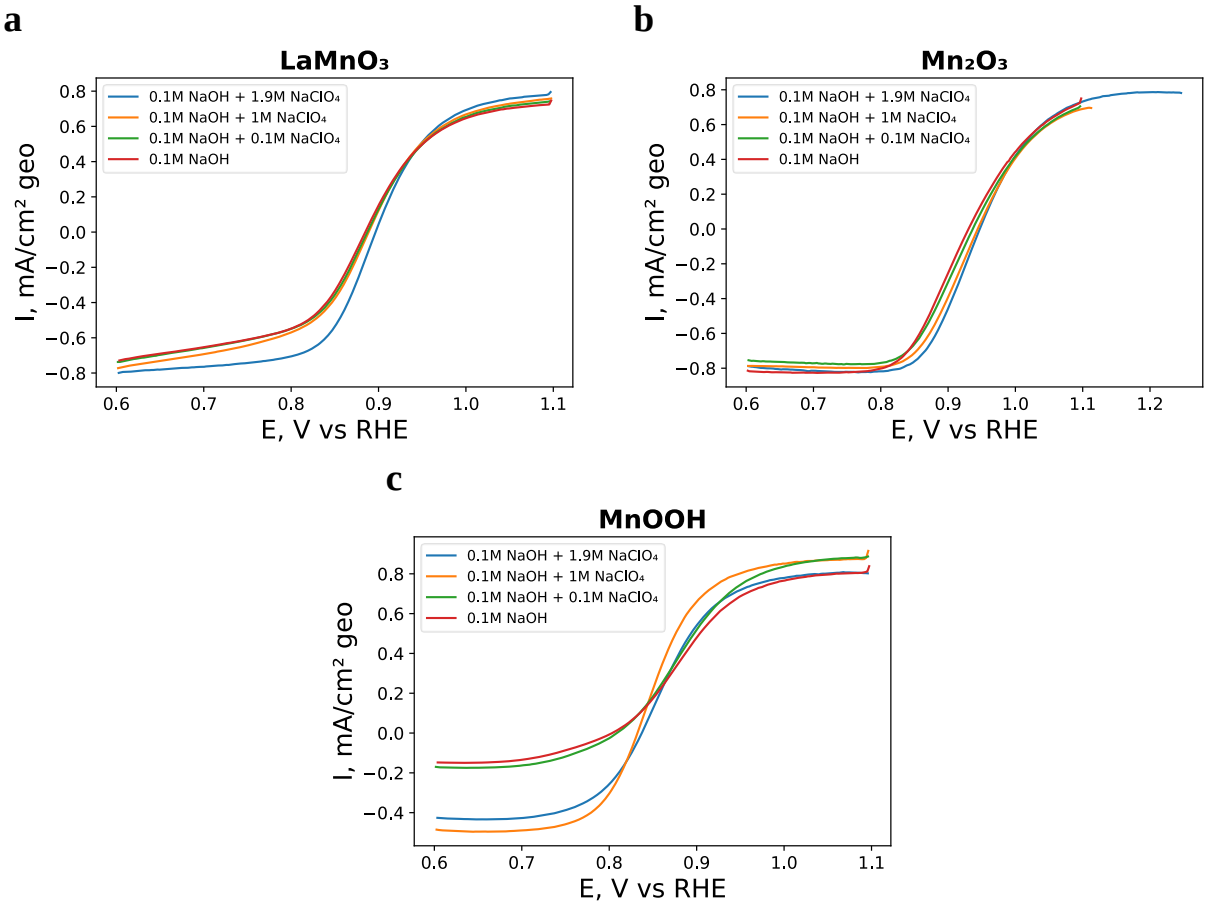

Fig. 84 RDE voltammograms in N_2-purged alkaline solution (at different concentration of Na^+ and constant pH) in the presence of 0.84 mM H_2O_2 at 10 mV s^{-1} and 900 rpm for GC supported thin films of $LaMnO_3$ (a), Mn_2O_3 (b), MnOOH (c). Oxide and carbon loadings are 91 μg cm^{-2} each. Currents are normalized to the electrode geometric area and corrected to the background currents measured in the N_2 atmosphere.

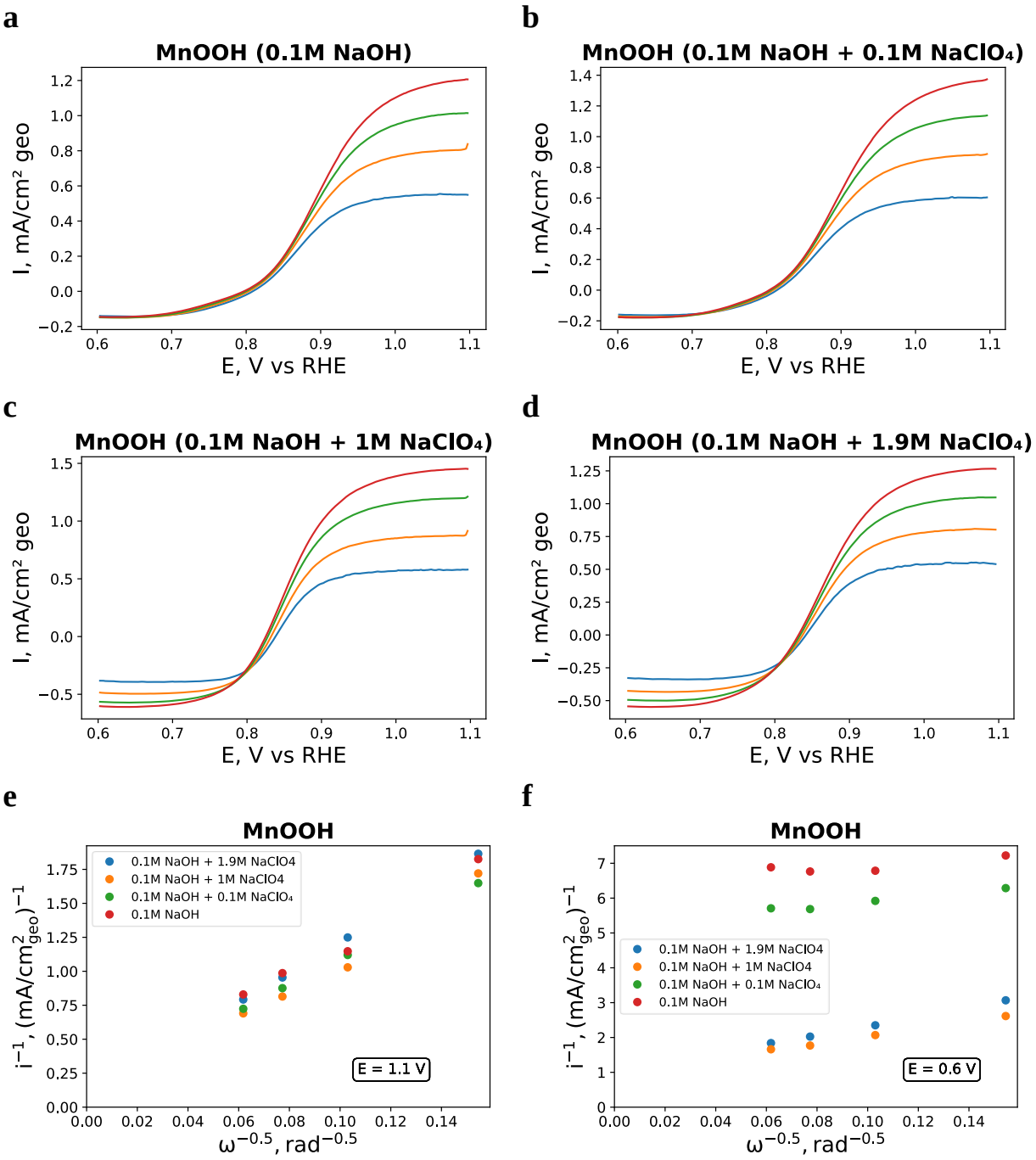

Fig. 85 RDE voltammograms in N_2-purged alkaline solution (at different concentration of Na^+ and constant pH) in the presence of 0.84 mM H_2O_2 at 10 mV s^{-1} for GC supported thin films of MnOOH at different rotational rate (a-d). Catalyst loadings are 91 μg cm^{-2} oxide + 91 μg cm^{-2} carbon. Currents are normalized to the electrode geometric area and corrected to the background currents measured in the N_2 atmosphere. Koutecký–Levich plots of anodic and cathodic currents for $LaMnO_3$ (c and e respectively) and Mn_2O_3 (d and f respectively).

For Mn_2O_3 and $LaMnO_3$, not only the limiting currents, but the HPRR/HPOR RDE curves as a whole change very little with the Na^+ concentration (Fig. 84). On the contrary, for MnOOH a significant effect is observed upon increase of the cation concentration, notably in the reduction of

H_2O_2. Thus, with an increase in the concentration of Na^+ (Fig. 85) the limiting current increases, and a dependence on the rotation speed appears, which indicates an improvement in the chemical step k_5 (see ORR mechanism in Fig. 25). This analysis agrees with the Levich - Koutecky dependences obtained. While for $LaMnO_3$ and Mn_2O_3 the slopes of the curves remain constant and cross through the origin both for the anodic and for the cathodic limiting current, for MnOOH similar behavior is only observed for the oxidation of H_2O_2. However, with an increase in the Na^+ concentration, a dependence on the rotation speed also appears in the cathodic region, even if the current does not reach the diffusion-limited value.

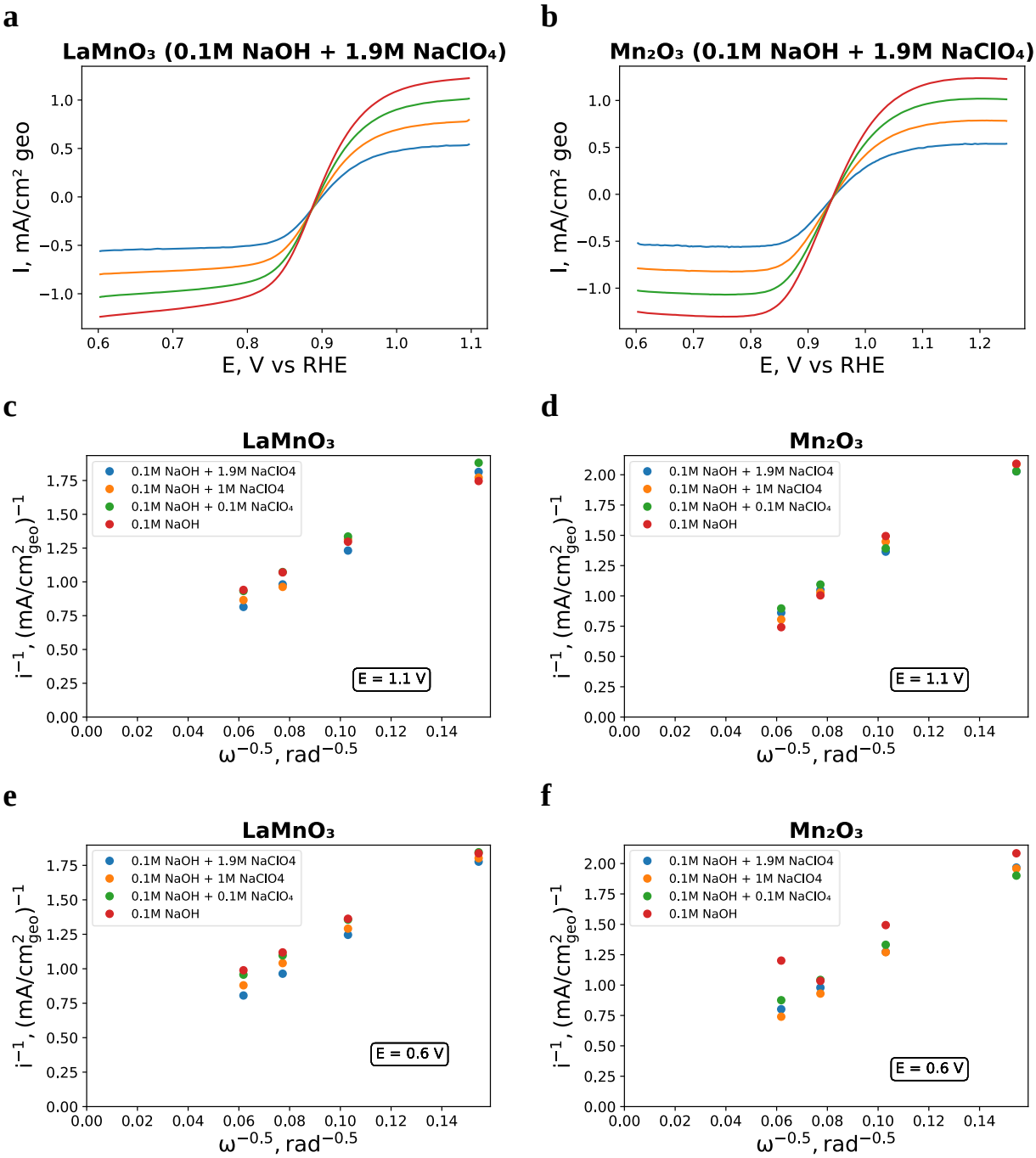

Fig. 86 RDE voltammograms in N_2-purged alkaline solution (0.1M NaOH + 1.9M $NaClO_4$) + 0.84 mM H_2O_2 at 10 mV s^{-1} for GC supported thin films of $LaMnO_3$ (a) and Mn_2O_3

(b) at different rotation rate. Catalyst loadings are 91 μg cm^{-2} oxide + 91 μg cm^{-2} carbon. Currents are normalized to the electrode geometric area and corrected to the background currents measured in the N_2 atmosphere. Koutecký–Levichplots of anodic (e) and cathodic (f) currents.

We now move to the discussion of the oxygen reduction in electrolytes with constant pH and variable Na^+ concentration. Fig. 87 represents RDE voltammograms for oxides and for Sibunit carbon in O_2-saturated electrolytes. One may see that the cathodic limiting currents strongly decrease with the Na^+ concentration. Thus, we conclude that a change in the concentration of sodium perchlorate has significant effect on the solubility of oxygen (we remind that the limiting currents for the HPRR/HPOR on Mn_2O_3 and $LaMnO_3$ turned out to be nearly independent of the $NaClO_4$ concentration (Fig. 84)). It should be noted that we made an assumption about similar effect of the electrolyte composition on the values of the diffusion constants of O_2 and H_2O_2. The conclusion on the influence of the Na^+ concentration on the oxygen solubility is consistent with the calculation according to Henry's law (Table 19). Indeed, analysis of the Table shows reasonable correlation between the calculated O_2 concentration and the limiting ORR diffusion current measured on Sibunit carbon.

Table 19. Concentration of dissolved oxygen in solutions with a constant content of NaOH and a variable concentration of $NaClO_4$ calculated according to Henry's law. Limiting current for the ORR on Sibunit carbon at an electrode rotation speed of 900 rpm is presented for comparison.

Solution	**O_2 solubility from Henry's law (mM)**	**Limiting cathodic current for Sibunit carbon at 900 rpm (mA/cm^2 geo)**
0.1M NaOH	1.17	1.95
0.1M NaOH + 0.1M $NaClO_4$	1.12	1.91
0.1M NaOH + 1M $NaClO_4$	0.79	1.44
0.1M NaOH + 1.9M $NaClO_4$	0.56	1.08

Assuming that increase in the $NaClO_4$ concentration only affects the oxygen concentration and has minor effect on the viscosity and O_2 diffusion coefficient, to correct for the oxygen concentration in solution, for further analysis we normalize RDE voltammograms for MnOOH, $LaMnO_3$, and Mn_2O_3 to the diffusion-limited current measured for Sibunit carbon (Fig. 87). It should however be noted that such a normalization procedure is only valid within the validity of

the 1st order ORR, which has been documented for different materials in the literature [10] but was not verified in this work.

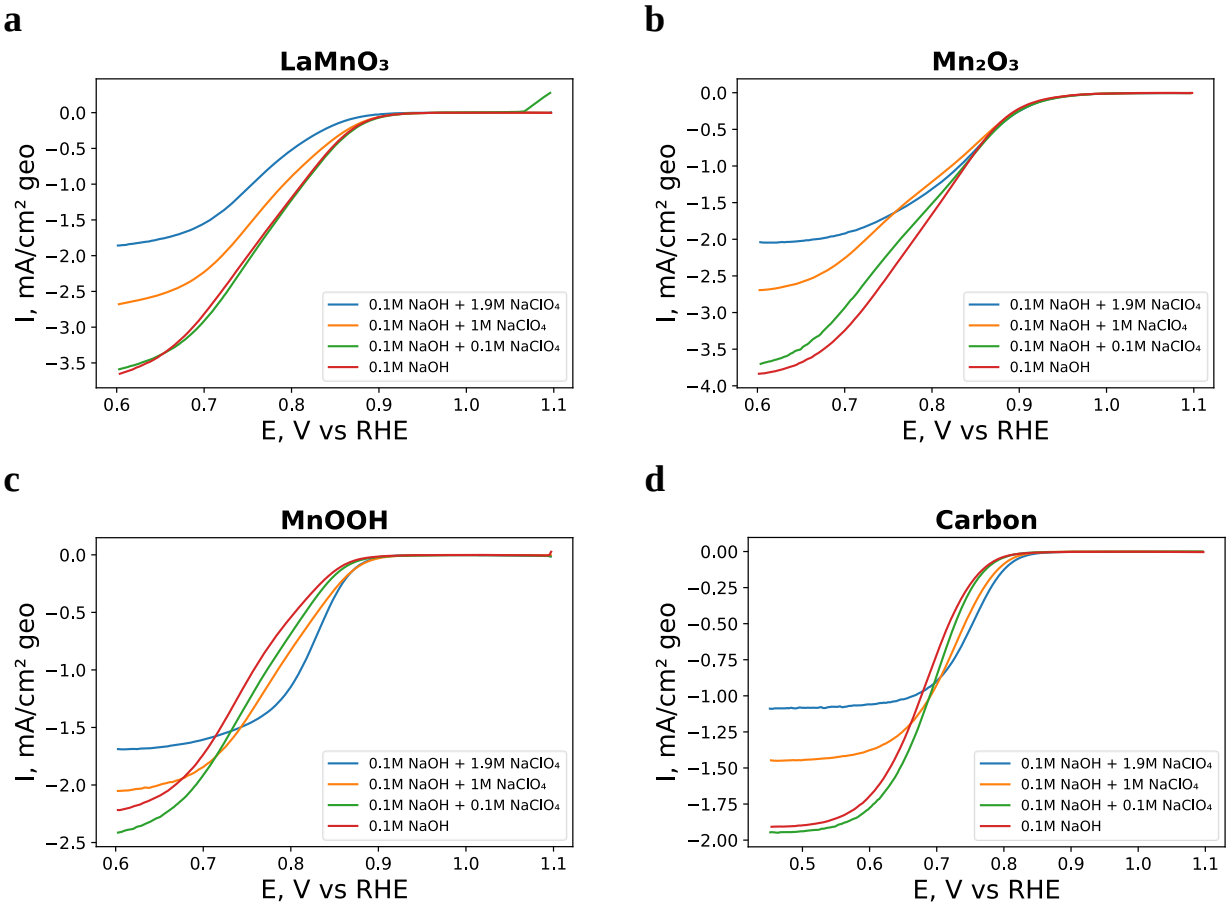

Fig. 87 RDE voltammograms in O_2-saturated alkaline solution (at different concentration of Na^+ and constant pH) at 10 mV s^{-1} at 900 rpm for GC supported thin films of $LaMnO_3$ (a), Mn_2O_3 (b), MnOOH (c), Carbon (d). Currents are normalized to the electrode geometric area and corrected to the background currents measured in the N_2 atmosphere.

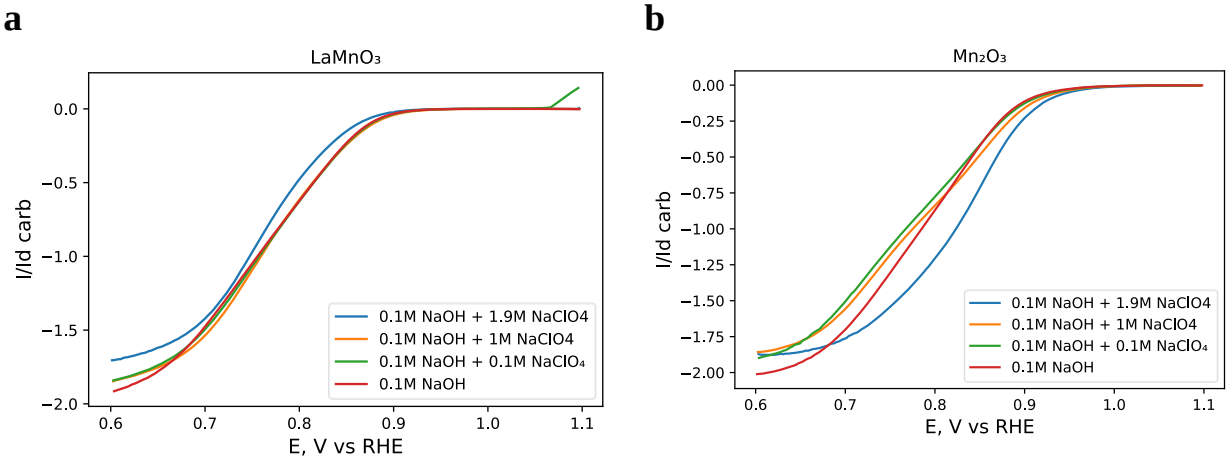

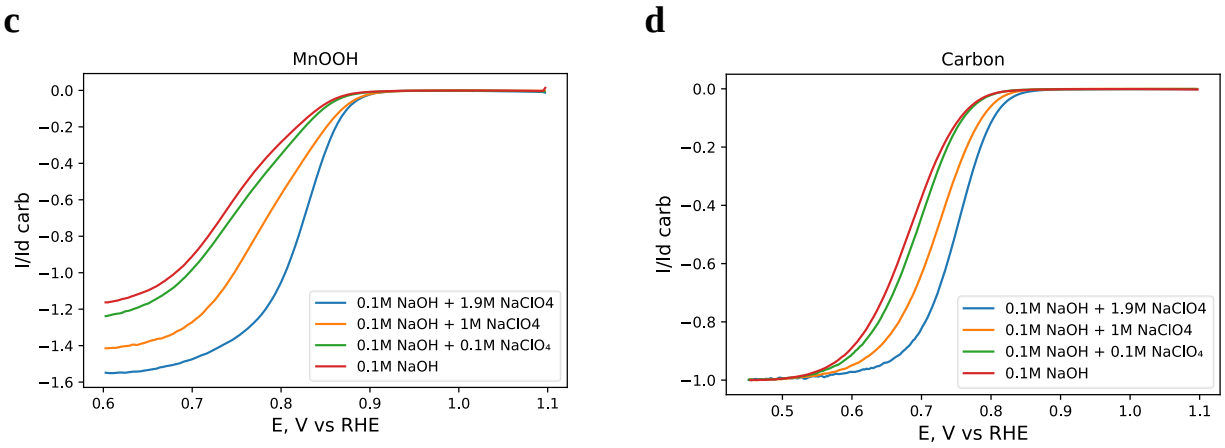

Fig. 88. RDE voltammograms in O_2-saturated alkaline solution (at different concentration of Na^+ and constant pH) at 10 mV s^{-1} and 900 rpm for GC supported thin films of $LaMnO_3$ (a), Mn_2O_3 (b), MnOOH (c), Carbon (d). Currents are corrected to the background currents measured in the N_2 atmosphere and normalized to the diffusion-limited current of carbon.

Analysis of the normalized voltammograms presented in Figure 88 suggests that increase of the Na^+ concentration results in an improved ORR kinetics for all studied materials (including carbon), with the exception of $LaMnO_3$. This will be further discussed in the General Discussion section.

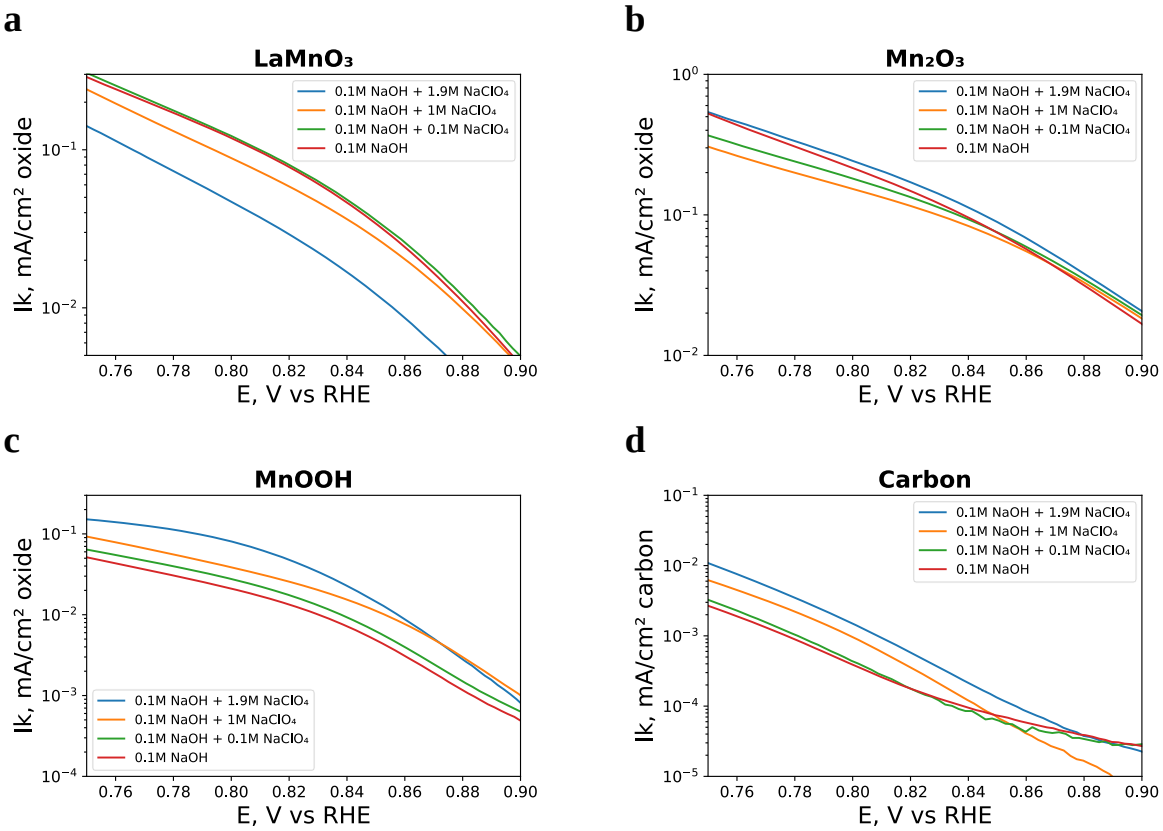

Fig. 89 Tafel plots for $LaMnO_3$ (a), Mn_2O_3 (b), MnOOH (c), Carbon (d). Currents are normalized to the BET surface area. The currents are given without deducting the contribution of carbon. Currents are corrected to the O_2 concentration assuming 1st order kinetics.

Table 20. Tafel slopes defined for carbon, $LaMnO_3$, Mn_2O_3, MnOOH.

	Carbon	**$LaMnO_3$**		**Mn_2O_3**		**MnOOH**	
Linearization interval (V vs RHE):	0.78 - 0.82	0.84 - 0.9	0.82-0.78	0.84 - 0.9	0.82-0.78	0.84 - 0.9	0.82-0.78
0.1 M NaOH + 1.9M $NaClO_4$	0.05	0.05		0.079	0.121	0.038	
0.1 M NaOH +1 M $NaClO_4$	0.047	0.05	0.115	0.082	0.18	0.047	0.123
0.1M NaOH+0.1 M $NaClO_4$	0.05	0.05	0.112	0.077	0.18	0.047	0.123
0.1 M NaOH M $NaClO_4$	0.05	0.05	0.109	0.072	0.122	0.047	0.123

*Without correction for the carbon contribution

Reasoning in the analysis of Tafel slopes is similar to that carried out in (5.4.1). Two slopes can also be observed in the region of low and high overpotential. Comparison of kinetic currents confirms the above conclusion of the enhancement of the ORR kinetics with the cation concentration for all studied materials except for $LaMnO_3$. It is worth noting that we prefer to avoid drawing conclusions about the reaction mechanism based on the Tafel slopes, which is due to the complexity of their interpretation, as well as a large number of factors, in addition to changing the reaction path, that affect the Tafel slopes. These factors include adsorption, interaction between adsorbates, occupancy of catalytic sites, etc.

5.3.3 General discussion

In what follows we combine all available data for MnOOH, Mn_2O_3 and $LaMnO_3$ oxides (CVs and titration curves from Chapter 4, as well as HPOR/HPRR and ORR voltammograms from Chapter 5) in order to gain better understanding of the influence of the electrolyte composition on the electrocatalytic properties. According to microkinetic modeling of the ORR carried out for $LaMnO_3$, Mn_2O_3 and MnOOH in previous publications [32,34], comparison of RDE voltammograms in O_2-saturated electrolytes and in the presence of H_2O_2 is instrumental to

understand particularities of the ORR electrocatalysts. Such comparison can be found in (Fig. 90), where we also plot the dependence of the mixed potential (E_{mix}) in 0.84 mM H_2O_2 on the OH^- and Na^+ concentration (Fig. 90). We recall that mixed potential results from the simultaneous occurrence of several electrochemical reactions: anodic HPOR (on oxide), cathodic HPRR (on oxide) and cathodic ORR (on oxide and on carbon) with O_2 resulting from the HPOR [35].

First, we conclude that our results are in good agreement with both previous experiments and modeling data confirming the validity of the previously proposed ORR mechanism (Figure 25 of Chapter 1). For MnOOH in all studied electrolytes the E_{mix} is negative of the ORR 'onset', which is in agreement with the slow HPRR on this oxide limited by the slow O-O bond breaking step (step 5). Indeed, according to Ref.[32], the slow rate of the HPRR (determined by step 5) compared to that of the HPOR (determined by rate constants of steps 2 and 3) shifts E_{mix} to the cathodic region. On the other hand, in an O_2-saturated solution, the reduction of oxygen to peroxide predominates, making the resulting current negative (hence positive shift of the ORR 'onset' compared to the E_{mix}). For Mn_2O_3 and $LaMnO_3$ the ORR and the HPRR/HPOR voltammograms cross, which confirms significantly faster kinetics of step 5 on these two oxides (compared to MnOOH), in agreement with the previous publications ([34]). With an increase in pH and with an increase in the Na^+ concentration, the mixed potential increases for all oxides under study, with the strongest effect observed for MnOOH. On the other hand, for MnOOH we also observe significant enhancement of the step 5 kinetics (which can be clearly seen from an increase of the cathodic limiting current, which is defined by kinetics of step 5) with either increase of the cation concentration, or pH *decrease*. Increase of rate constant of step 5 with the cation concentration is in agreement with the positive shift of E_{mix} (Fig 90). The possible origin of this shift will be discussed below. However, in what concerns with the pH, *increase of the rate constant of step 5 with the decrease of pH* is expected (other conditions being equal) to result in a decrease of the E_{mix} with pH, which contradicts the experimental observation (Figure 90). This positive shift of E_{mix} with pH could be explained if the rate constants of steps 2 and 3 decreased with pH even stronger than the rate constant of step 5. This is, however, in contradiction with the increase of the ORR kinetics with pH. Thus, understanding of the pH on the ORR and HPRR/HPOR kinetics requires microkinetic modeling.

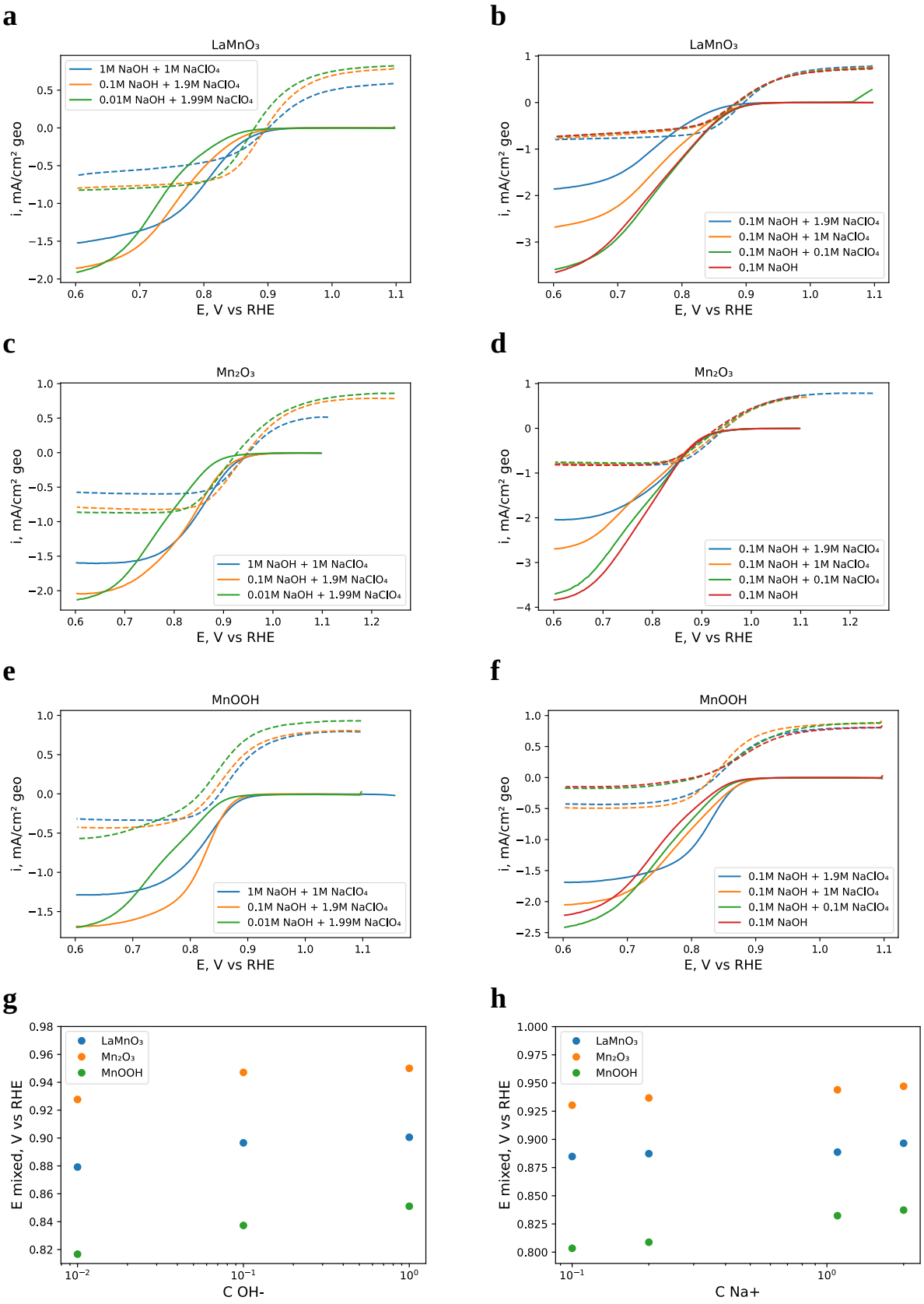

Fig. 90 (a-f) Comparison of the RDE curves for the HPOR/HPRR and ORR in solutions with different pH (a, c, e), and with different concentrations of Na^+ (b, d, f) for $LaMnO_3$ (a, b), Mn_2O_3 (c, d), MnOOH (e,f). Mixed potentials in the presence of H_2O_2 are shown in panels (g) and (h) in solutions with different pH (g), and with different concentrations of Na^+ (h).

When comparing the catalytic activity of oxides at a potential of 0.9 V (Table 21), it can be seen that for all oxides, the catalytic activity increases with pH. As to the Na^+ concentration, the strongest effect is observed for MnOOH, the ORR activity increasing by a factor of 2.7. Since increase of the Na^+ concentration results in a decrease of the oxygen solubility, the rate constant increase must be ~2 times higher (assuming 1st order with respect to O_2). For Mn_2O_3 the ORR activity increases to a much lesser extent (~ 1.3 fold), while for $LaMnO_3$ it decreases by a factor of 2. However, this decrease is not systematic, and may be due to an artefact.

Table 21. Kinetic currents (i_k*) for Mn_2O_3, MnOOH, and $LaMnO_3$ calculated at 0.9 V vs. RHE in solutions with variable OH^- concentration and constant ionic strength.

Electrolyte composition	**Mn_2O_3** i_k mA cm^{-2}	**MnOOH** i_k mA cm^{-2}	**$LaMnO_3$** i_k mA cm^{-2}
1M NaOH + 1M $NaClO_4$	0.029	$1.4*10^{-3}$	$2.7*10^{-3}$
0.1M NaOH + 1.9M $NaClO_4$	0.02	$7.8*10^{-4}$	$1.5*10^{-3}$
0.01M NaOH + 1.99M $NaClO_4$	0.006	$5.6*10^{-4}$	$7.4*10^{-4}$

* The kinetic current is related to the oxide area determined by the BET method after subtracting the carbon contribution.

Table 22. Kinetic currents (i_k*) for Mn_2O_3, MnOOH, and $LaMnO_3$ calculated at 0.9 V vs. RHE in solutions with varible Na^+ concentrations.

Electrolyte composition	**Mn_2O_3** i_k mA cm^{-2}	**MnOOH** i_k mA cm^{-2}	**$LaMnO_3$** i_k mA cm^{-2}
0.1M NaOH + 1.9M $NaClO_4$	0.020	$10*10^{-4}$	0.002
0.1M NaOH + 1M $NaClO_4$	0.018	$7.8*10^{-4}$	0.004
0.1M NaOH + 0.1M $NaClO_4$	0.018	$5.1*10^{-4}$	0.004
0.1M NaOH	0.016	$3.73*10^{-4}$	0.004

*The kinetic current is related to the oxide area determined by the BET method after subtracting the carbon contribution.

Considering that each of the oxide materials studied in this work demonstrated its peculiarities, in what follows we discuss each of them separately. Since oxides are studied in the form of oxide/carbon compositions, the behavior of carbon is discussed first.

Carbon

The ORR voltammograms shift positive on the RHE scale with the increase of pH. Overpotential measured at constant current density (1 μA cm^{-2}) increases by ~ 30 mV per unit pH. This shift is purely thermodynamic, and is in agreement with a two-electron reduction of O_2 to HO_2^- on carbon in the studied pH interval (see Pourbaix diagram of Figure 74). This Nernstian pH dependence advocates for the proton-coupled electron transfer mechanism on carbon. However, considering that pH also affects the electrode charge (see Chapter 4) and the electric double layer, this conclusion is not unambiguous and requires further investigations. The kinetic current also increases with the concentration of cations, which may be attributed to the formation of negatively charged ORR intermediates, which are stabilized on the surface by cations from the electrolyte, the latter decreasing the repulsion from the surface. The observed Tafel slope (ca. 50 mV/decade) is not compatible with a charge-transfer step as the rds, and is rather indicative of a chemical limiting step preceded by an equilibrium electrochemical step. One should keep in mind, however, that Tafel slope is affected by various intrinsic and extrinsic factors and its interpretation may be ambiguous. Further discussion of the ORR mechanism on carbon is beyond the scope of this work.

$LaMnO_3$

For the Mn perovskite, CVs experience little effect of the electrolyte (either pH or Na^+ concentration), the only noticeable change being increase of pseudocapacitance with the decrease of pH. The interfacial Mn(IV)/Mn(III) transition is fast in all studied electrolytes as confirmed by the CVs measured at variable scan rate.

Increase of pH results in a ~ 20 mV/pH ORR voltammograms which is smaller than the shift observed for carbon. Note that if the rds of the ORR were O_2 reduction with formation of superoxide ($O_2 + e^- \rightarrow O_2^-$), one would expect ORR voltammograms to be independent of pH on the SHE scale, which means that on the RHE scale (which is itself pH-dependent) we would have observed a 60 mV positive shift per unit pH. The fact that we do not experimentally observe such a shift may be tentatively explained by the ORR occurring through proton-coupled electron transfer (PCET) mechanism as previously proposed in Ref [34] and obeys mechanism depicted in Fig. 25 of Chapter 1. As mentioned above, increase of the mixed potential with pH in the presence of hydrogen peroxide may result from either acceleration of the HPRR kinetics, or, alternatively, deceleration of the HPOR kinetics. The HPRR and HPOR currents are diffusion-limited in all

studied electrolytes, which confirms fast kinetics of step 5, in agreement with previous publications. Considering that step 5 is very fast, we attribute the positive E_{mix} shift to the negative effect of pH on the HPOR (steps 2 and 3). Deceleration of steps 2 and 3 of the ORR mechanism with pH may also explain smaller than Nerstian (~20 mV rather than ~60 mV per pH unit for the O_2/OH^- equilibrium) shift of the ORR with pH on the RHE scale. Comparison of RDE voltammograms for ORR and HPRR/HPOR (Fig. 90) proves that the ORR 'onset' is close to the mixed potential in agreement with the previous studies. Cation concentration has little effect either on the HPRR or on the ORR.

Mn_2O_3

For Mn_2O_3 the interfacial redox transition is fast (cf. scan rate dependence in Fig 66 e-h of Chapter 4) in all studied electrolytes. However, both pH and cation concentration exert strong effect on the position of the interfacial redox transition, E_f shifting negative with pH and with the cation concentration. In the framework of kinetic model proposed in Ref [34] such a negative shift of the E_f is expected to result in a decrease of the number of Mn(III) sites available for O_2 adsorption and thus slow-down of the ORR kinetics which is however not observed. This may be attributed to various counteracting factors affecting the ORR kinetics. Such a conclusion is confirmed by the crossing of the Tafel plots (Fig 83) acquired at different pH. Same as above, ORR voltammograms on the SHE scale are pH-dependent being suggestive of a PCET mechanism. As concerned step 5, it is fast under all studied conditions as confirmed by the diffusion-limited current of the HPRR and HPOR. Increase of the cation concentration does not have noticeable effect on the E_{mix} (Fig. 90), but improves the ORR kinetics if one considers normalized RDE voltammograms, Fig. 88 (which are only valid within the assumption of the 1st order reaction with respect to O_2). The improvement of the kinetics of the ORR with the cation concentration may be tentatively attributed to the stabilization of negatively charged intermediate (HO_2^-) by cations.

MnOOH

MnOOH demonstrates the most peculiar behavior either depending on pH or on the cation concentration. First of all, we recall that the interfacial redox transition (step 1 of the ORR mechanism) is slow for MnOOH and further decelerates with a pH decrease. CV measurements suggest the existence of two types of surface sites (Mn(III)OH and Mn(III)ONa) their relative coverage depending on pH and cation concentration. Both pH and cation concentration exert very strong influence on the ORR and HPRR/HPOR kinetics. The most remarkable effect is concerned with the increase of kinetic currents observed either upon increase of the cation concentration or decrease of pH. The observed changes may be explained by an increase of the rate constant of step

5, the step which is fast on the $LaMnO_3$ or Mn_2O_3 surface but slow on MnOOH. Positive cation effect may be tentatively explained by decrease of the activation barrier of the O-O breaking step upon H^+/Na^+ exchange at the interface. Note that increase of the Na^+ concentration results in an increase of the relative intensity of the low potential peak in the CV, which we attribute to the - ONa species. As discussed in the literature review (Chapter 1), the authors of Ref. [36] suggested that the significantly lower ORR catalytic activity of MnOOH compared with Mn_2O_3 is associated with a large distance between the manganese cations on the surface, which does not allow for the adsorbate-adsorbate (OH—O_2H) interactions, the latter decreasing the activation barrier on the surface of Mn_2O_3. Let us analyze possible changes occurring at the interface at high Na^+ concentration. We assume that the interfacial redox transition involves proton intercalation/deintercalation (both on the surface and in the subsurface):

$$MnO_2 + H_2O + e^- \rightarrow MnOOH + OH^- \quad (94)$$

And, at high Na^+ concentration, cation may also intercalate in the oxide structure:

$$MnO_2 + Na^+ + e^- \rightarrow MnOONa \quad (95)$$

As shown in Chapter 4, these processes occur during the operation of MnO_2 as a supercapacitor. Since Na^+ is larger than proton, one can expect distortion of MnO_6 octahedra resulting in an increase of the width of the channels where Na^+ is located, along with a decrease in the size of the channels in which the protons are located (Fig. 91). These structural changes may lead to the convergence of some manganese centers at the interface, the latter favoring adsorbate-adsorbate interactions and hence O-O bond breaking. In the future it would be interesting to verify this hypothesis by quantum chemical calculations.

In what the influence of the pH is concerned, it is currently not fully clear why step 5 deccelerates upon increase of the pH. Probably, it is related to a smaller negative charge at the oxide surface and also to the increase in the fraction of protonated (uncharged) H_2O_2 species.

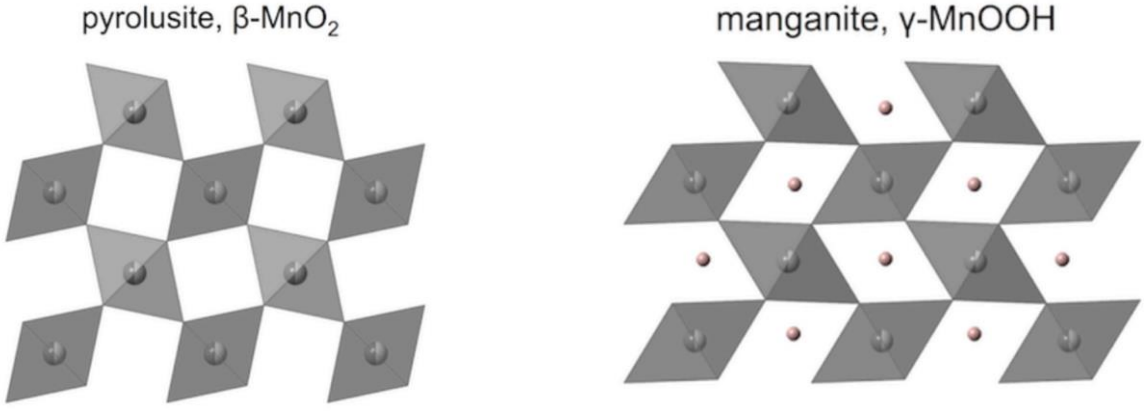

Fig. 91. Structures of β-MnO_2 and γ-MnOOH. Pink circles stand for protons.

As mentioned above, it is MnOOH, which exhibits the strongest shift of E_{mix} with the cation concentration. This shift can be corroborated within the above-discussed increase of the rate constant of step 5. As concerns the pH, its increase seems to have negative effect on the kinetics of steps 2, 3 and 5 (see discussion above).

5.4 Conclusions

Investigation of the influence of the electrolyte composition on the kinetics of the ORR and hydrogen peroxide oxidation/reduction on Mn oxides (MnOOH, Mn_2O_3 and $LaMnO_3$), has shown that the reaction rates are strongly affected by the electrolyte composition (Na^+ and OH^- concentration) and that these effects are different for the studied oxides.

Overall the results are in agreement with the previously proposed 'series' ORR mechanism, occurring through the intermediate formation of hydrogen peroxide, comprised of proton-coupled electron transfer steps and a chemical step of the O-O bond breaking. It is shown that this chemical step is not only sensitive to the oxide structure (in agreement with the previous studies) but also to the electrolyte composition. It was found that the concentration of $NaClO_4$ has a strong influence on the rate constant of the chemical O-O breaking in the peroxo-intermediate of the ORR (step 5 of the ORR mechanism), with the greatest effect for MnOOH. For Mn_2O_3, the greatest cation effect is observed for step 1 (interfacial redox transition).

pH influences the ORR for all studied materials. However, its understanding requires further computational studies.

5.5 References

[1] M. Auinger, I. Katsounaros, J.C. Meier, S.O. Klemm, P.U. Biedermann, A.A. Topalov, M. Rohwerder, K.J.J. Mayrhofer, Near-surface ion distribution and buffer effects during electrochemical reactions, Physical Chemistry Chemical Physics. 13 (2011) 16384–16394. https://doi.org/10.1039/c1cp21717h.

[2] V. Briega-Martos, E. Herrero, J.M. Feliu, The inhibition of hydrogen peroxide reduction at low potentials on Pt(111): Hydrogen adsorption or interfacial charge?, Electrochemistry Communications. 85 (2017) 32–35. https://doi.org/10.1016/j.elecom.2017.10.016.

[3] M.T.M. Koper, Theory of multiple proton-electron transfer reactions and its implications for electrocatalysis, Chemical Science. 4 (2013) 2710–2723. https://doi.org/10.1039/c3sc50205h.

[4] S. Strbac, The effect of pH on oxygen and hydrogen peroxide reduction on polycrystalline Pt electrode, Electrochimica Acta. 56 (2011) 1597–1604. https://doi.org/10.1016/j.electacta.2010.10.057.

[5] P. Rodriguez, M.T.M. Koper, Electrocatalysis on gold, Physical Chemistry Chemical Physics. 16 (2014) 13583–13594. https://doi.org/10.1039/c4cp00394b.

[6] Cation Overcrowding Effect on the Oxygen Evolution Reaction | JACS Au, (n.d.). https://pubs.acs.org/doi/10.1021/jacsau.1c00315 (accessed October 30, 2022).

[7] Exceptional oxygen evolution reactivities on $CaCoO_3$ and $SrCoO_3$ | Science Advances, (n.d.). https://www.science.org/doi/10.1126/sciadv.aav6262 (accessed October 16, 2022).

[8] A. Grimaud, O. Diaz-Morales, B. Han, W.T. Hong, Y.-L. Lee, L. Giordano, K.A. Stoerzinger, M.T.M. Koper, Y. Shao-Horn, Activating lattice oxygen redox reactions in metal oxides to catalyse oxygen evolution, Nature Chem. 9 (2017) 457–465. https://doi.org/10.1038/nchem.2695.

[9] B.-J. Kim, E. Fabbri, M. Borlaf, D.F. Abbott, I.E. Castelli, M. Nachtegaal, T. Graule, T.J. Schmidt, Oxygen evolution reaction activity and underlying mechanism of perovskite electrocatalysts at different pH, Mater. Adv. 2 (2021) 345–355. https://doi.org/10.1039/D0MA00661K.

[10] I. Roche, E. Chaînet, M. Chatenet, J. Vondrák, Carbon-Supported Manganese Oxide Nanoparticles as Electrocatalysts for the Oxygen Reduction Reaction (ORR) in Alkaline Medium: Physical Characterizations and ORR Mechanism, J. Phys. Chem. C. 111 (2007) 1434–1443. https://doi.org/10.1021/jp0647986.

[11] I. Roche, K. Scott, Effect of pH and temperature on carbon-supported manganese oxide oxygen reduction electrocatalysts, Journal of Electroanalytical Chemistry. 638 (2010) 280–286. https://doi.org/10.1016/j.jelechem.2009.10.030.

[12] G. Jürmann, D.J. Schiffrin, K. Tammeveski, The pH-dependence of oxygen reduction on quinone-modified glassy carbon electrodes, Electrochimica Acta. 53 (2007) 390–399. https://doi.org/10.1016/j.electacta.2007.03.053.

[13] P.N. Ross Jr, Oxygen reduction reaction on smooth single crystal electrodes, in: Handbook of Fuel Cells, John Wiley & Sons, Ltd, 2010. https://doi.org/10.1002/9780470974001.f205035.

[14] J.J. Li, J. Wei, J. Cai, Y.X. Chen, PH effect on oxidation of hydrogen peroxide on Au(111) electrode in alkaline solutions, Chinese Journal of Chemical Physics. 31 (2018) 779–783. https://doi.org/10.1063/1674-0068/31/cjcp1804064.

[15] W.R. Fawcett, Fifty years of studies of double layer effects in electrode kinetics—a personal view, J Solid State Electrochem. 15 (2011) 1347. https://doi.org/10.1007/s10008-011-1337-4.

[16] W.R. Fawcett, The effect of ionic size in the double layer on the kinetics of electrode reactions, Journal of Electroanalytical Chemistry and Interfacial Electrochemistry. 22 (1969) 19–28. https://doi.org/10.1016/S0022-0728(69)80142-7.

[17] G. Hussain, L. Pérez-Martínez, J.-B. Le, M. Papasizza, G. Cabello, J. Cheng, A. Cuesta, How cations determine the interfacial potential profile: Relevance for the CO2 reduction reaction, Electrochimica Acta. 327 (2019) 135055. https://doi.org/10.1016/j.electacta.2019.135055.

[18] R.R. Nazmutdinov, D.V. Glukhov, G.A. Tsirlina, O.A. Petrii, Exploring the molecular features of cationic catalysis phenomenon: Peroxodisulfate reduction at a mercury electrode, Journal of Electroanalytical Chemistry. 582 (2005) 118–129. https://doi.org/10.1016/j.jelechem.2005.03.021.

[19] N.V. Nikolaeva-Fedorovich, O.A. Petrii, B.B. Damaskin, G.A. Furazhkova, Vestnik Mosk. Univ. 40 (1961).

[20] I.T. McCrum, X. Chen, K.A. Schwarz, M.J. Janik, M.T.M. Koper, Effect of Step Density and Orientation on the Apparent pH Dependence of Hydrogen and Hydroxide Adsorption on Stepped Platinum Surfaces, Journal of Physical Chemistry C. 122 (2018) 16756–16764. https://doi.org/10.1021/acs.jpcc.8b03660.

[21] M.C.O. Monteiro, A. Goyal, P. Moerland, M.T.M. Koper, Understanding Cation Trends for Hydrogen Evolution on Platinum and Gold Electrodes in Alkaline Media, ACS Catal. 11 (2021) 14328–14335. https://doi.org/10.1021/acscatal.1c04268.

[22] D. Strmcnik, D.F. van der Vliet, K.-C. Chang, V. Komanicky, K. Kodama, H. You, V.R. Stamenkovic, N.M. Marković, Effects of Li^+, K^+, and Ba^{2+} Cations on the ORR at Model and High Surface Area Pt and Au Surfaces in Alkaline Solutions, J. Phys. Chem. Lett. 2 (2011) 2733–2736. https://doi.org/10.1021/jz201215u.

[23] G. Jones, M. Dole, The viscosity of aqueous solutions of strong electrolytes with special reference to barium chloride, J. Am. Chem. Soc. 51 (1929) 2950–2964. https://doi.org/10.1021/ja01385a012.

[24] H.D.B. Jenkins, Y. Marcus, Viscosity B-Coefficients of Ions in Solution, Chem. Rev. 95 (1995) 2695–2724. https://doi.org/10.1021/cr00040a004.

[25] D. Strmcnik, K. Kodama, D. van der Vliet, J. Greeley, V.R. Stamenkovic, N.M. Marković, The role of non-covalent interactions in electrocatalytic fuel-cell reactions on platinum, Nature Chem. 1 (2009) 466–472. https://doi.org/10.1038/nchem.330.

[26] P.P. Lopes, D. Strmcnik, J.S. Jirkovsky, J.G. Connell, V. Stamenkovic, N. Markovic, Double layer effects in electrocatalysis: The oxygen reduction reaction and ethanol oxidation reaction on Au(1 1 1), Pt(1 1 1) and Ir(1 1 1) in alkaline media containing Na and Li cations, Catalysis Today. 262 (2016) 41–47. https://doi.org/10.1016/j.cattod.2015.09.010.

[27] J. Suntivich, E.E. Perry, H.A. Gasteiger, Y. Shao-Horn, The Influence of the Cation on the Oxygen Reduction and Evolution Activities of Oxide Surfaces in Alkaline Electrolyte, Electrocatalysis. 4 (2013) 49–55. https://doi.org/10.1007/s12678-012-0118-x.

[28] F. Moureaux, P. Stevens, M. Chatenet, Effect of Lithium and Potassium Cations on the Electrocatalytic Properties of Carbon and Manganese Oxide Electrocatalysts Towards the Oxygen Reduction Reaction in Concentrated Alkaline Electrolyte, Electrocatalysis. 4 (2013) 123–133. https://doi.org/10.1007/s12678-013-0127-4.

[29] X. Chen, I.T. McCrum, K.A. Schwarz, M.J. Janik, M.T.M. Koper, Co-adsorption of Cations as the Cause of the Apparent pH Dependence of Hydrogen Adsorption on a Stepped Platinum Single-Crystal Electrode, Angewandte Chemie. 129 (2017) 15221–15225. https://doi.org/10.1002/ange.201709455.

[30] A.C. Garcia, T. Touzalin, C. Nieuwland, N. Perini, M.T.M. Koper, Enhancement of Oxygen Evolution Activity of Nickel Oxyhydroxide by Electrolyte Alkali Cations, Angewandte Chemie - International Edition. 58 (2019) 12999–13003. https://doi.org/10.1002/anie.201905501.

[31] F. Moureaux, P. Stevens, G. Toussaint, M. Chatenet, Timely-activated 316L stainless steel: A low cost, durable and active electrode for oxygen evolution reaction in concentrated alkaline environments, Applied Catalysis B: Environmental. 258 (2019) 117963. https://doi.org/10.1016/j.apcatb.2019.117963.

[32] A.S. Ryabova, A. Bonnefont, P. Zagrebin, T. Poux, R. Paria Sena, J. Hadermann, A.M. Abakumov, G. Kéranguéven, S.Y. Istomin, E.V. Antipov, G.A. Tsirlina, E.R. Savinova, Study of Hydrogen Peroxide Reactions on Manganese Oxides as a Tool To Decode the Oxygen Reduction Reaction Mechanism, ChemElectroChem. 3 (2016) 1667–1677. https://doi.org/10.1002/celc.201600236.

[33] B.N. Efremov, M.R. Tarasevich, Kinetics and mechanism of electroreduction reactions and oxygen liberation on cobalt spinels, Electrochemistry. 17 (1981) 1672–1679.

[34] A.S. Ryabova, F.S. Napolskiy, T. Poux, S.Ya. Istomin, A. Bonnefont, D.M. Antipin, A.Ye. Baranchikov, E.E. Levin, A.M. Abakumov, G. Kéranguéven, E.V. Antipov, G.A. Tsirlina, E.R. Savinova, Rationalizing the Influence of the Mn(IV)/Mn(III) Red-Ox Transition on

the Electrocatalytic Activity of Manganese Oxides in the Oxygen Reduction Reaction, Electrochimica Acta. 187 (2016) 161–172. https://doi.org/10.1016/j.electacta.2015.11.012.

[35] T. Poux, A. Bonnefont, G. Kéranguéven, G.A. Tsirlina, E.R. Savinova, Electrocatalytic Oxygen Reduction Reaction on Perovskite Oxides: Series versus Direct Pathway, ChemPhysChem. 15 (2014) 2108–2120. https://doi.org/10.1002/cphc.201402022.

[36] V.A. Nikitina, A.A. Kurilovich, A. Bonnefont, A.S. Ryabova, R.R. Nazmutdinov, E.R. Savinova, G.A. Tsirlina, ORR on Simple Manganese Oxides: Molecular-Level Factors Determining Reaction Mechanisms and Electrocatalytic Activity, J. Electrochem. Soc. 165 (2018) J3199. https://doi.org/10.1149/2.0261815jes.

General Conclusions and Outlook

This thesis had two objectives. The first objective was to establish relationship between the composition of Mn oxides and their stability and ORR activity. The second objective was to unveil the influence of the pH and the cation (Na^+) concentration on the ORR on Mn oxides.

To solve the **first objective**, a series of spinels AMn_2O_4 (A=Mn(II), Mg(II), Li(I) and Cd(II)) was synthesised. Using electrochemical techniques (cyclic voltammetry and rotating disc electrode voltammetry), we studied activity in the oxygen reduction reaction (ORR) in an alkaline solution as well as the surface interfacial redox transitions. With the help of post-mortem XPS characterization we demonstrate that the surface of the studied spinels (except for $MgMn_2O_4$) undergoes essential modification not only under potential cycling but also after contacting alkaline solution under open circuit conditions, and even during the electrode preparation.

The widely studied Mn_3O_4 spinel demonstrates the strongest surface modifications. We conclude that Mn(II) at the Mn_3O_4 surface is unstable in the presence of oxygen and is oxidized into Mn(III) and Mn(IV). This transformation is observed already for the dry sample exposed to air and is further enhanced upon its contact with either water or with NaOH electrolyte. Oxidation of Mn(II) results in dramatic catalyst degradation, likely leading to the loss of the spinel structure in the near-surface layers in short-term experiments and complete structure collapse in the long run. Hence, it is risky to include spinel Mn_3O_4 oxide (as well as other Mn(II)-containing oxides) in any structure/composition/ORR activity correlation. This brings us to a conclusion that evaluation of the materials stability must be included as an essential part of the measurement protocol for comparing ORR activities of different materials.

It is shown that different AMn_2O_4 spinels are transformed at different stages of the experiment. $LiMn_2O_4$ loses lithium ions from the near-surface layers but is likely to preserve its spinel structure through lithium replacement by protons resulting in a $Li_{1-x}Mn_2O_{4-y}OH_y$ composition. $CdMn_2O_4$ undergoes the greatest changes during potential cycling in the potential interval of the interfacial Mn(III)/Mn(IV) transition. In this case, the surface becomes depleted in Cd, and the spinel structure itself is not preserved on the surface. Mn_3O_4 (apparently due to the presence of Mn^{2+} cations, which are not stable in an alkaline solution) showed the greatest changes both when soaked in alkali and when cycling the potential. However, it is shown that cation substitution with a reductively inactive cation can increase the stability of the spinel structure. Thus, $MgMn_2O_4$ proved to be the most stable spinel, both when cycling potential, or when soaking in alkali, or during the ORR electrocatalysis.

The results of this work show how changing the composition of the spinel can affect its stability. However, this work lacks operando methods (such as online mass spectroscopy, or in

situ XAS) which would allow more detailed information regarding potential- and reaction-induced dynamic surface transformations, and hence the products of the degradation and the degradation mechanisms.

To achieve the **second objective**, the following studies have been carried out:

- Mn-containing oxides with different structures and different kinetics of the ORR ($LaMnO_3$, MnOOH, Mn_2O_3) have been obtained and characterized.
- The stability of manganese oxides was studied under the conditions of an electrochemical experiment and under conditions of prolonged contact with a background electrolyte.
- The effect of the electrolyte composition on the interface of oxides was studied by electrochemical methods and acid-base titration methods.
- The oxides were studied in the reactions of the oxygen reduction and the hydrogen peroxide oxidation and reduction at various pH and various concentrations of Na^+.

The results of the cyclic voltammetry measurements indicate that both the OH^- concentration (at a constant ionic strength) and Na^+ concentration (at a constant pH) affect the interfacial Mn(III)/Mn(IV) redox transition, and the effects are different for the studied oxides.

The position of the $LaMnO_3$ redox peaks on the RHE scale was pH and Na^+ concentration-independent, which agrees with the first step of the previously proposed ORR mechanism ($Mn(IV)=O + H_2O + e^- \rightarrow Mn(III)\text{-}OH + OH^-$). On the other hand, a very strong influence of both pH and Na^+ concentration was found for Mn_2O_3 and MnOOH. For MnOOH two pairs of redox peaks were observed, which were attributed to the presence of two types of active centers on the surface, namely Mn(III)OH or Mn(III)ONa, their relative intensity depending both on the pH and on the Na^+ concentration. This can be attributed to the H^+/Na^+ substitution occurring on the MnOOH/electrolyte interface resulting in the equilibrium shift between Mn(III)OH or Mn(III)ONa centers.

Cyclic voltammetry experiments performed with different scan rates indicate that the interfacial Mn(III)/Mn(IV) recharging is fast for Mn_2O_3 and $LaMnO_3$. Different behavior was observed for MnOOH, with an important contribution of slow processes, which may be attributed to the H^+/Na^+ intercalation. These processes of Na^+ intercalation/deintercalation can lead to structural changes, in particular to the change of unit cell parameters at the oxide/electrolyte interface.

Titration experiments have shown that the point of zero charge for all of the studied oxides is lower than 7, from which it can be concluded that in alkaline electrolytes they are all negatively

charged. For Mn_2O_3 and MnOOH the concentration of acid-base centres on the surface is shown to differ strongly from the one calculated from the crystallographic density of Mn cations, which is tentatively attributed to the coexistence of -OH and -ONa sites on the oxide surface, the latter inaccessible to the acid-base titration.

The investigation of the influence of the electrolyte composition on the kinetics of the ORR and hydrogen peroxide oxidation/reduction on Mn oxides (MnOOH, Mn_2O_3 and $LaMnO_3$) has shown that the reaction rates are strongly affected by the electrolyte composition (Na^+ and OH^- concentration) and that these effects are different for the studied oxides.

Overall the results of Chapter 5 confirm previously proposed 'series' ORR, occurring through the intermediate formation of hydrogen peroxide, comprised of proton-coupled electron transfer steps and a chemical step of the O-O bond breaking. It is shown that this chemical step is not only sensitive to the oxide structure (in agreement with the previous studies) but also to the electrolyte composition. It was found that the concentration of $NaClO_4$ has a strong influence on the rate constant of the chemical O-O breaking in the peroxo-intermediate of the ORR, with the greatest effect for MnOOH. For Mn_2O_3, the greatest cation effect is observed for step 1 (interfacial redox transition).

The results documented in this thesis when studying the effect of the electrolyte on the electrocatalytic properties of oxides provide answers to a number of questions related to the ORR mechanism. However, the interpretation of the results is not unambiguous due to a large number of factors that are simultaneously affected by changes in the concentrations of OH^- and Na^+. Microkinetic modeling, as well as quantum chemical calculations, can help to separate these influences. In a review of the literature, it was shown how informative it can be to study the influence of the size and charge of the electrolyte cation. This study can be especially important for understanding the processes occurring on MnOOH (for which the greatest influence of the Na^+ concentration and the occurrence of intercalation processes are shown in this work).

To sum up, the following perspectives could be proposed:

- ✓ More detailed study of the pH effect, including microkinetic modeling to clearly separate the influence of pH on different reaction steps (k_2, k_3 and k_5).
- ✓ Study of the influence of cation indentity on the electrochemical behavior of oxides.
- ✓ In situ measurements to determine the degradation mechanisms.

Annexes

Annex to Chapter 3

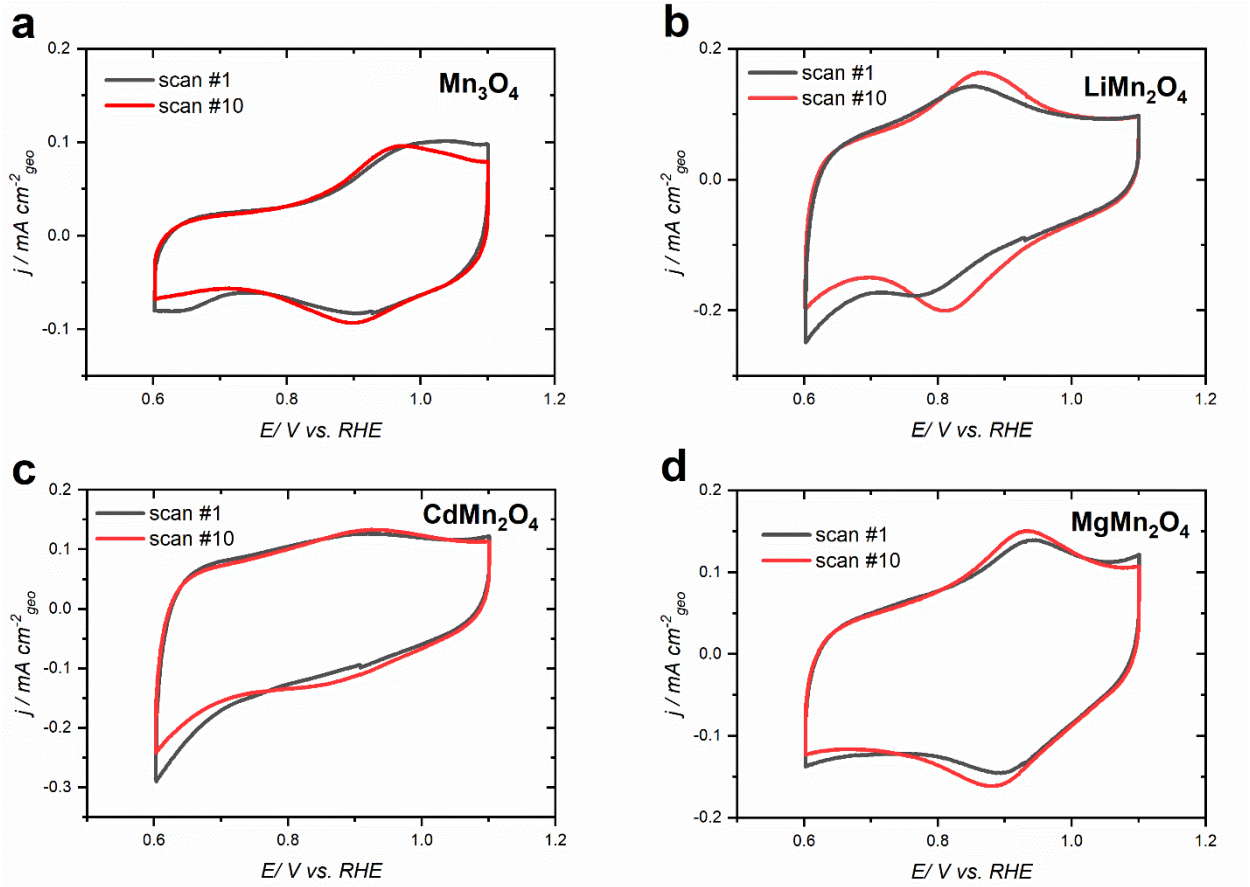

Fig. S1 CVs recorded during 1st and 10th cycles of the potential at 0.6-1.15 V of GC-supported thin films of oxide/carbon composites in N_2-purged 1 M NaOH at 10 mV s^{-1} for Mn_3O_4 (a) $LiMn_2O_4$ (b), $CdMn_2O_4$ (c) and $MgMn_2O_4$ (d). Loadings are 91 µg cm^{-2} oxide + 91 µg cm^{-2} carbon. Currents are normalized to the geometric area of the electrode. Note change in the CV shape and peak positions. One cannot exclude that while starting ORR measurements after 2-3 cycles in oxygen-free solution the near-surface layer of spinels is already transformed from its pristine state.

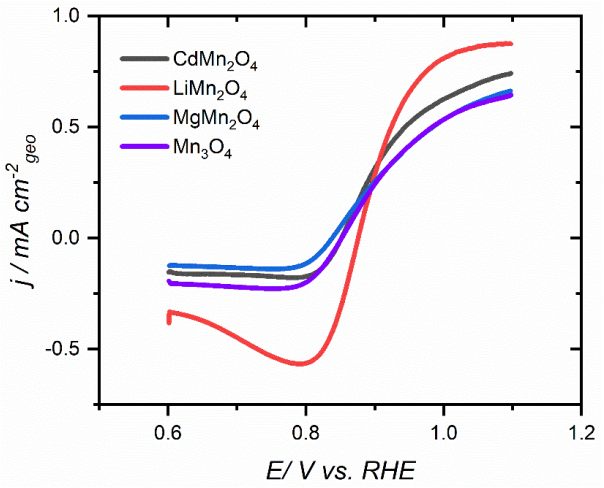

Fig. S2 Comparison of RDE voltammograms acquired in N_2-saturated 1M NaOH with 0.84 mM H_2O_2 at 10 mV s^{-1} for GC supported thin films of Mn_3O_4, $LiMn_2O_4$, $MgMn_2O_4$, $CdMn_2O_4$ at 900 rpm. Loading are: 91 μg cm^{-2} carbon + 91 μg cm^{-2} oxide. The current is normalized to the geometric surface of the electrode after subtracting the response in the H_2O_2-free solution.

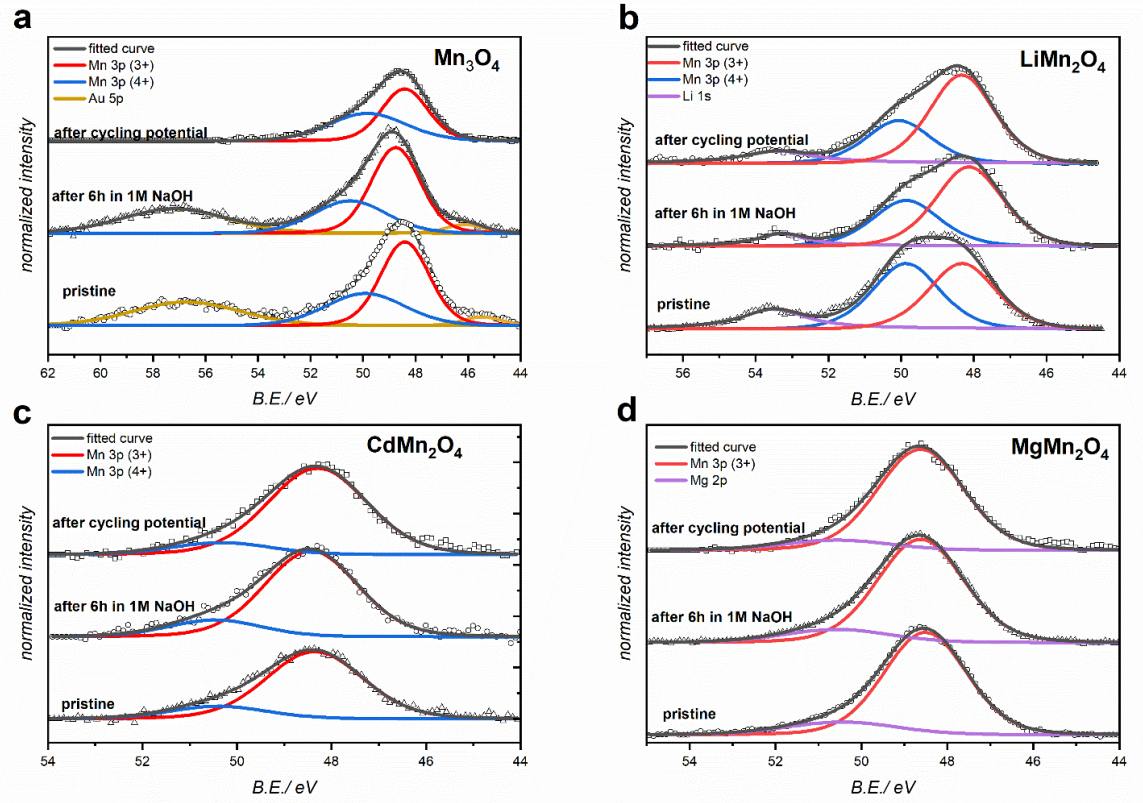

Fig. S3 Mn 3p XP spectra for Mn_3O_4 (a), $LiMn_2O_4$ (b), $CdMn_2O_4$ (c) and $MgMn_2O_4$ (d) (pristine samples and after preparation of aqueous suspension using ultrasound, soaking in 1 M NaOH for 6 h and after 10 cycles of CV at 0.6-1.15 V potential range. Black solid line corresponds to deconvolution of the spectra assuming the presence of Mn(II) (green), Mn(III) (red) and Mn(IV) (blue). Spectra are collected at ISSIS station of Bessy-II synchrotron and excitation energy 500 eV (λ=1.4 nm).

Annex to Chapter 4

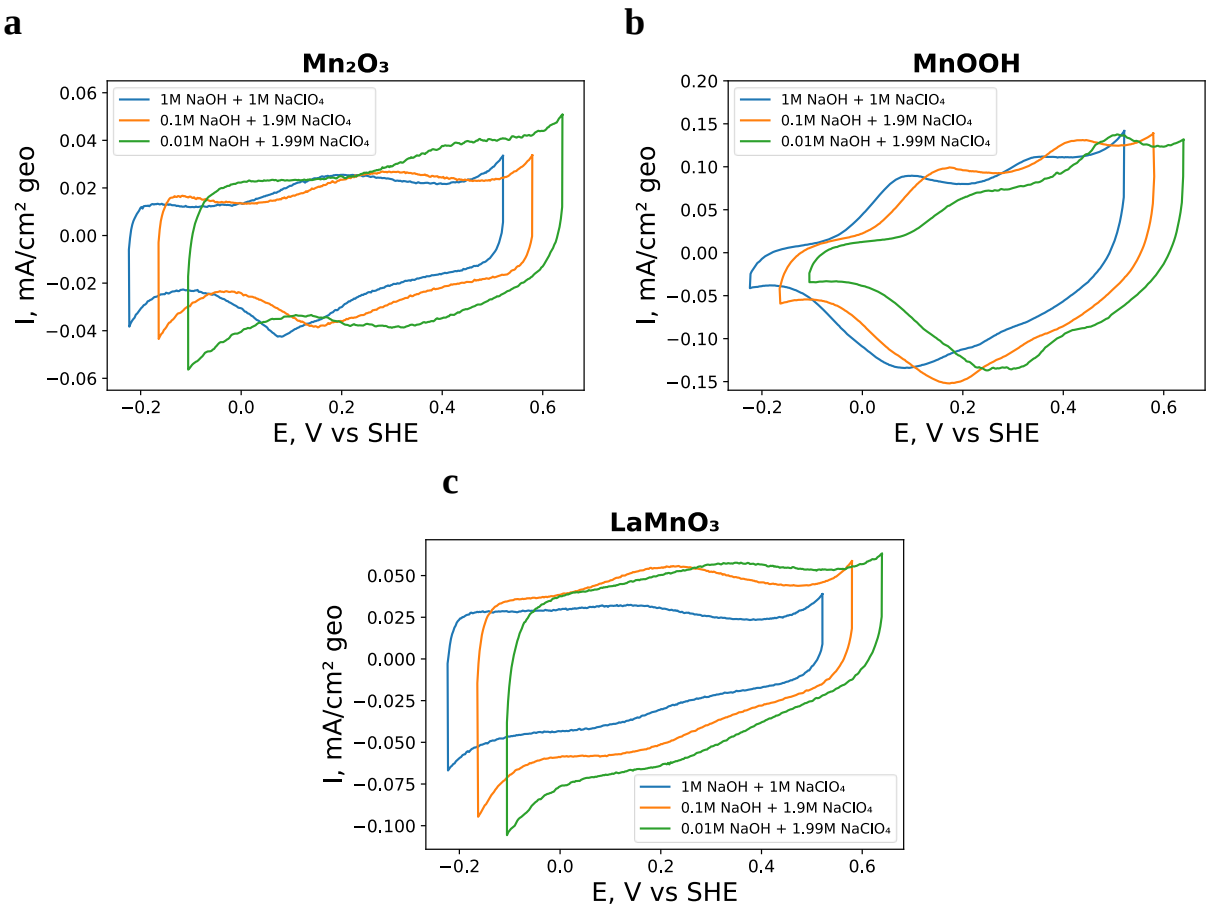

Fig. S4 CVs in N_2-saturated alkaline solutions for $LaMnO_3$ (a), Mn_2O_3 (b), MnOOH (c) and Sibunit Carbon (d) at different OH^- concentration and constant ionic strength (as indicated in the panels). Loading are: 91 μg cm^{-2} carbon + 91 μg cm^{-2} oxide. The current is normalized to the geometric surface of the electrode. The scale is relative to SHE.

Carbon

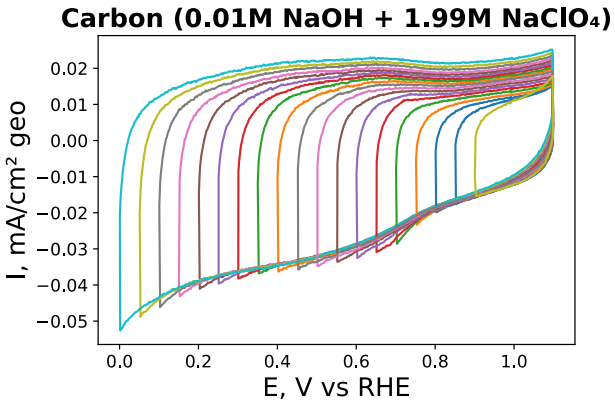
Carbon (0.01M NaOH + 1.99M NaClO₄)
I, mA/cm² geo
E, V vs RHE

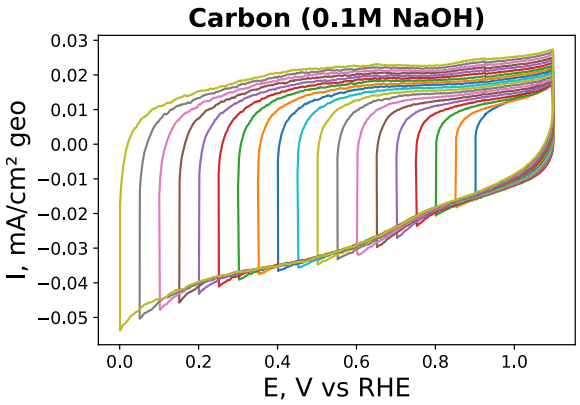
Carbon (0.1M NaOH)
I, mA/cm² geo
E, V vs RHE

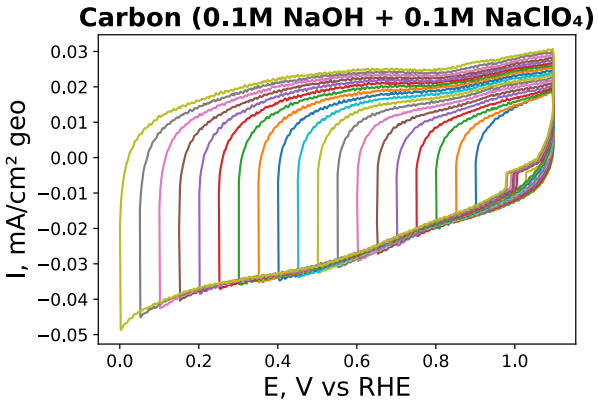
Carbon (0.1M NaOH + 0.1M NaClO₄)
I, mA/cm² geo
E, V vs RHE

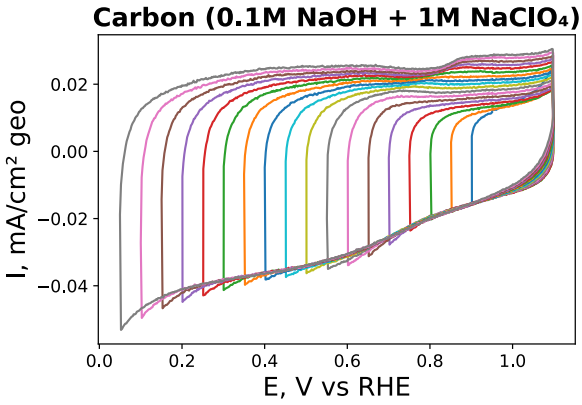
Carbon (0.1M NaOH + 1M NaClO₄)
I, mA/cm² geo
E, V vs RHE

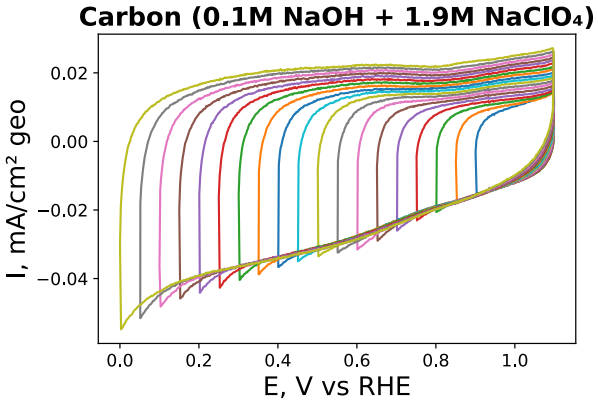
Carbon (0.1M NaOH + 1.9M NaClO₄)
I, mA/cm² geo
E, V vs RHE

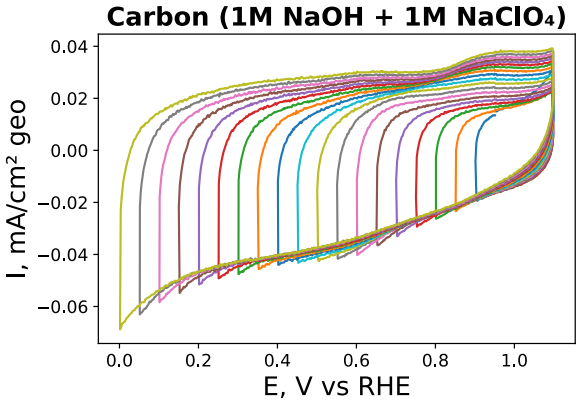
Carbon (1M NaOH + 1M NaClO₄)
I, mA/cm² geo
E, V vs RHE

$LaMnO_3$

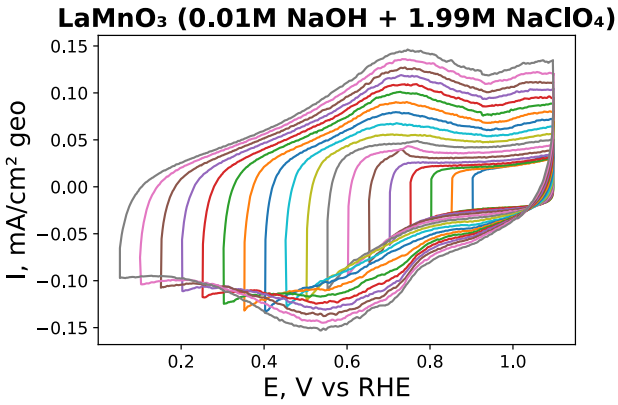
LaMnO₃ (0.01M NaOH + 1.99M NaClO₄)
I, mA/cm² geo
E, V vs RHE

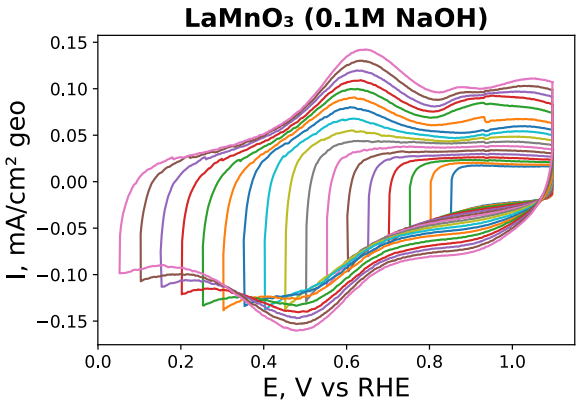
LaMnO₃ (0.1M NaOH)
I, mA/cm² geo
E, V vs RHE

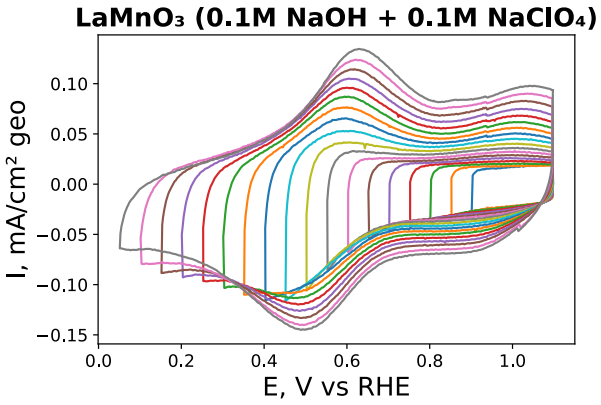
LaMnO₃ (0.1M NaOH + 0.1M NaClO₄)
I, mA/cm² geo
E, V vs RHE

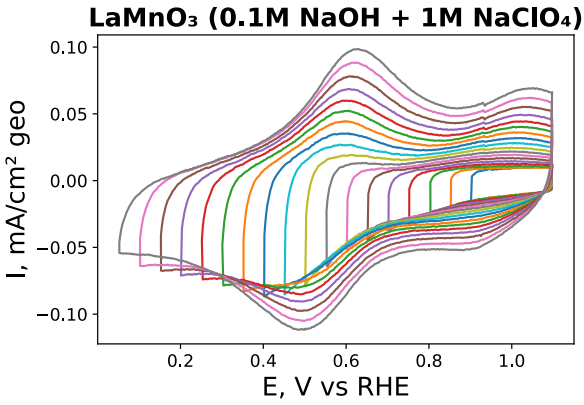
LaMnO₃ (0.1M NaOH + 1M NaClO₄)
I, mA/cm² geo
E, V vs RHE

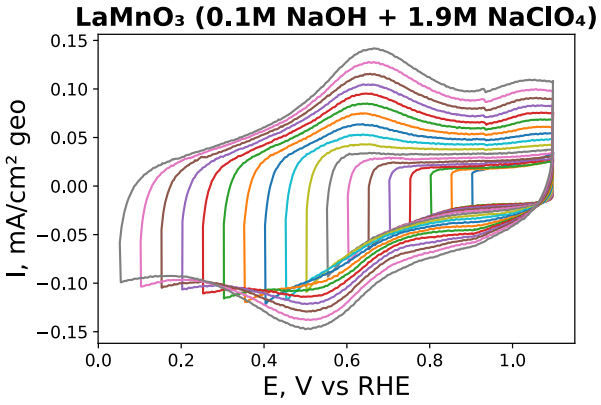
LaMnO₃ (0.1M NaOH + 1.9M NaClO₄)
I, mA/cm² geo
E, V vs RHE

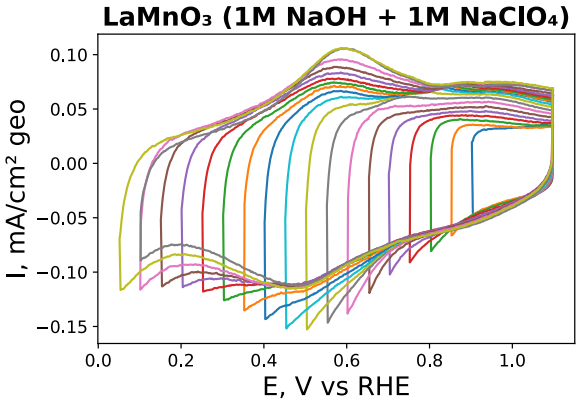
LaMnO₃ (1M NaOH + 1M NaClO₄)
I, mA/cm² geo
E, V vs RHE

Mn_2O_3

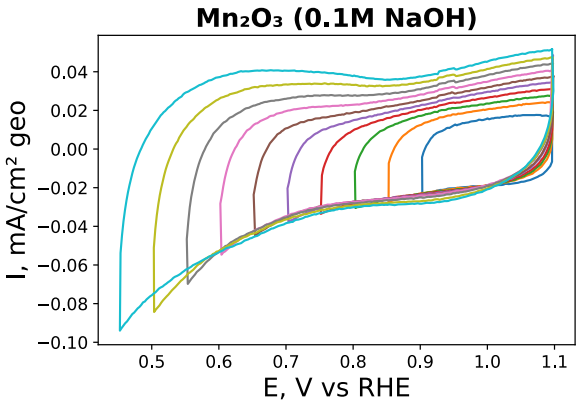
Mn₂O₃ (0.1M NaOH)
I, mA/cm² geo
E, V vs RHE

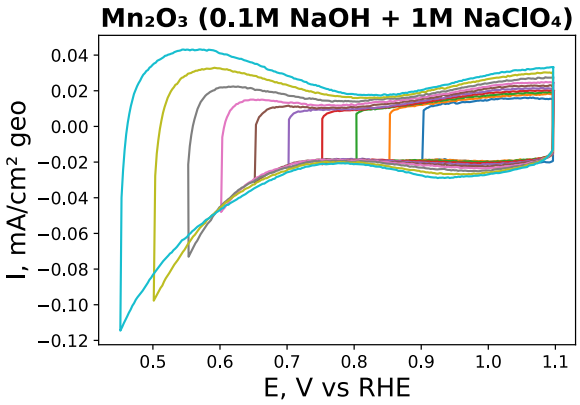
Mn₂O₃ (0.1M NaOH + 1M NaClO₄)
I, mA/cm² geo
E, V vs RHE

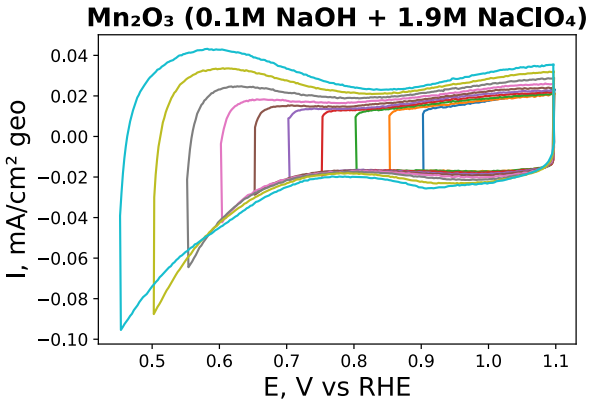
Mn₂O₃ (0.1M NaOH + 1.9M NaClO₄)
I, mA/cm² geo
E, V vs RHE

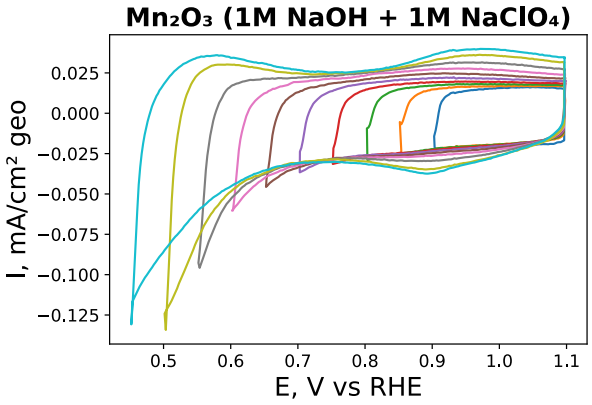
Mn₂O₃ (1M NaOH + 1M NaClO₄)
I, mA/cm² geo
E, V vs RHE

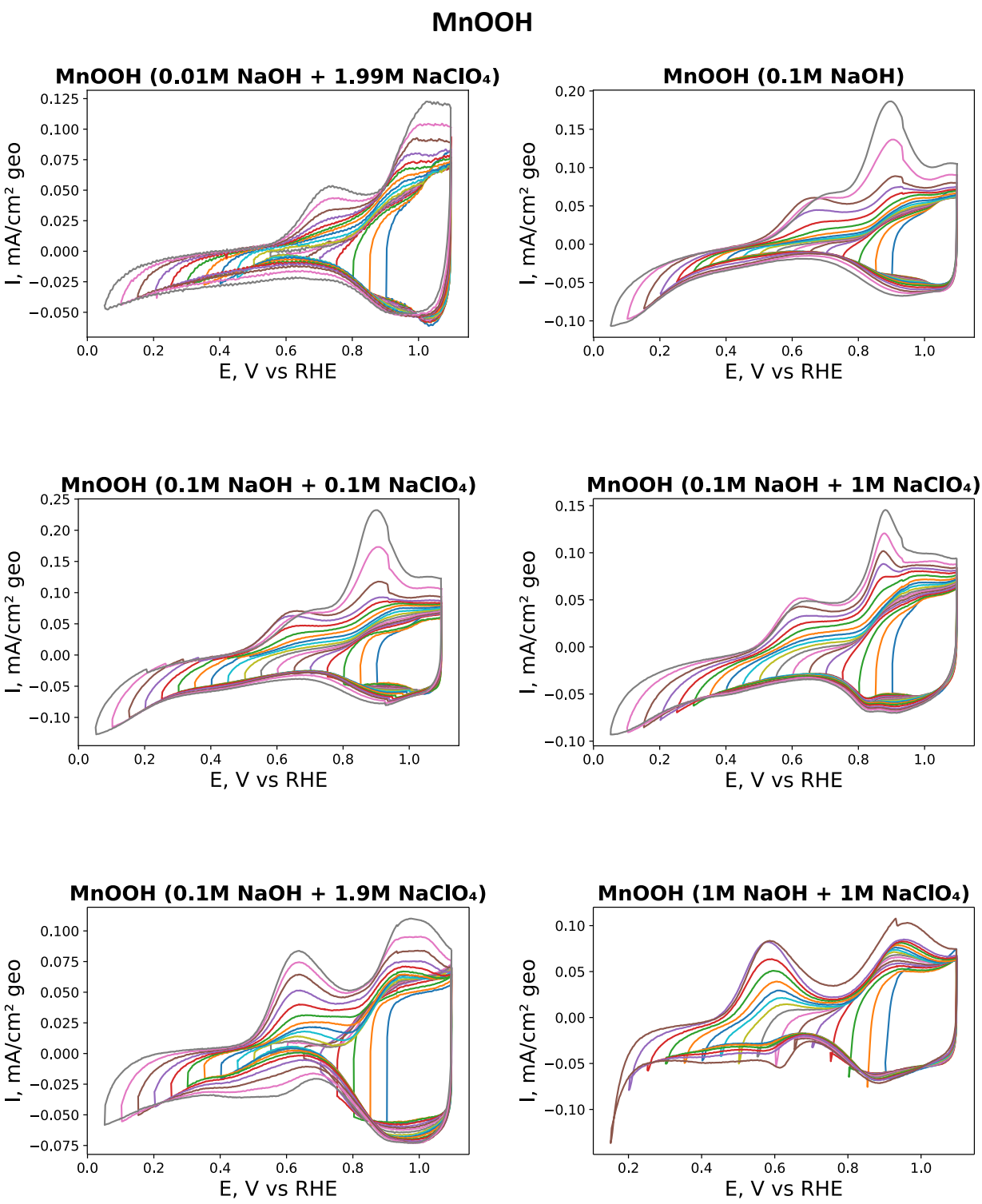

Fig. S5 CVs with a decreasing cathodic potential limit for GC-supported thin films of oxide/carbon composites in N_2-purged 1 M NaOH at 10 mV s^{-1} registered for Mn_2O_3, $LaMnO_3$, MnOOH and $MgMn_2O_4$ (d). Currents are normalized to the geometric area of the electrode. For each cathodic limit the third CV is shown. Loadings are 91 μg cm^{-2} oxide + 91 μg cm^{-2} carbon.

Carbon

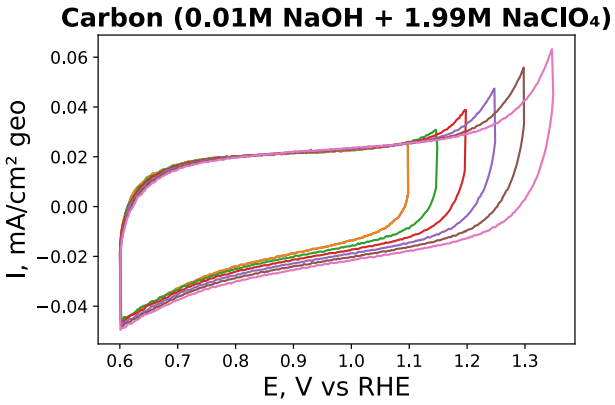
Carbon (0.01M NaOH + 1.99M NaClO₄)
I, mA/cm² geo
E, V vs RHE

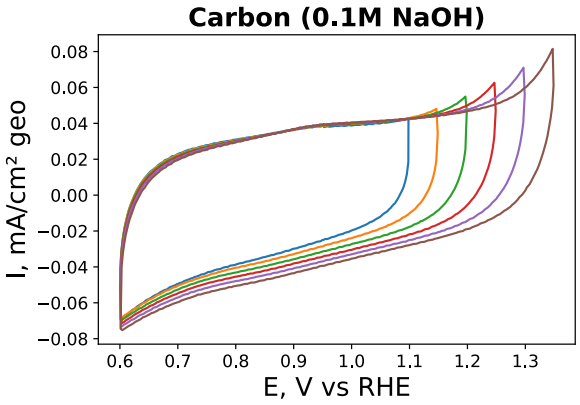
Carbon (0.1M NaOH)
I, mA/cm² geo
E, V vs RHE

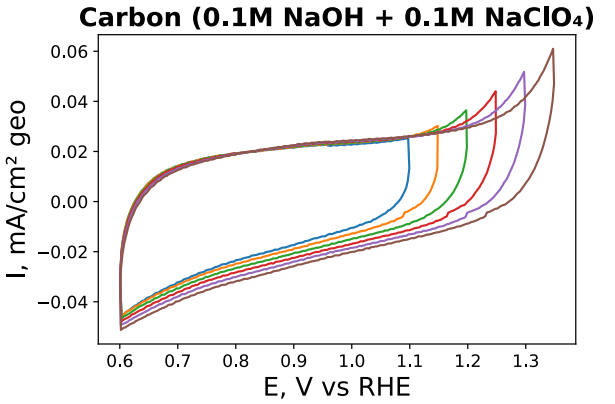
Carbon (0.1M NaOH + 0.1M NaClO₄)
I, mA/cm² geo
E, V vs RHE

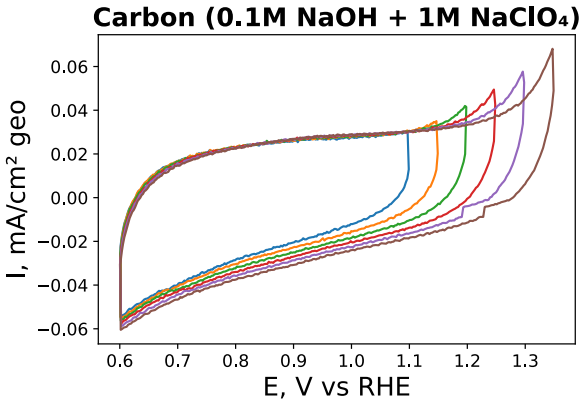
Carbon (0.1M NaOH + 1M NaClO₄)
I, mA/cm² geo
E, V vs RHE

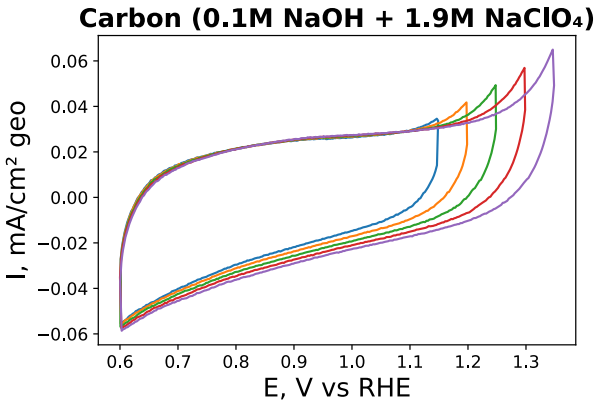
Carbon (0.1M NaOH + 1.9M NaClO₄)
I, mA/cm² geo
E, V vs RHE

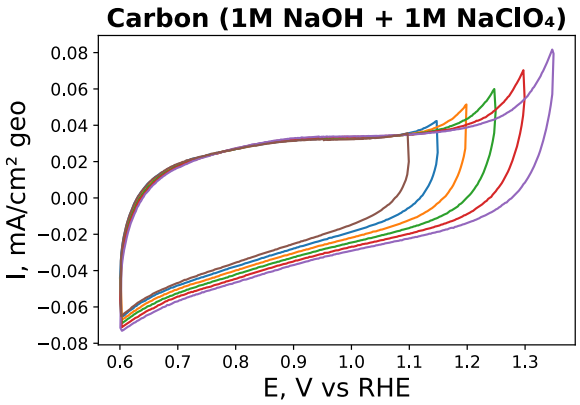
Carbon (1M NaOH + 1M NaClO₄)
I, mA/cm² geo
E, V vs RHE

$LaMnO_3$

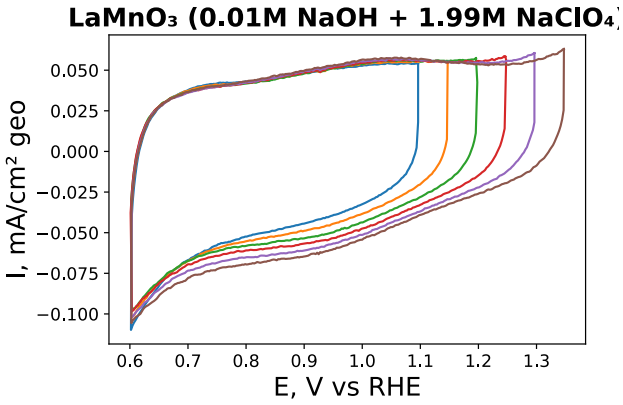
LaMnO₃ (0.01M NaOH + 1.99M NaClO₄)
I, mA/cm² geo
E, V vs RHE

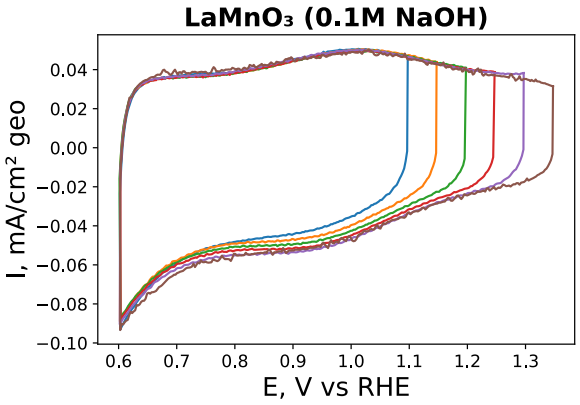
LaMnO₃ (0.1M NaOH)
I, mA/cm² geo
E, V vs RHE

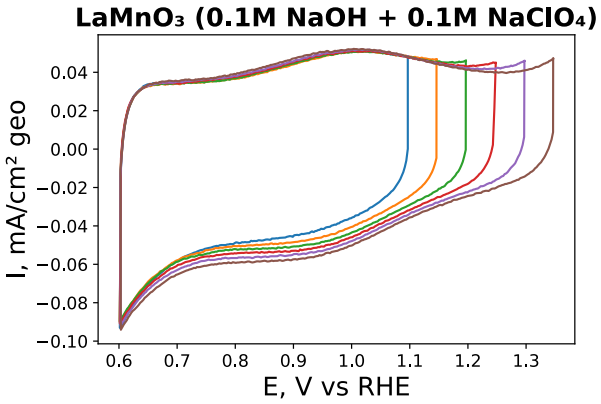
LaMnO₃ (0.1M NaOH + 0.1M NaClO₄)
I, mA/cm² geo
E, V vs RHE

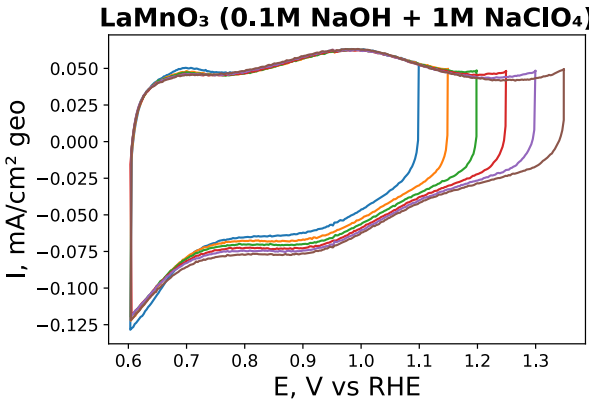
LaMnO₃ (0.1M NaOH + 1M NaClO₄)
I, mA/cm² geo
E, V vs RHE

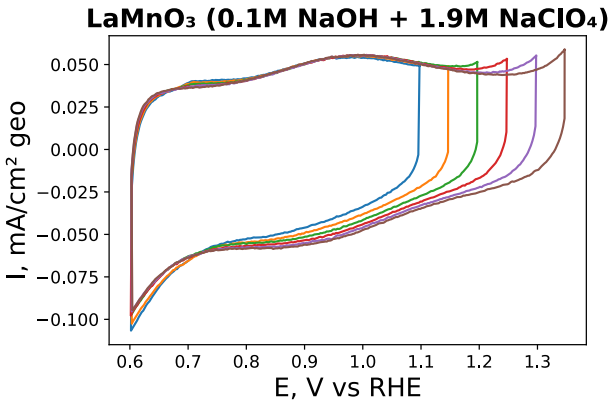
LaMnO₃ (0.1M NaOH + 1.9M NaClO₄)
I, mA/cm² geo
E, V vs RHE

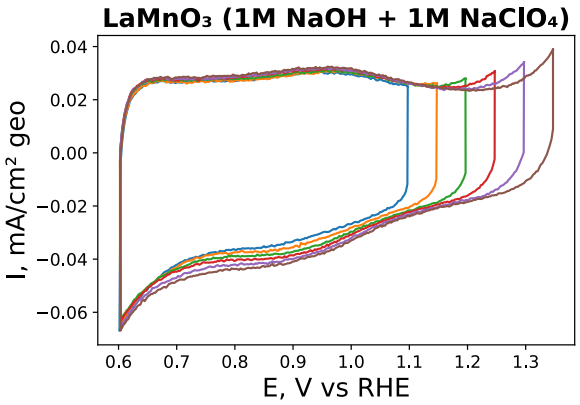
LaMnO₃ (1M NaOH + 1M NaClO₄)
I, mA/cm² geo
E, V vs RHE

Mn_2O_3

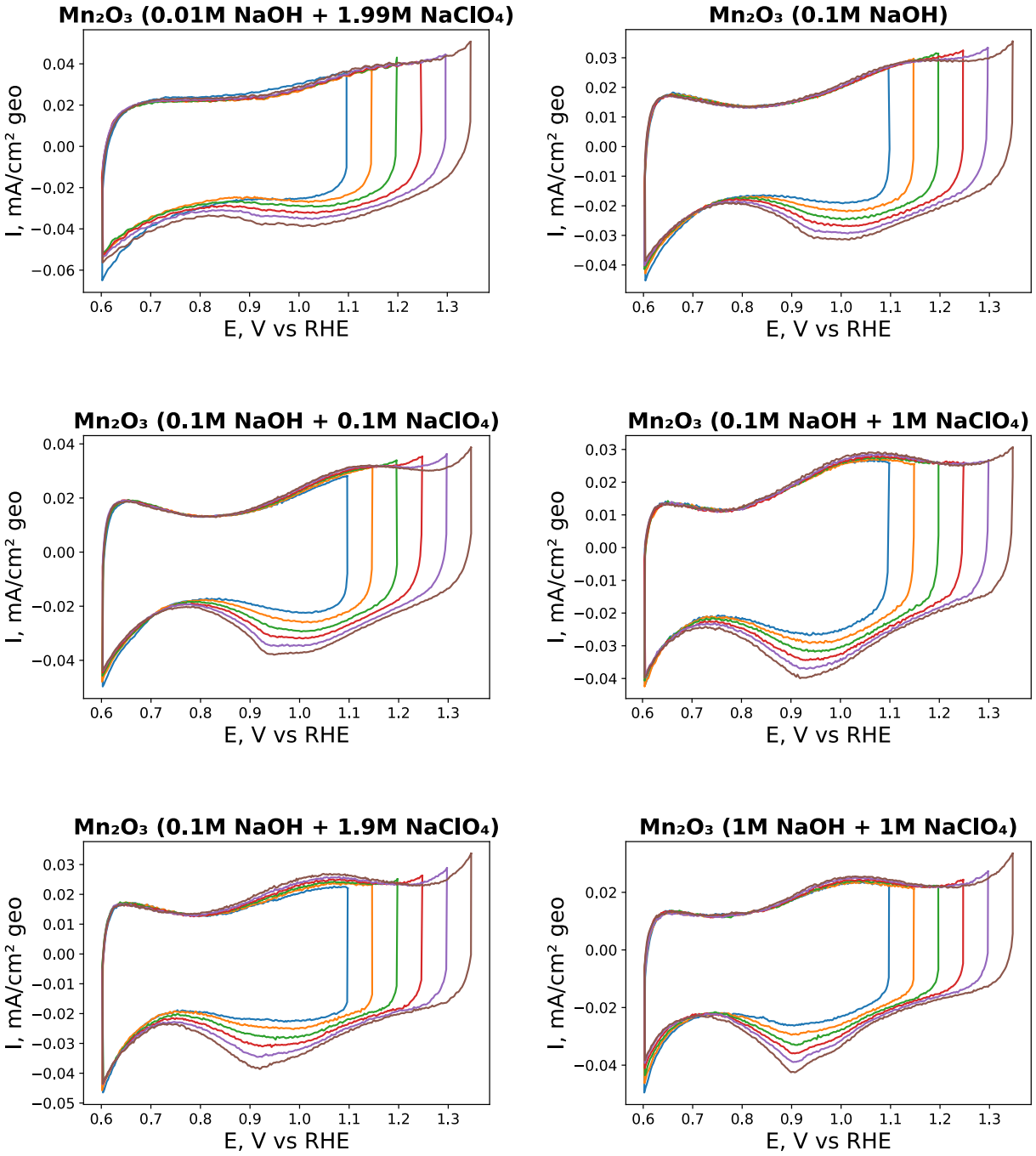
Mn₂O₃ (0.01M NaOH + 1.99M NaClO₄)
Mn₂O₃ (0.1M NaOH)
Mn₂O₃ (0.1M NaOH + 0.1M NaClO₄)
Mn₂O₃ (0.1M NaOH + 1M NaClO₄)
Mn₂O₃ (0.1M NaOH + 1.9M NaClO₄)
Mn₂O₃ (1M NaOH + 1M NaClO₄)
I, mA/cm² geo
E, V vs RHE

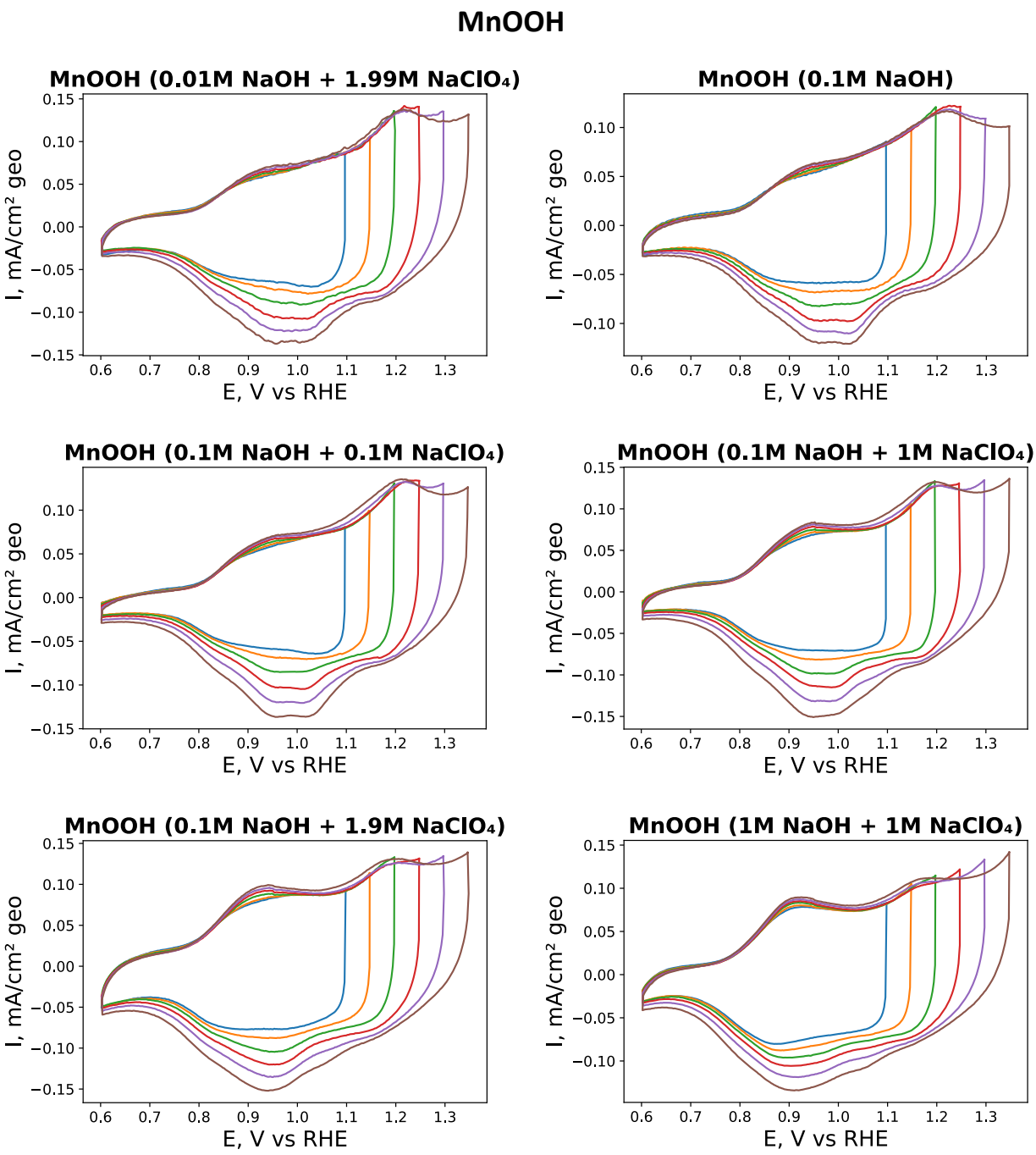

Fig. S 6 CVs with a decreasing anodic potential limit for GC-supported thin films of oxide/carbon composites in N_2-purged 1 M NaOH at 10 mV s^{-1} registered for Mn_2O_3, $LaMnO_3$, MnOOH and $MgMn_2O_4$ (d). Currents are normalized to the geometric area of the electrode. For each cathodic limit the third CV is shown. Loadings are 91 μg cm^{-2} oxide + 91 μg cm^{-2} carbon.

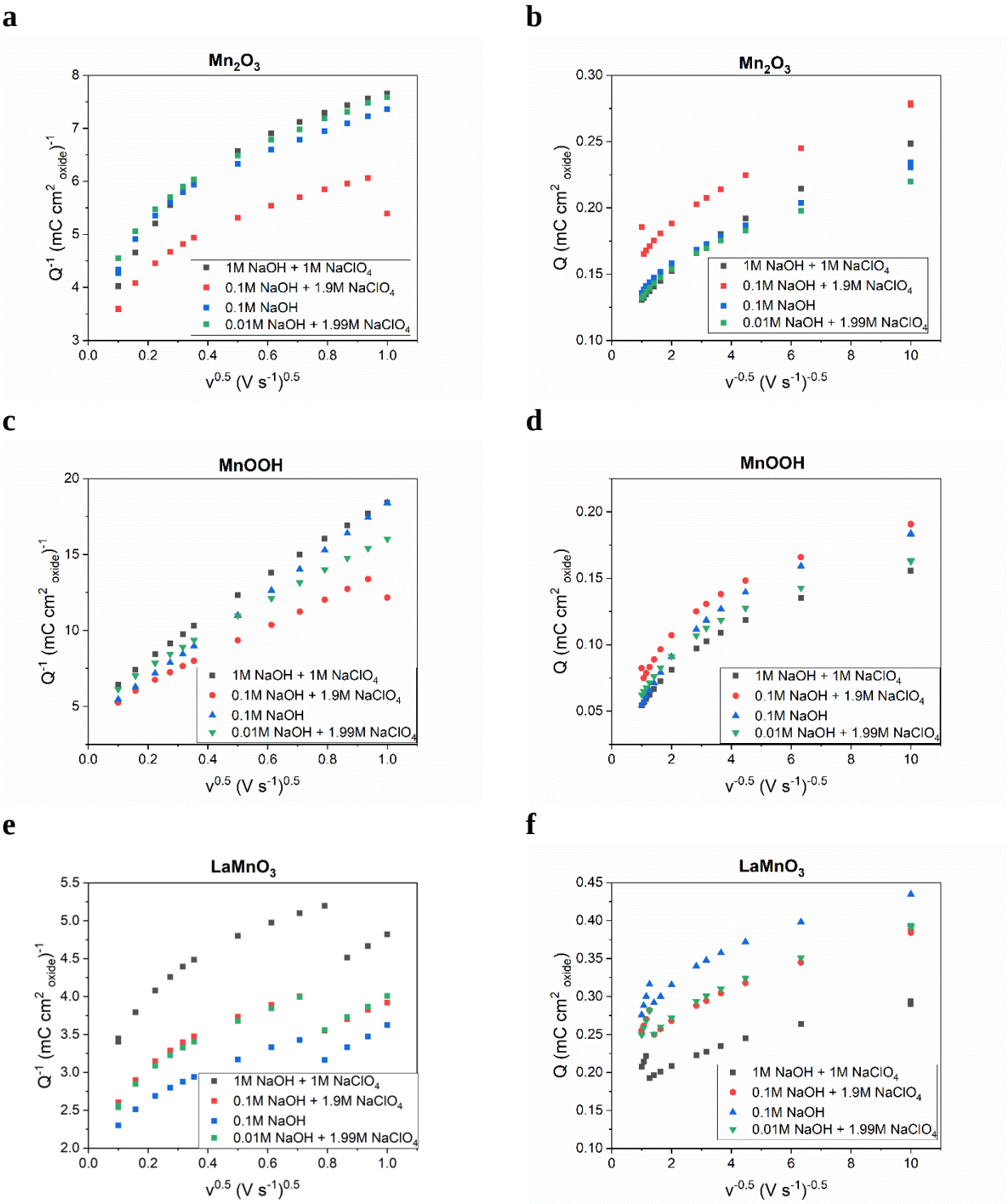

Fig. S 7 Dependencies of the reciprocal value of the cathodic charge(Q^{-1}) for Mn_2O_3 (a,b), MnOOH (c,d), $LaMnO_3$(e,f) on the square root of the potential scan rate ($n^{½}$) (left) and Q on $n^{-½}$ (right). Q is calculated from the CVs Fig. 66.

Annex to Chapter 5

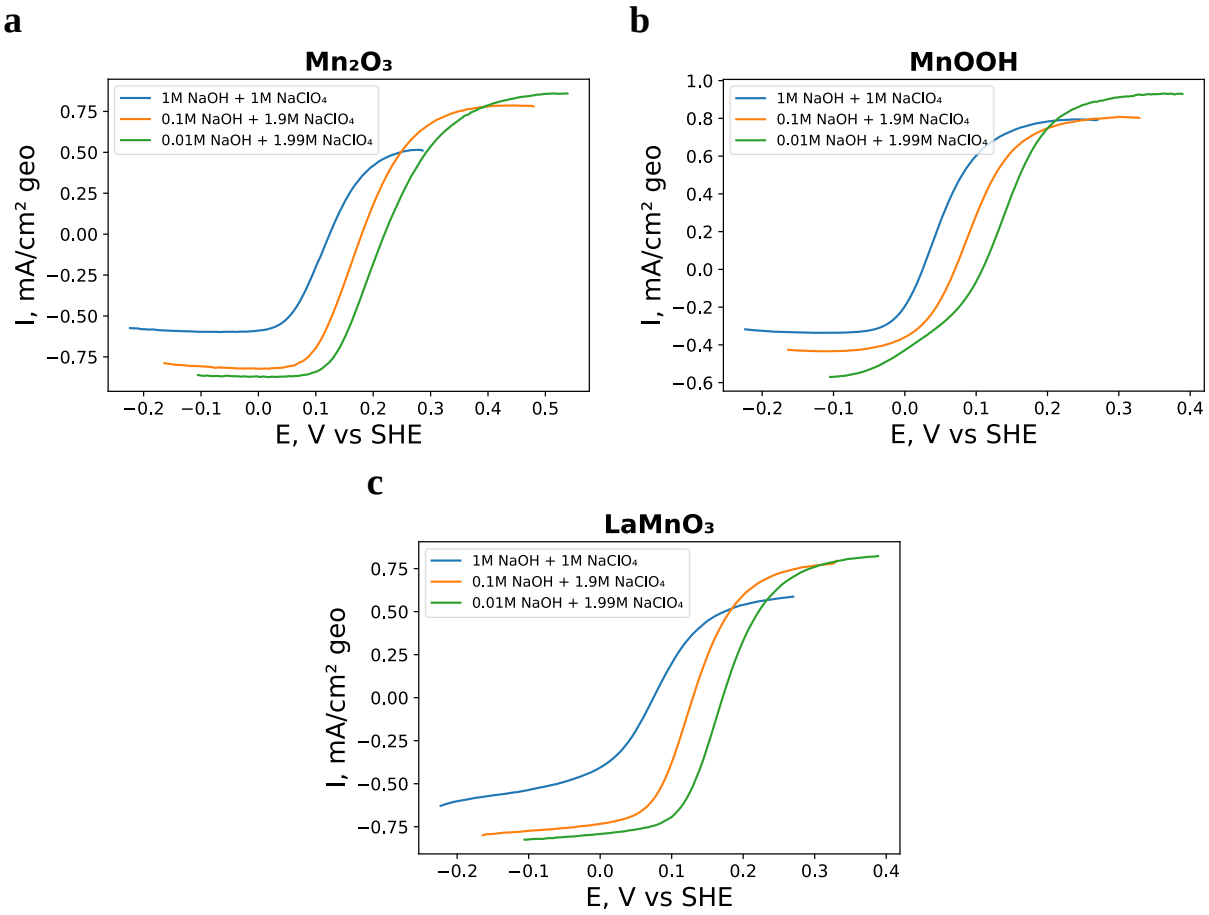

Fig. S 8 RDE voltammograms in N_2-purged alkaline solution (at different pH and constant ionic strength) in the presence of 0.84 mM H_2O_2 at 10 mV s^{-1} for GC supported thin films of $LaMnO_3$ (a), Mn_2O_3 (b), MnOOH (c). Catalyst loadings are 91 µg cm^{-2} oxide + 91 µg cm^{-2} carbon. Currents are normalized to the electrode geometric area and corrected to the background currents measured in the N_2 atmosphere. The scale is relative to SHE.

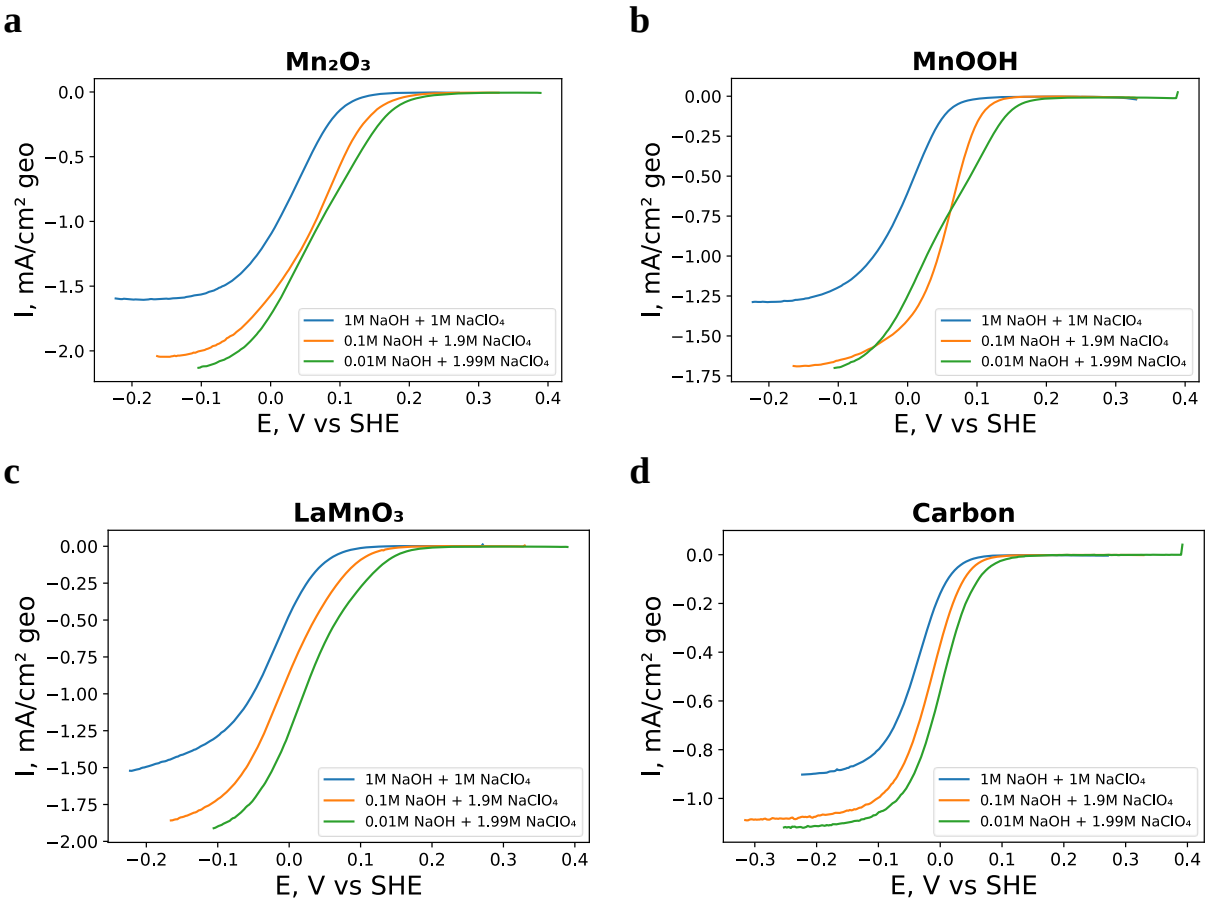

Fig. S 9 RDE voltammograms in O_2-saturated alkaline solutions for $LaMnO_3$ (a), Mn_2O_3 (b), MnOOH (c) and Sibunit Carbon (d) at different OH^- concentration and constant ionic strength (as indicated in the panels). Loading are: 91 μg cm^{-2} carbon + 91 μg cm^{-2} oxide. The current is normalized to the geometric surface of the electrode. The scale is relative to SHE

$LaMnO_3$

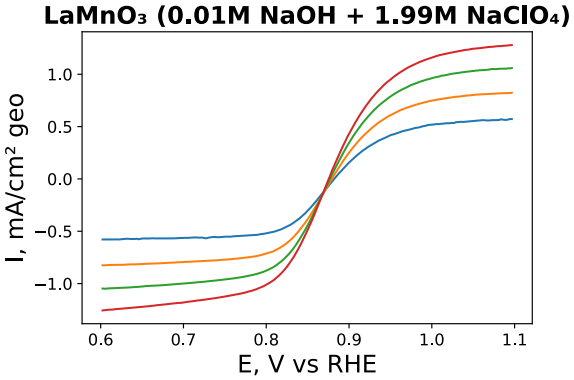
LaMnO₃ (0.01M NaOH + 1.99M NaClO₄)
I, mA/cm² geo
E, V vs RHE

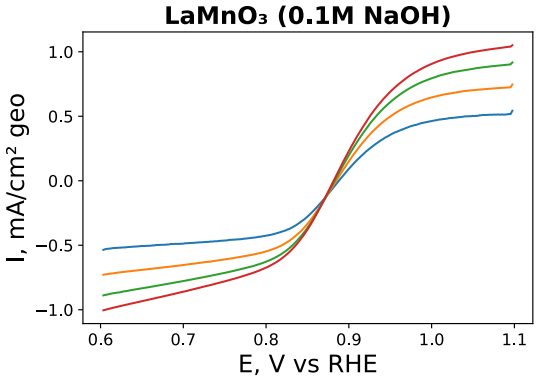
LaMnO₃ (0.1M NaOH)
I, mA/cm² geo
E, V vs RHE

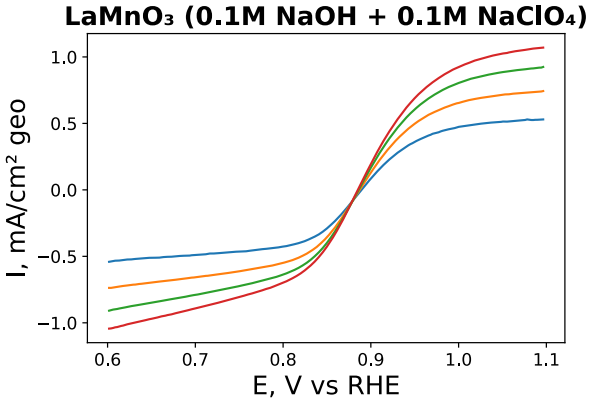
LaMnO₃ (0.1M NaOH + 0.1M NaClO₄)
I, mA/cm² geo
E, V vs RHE

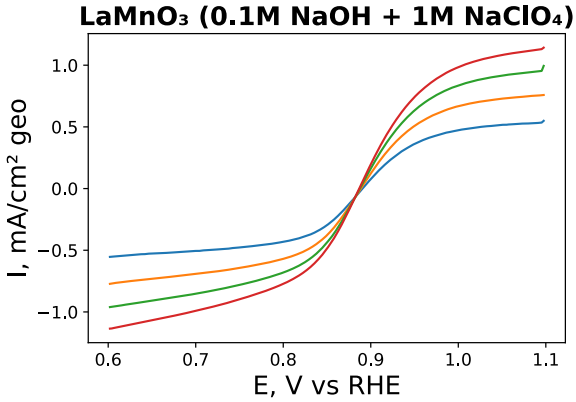
LaMnO₃ (0.1M NaOH + 1M NaClO₄)
I, mA/cm² geo
E, V vs RHE

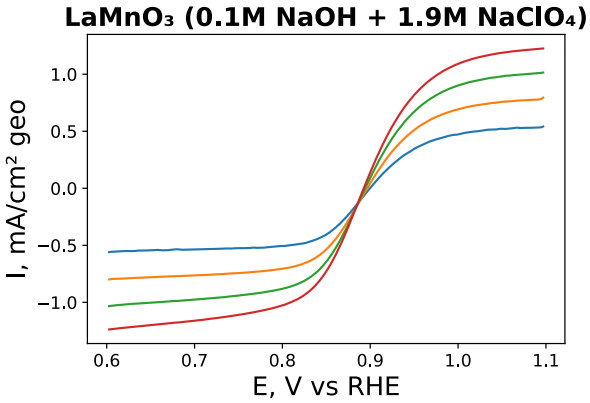
LaMnO₃ (0.1M NaOH + 1.9M NaClO₄)
I, mA/cm² geo
E, V vs RHE

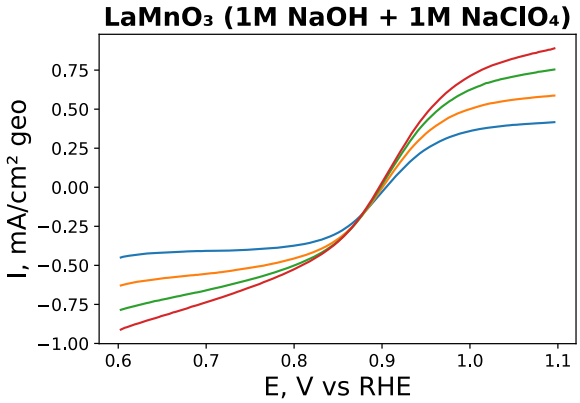
LaMnO₃ (1M NaOH + 1M NaClO₄)
I, mA/cm² geo
E, V vs RHE

Mn_2O_3

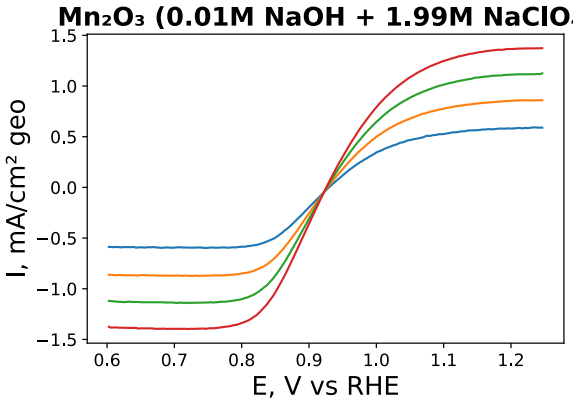
Mn₂O₃ (0.01M NaOH + 1.99M NaClO₄)
I, mA/cm² geo
E, V vs RHE

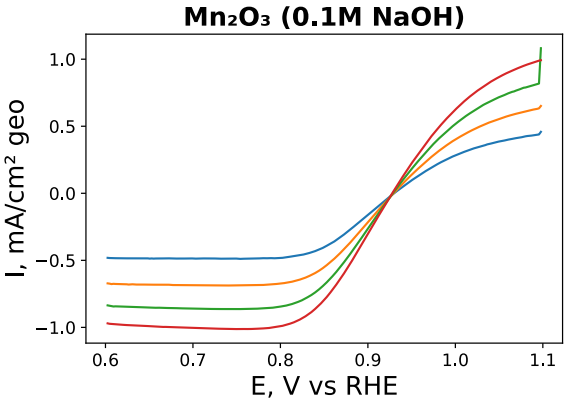
Mn₂O₃ (0.1M NaOH)
I, mA/cm² geo
E, V vs RHE

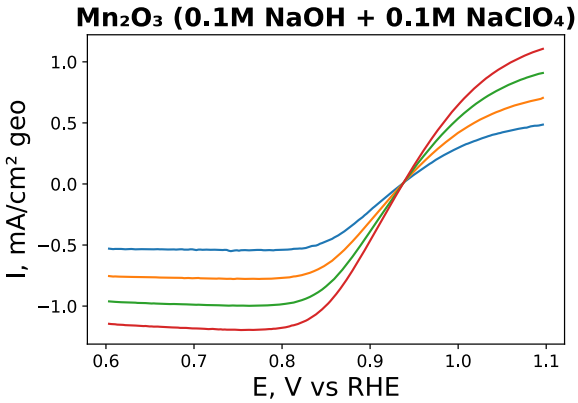
Mn₂O₃ (0.1M NaOH + 0.1M NaClO₄)
I, mA/cm² geo
E, V vs RHE

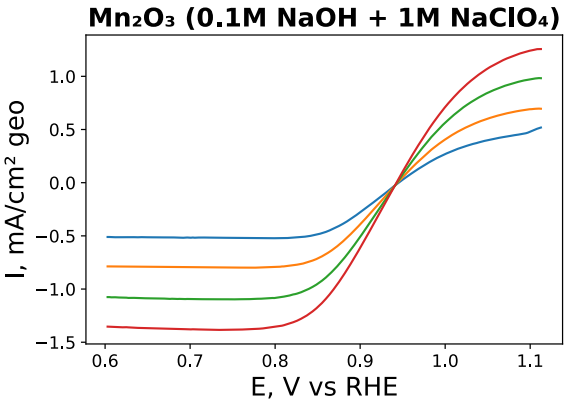
Mn₂O₃ (0.1M NaOH + 1M NaClO₄)
I, mA/cm² geo
E, V vs RHE

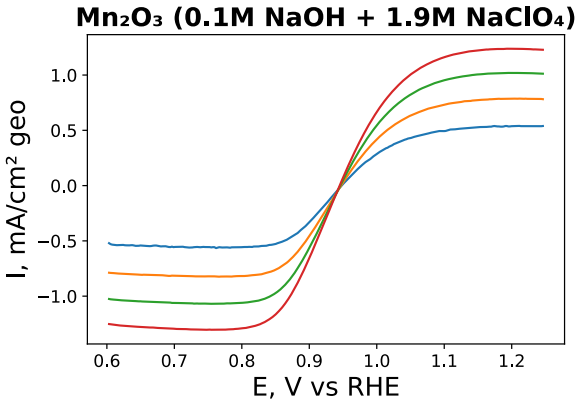
Mn₂O₃ (0.1M NaOH + 1.9M NaClO₄)
I, mA/cm² geo
E, V vs RHE

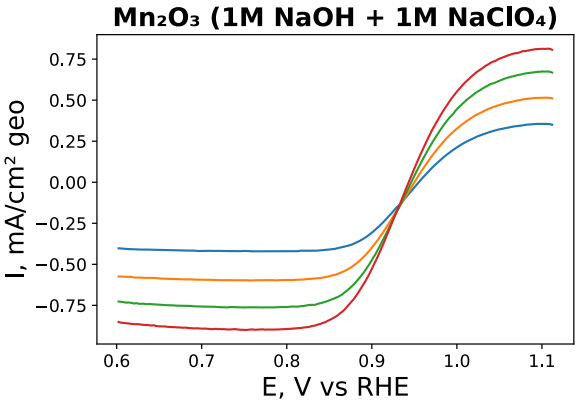
Mn₂O₃ (1M NaOH + 1M NaClO₄)
I, mA/cm² geo
E, V vs RHE

MnOOH

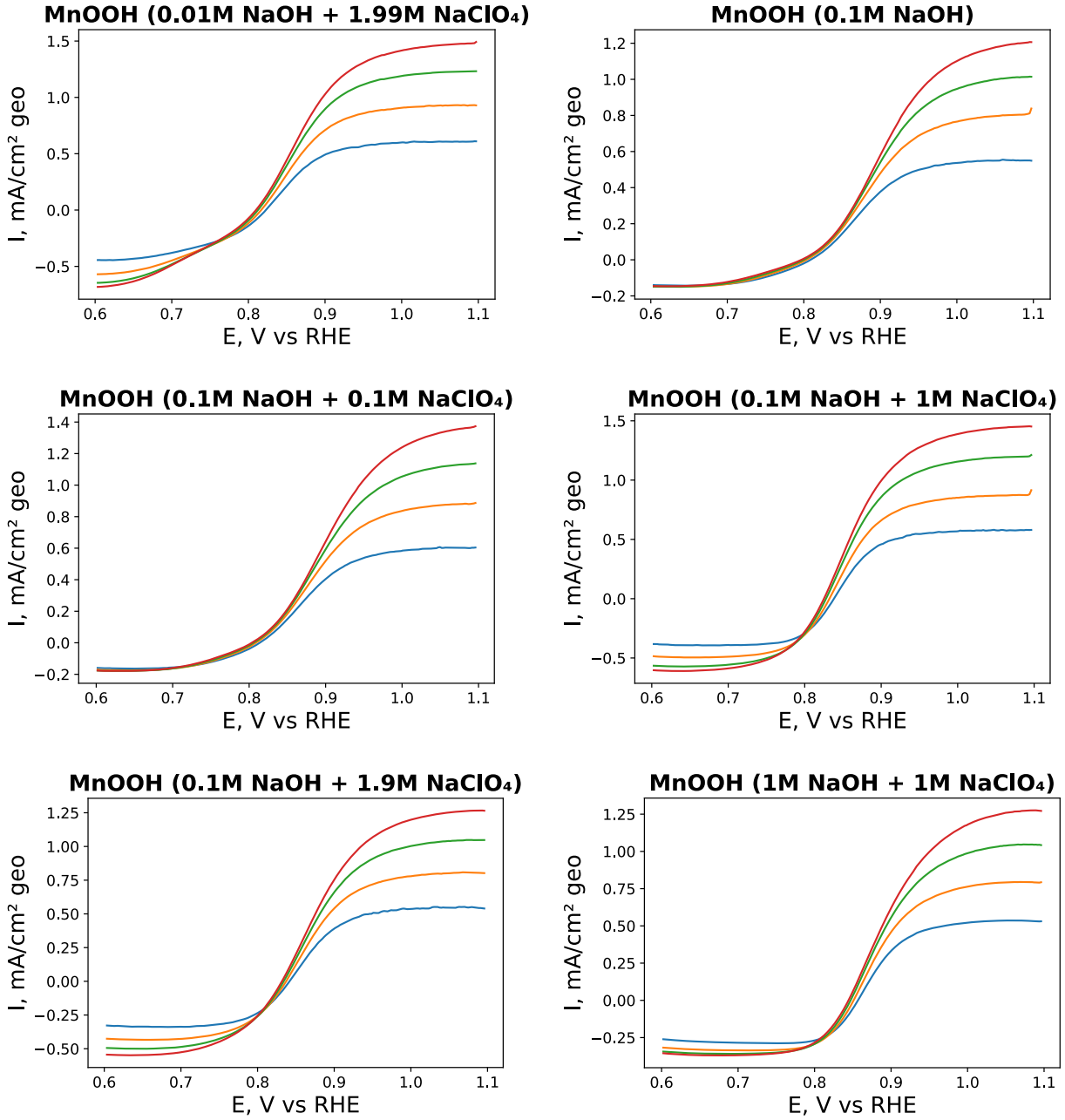

Fig. S10 RDE voltammograms in N_2-purged alkaline solutions with 0.84 mM H_2O_2 for GC-supported thin films of $LaMnO_3$, MnOOH and Mn_2O_3. The oxide and carbon loadings are 91 μg cm^{-2} each. Color codes: 400 (blue), 900 (orange), 1600 (green), 2500 (red) rpm. Currents are normalized to the electrode geometric area and corrected to the background currents measured in the N_2 atmosphere.

$LaMnO_3$

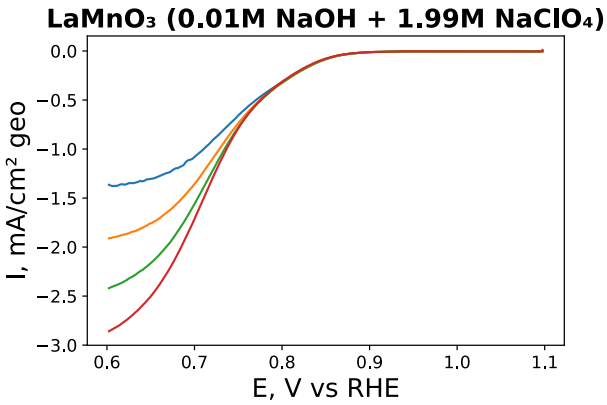
LaMnO₃ (0.01M NaOH + 1.99M NaClO₄)
I, mA/cm² geo
E, V vs RHE

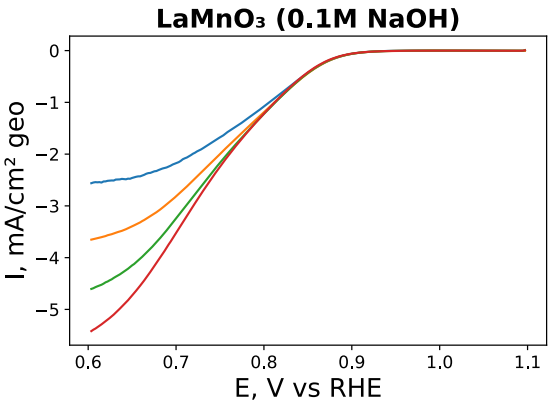
LaMnO₃ (0.1M NaOH)
I, mA/cm² geo
E, V vs RHE

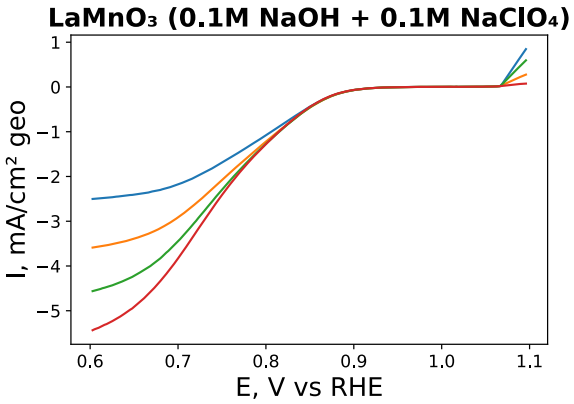
LaMnO₃ (0.1M NaOH + 0.1M NaClO₄)
I, mA/cm² geo
E, V vs RHE

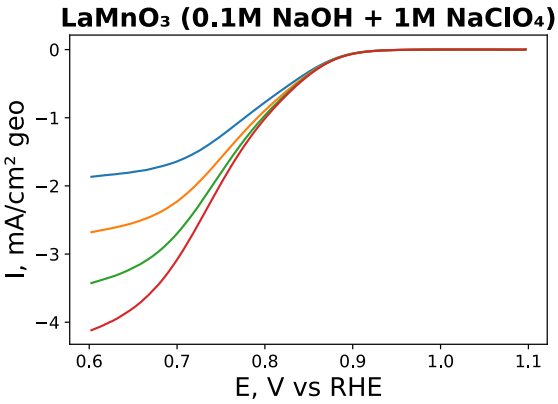
LaMnO₃ (0.1M NaOH + 1M NaClO₄)
I, mA/cm² geo
E, V vs RHE

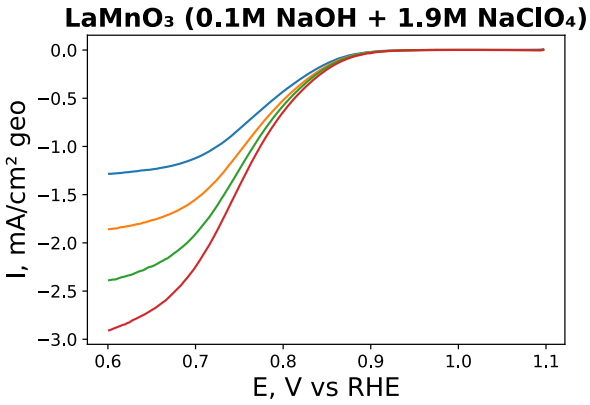
LaMnO₃ (0.1M NaOH + 1.9M NaClO₄)
I, mA/cm² geo
E, V vs RHE

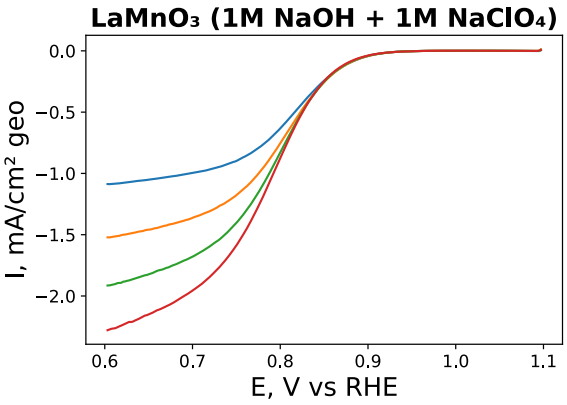
LaMnO₃ (1M NaOH + 1M NaClO₄)
I, mA/cm² geo
E, V vs RHE

Mn_2O_3

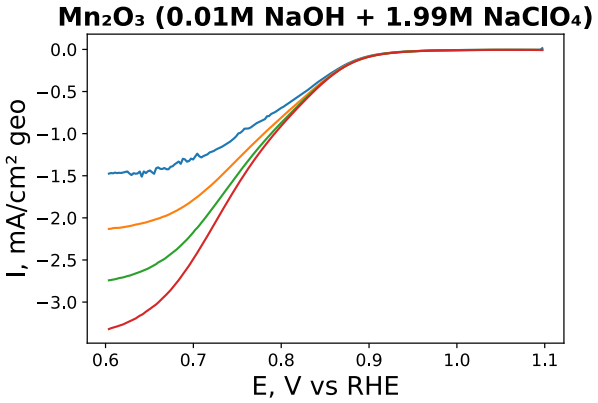
Mn₂O₃ (0.01M NaOH + 1.99M NaClO₄)
I, mA/cm² geo
E, V vs RHE

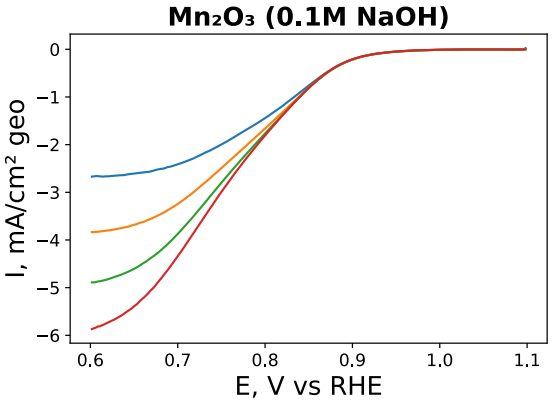
Mn₂O₃ (0.1M NaOH)
I, mA/cm² geo
E, V vs RHE

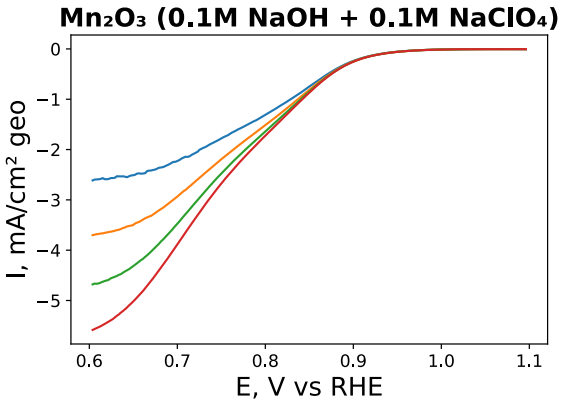
Mn₂O₃ (0.1M NaOH + 0.1M NaClO₄)
I, mA/cm² geo
E, V vs RHE

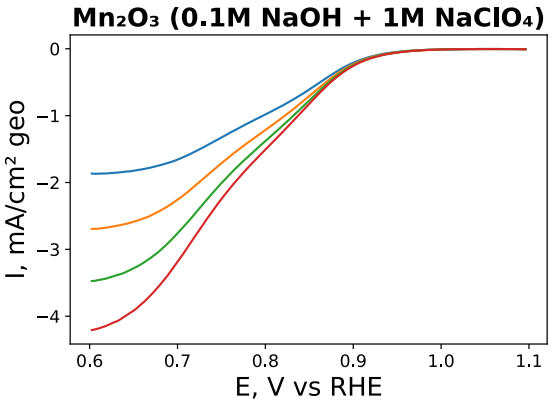
Mn₂O₃ (0.1M NaOH + 1M NaClO₄)
I, mA/cm² geo
E, V vs RHE

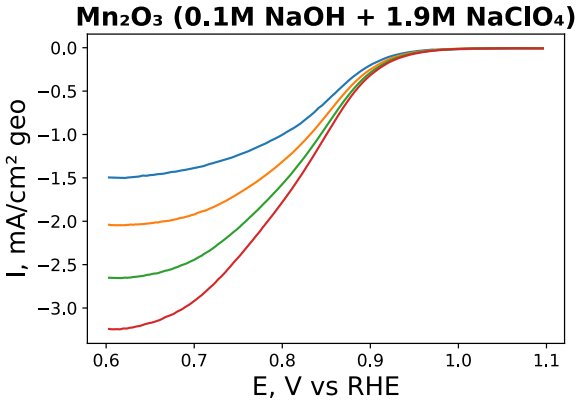
Mn₂O₃ (0.1M NaOH + 1.9M NaClO₄)
I, mA/cm² geo
E, V vs RHE

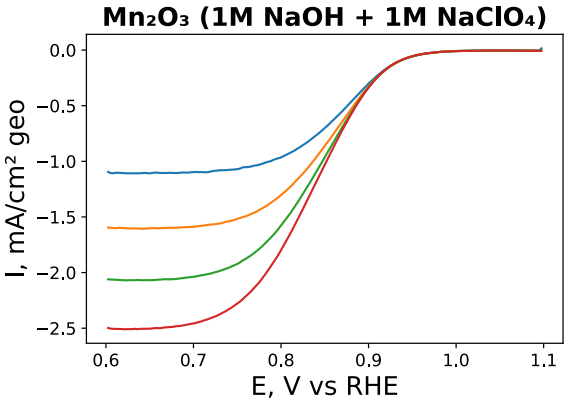
Mn₂O₃ (1M NaOH + 1M NaClO₄)
I, mA/cm² geo
E, V vs RHE

MnOOH

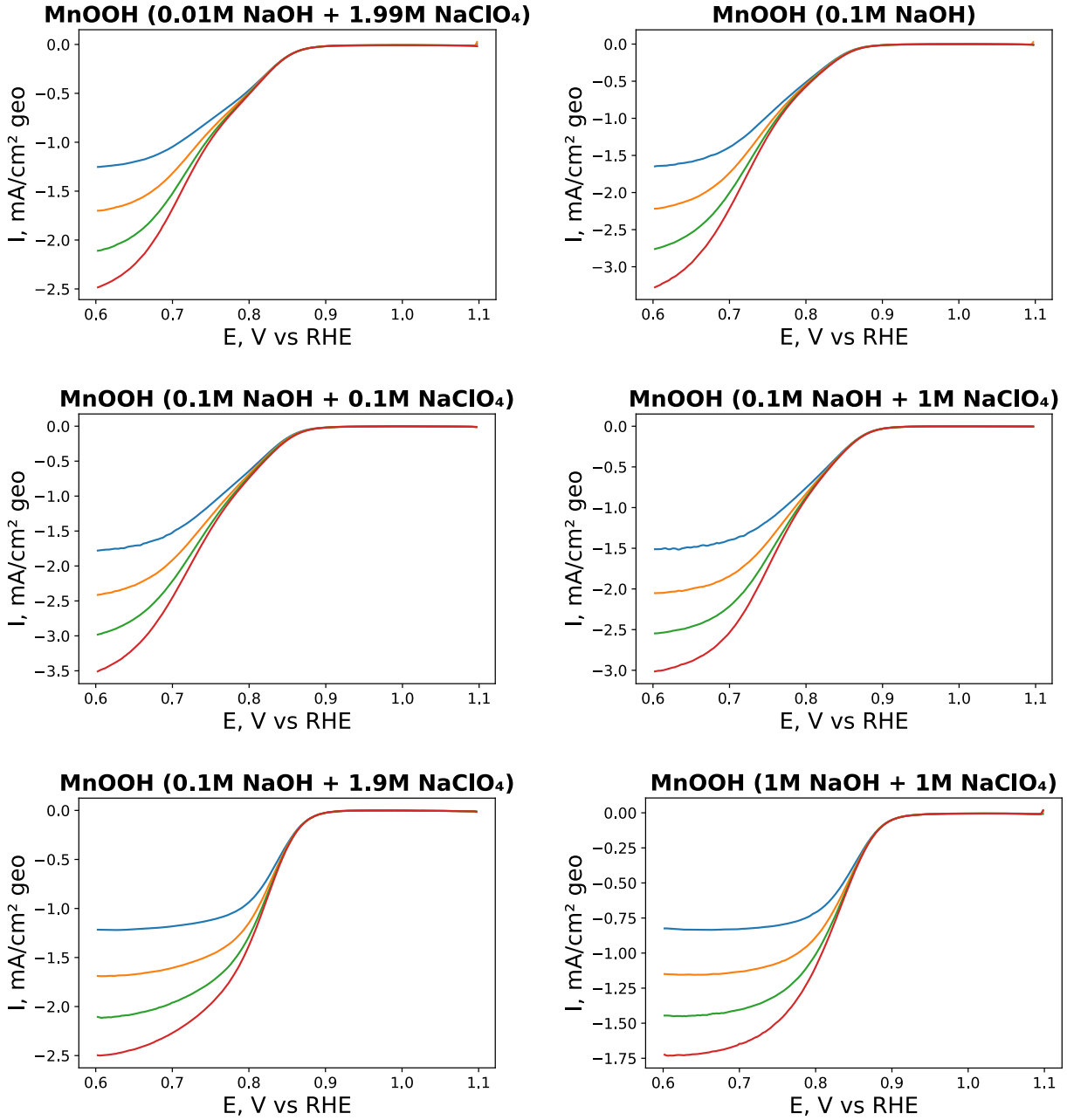

Fig. S11 RDE voltammograms in O_2-purged alkaline solutions for GC-supported thin films of $LaMnO_3$, MnOOH and Mn_2O_3. The oxide and carbon loadings are 91 μg cm^{-2} each. Color codes: 400 (blue), 900 (orange), 1600 (green), 2500 (red) rpm. Currents are normalized to the electrode geometric area and corrected to the background currents measured in the N_2 atmosphere.

RESUME

1) Introduction

Les piles à combustible alcalines à électrolyte liquide (AFC – «alkaline fuel cells» en anglais) ou à membrane échangeuse d'anions (AEMFC – «anion exchange membrane fuel cell» en anglais) sont parmi les solutions les plus prometteuses pour convertir l'énergie chimique en énergie électrique. Cependant, il existe aujourd'hui plusieurs problèmes qui empêchent leur commercialisation, nommément l'utilisation de métaux nobles par nature dispendieux (e.g., platine) en tant qu'électrocatalyseurs pour les réactions ayant lieu aux électrodes. Les métaux nobles sont particulièrement importants à la cathode, où a lieu la réduction de l'oxygène (ORR – «oxygen reduction reaction» en anglais), mais leur prix aura conduit à l'émergence de nombreuses études consacrées au développement d'électrocatalyseurs à base d'oxydes de métaux de transition, de facto ne contenant aucun métal noble, afin de les remplacer. Malgré les progrès réalisés au cours des dernières décennies, le mécanisme de l'ORR est encore insuffisamment compris. De plus, les corrélations entre la composition chimique et la structure cristalline des oxydes de métaux de transition d'une part, et leur activité électrocatalytique pour l'ORR, d'autre part, n'ont pas encore été établies. Ces incompréhensions peuvent être liées à l'effet de facteurs intrinsèques (structure et composition des matériaux) et extrinsèques (composition de l'électrolyte, ajout de liants carbonés aux électrodes, *etc*.) sur l'électrocatalyse de l'ORR par les oxydes de métaux de transition. Cette thèse se compose de deux parties.

La première partie porte sur l'étude de l'influence de (i) la structure des oxydes de type AB_2O_4 (spinelle) et de (ii) leur composition sur leurs propriétés électrochimiques et électrocatalytiques. Les spinelles suscitent beaucoup d'intérêt en tant qu'électrocatalyseurs. En effet, il est possible de substituer divers atomes dans le sous-réseau des cations A. De fait, Mn_3O_4 et divers AMn_2O_4 substitués ont été déjà étudiés en tant qu'électrocatalyseur de l'ORR dans le passé. Cependant, les valeurs d'activité électrocatalytique rapportées par différents équipes scientifiques sont plutôt contradictoires, ce qui pourrait provenir d'une éventuelle instabilité de ces matériaux dans leurs conditions de fonctionnement.

Au cours de ce projet de recherche, le cation Mn(II) de Mn_3O_4 (r(Mn(II))=0.80 Å [1]) a été remplacé par des cations ne présentant aucune transition redox dans la gamme de potentiel opératoires, et dotés d'un rayon soit plus important: Cd(II) avec un rayon r(Cd(II)) de 0,92 Å [1], soit plus petit: Mg(II) et Li(I) (r(Mg(II))=0,71 Å, r(Li(I))=0,73 Å [1]). Les oxydes $LiMn_2O_4$, $CdMn_2O_4$ et $MgMn_2O_4$ sont donc des spinelles où seul le Mn est sujet à des changement d'état d'oxydation dans les conditions de l'ORR. Ces oxydes ont été étudiés comme électrocatalyseurs pour l'ORR ainsi que pour l'oxydation/réduction du peroxyde d'hydrogène (HPOR/HPRR – «hydrogen peroxide oxidation reaction/hydrogen peroxide reduction reaction» en anglais), étant

donné qu'H_2O_2 est un intermédiaire réactionnel clé de l'ORR. Une attention particulière a été dédiée à l'étude de la stabilité des oxydes de Mn en électrolyte alcalin en conditions opératoires, via des méthodes électrochimiques et physicochimiques e.g., la diffraction de rayons X (DRX), la spectroscopie de photoélectrons X (XPS) en laboratoire ainsi que des méthodes à la base du rayonnement synchrotron – XPS et NEXAFS (spectroscopie de structure près du seuil d'absorption de rayons X).

La deuxième partie de la thèse porte sur l'influence de la composition de l'électrolyte (le pH et la concentration des cations Na^+) sur la cinétique de l'ORR, effets qui pour l'instant ont été très peu étudiés pour des catalyseurs à base d'oxydes de métaux de transition. De telles études peuvent toutefois être très utiles pour éclaircir le mécanisme de l'ORR (*cf.* Fig. 1 qui montre le mécanisme multi-étapes de l'ORR, proposé dans des études précédentes). Compte tenu de problèmes de stabilité des spinelles de Mn (discuté en détails dans les sections suivantes) des structures plus stables ont été sélectionnées pour cette partie, i.e. Mn_2O_3, $LaMnO_3$ et MnOOH [2]. Des études antérieures ont mis en évidence des différences significatives dans la cinétique de l'ORR pour ces trois oxydes. Ainsi, pour les étapes 2, 3 et 5, les constantes de vitesse les plus importantes ont été observés pour Mn_2O_3 (*cf.* Fig. 1 et Tableau 1). De fait, cet oxyde possède l'activité la plus élevée pour la réduction de l'oxygène. La constante de vitesse la plus faible de l'étape de la rupture chimique de la liaison O-O dans l'intermédiaire réactionnel -OOH (étape 5) est observée pour le MnOOH, ainsi que les cinétiques les plus basses pour l'ORR. Finalement, le $LaMnO_3$ combine la cinétique lente des étapes électrochimiques 2 et 3 avec la cinétique rapide de l'étape chimique 5.

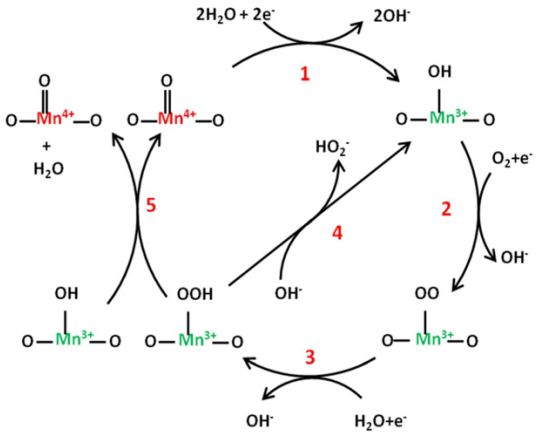

Fig. 1. Mécanisme de l'ORR proposé par Rybova *et al.* [2].

Tableau 1. Les constantes de vitesse des étapes 2, 3, 5 de l'ORR (*cf.* Fig. 1) pour Mn_2O_3, $LaMnO_3$ et MnOOH [2]

Oxyde	k_2, 10^{13} $cm^3\ mol^{-1}\ s^{-1}$	k_3, $10^{10}\ s^{-1}$	k_5, s^{-1}
Mn_2O_3	1.5	5.1	50
$LaMnO_3$	0.03	0.1	10
MnOOH	0.15	0.5	0.05

Afin de maintenir une force ionique constante dans des électrolytes de pH différents, un électrolyte support ($NaClO_4$) a été utilisé. Ainsi, une partie importante de ce projet de recherche a été liée à l'étude de l'influence de la concentration de l'électrolyte support sur la cinétique de l'ORR. De plus, nous avons étudié l'influence du pH et de la concentration en électrolyte support sur la transition redox Mn(IV/III) observée à la surface de l'électrocatalyseur (étape 1 sur la Fig. 1), et sur les cinétiques de l'HPOR/HPRR, ce qui aidera à mieux comprendre le mécanisme de l'ORR sur ces matériaux.

2) Résultats et discussions

2.1 Les spinelles AMn_2O_4 en tant que catalyseurs de l'ORR : influence de la coordination du Mn et de son état d'oxydation sur l'activité catalytique et sur la stabilité

2.1.1 Activités électrocatalytiques

Les courbes de voltampérométrie cyclique (CV) mesurées dans 1M de NaOH dégazé ainsi que les voltampérogrammes obtenus sur une électrode à disque tournant (RDE – «Rotating Disc Electrode» en anglais), obtenus dans le même électrolyte saturé en O_2 sont présentés, respectivement, en Fig. 2a et 2b. Les pics caractéristiques correspondant à la transition redox Mn(IV/III) sont observés dans l'intervalle de potentiel de 0.7 à 1.1 V vs. RHE (Reversible Hydrogen Electrode – en anglais). Pour $LiMn_2O_4$, les pics sont décalés vers les potentiels négatifs par rapport aux autres oxydes, ce qui entraîne une valeur inférieure du potentiel formel (E_f, calculé comme une valeur moyenne des potentiels anodique et cathodique des pics redox). Cette faible valeur de E_f (0.83 V vs. RHE) peut s'expliquer par la flexibilité de la structure $LiMn_2O_4$ qui pourrait contenir un nombre important de lacunes cationiques et d'oxygène [3]. On peut supposer qu'un tel comportement se traduit par une facilité de la transition redox Mn(IV/III).

Pour tous les spinelles, l'ORR commence en dessous de 0.9 V vs. RHE (Fig. 2b). Leurs activités électrocatalytiques sont ainsi similaires à celle de MnOOH mais inférieures à celle de Mn_2O_3. Ceci est confirmé par la Fig. 2c où sont présentés les courants cinétiques de l'ORR. La Fig. 2d présente l'influence d'E_f sur l'activité spécifique. Des études précédentes [2] ont démontré une corrélation entre le E_f de la transition redox interfaciale Mn(IV/III) et l'activité spécifique (*cf.* Fig. 1), ce que confirme le rôle de la première dans le mécanisme de l'ORR.

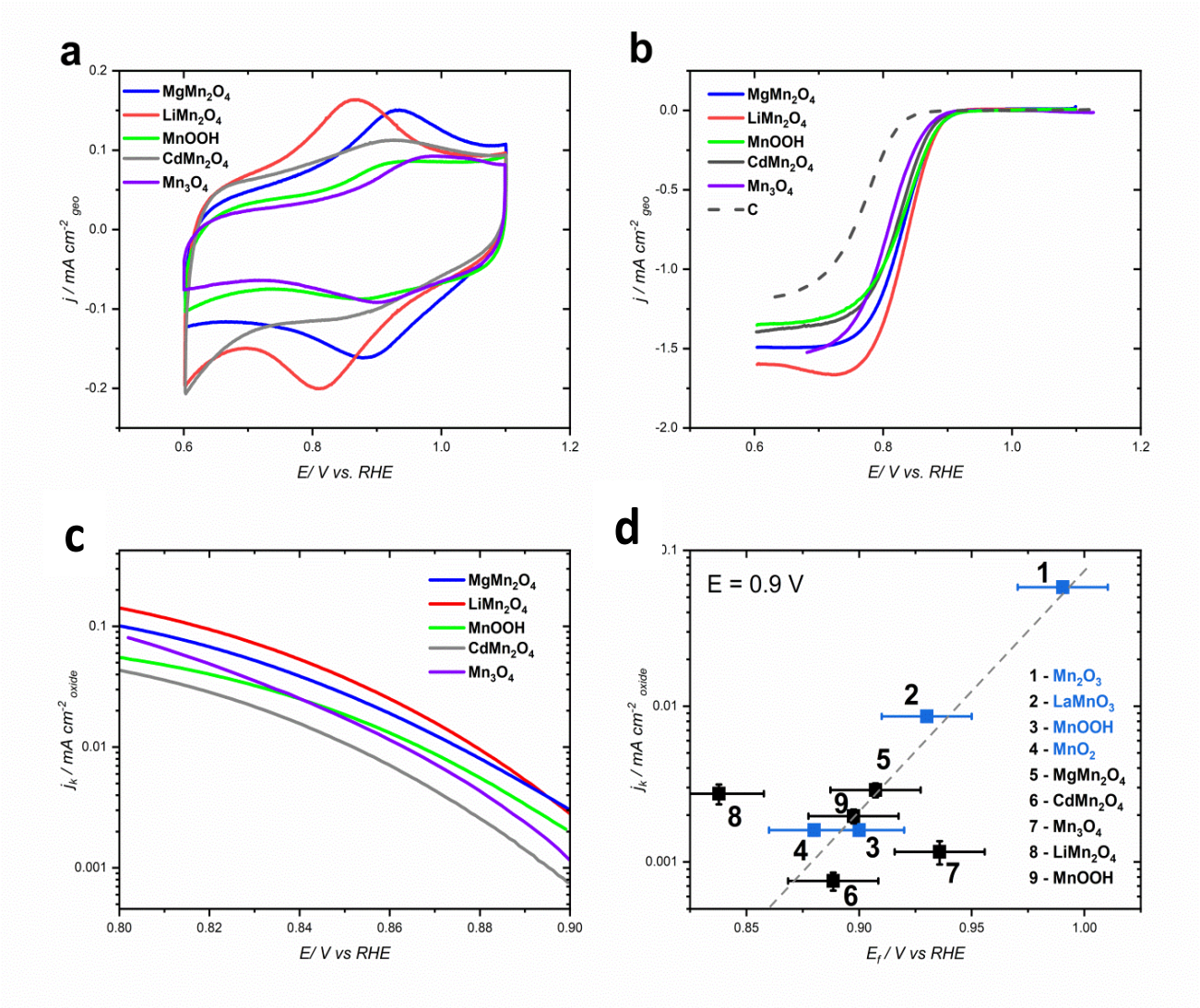

Fig. 2. (a) Courbes de voltampérométrie cyclique (CV) mesurées dans NaOH 1 M dégazée et (b) voltampérogrammes sur électrode à disque tournant obtenus dans le même électrolyte saturé en O_2 à 900 rpm et à 10 mV s^{-1} pour $MgMn_2O_4$, Mn_3O_4, $LiMn_2O_4$, $CdMn_2O_4$ et MnOOH. Les chargements de l'électrode en catalyseur et en carbone sont identiques, de 91 µg cm^{-2}. (c) Les courants cinétiques de l'ORR calculés par unité de surface BET (c'est-à-dire la surface déterminée par l'adsorption d'azote à basse température et calculée dans le cadre du modèle BET - Brunauer–Emmett–Teller) en fonction du potentiel de l'électrode et (d) en fonction du potentiel formel E_f. Outre les données obtenues lors de cette thèse (symboles noirs), les résultats démontrés dans les publications précédentes de l'équipe strasbourgeoise (symboles bleu) [2] sont présentés.

2.1.2 Stabilité des spinelles de Mn : études physico-chimiques et électrochimiques

Tous les échantillons ont été caractérisés par DRX, MEB (microscopie électronique à balayage), adsorption d'azote, NEXAFS et XPS pour identifier leur structure, leur morphologie et surface spécifique, ainsi que leur composition et le degré d'oxydation du Mn. Par la suite, afin d'étudier leur stabilité, tous les échantillons ont été examinés par XPS après différents traitements :

(i) après la préparation de la suspension (l'étape nécessaire pour la conception des électrodes), (ii) après 6h dans du NaOH 1 M, et (iii) après 10 cycles du potentiel de 0.6 à 1.15 V vs. RHE dans du NaOH 1 M (Fig. 3).

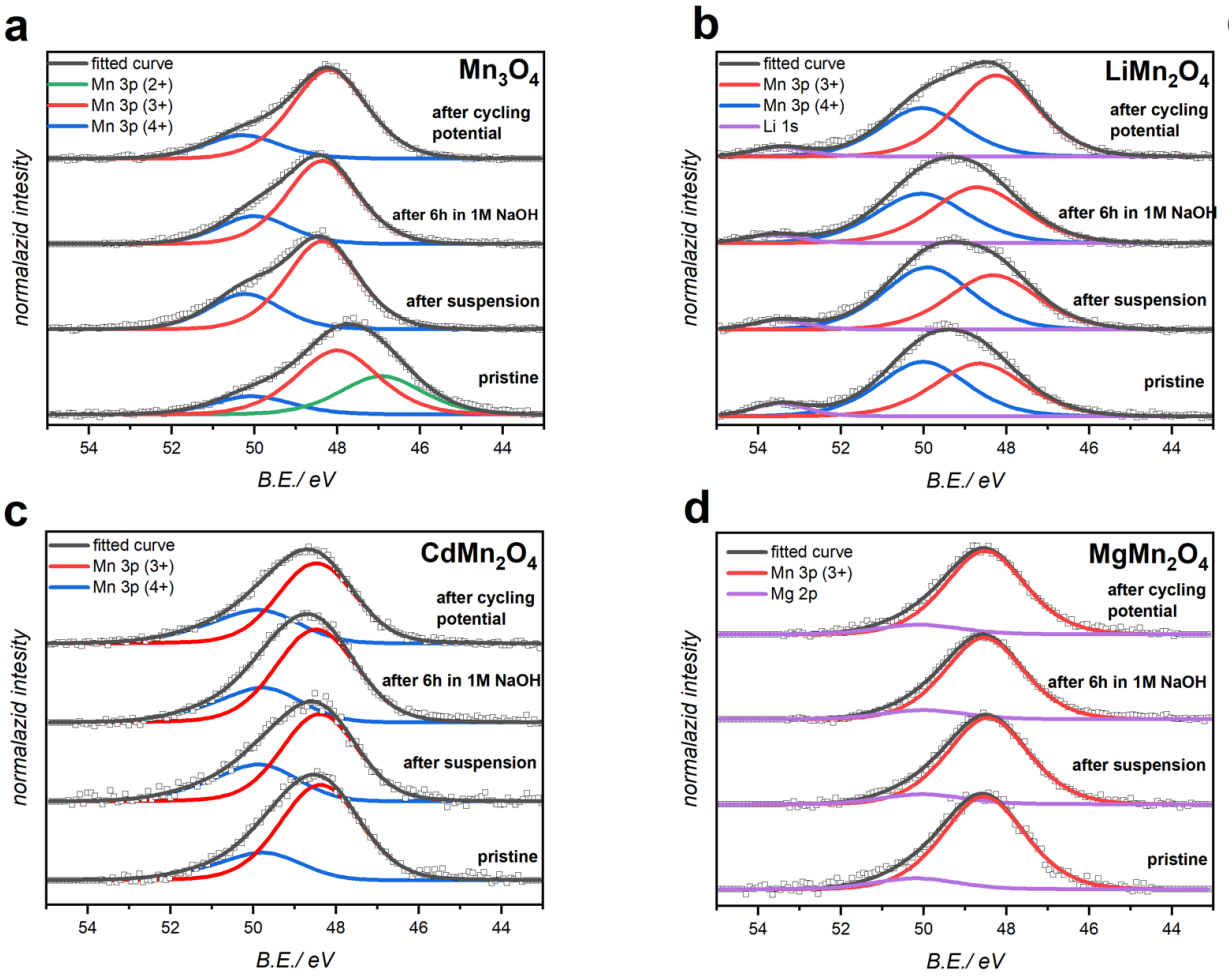

Fig. 3. Spectres Mn3p pour Mn_3O_4 (a), $LiMn_2O_4$ (b), $CdMn_2O_4$ (c) et $MgMn_2O_4$ (d) suite à divers traitements (comme indiqué sur les graphiques). La ligne continue noire correspond à la déconvolution des spectres en supposant la présence de Mn(II) (vert), Mn(III) (rouge) et Mn(IV) (bleu). Les spectres sont collectés avec un spectromètre de laboratoire Thermo VG-Microtech avec la cathode en Al (énergie d'excitation 1486.6 eV).

Tableau 2. Les fractions de Mn dans différents états d'oxydation, l'état d'oxydation moyen du Mn calculé à partir de ces valeurs, et la teneur en cations A (x dans $A_xB_2O_4$) dans la couche proche de la surface calculée à partir des spectres XP de laboratoire.

Oxyde	Traitement	La teneur en cation A	La fraction de Mn^{z+}			L'état d'oxydation moyen du Mn
			Mn^{2+}	Mn^{3+}	Mn^{4+}	
Mn_3O_4	(i) vierge	--	0.3 ± 0.05	0.5 ± 0.05	0.2 ± 0.05	+2.9 ± 0.1
	(ii) suspension	--	--	0.7 ± 0.05	0.3 ± 0.05	+3.3 ± 0.1
	(iii) 6h dans du NaOH 1 M	--	--	0.75 ± 0.05	0.25 ± 0.05	+3.25 ± 0.1
	(iv) après CV	--	--	0.8 ± 0.05	0.2 ± 0.05	+3.2 ± 0.1
$MgMn_2O_4$	(i) vierge	1 ± 0.1	--	1.0 ± 0.1	--	+3.0 ± 0.1
	(ii) suspension	1 ± 0.1	--	1.0 ± 0.1	--	+3.0 ± 0.1
	(iii) 6h dans du NaOH 1 M	0.95 ±0.1	--	1.0 ± 0.1	--	+3.0 ± 0.1
	(iv) après CV	1.0 ± 0.1	--	1.0 ± 0.1	--	+3.0 ± 0.1
$LiMn_2O_4$	(i) vierge	0.9 ± 0.15	--	0.50 ± 0.05	0.5 ± 0.05	+3.5 ± 0.1
	(ii) suspension	0.6 ± 0.1	--	0.47 ± 0.05	0.53 ± 0.05	+3.53 ± 0.1
	(iii) 6h dans du NaOH 1 M	0.5 ± 0.1	--	0.53 ± 0.05	0.47 ± 0.05	+3.47 ± 0.1
	(iv) après CV	0.6 ± 0.1	--	0.63 ± 0.05	0.37 ± 0.05	+3.37 ± 0.1
$CdMn_2O_4$	(i) vierge	1.0 ± 0.1	--	0.8 ± 0.05	0.2 ± 0.05	+3.2 ± 0.1
	(ii) suspension	0.9 ± 0.1	--	0.7 ± 0.05	0.3 ± 0.05	+3.3 ± 0.1
	(iii) 6h dans du NaOH 1 M	1.1 ± 0.1	--	0.75 ± 0.05	0.25 ± 0.05	+3.25 ± 0.1
	(iv) après CV	0.36 ± 0.1	--	0.7 ± 0.05	0.3 ± 0.05	+3.3 ± 0.1

Les études XPS post-mortem mettent en évidence des changements significatifs à la surface des échantillons à la suite de ces différents traitement (voir Fig. 3). Pour l'échantillon du Mn_3O_4 exposé à l'air, la composition de surface s'écarte significativement du Mn(II) : Mn(III)=1 : 2 attendu pour le spinelle de Mn. Cela suggère que la surface de Mn_3O_4 est oxydée entraînant une diminution du rapport de Mn(II) et Mn(III), ainsi que la formation de Mn(IV) à la surface. Le contact du Mn_3O_4 avec l'eau (au cours de la préparation de la suspension) ou avec une solution aqueuse de NaOH 1 M entraîne la disparition complète de Mn(II) de la surface [3]. Cette transformation de la surface est accompagnée de changements dans la forme des CV (Fig. 4a), et d'un déséquilibre prononcé entre les charges cathodiques et anodiques (Qc/Qa).

Le remplacement isovalent des cations Mn(II) par Mg(II) a considérablement augmenté la stabilité de la structure spinelle. En effet, les spectres XP n'ont montré aucun changement ni dans l'état d'oxydation du Mn (qui ne s'écartait pas du Mn(III) attendu) ni dans la teneur en cations Mg suite aux divers traitements. En revanche, le remplacement isovalent de Mn(II) par un cation, plus gros, le Cd(II), déstabilise la structure spinelle. En effet, si la composition de surface de $CdMn_2O_4$ ne montre pas de changements notables via XPS lorsque l'échantillon est exposé à l'eau ou à du NaOH 1 M, le cyclage en potentiel dans l'intervalle de 0.6 à 1.15 V vs. RHE entraîne une perte de cations Cd de la surface. Les données électrochimiques laissent supposer que la désintercalation du Cd des sites tétraédriques du spinelle est concomitante à la transition redox des cations Mn(IV/III). De tels changements de composition conduisent à des changements significatifs dans les CVs (Fig. 4c). Selon les données XPS (Fig. 3), la composition chimique de la couche surfacique après le cyclage en potentiel correspond à la stœchiométrie suivante : $Cd_{0.36}Mn_2O_4$ (Tableau 2). Par ailleurs, le remplacement hétérovalent de Mn(II) par le cation lithium a entraîné une augmentation du degré d'oxydation de Mn dans $LiMn_2O_4$ jusqu'à +3,5. Le lithium, toutefois, disparait de la couche surfacique à la suite des traitements. Il est intéressant de noter que la perte de Li n'entraîne que de faibles changements dans l'état d'oxydation du Mn (Fig. 3, Tableau 2). En comparant les données XPS post-mortem et les données électrochimiques, nous pouvons conclure que la structure spinelle de $LiMn_2O_4$ est susceptible d'être préservée et que la perte du lithium est compensée par l'intercalation de protons de l'électrolyte [4].

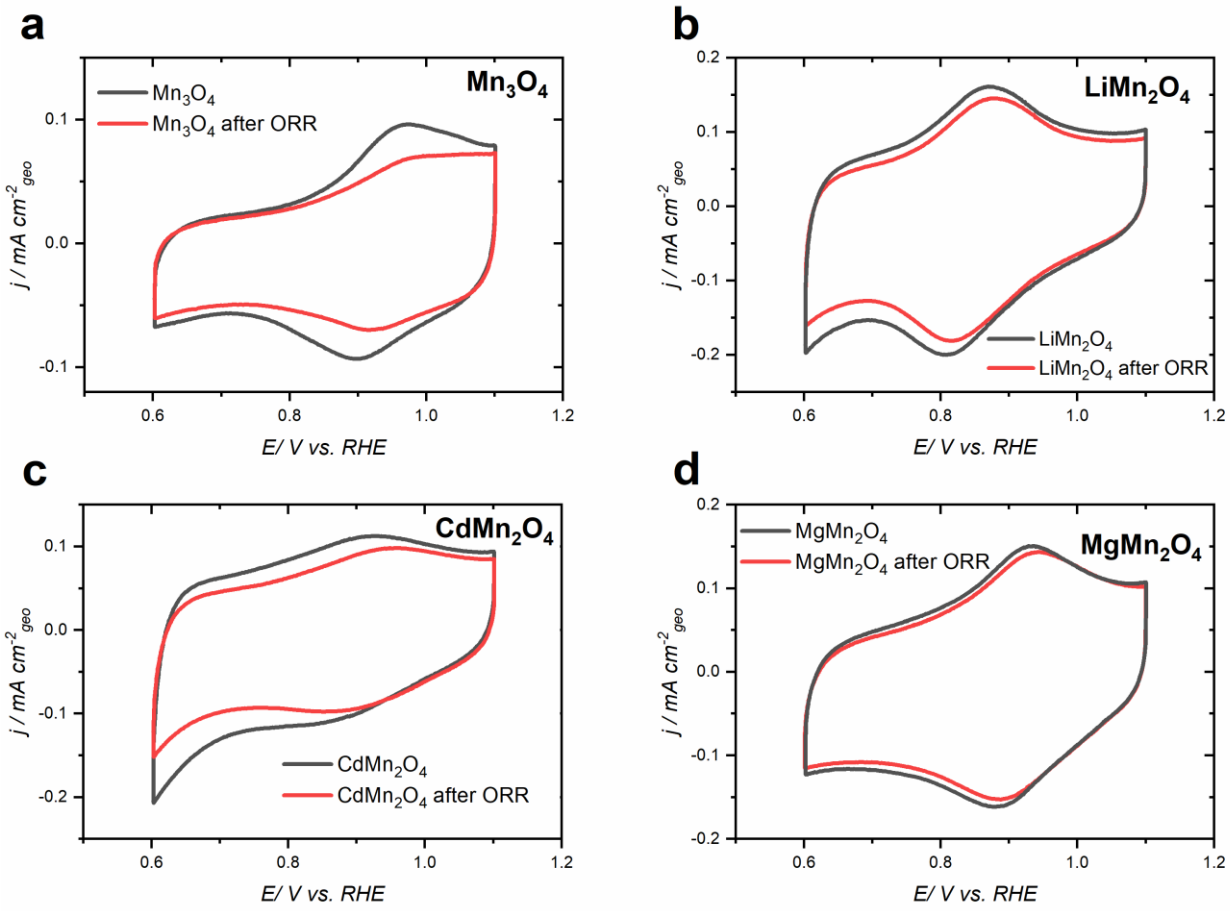

Fig. 4. Courbes de voltampérométrie cyclique (CV) dans du NaOH 1 M pour des échantillons de Mn_3O_4, $LiMn_2O_4$, $CdMn_2O_4$ et $MgMn_2O_4$ avant (courbe noire) et après (courbe rouge) la réalisation des expériences de réduction de l'oxygène. Les chargements de l'électrode en catalyseur et en carbone sont identiques, de 91 µg cm^{-2}. Les courants sont donnés par unité de surface géométrique de l'électrode.

2.2 L'influence de la composition de l'électrolyte sur l'interface et la cinétique

2.2.1 Influence de la composition de l'électrolyte sur l'interface oxyde/électrolyte

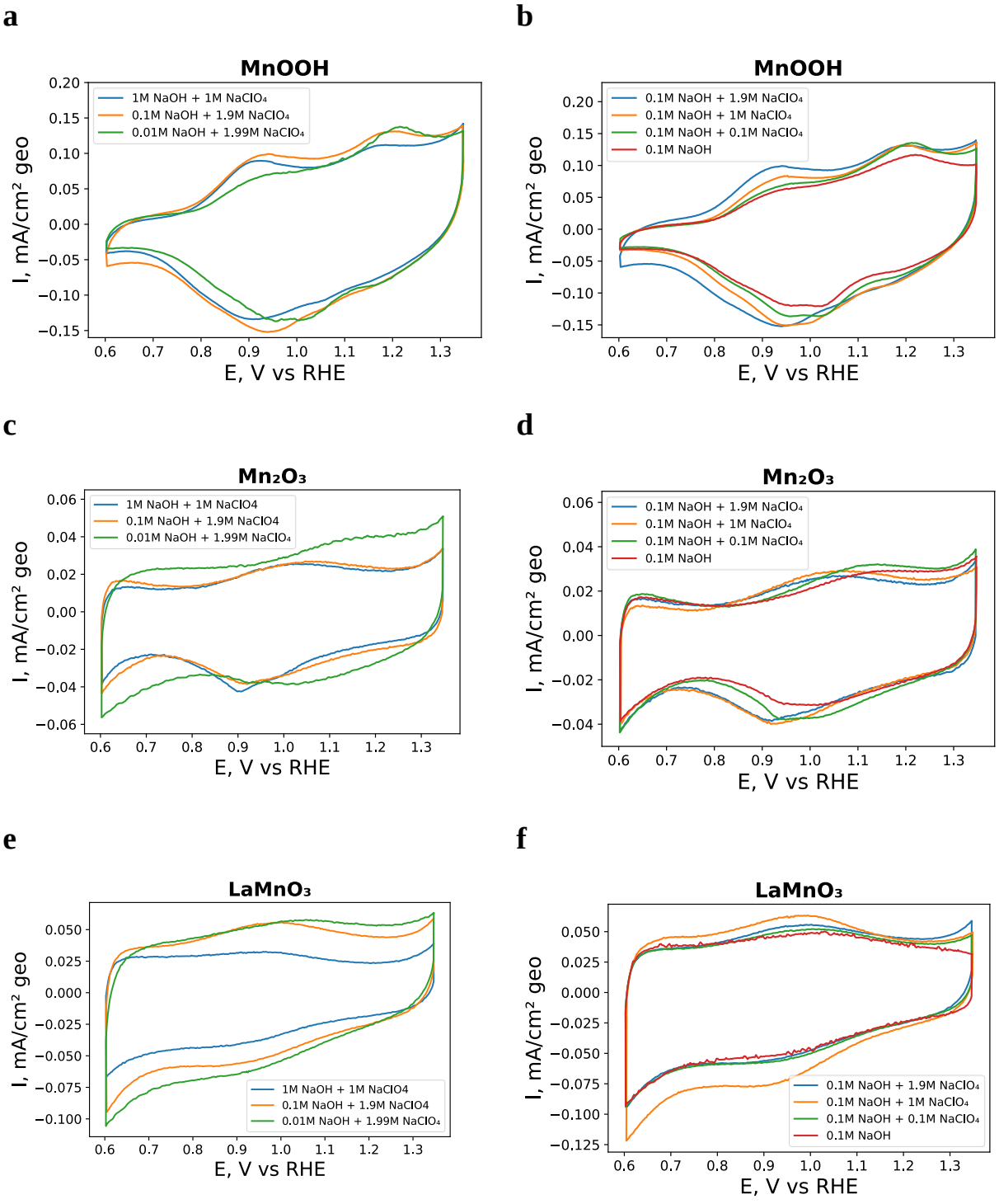

Fig. 5 Courbes de voltampérométrie cyclique (CV) pour MnOOH/C (a,b), Mn_2O_3/C (c,d) et $LaMnO_3$/C (e,f) mesurées dans des électrolytes dégazés de composition différente: NaOH + $NaClO_4$ à force ionique constante et à différents pH (à gauche), et NaOH 0.1 M sans ou avec l'ajout de différentes concentrations de $NaClO_4$ (à droite). La vitesse de balayage est de 10 mV s^{-1}. Les chargements de l'électrode en catalyseur et en carbone sont identiques, de 91 µg cm^{-2}.

Parmi les trois oxydes étudiés, le MnOOH est le plus fortement affecté par la concentration en OH^-. Les CVs montrent deux pics anodiques à des potentiels très différents, et un large pic cathodique accompagné d'un épaulement (résultant probablement d'un chevauchement de deux pics cathodiques). Le pic à haut potentiel montre une plus forte dépendance au pH (avec environ 20 mV par pH) par rapport à son homologue à bas potentiel. Le rapport entre les intensités des deux pics anodiques dépend également de la concentration en OH^-, tandis que l'intensité relative des deux pics anodiques/cathodiques dépend de la concentration en Na^+ bien que leurs potentiels en soient presque indépendants (Fig. 5). Sur cette base, nous supposons que deux types de centres redox de Mn sont présents sur la surface du MnOOH. Le premier type de centres redox, qui est presque indépendant du Na^+, peut être caractérisé par l'équilibre suivant:

$$Mn(IV)=O + e^- + H_2O \rightarrow Mn(III)\text{-}OH + OH^- \quad (1)$$

Ou, bien:

$$Mn(IV)\begin{matrix}-OH\\-OH\end{matrix} + e^- \rightarrow Mn(III)\text{-}OH + OH^- \quad (1')$$

Le deuxième type de centres redox implique les cations de Na^+ :

$$Mn(IV)\begin{matrix}-ONa\\-OH\end{matrix} + e^- \rightarrow Mn(III)\text{-}ONa + OH^- \quad (2)$$

Il est intéressant de noter que les sites $Mn(IV)(OH)_2$ et Mn(IV)(OH)ONa montrent un comportement de recharge très différent. La recharge des sites Mn(OH)ONa se produit à des potentiels d'électrode plus bas et démontre une plus grande réversibilité (plus petite différence entre les potentiels des pics anodiques et cathodiques). Cette différence de potentiel entre les deux types de centres redox sur la surface de MnOOH peut provenir de la stabilisation des sites Mn(IV) par les cations Na^+, résultant en une diminution du potentiel formel de la transition redox interfaciale Mn(III)/Mn(IV). La couverture relative des deux types de centres dépend de la concentration en Na^+ , en raison de l'apparition des équilibres :

$$Mn(III)OH + Na^+ + OH^- \rightarrow Mn(III)ONa + H_2O \quad (3)$$

$$Mn(IV)\begin{matrix}-OH\\-OH\end{matrix} + Na^+ + OH^- \rightarrow Mn(IV)\begin{matrix}-ONa\\-OH\end{matrix} + H_2O \quad (4)$$

Pour Mn_2O_3, les pics anodiques et cathodiques dépendent à la fois du pH et de la concentration en Na^+, ce qui suggère que les cations entrent dans l'équilibre de la transition redox. L'E_f suit une dépendance suivante:

$$E_f = \text{const} - 0.058 \log (C_{Na^+}) \quad (5)$$

L'effet de la concentration en OH^- et en Na^+ pourrait être attribué à l'équilibre interfacial suivant, qui s'établit à l'interface Mn_2O_3/électrolyte :

$$Mn(IV)\begin{matrix}-ONa\\-OH\end{matrix} + e^- + H_2O \rightarrow Mn(III)\text{-}OH + 2OH^- + Na^+ \quad (6)$$

Pour Mn_2O_3, l'influence des cations Na^+ est similaire à celle observée pour MnOOH, *i.e.* deux paires de pics anodiques/cathodiques larges, avec des valeurs de E_f proches, qui se chevauchent. On peut supposer que les pics ne se déplacent pas avec la concentration en cations, mais c'est plutôt le rapport de leurs intensités qui change, ce qui entraîne le déplacement apparent du pic observé. Malheureusement, il est impossible de confirmer ou d'écarter cette hypothèse de manière fiable sur la base de l'ensemble des données disponibles en raison de la grande largeur des pics. Enfin, pour $LaMnO_3$ les pics redox sont quasi-indépendants de la concentration en Na^+, leur dépendance vis-à-vis du pH étant en accord avec l'équation de Nernst pour l'équilibre (1) ou (1').

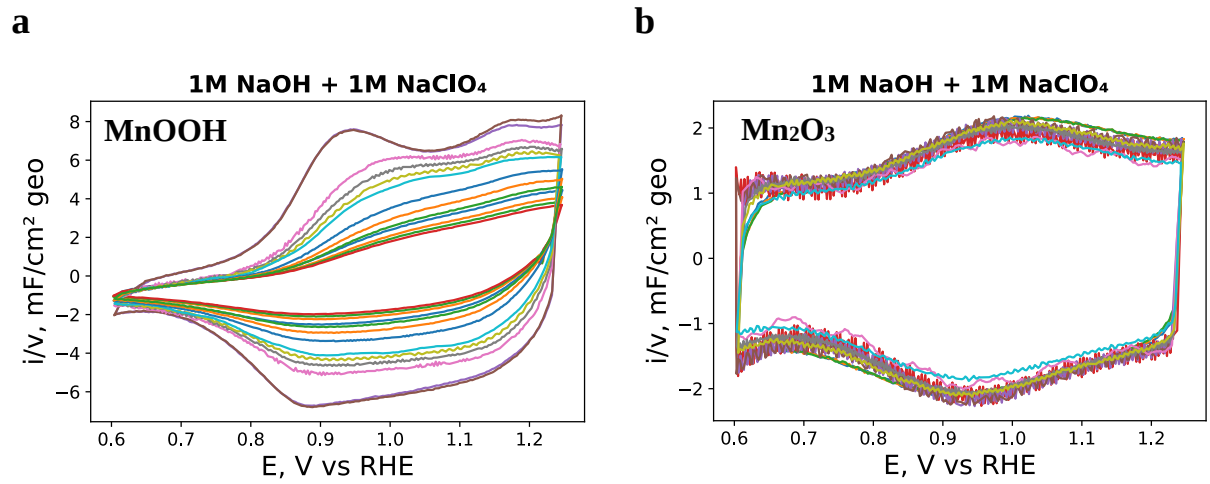

Fig. 6 Courbes de voltampérométrie cyclique (CV) acquises à différentes vitesses de balayage (de 10 à 1000 mV s^{-1}) dans l'électrolyte dégazé contenant du NaOH 1 M et du $NaClO_4$ 1 M pour MnOOH et Mn_2O_3. Les chargements de l'électrode en catalyseur et en carbone sont identiques, de 91 µg cm^{-2}. Les courants sont donnés par unité de surface géométrique de l'électrode.

L'étude de l'influence de la vitesse de balayage sur les courbes de voltampérométrie cyclique (CV) est utile pour délimiter les étapes électrochimiques "lentes" et "rapides". L'analyse de la Fig. 6 nous amène à conclure que pour le Mn_2O_3, la transition redox Mn(IV)/Mn(III) est rapide dans tous les électrolytes étudiés (cf. faible influence de la vitesse de balayage sur la forme du CV et sur la pseudo-capacité). En revanche, pour le MnOOH, la charge sous la CV et donc la pseudocapacité diminuent fortement avec la vitesse de balayage, ce qui indique la contribution d'étapes lentes au signal électrochimique. Ceci peut être attribué à l'intercalation de Na^+ dans la couche surfacique de l'oxyde MnOOH. De plus, la diminution de la concentration en OH^- conduit à une diminution de la cinétique de la transition redox à l'interface (étape 1, Fig. 1).

Pour mieux comprendre les phénomènes se produisant à l'interface oxyde/électrolyte, des titrages acidobasiques ont été réalisés, ce qui nous a permis de déterminer le point de charge zéro des matériaux étudiés (Tableau 3).

Tableau 3. Point de zéro charge (PZC) déterminé à partir de courbes de titration

Materiel	$LaMnO_3$	Mn_2O_3	MnOOH	Carbone Sibunit
PZC (unite de pH)	5.82	6.57	5.18	5.38

On peut voir que pour tous les oxydes étudiés, le PZC est inférieur à 7 (Tableau 3). Cela signifie qu'en milieu alcalin, ils sont tous chargés négativement et attirent donc le Na^+ de l'électrolyte.

2.2.2 Influence de la composition de l'électrolyte sur la cinétique de l'ORR et HPOR/HPRR

Influence de la concentration des cations Na^+

Nous commençons la discussion en analysant l'effet de la concentration en Na^+ sur la cinétique de l'HPOR/HPRR. Les Fig. 7a à 7d montrent que la concentration des cations Na^+ de l'électrolyte a une forte influence sur la cinétique de l'HPOR/HPRR, notamment pour MnOOH. En effet, on peut noter une diminution du potentiel mixte en présence de $NaClO_4$ et une augmentation du courant limite cathodique, qui devient dépendant de la vitesse de rotation de l'électrode.

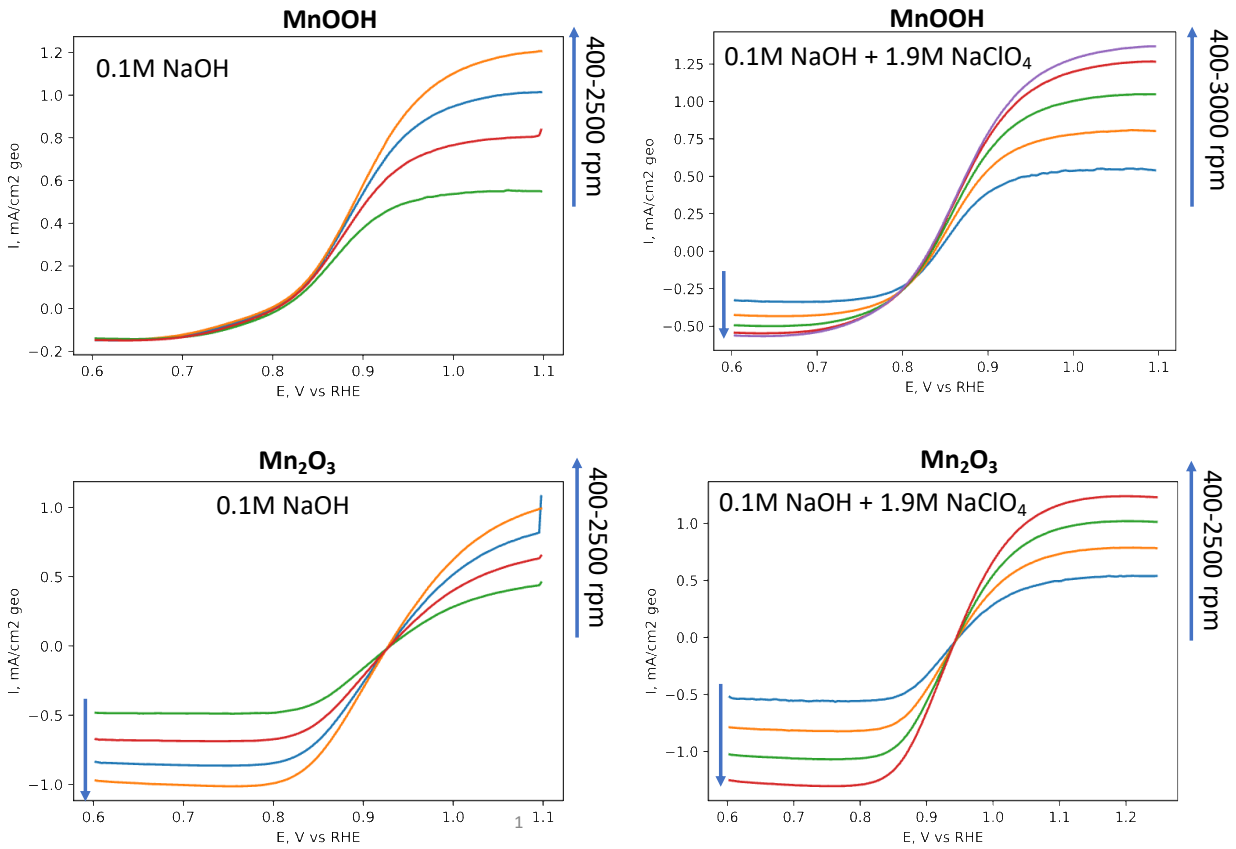

Fig. 7. Voltampérogrammes mesurés sur électrode à disque tournant pour MnOOH et Mn_2O_3 dans du NaOH 0.1 M et 0.84 mM en H_2O_2 avec ou sans ajout de $NaClO_4$ à différentes vitesses de rotation de l'électrode et à 10 mV s^{-1}. Les chargements de l'électrode en catalyseur et en carbone sont identiques, de 91 µg cm^{-2}.

Ces observations nous amènent à conclure que la constante de vitesse de l'étape de la rupture chimique de la liaison O-O (étape 5 du mécanisme ORR, *cf.* Fig. 1) augmente avec la concentration des cations Na^+. Ceci est probablement lié à une déprotonation de la surface de l'oxyde, c'est-à-dire un remplacement partiel des groupements -OH par des groupement -ONa, comme cela a été démontré précédemment pour l'oxyhydroxyde de Ni, NiOOH [5]. Des effets similaires sont également observés pour d'autres oxydes de Mn, mais dans une bien moindre mesure. Puisque le diamètre du Na^+ et supérieur à celui du H^+, on peut s'attendre à une distorsion des octaèdres de MnO_6 entraînant une augmentation de la largeur des canaux où se trouve Na^+, ainsi qu'une diminution de la taille des canaux dans lesquels se trouvent les protons (Fig. 8). Nikitina *et al.* [8] ont suggéré que la constante de vitesse significativement plus faible de l'étape de rupture O-O pour MnOOH par rapport à Mn_2O_3 est induite par une plus grande distance entre les cations de manganèse sur la surface, qui ne permet pas les interactions adsorbat-adsorbat (OH-O_2H), ces dernières diminuant la barrière d'activation sur la surface de Mn_2O_3.

Nous supposons que les changements structuraux survenant lors de l'intercalation de Na^+ conduisent à la convergence de certains centres de manganèse à l'interface, ces derniers favorisant les interactions adsorbat-adsorbat et donc la rupture des liaisons O-O à la surface du MnOOH en présence de Na^+ dans l'électrolyte. Dans le futur, il serait intéressant de vérifier cette hypothèse par des calculs de chimie quantique.

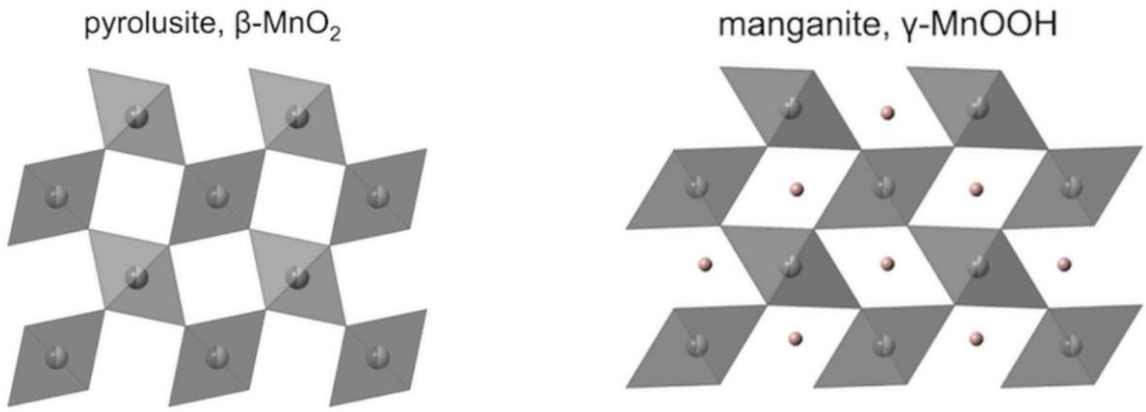

Fig. 8. Structures de β-MnO_2 et γ-MnOOH. Les cercles roses représentent les protons.

Dans le cadre de l'influence des cations sur la cinétique de l'ORR, les courbes de polarisation de l'ORR dans des électrolytes avec une concentration différente en Na^+ et un pH constant pour le Mn_2O_3, $LaMnO_3$, MnOOH et le carbone Sibunit sont présentés en Fig. 9a-d. Il convient de noter que la concentration des cations Na^+ influence à la fois le courant cinétique et le courant limite de diffusion. La concentration de Na^+ exerce une influence différente sur les trois oxydes étudiés, qui conduit à des variations de leur activité relative. En effet, le MnOOH, qui est beaucoup moins actif que $LaMnO_3$ pour une faible concentration de Na^+, atteint une activité similaire à celle de $LaMnO_3$ pour de fortes concentrations de Na^+. Comme discuté ci-dessus, la vitesse de l'étape 5 augmente avec la concentration de Na^+, affectant à la fois la cinétique de l'HPOR/HPRR et la cinétique de l'ORR. Toutefois, les constantes de vitesse des étapes 2 et 3 semblent également être affectées par la concentration de Na^+.

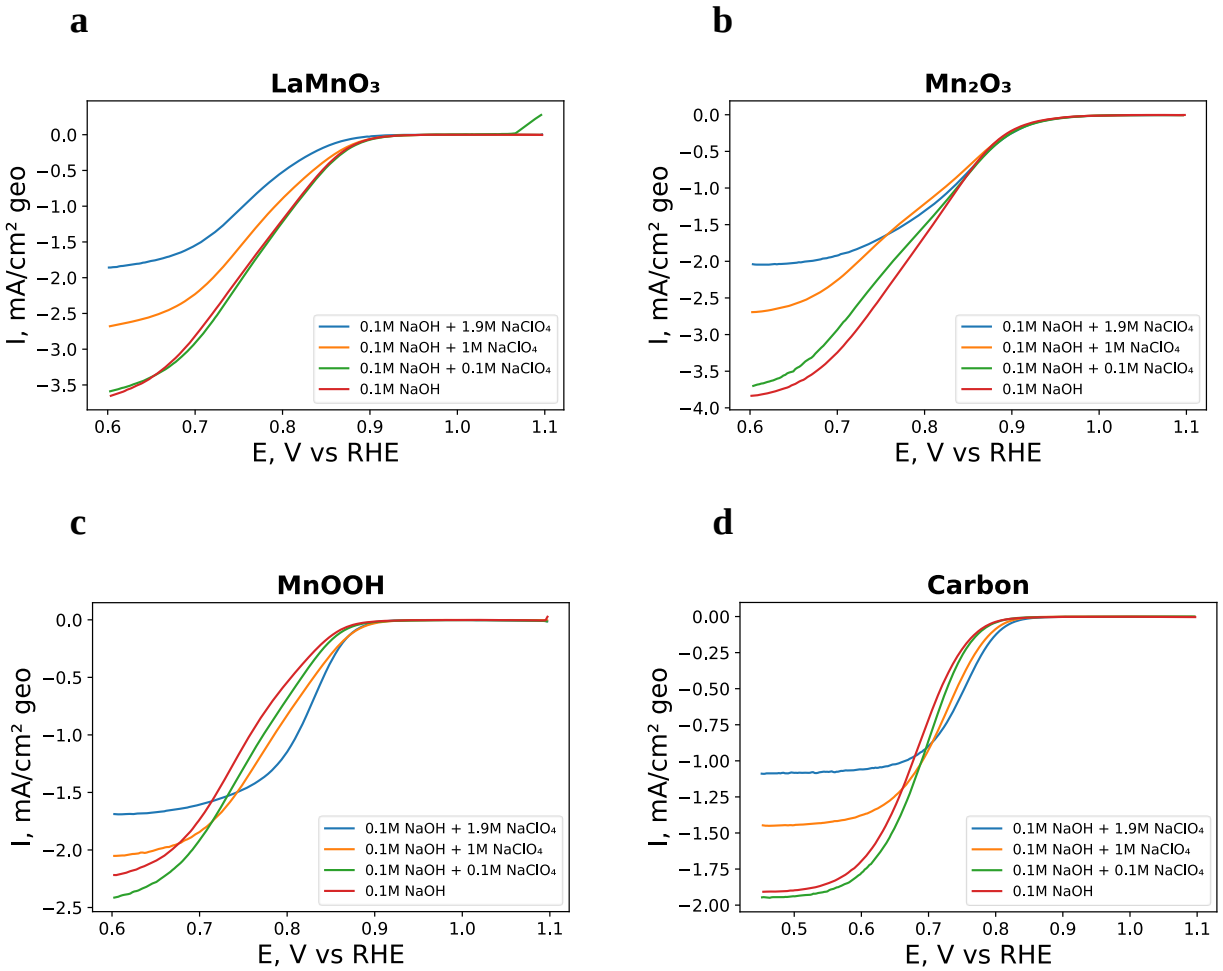

Fig. 9 Voltampérogrammes mesurés sur électrode à disque tournant dans l'électrolyte saturé en O_2 au pH constant et $NaClO_4$ concentrations différentes pour Mn_2O_3, $LaMnO_3$, MnOOH et carbone Sibunit. Les courbes de polarisation sont présentées à une vitesse de rotation de 900 rpm. La vitesse de balayage est de 10 mV s^{-1}. Les chargements de l'électrode en catalyseur et en carbone sont identiques, de 91 µg cm^{-2}.

Influence du pH

Pour l'ensemble des matériaux étudiés, les courbes de polarisations (Fig. 10a à 10c) présentent un décalage vers les potentiels positifs concomitant à l'augmentation du pH. Pour le carbone Sibunit, le décalage des voltammogrammes ORR est de ~ +30 mV/pH à l'échelle de l'électrode à hydrogène réversible (RHE). Ce décalage est purement thermodynamique, il est en accord avec une réduction de O_2 en HO_2^- à deux électrons se produisant à la surface de carbone dans l'intervalle de pH étudié. Cette dépendance plaide en faveur d'une étape cinétiquement déterminante inhérente à un transfert d'électrons couplé aux protons sur le carbone. Cependant, étant donné que le pH affecte également la charge de l'électrode et la double couche électrique, cette conclusion n'est pas sans ambiguïté et nécessite des investigations supplémentaires.

Pour les oxydes, un décalage plus faible est observé avec le pH. Cependant, l'effet du pH n'est pas le même pour les différents oxydes. Puisque l'échelle RHE est elle-même dépendante du pH (déplacement de 60 mV négatif par unité de pH), pour aider à la compréhension, les voltammogrammes ORR ont également été comparés sur l'échelle de l'électrode standard à hydrogène, SHE (cf. annexe). Nous avons observé qu'à faibles courants, l'ORR est également dépendante du pH sur l'échelle de SHE, ce qui suggère que l'étape cinétiquement déterminante dans cette gamme de potentiel implique un transfert de protons. Il faut toutefois garder à l'esprit que le carbone est ajouté comme liant à la couche catalytique et qu'en milieu alcalin, celui-ci agit comme co-catalyseur de l'ORR. Cela complique l'analyse de l'influence du pH sur la cinétique de l'ORR. On constate que non seulement la cinétique de l'ORR mais également la cinétique de HPOR/HPRR est affectée par le pH (cf. Fig. 10).

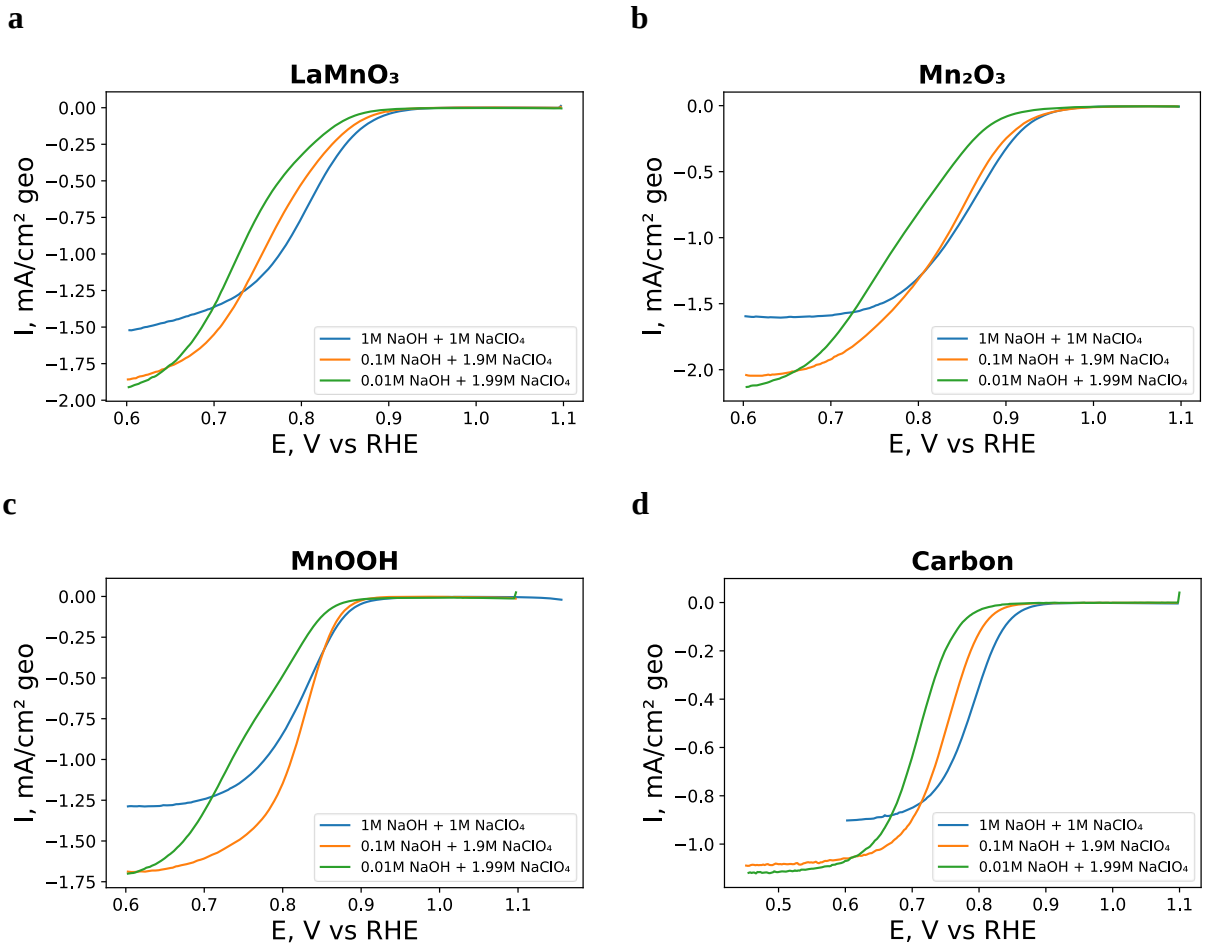

Fig. 10 Voltampérogrammes mesurés sur électrode à disque tournant pour l'ORR dans les électrolytes saturé en O_2, au pH différents et à une force ionique constante, pour Mn_2O_3, $LaMnO_3$, MnOOH et carbone Sibunit. Les courbes de polarisation sont présentées à une vitesse de rotation de 900 rpm. La vitesse de balayage est de 10 mV s^{-1}. Les chargements de l'électrode en catalyseur et en carbone sont identiques, de 91 µg cm^{-2}.

Une comparaison des voltampérogrammes pour l'ORR et l'HPRR/HPOR suggère que nos résultats sont en accord avec du mécanisme de l'ORR proposé précédemment (Fig. 1). Pour le MnOOH, dans tous les électrolytes étudiés, le potentiel mixte (l'E_{mix}) est négatif par rapport à l''onset' de l'ORR, ce qui est en accord avec une cinétique de l'HPRR lente, car la réaction est limitée par l'étape lente de rupture de la liaison O-O (étape 5). En effet, selon Ryabova *et al.* [7], la cinétique lente de l'étape 5, comparée à celle des étapes 2 et 3, déplace E_{mix} vers les potentiels plus bas. Cependant, dans une solution saturée en O_2, la réduction de l'oxygène rend le courant résultant négatif (d'où un décalage positif de l''onset' de l'ORR par rapport à l'E_{mix}). Pour Mn_2O_3 et $LaMnO_3$ les voltampérogrammes de l'ORR et de l'HPRR/HPOR se croisent, ce qui confirme une cinétique significativement plus rapide de l'étape 5 sur ces deux oxydes (par rapport au MnOOH), en accord avec Ryabova *et al.* [2]. Avec une augmentation du pH et avec une augmentation de la concentration en Na^+, le potentiel mixte augmente pour tous les oxydes étudiés, avec l'effet le plus fort observé pour le MnOOH.

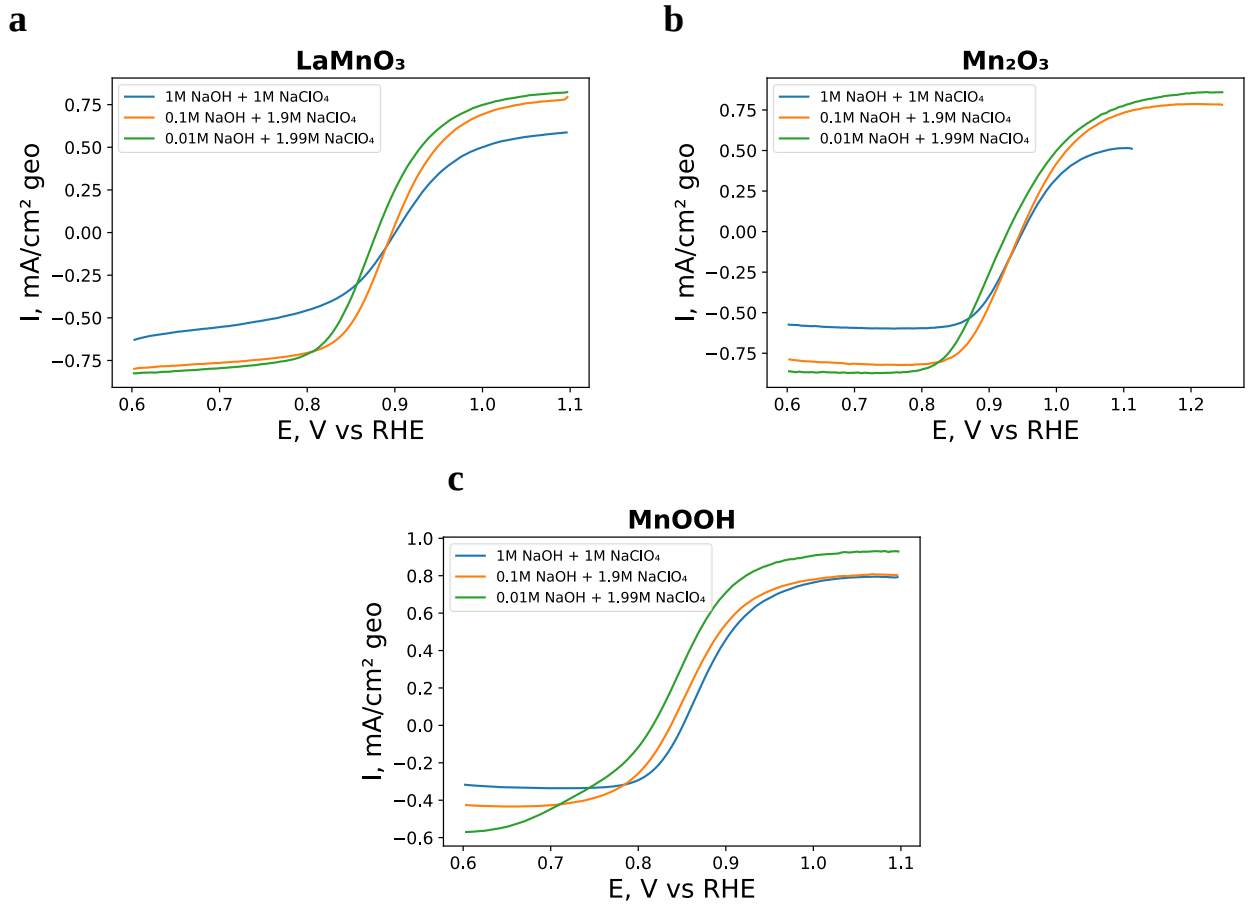

Fig. 11 Voltampérogrammes mesurés sur électrode à disque tournant pour $LaMnO_3$, Mn_2O_3, et MnOOH dans l'électrolytes au pH différents et une force ionique constante et en présence de 0.84 mM en H_2O_2. Les courbes de polarisation sont présentées à une vitesse de rotation de 900 rpm. La vitesse de balayage est de 10 mV s^{-1}. Les chargements de l'électrode en catalyseur et en carbone sont identiques, de 91 µg cm^{-2}.

3) Conclusion générale

Une série d'oxydes de manganèse à structure spinelle (Mn_3O_4, $MgMn_2O_4$, $CdMn_2O_4$ et $LiMn_2O_4$) a été synthétisée et caractérisée par DRX, adsorption d'azote, MEB, NEXAFS, XPS ainsi que par des méthodes électrochimiques.

Les résultats montrent que le Mn(II) à la surface du Mn_3O_4 est instable en présence d'oxygène et s'oxyde en Mn(III) et Mn(IV). Cette transformation s'observe dès lors où un échantillon sec est exposé à l'air et est favorisée lors d'un contact avec de l'eau ou du NaOH, entraînant probablement la perte de la structure spinelle sur la couche surfacique. Ainsi, l'activité du Mn_3O_4 pour la réaction de la réduction de l'oxygène (ORR) ne peut être attribuée à la structure spinelle, contrairement à ce qui a été fait dans la littérature. Par la suite, il a été démontré que le remplacement du Mn(II) dans la spinelle par certains cations inactifs à l'oxydoréduction est une stratégie viable pour améliorer leur stabilité pendant l'ORR. Parmi les trois oxydes spinelles AMn_2O_4 substitués (A = Li, Cd et Mg), seul la spinelle $MgMn_2O_4$ s'est avéré stable pendant l'ORR. Le $LiMn_2O_4$ perd des ions de lithium à la surface mais est susceptible de conserver sa structure spinelle grâce au remplacement du lithium par des protons.

Tous les oxydes de type AMn_2O_4 ici étudiés sont actifs pour l'ORR, $LiMn_2O_4$ et $MgMn_2O_4$ étant les plus actifs. Néanmoins, il convient de noter que l'activité spécifique des spinelles AMn_2O_4 est similaire à celle de MnOOH mais nettement inférieure à l'activité du Mn_2O_3. Pour tous les spinelles étudiés, la réduction de H_2O_2 se produit via une étape chimique lente, étant donné que le courant ne dépend ni du potentiel, ni de la vitesse de rotation, entre 0.6 et 0.8 V vs. RHE. Le $LiMn_2O_4$ présente la cinétique la plus rapide pour l'étape chimique, ce que nous attribuons au remplacement du lithium par le proton et à la formation du spinelle $Li_{1-x}H_xMn_2O_4$ à la surface du matériau.

L'étude de l'influence de la composition de l'électrolyte sur la cinétique de l'ORR et de l'HPRR/HPOR à la surface d'oxydes de Mn (MnOOH, Mn_2O_3 et $LaMnO_3$) a montré que non seulement les vitesses de réaction mais aussi l'activité relative des matériaux sont affectés par la composition de l'électrolyte (concentration de Na^+ et de OH^-). Il a été constaté que la concentration de $NaClO_4$ exerce une forte influence sur la constante de vitesse de l'étape de la rupture chimique de la liaison O-O dans l'intermédiaire réactionnel -OOH (l'étape 5 du mécanisme), avec l'effet le plus important observé pour MnOOH. Par ailleurs, les résultats indiquent que, sur Mn_2O_3, la concentration de Na^+ impacte principalement la première étape de l'ORR.

L'influence du pH étant différente en fonction de la nature de l'oxyde métallique, il aura été établi, dans la continuité d'études réalisées à l'ICPEES, que l'étape cinétiquement déterminante est dépendante du type d'oxyde [2].

Dans l'ensemble, les résultats de ce chapitre sont en accord avec le mécanisme ORR "en série" proposé précédemment, se produisant par la formation intermédiaire de peroxyde d'hydrogène, comprenant des étapes de transfert d'électrons couplés à des protons et une étape chimique de rupture de la liaison O-O.

Enfin, une modélisation cinétique est nécessaire afin de mieux comprendre l'effet du pH et des différents cations de l'électrolyte sur la cinétique et le mécanisme de l'ORR sur des oxydes de Mn.

4) Références

[1] R.D. Shannon, Revised effective ionic radii and systematic studies of interatomic distances in halides and chalcogenides, Acta Cryst A. 32 (1976) 751–767. https://doi.org/10.1107/S0567739476001551.

[2] A.S. Ryabova, F.S. Napolskiy, T. Poux, S.Ya. Istomin, A. Bonnefont, D.M. Antipin, A.Ye. Baranchikov, E.E. Levin, A.M. Abakumov, G. Kéranguéven, E.V. Antipov, G.A. Tsirlina, E.R. Savinova, Rationalizing the Influence of the Mn(IV)/Mn(III) Red-Ox Transition on the Electrocatalytic Activity of Manganese Oxides in the Oxygen Reduction Reaction, Electrochimica Acta. 187 (2016) 161–172. https://doi.org/10.1016/j.electacta.2015.11.012.

[3] M. Pourbaix, H. Zhang, A. Pourbaix, Presentation of an Atlas of Chemical and Electrochemical Equilibria in the Precence of a Gaseous Phase, MSF. 251–254 (1997) 143–148. https://doi.org/10.4028/www.scientific.net/MSF.251-254.143.

[4] M. Jayalakshmi, M. Mohan Rao, F. Scholz, Electrochemical Behavior of Solid Lithium Manganate ($LiMn_2O_4$) in Aqueous Neutral Electrolyte Solutions, Langmuir. 19 (2003) 8403–8408. https://doi.org/10.1021/la0340448.

[5] O. Diaz-Morales, D. Ferrus-Suspedra, M.T. M. Koper, The importance of nickel oxyhydroxide deprotonation on its activity towards electrochemical water oxidation, Chemical Science. 7 (2016) 2639–2645. https://doi.org/10.1039/C5SC04486C.

[6] P.N. Ross Jr, Oxygen reduction reaction on smooth single crystal electrodes, in: Handbook of Fuel Cells, John Wiley & Sons, Ltd, 2010. https://doi.org/10.1002/9780470974001.f205035.

[7] A.S. Ryabova, A. Bonnefont, P. Zagrebin, T. Poux, R. Paria Sena, J. Hadermann, A.M. Abakumov, G. Kéranguéven, S.Y. Istomin, E.V. Antipov, G.A. Tsirlina, E.R. Savinova, Study of Hydrogen Peroxide Reactions on Manganese Oxides as a Tool To Decode the Oxygen Reduction Reaction Mechanism, ChemElectroChem. 3 (2016) 1667–1677. https://doi.org/10.1002/celc.201600236.

[8] V.A. Nikitina, A.A. Kurilovich, A. Bonnefont, A.S. Ryabova, R.R. Nazmutdinov, E.R. Savinova, G.A. Tsirlina, ORR on Simple Manganese Oxides: Molecular-Level Factors Determining Reaction Mechanisms and Electrocatalytic Activity, J. Electrochem. Soc. 165 (2018) J3199. https://doi.org/10.1149/2.0261815jes.

[9] M. Toupin, T. Brousse, D. Bélanger, Charge Storage Mechanism of MnO_2 Electrode Used in Aqueous Electrochemical Capacitor, Chem. Mater. 16 (2004) 3184–3190. https://doi.org/10.1021/cm049649j.

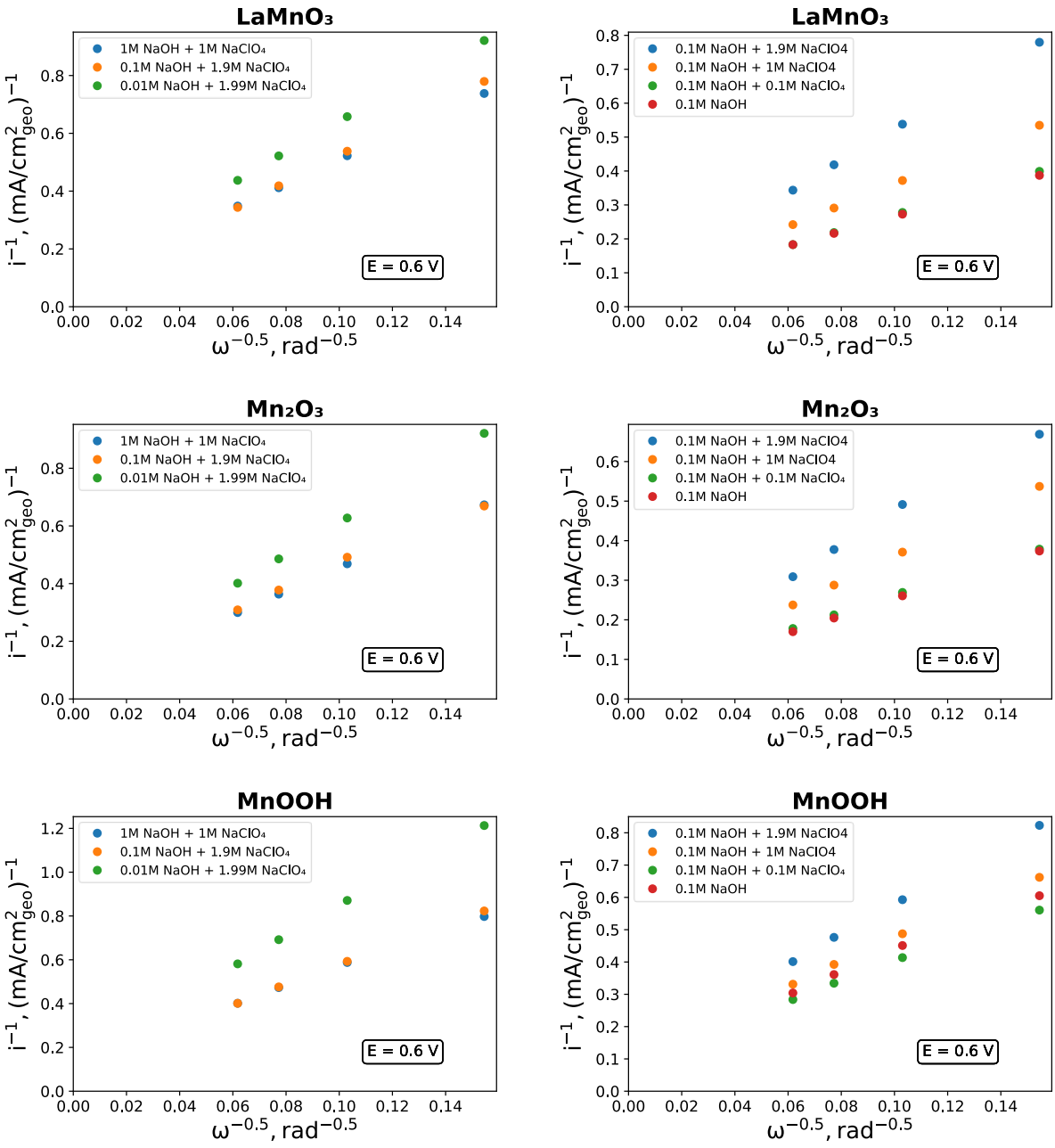

Fig. S12 Koutecký–Levichplots of cathodic currents for Mn_2O_3, $LaMnO_3$, MnOOH. calculated from Fig. S11.

Kirill DOSAEV

Composés à base de Mn (III): synthèse et propriétés électrocatalytiques dans la réaction de réduction de l'oxygène

Résumé

De nombreux travaux de recherche étudient la réaction de réduction de l'oxygène (ORR). En effet, d'importants processus technologiques découlent de cette réaction. Cependant, malgré de récentes avancées, il existe encore des lacunes dans la compréhension des étapes clés de l'ORR et des facteurs affectant sa cinétique. Cette thèse est consacrée à (i) l'étude de l'influence de la composition des oxydes spinelles de Mn sur leur stabilité et leur activité pour l'ORR, et (ii) l'effet de la composition de l'électrolyte (pH et concentration en Na^+) sur l'interface oxyde de Mn/électrolyte et sur la cinétique ORR. Alors que Mn_3O_4 est instable dans les conditions de l'ORR, il a été observé que la substitution de Mn (II) par des cations inactifs électrochimiquement permet d'améliorer la stabilité du spinelle. $MgMn_2O_4$ est le composé le plus stable dans tous les tests de résistance effectués. Les résultats démontrent également une forte influence du pH et de la concentration des ions Na^+ de l'électrolyte sur le comportement électrochimique des oxydes de manganèse. MnOOH présente par exemple une amélioration significative de la cinétique de l'ORR avec la concentration en cations. Ceci est attribué à l'augmentation de la cinétique de l'étape de rupture de liaison O-O dans l'intermédiaire H_2O_2.

Mots clés : Oxydes de Mn (III), spinelle, réaction de réduction de l'oxygène (ORR), oxydation et réduction du peroxyde d'hydrogène, effet du pH, effet du cation

Résumé en anglais

The oxygen reduction reaction (ORR) attracts close attention of researchers since it underlies many technologically important processes. Despite significant recent advances, there are still important fundamental gaps in understanding the key steps of the ORR and factors affecting its kinetics. The thesis is devoted to (i) the study of the influence of the composition of the Mn spinel oxides on their stability and ORR activity, and (ii) the effect of electrolyte composition (pH and Na^+ concentration) on the Mn oxide/electrolyte interface and on the ORR kinetics. While Mn_3O_4 is unstable under the ORR conditions, Mn (II) substitution by red-ox inactive cations allows to enhance spinel stability, $MgMn_2O_4$ being the most stable in all stress tests. Results of the second part of the work show a strong influence of pH and concentration of Na^+ ions on the electrochemical behavior of manganese oxides. The strongest effect is discovered for MnOOH, which exhibits significant enhancement of the ORR kinetics with the cation concentration. This is ascribed to the increase in the kinetics of the O-O bond-breaking step in the H_2O_2 intermediate.

Keywords: Mn (III)-containing oxides, spinel, oxygen reduction reaction (ORR), hydrogen peroxide reactions, pH effect, cation effect.